ASSESSMENT OF DEFECTS IN FERROMAGNETIC METALS WITH EDDY CURRENTS

A thesis submitted for the degree of Doctor of Philosophy

by

Susan Rosemary Owen

Department of Physics

Brunel University

Uxbridge, Middlesex.

December 1989

This thesis is dedicated to all those friends and relatives who suffered me throughout this work, especially my husband, Mr. R. Elsdon.

ABSTRACT

A study was made to identify and size surface breaking defects in ferromagnetic materials with eddy currents, whilst eliminating unwanted signals due to changes in magnetic permeability and probe lift-off. The former was overcome by the use of high frequencies and the latter by utilising the lift-off to characterise the defects. The lift-off or "touch" method was shown to be advantageous in that one could test steel objects having irregular surfaces, such as occurring with the presence of welds.

In addition a theoretical investigation was undertaken to relate changes in the magnetic permeability, electrical conductivity and values of lift-off to the components of impedance of a detecting coil located above the plane surface of a ferromagnetic metal. The resultant theory was confirmed by experimental measurements.

ACKNOWLEDGEMENTS

I would like to thank my supervisor Dr. J. Blitz for his advice and support throughout this work. My gratitude is also due to my fellow researchers Dr. N.T. Hajian, Mr. V. Willstatter and Mr. D. Walsh for their collaboration in parts of this thesis. Encouragement and support were also gratefully received from Professor D.C. Imrie, Mr. R.B. Hall, Mr. K. Schlachter, Mr. F. Goodliffe and Mr. L. Lightowler of the Physics department of Brunel University. Measurements of real defects were aided by Mr. D. Topp of University College, London, and Mr. A. Raine and his team at E.R.S., British Gas, Killingworth, Newcastle-Upon-Tyne.

Special thanks are due to my sponsors for this work, British Gas plc. On-Line Inspection Centre, Cramlington, Newcastle-Upon-Tyne, especially to Dr. L. Morgan for his constructive comments, patience and encouragement.

ASSESSMENT OF DEFECTS IN FERROMAGNETIC METALS WITH EDDY CURRENTS

CONTENTS

CHAPTER 1

INTRODUCTION

The eddy current method [1,2] is well established in the nondestructive testing of metals for detecting flaws such as cracks and for measuring differences in electrical conductivities and magnetic permeabilities. The main advantages of this method are that no direct contact with the object being tested is necessary and it is quick, clean and readily lends itself to automation. For flaw detection in ferromagnetic materials difficulties arise because the detecting coil responds to changes in the magnetic permeability and electrical conductivity of the metal as well as to the presence of defects. In the investigations described here eddy currents were used to evaluate surface breaking cracks in ferromagnetic materials whilst eliminating the unwanted signals caused by changes in magnetic permeability, electrical conductivity and lift-off.

Studies were made of the variations in the resistive, R, and inductive, ωL, components of impedance of a detecting coil with changes in electrical conductivity σ, magnetic permeability μ, lift-off, i.e., vertical height of the coil from the surface of the sample, and defect size.

Much of the early theoretical work in eddy current testing was carried out by Förster [3], who analysed the components of impedance of an encircling coil, assumed to be of infinite length, encircling infinitely long defect-free metal rods and tubes (Section 2.1). The tests were standardised by normalising the values of the components of impedance of the coil, by dividing them by the values with the coil empty, i.e., $R/\omega L_0$ and $\omega L/\omega L_0$. These components were related to a parameter called the normalised frequency, $f_0 = \omega\mu\sigma a^2$, where a is the radius, σ the electrical conductivity and μ the

magnetic permeability of the rod. For air and all other non-ferromagnetic materials μ can be considered equal to $\mu_0 = 4\pi \times 10^{-7}$ Hm^{-1}, the magnetic permeability of free space. For ferromagnetic materials, $\mu = \mu_r \mu_0$, where μ_r is the relative permeability. Förster considered initially a non-ferromagnetic rod with the rod completely filling the coil. He then considered the more general case where the cross-section of the rod did not fill t hat of the coil, by introducing the term fill-factor $\eta = a^2 / r^2 \leq 1$, where r is the radius of the coil. Values of $R/\omega L_0$ and $\omega L/\omega L_0$ were plotted for different values of η and f_0 (Fig. 2.1). From these curves the components of impedance of any coil encircling any non-ferromagnetic rod at any frequency could be predicted theoretically. For a coil encircling a ferromagnetic rod it was assumed that μ_r was constant. He showed that the values of both components of impedance were increased by the value of μ_r and that a change in μ_r changed both the normalised frequency and the flux leakage, i.e., as indicated by changes in η (Section 2.1). In practice, because coils and samples have finite lengths, Förster's analysis provides only an approximation, because of magnetic flux leakage at the ends of the coil and sample. Freeman and El-Markabi [4] and Dodd and Deeds [5] analysed the components of impedance of a coil of finite length encircling a non-ferromagnetic rod. Freeman and El-Markabi [4] attempted to represent the coil by an equivalent circuit of non-uniform transmission lines. Dodd and Deeds [5] considered the vector potential $\underline{A}$ of the coil and found solutions from which the components of impedance of the coil could be calculated. The values of the components of impedance obtained theoretically agreed well with experimental values.

The impedance of a surface-scanning coil is more difficult to analyse than that of an encircling coil because of the lack of symmetry about the x-y plane, where the axis of the coil lies in the z-direction, and the large leakage of magnetic flux associated with it.

Cheng [6] and Burrows [7] studied the impedance of a single loop circular coil in the vicinity of a semi-infinite plane of a non-ferromagnetic metal and Dodd and Deeds [5] and Dodd [8] superpositioned a number of these coils to model a "pancake coil ", i.e., a multi-turn coil of large radius-to-length ratio, of finite cross-section. They assumed symmetry about the z-axis and produced a theory, summarised in Section 2.2, to predict the components of impedance of the coil, by analysing the vector potential $\underline{A}$ which is symmetric about the axis of the coil. Because of difficulties involved with an analytical approach, Dodd et al. [9] then used a numerical finite element technique to evaluate the normalised components of impedance of the coil when located above a thick plate with two layers of conducting material and developed a complicated computer program to predict the changes of impedance [10]. Hajian and Blitz [11,12] adapted the theory of Dodd and Deeds, to evaluate analytically the normalised components of impedance of air-cored solenoid coils of finite length above a thick plate of a non-ferromagnetic metal. They related $R/\omega L_0$ and $\omega L/\omega L_0$ to f_0, given by $f_0 = \omega\mu\sigma r^2$, and normalised lift-off, h/r, where r is the radius of the coil. Here h/r is analogous to the fill-factor, η, used in the analysis for encircling coils. Numerical evaluations could be made using a simple program in BASIC suitable for use with a personal computer [13]. The theory can also be applied to a coil with a ferrite core, because the latter only alters the properties of the coil, i.e., by reducing the flux leakage at the ends of the coil, thus increasing the effective normalised length of the coil.

The theory of Hajian and Blitz can be applied to samples of ferromagnetic materials which have been saturated magnetically to reduce the recoil magnetic permeability to a value approaching that of free space, μ_0 (Section 5). However, it is not always practical to provide an effective degree of saturation, especially with surface-scanning coils, and the magnetic permeability changes non-linearly with applied magnetic field according to the magnetic state, as determined by the composition and history of the

material resulting from for example, heat treatment, method of manufacture and residual magnetism [14]. A definition of magnetic permeability appropriate to a given situation is necessary [15] and this may increase difficulties in the analysis of a coil in the vicinity of a ferromagnetic metal. In the investigations described here the recoil permeability was considered the most appropriate one to use (Section 5).

Deeds and Dodd [16] used a numerical method of finite differences to analyse the normalised components of impedance of a coil encircling a defect-free ferromagnetic rod. They calculated the contribution to the vector potential $\underline{A}$ from each point in a network of coarse and fine lattices and produced a highly involved computer program to calculate the values of the normalised components of impedance of the coil. In this report the work of Hajian and Blitz was modified to make analytical predictions of the normalised components of impedance of a solenoid coil of finite length above the plane surface of a ferromagnetic material (Section 3). A value of the recoil permeability of a steel sample was estimated [17] by comparing the depth of penetration of eddy currents in the sample with that in a sample of a non-ferromagnetic metal (Section 5) and the theory was confirmed by experiment (Chapter 6).

Difficulties arise when predictions are needed to characterise the effects of a flaw on the impedance of an eddy current coil, because the symmetry on which the theoretical analysis depends is removed on the introduction of a flaw, but some success has been achieved using numerical methods of analysis to model defects [18-26]. The eddy currents may also take differing paths around a defect. Förster [3] modelled flaws experimentally in non-ferromagnetic tubes and cylinders by inserting pieces of plastic in models of mercury contained by glass, to predict the changes of impedance of an encircling coil due to a flaw. Cecco and Bax [27] studied defects experimentally in ferromagnetic tubes of low magnetisation intensity, by saturating the area of interest so as to remove the interfering effects of changes in magnetic permeability within the tube. In this report the effects of changing magnetic

permeability, electrical conductivity and coil lift-off on the prediction of the depth of a crack were assessed with surface-scanning coils, using fine saw cuts to simulate surface breaking cracks (Section 7).

In theory, any unwanted signals from changes in magnetic permeability and lift-off could be eliminated by the use of multifrequencies [1,2], but in practice this is not always possible. The effects of magnetic permeability were minimised by using high values of frequency. The changes in lift-off were applied constructively in the development of the lift-off or "touch" method of eddy current testing [28], (Section 8.2). This method was used to assess the size of defects in different ferromagnetic samples containing fatigue cracks, and the results were compared either with those from magnetic particle and ACPD methods [1], or by direct measurement after breaking open the samples. In general the predictions of defect sizes made using the touch method were found to be in good agreement with the sizes found using the other methods.

CHAPTER 2

THE NATURE OF EDDY CURRENTS AND THEIR DETECTION

Here the analyses of the real (R) and imaginary (ωL) components of impedance of both encircling and surface-scanning coils are described briefly, with respect to the properties of the sample in which the eddy currents are induced. Eddy currents are induced within a conducting material when a coil carrying an alternating current is placed in the vicinity (Fig.2.1). The factors affecting eddy current induction are frequency of inducing current, the geometry of and distance between the coil and conducting sample, the electrical conductivity σ and magnetic permeability μ of the metal.

The impedance analysis of coils in the vicinity of a conductor are based on Maxwell's equations of electromagnetism, which describe the behaviour of an electric field $\underline{E}$ and magnetic field $\underline{H}$ around a conductor [29],

$$\text{div}\,\underline{H} = \nabla.\underline{H} = 0 \qquad (2.1)$$

$$\text{curl}\,\underline{E} = \nabla x\underline{E} = -\mu\partial\underline{H}/\partial t, \qquad (2.2)$$

$$\text{curl}\,\underline{H} = \nabla x\underline{H} = \sigma\underline{E} \qquad (2.3)$$

from which it can easily be shown that

$$-\nabla^2\underline{H} = -\mu\sigma\partial\underline{H}/\partial t \qquad (2.4)$$

The analysis of the impedance of an infinitely long coil encircling a rod, developed originally by Förster [3], is outlined in Section 2.1 and in Section 2.2 the analysis performed by Dodd and Deeds [5] of the impedance of a pancake coil above a flat surface of metal is described briefly.

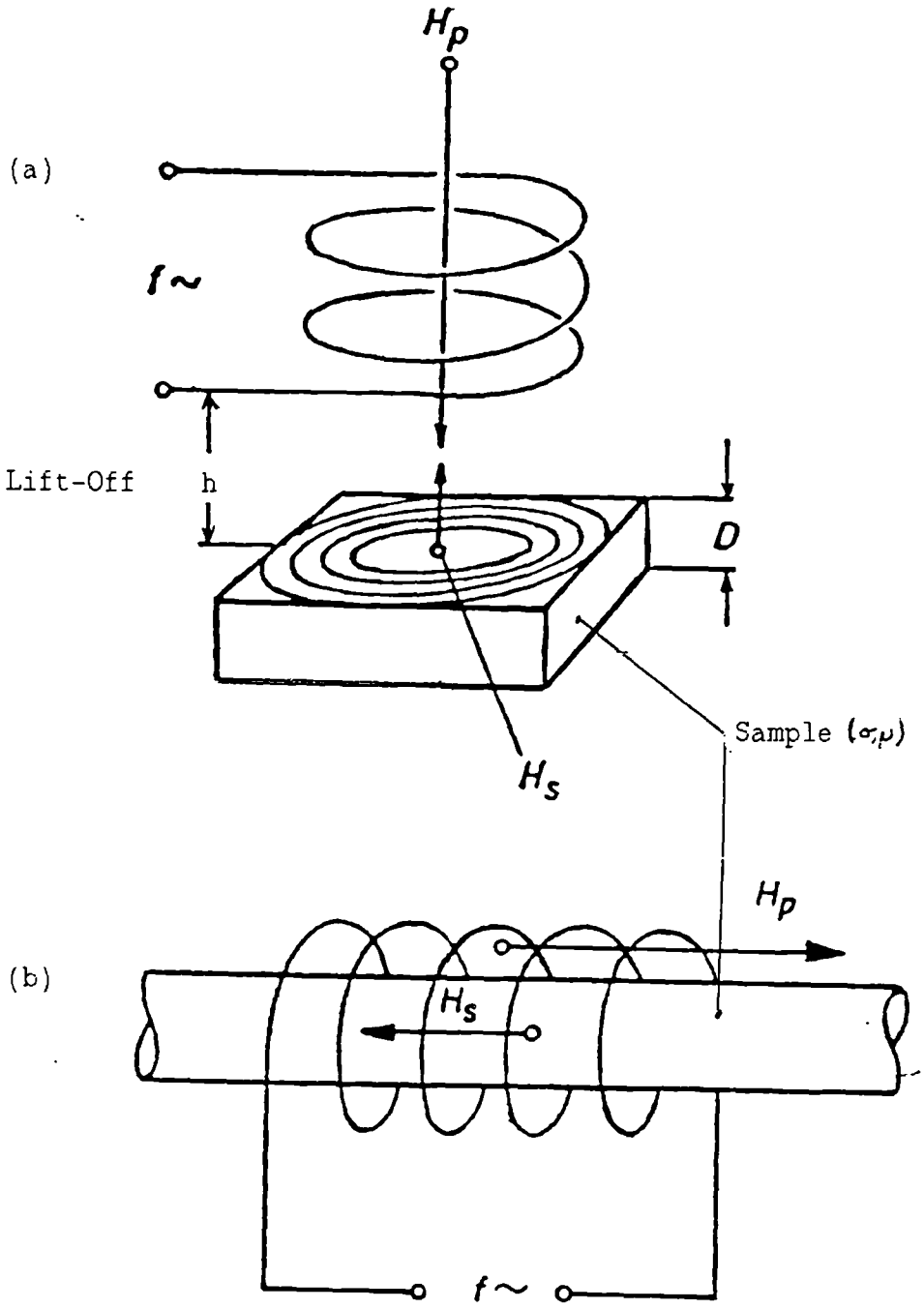

Figure 2.1: The induction of eddy currents in metals

(a) Surface-scanning coil above a flat plate

(b) Metal rod within a cylindrical encircling coil

H_p = Primary field of the coil in the absence of a test object

H_s = Secondary field produced by eddy currents in the test object

2.1 Förster's Impedance Analysis for a Coil Encircling a Rod

Förster [3] considered a coil of infinite length encircling an infinitely long rod of metal, and related the real (R) and imaginary (ωL) components of impedance of the coil with the rod present to the impedance of the coil away from any metal, ωL_0, as summarised below. He also applied the method of analysis to infinitely long tubes[1]

If $\underline{H}_0$ is the r.m.s. intensity of the magnetic field induced in a coil of radius r_0, carrying an alternating current at a frequency $f = \omega/2\pi$, then the r.m.s. magnetic flux density, $\underline{B}_0$, can be given by

$$\underline{B}_0 = \mu_0 \underline{H}_0 \tag{2.5}$$

where $\mu_0 = 4\pi \times 10^{-7}$ H/m is the magnetic permeability of free space. Both $\underline{H}_0$ and $\underline{B}_0$ are assumed to be constant across the cross-section of the coil if it is long.

When a metal sample of radius a is introduced, completely filling the coil, i.e., $a = r$, then the magnetic flux is changed to a value $\underline{B}$, due to induced eddy currents in the sample,

$$\underline{B} = \mu_r \mu_0 \underline{H}. \tag{2.6}$$

where μ_r is the magnetic permeability of the metal relative to air.

The flux within a conductor is not constant across its cross-section, but tends to concentrate close to the surface due to a phenomenon known as the skin effect (Fig. 2.2(a)). Förster introduced a complex quantity called effective permeability (μ_{eff}) to represent the field within the coil as being distributed constantly (Fig. 2.2(b)), where

$$\mu_{eff} = B_{mean}/\mu_r \underline{B}_0 = |\mu_{eff}| \cos\theta + j|\mu_{eff}| \sin\theta \tag{2.7}$$

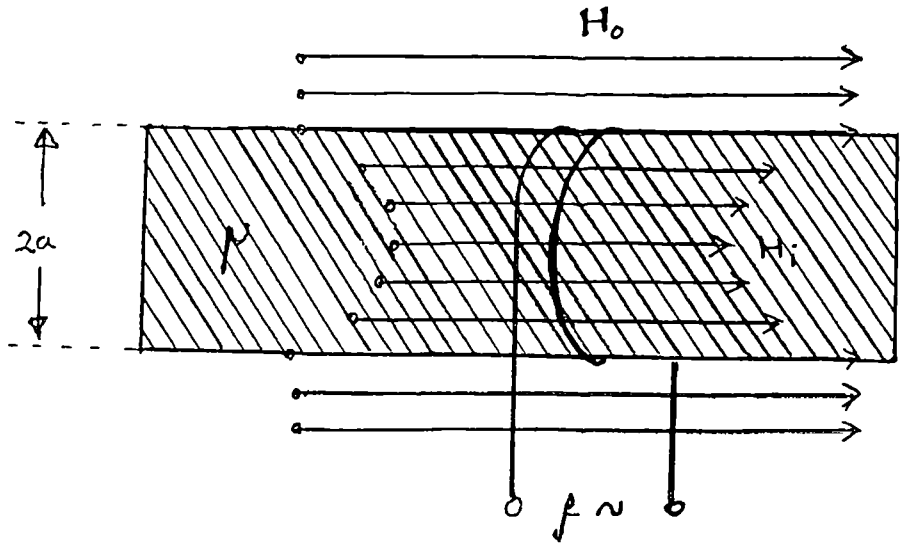

(a) Normal distribution when a metal sample is present

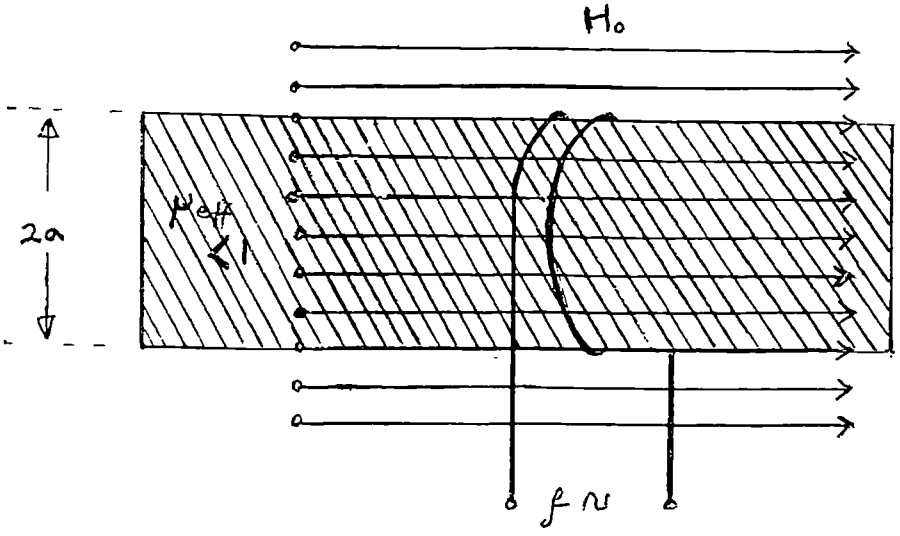

(b) Förster's constant disatribution, assuming an effective permeability less than unity and a constant field H_0.

Figure 2.2: Schematic representation of the distribution of magnetic fields within a test coil.

From Maxwell's equations the field $\underline{B}$ can be given by (equation 2.4)

$$\nabla^2\underline{B} = \mu\,\sigma\,\partial\underline{B}/\partial t \qquad (2.8)$$

If B varies periodically with frequency such that $\underline{B} = \underline{B}_0.\exp(-jwt)$, then equation (2.8) can be written

$$\nabla^2\underline{B} = j\omega\mu\sigma\,\underline{B} = k^2\underline{B} \qquad (2.9)$$

where $k^2 = j\omega\mu\sigma$.

Expressed in terms of cylindrical co-ordinates, this equation becomes

$$(1/r)\,\partial/\partial r\,(r\partial\underline{B}/\partial r) + (1/r^2)\partial^2\underline{B}/\partial\theta^2 + \partial^2\underline{B}/\partial z^2 = k^2\underline{B} \qquad (2.10)$$

where r, θ represent the polar co-ordinates in the x-y plane, and because $\underline{B}$ only varies in the direction of r, equation (2.10) can be written in the non-vectorial form:

$$\partial^2B/\partial r^2 + (1/r)\,\partial B/\partial r - k^2B = 0 \qquad (2.11)$$

This is a modified form of Bessel's equation of the zeroth order [30]. At the surface of the rod, i.e., at $r = a$, $B = \mu_r\mu_0H = \mu_r B_0$

and at $r = 0$, $B = \mu_r B_0 J_0(kr)/J_0(ka)$ (2.12)

where $J_0(kr)$ and $J_0(ka)$ are Bessel functions of zeroth order.

The total flux Φ over the cross-section of the coil is given by

$$\Phi = 2\pi\int_0^a B.r.dr = \pi a^2 B_{mean} \qquad (2.13)$$

Therefore from equation (2.12),

$$B = \{2\mu_r B_0/a^2 J_0(ka)\}\int_0^a r.J_0(kr)\,dr \qquad (2.14)$$

The solution to the integral is [31]:

$$\int_0^a r.J_0(kr)\,dr = \left[(r/k)\,J_1(kr)\right]_0^a = (a/k)\,J_1(ka) \qquad (2.15)$$

where $J_1(kr)$ and $J_1(ka)$ are Bessel functions of the first order.

Therefore from equations (2.13) to (2.15) and (2.7),

$$\begin{aligned} B_{mean} &= (2\mu_r B_0/ka)\,J_1(ka)/J_0(kr) \\ &= \mu_{eff}\,\mu_r B_0 J_1(ka)/J_0(kr) \end{aligned} \qquad (2.16)$$

In practice it is the impedance or voltage of the coil that is measured. If current is constant it can be shown that for a non-ferromagnetic metal the real and imaginary components of effective permeability are the resistive R, and inductive ωL, components of coil impedance, normalised with respect to the impedance of the coil away from any metal, ωL_0, as follows;

$$|\mu_{eff}| \cos\theta = \omega L/\omega L_0 = V_{imag}/V_0 \qquad (2.17a)$$

and

$$|\mu_{eff}| \sin\theta = R/\omega L_0 = V_{real}/V_0 \qquad (2.17b)$$

where L_0 and V_0 are the inductance and voltage respectively of the empty coil.

Because the sample cannot completely fill the coil, the expressions for coil impedance have to be modified. The ratio of the cross-sectional areas of the coil and the rod is called the "fill-factor" η, defined as

$$\eta = (r_{rod}/r_{coil})^2 = (a/r_0)^2 \le 1. \qquad (2.18)$$

The total flux within the coil becomes

$$\Phi_{tot} = \Phi_{metal} + \Phi_{air} = \pi r_0^2 B_{mean} \qquad (2.19)$$

The flux in the air is $\Phi_{air} = (r_0^2 - a^2) B_0 = (1 - \eta) B_0$ (2.20)

and the flux in the metal is

$$\Phi_{metal} = 2\pi \mu_r \int_0^a B.r.dr = (2\pi \mu_r a B_0 / k) J_1(ka) / J_0(ka) \qquad (2.21)$$

Therefore

$$\pi r_0^2 B_{mean} = \pi r_0^2 \{\eta \mu_r B_0 (2 / ka) J_1(ka) / J_0(ka)\} + (1 - \eta) \qquad (2.22)$$

$$= \pi r_0^2 B_0 \eta \mu_r \mu_{eff} + (1 - \eta)$$

hence $\omega L / \omega L_0 = V_{imag} / V_0 = (1 - \eta + \eta \mu_r \mu_{eff(real)})$ (2.23a)

and $R / \omega L_0 = V_{real} / V_0 = (\eta \mu_r \mu_{eff(imag)})$ (2.23b)

These equations take account of both non-ferromagnetic and ferromagnetic rods by using a value of relative magnetic permeability μ_r. The nature of μ_r should be considered with respect to the magnetic state of the material, discussed in Chapter 5. Fig. 2.3 shows the variations of the two components of normalised impedance with changes in $k^2a^2 = \omega\mu\sigma a^2$, known as the normalised frequency, for different values of fill-factor. Fig. 2.4 shows the variations of the components of impedance for different values of μ_r. A decrease in the sample radius to zero brings the value of coil impedance towards point A independently of the value of μ.

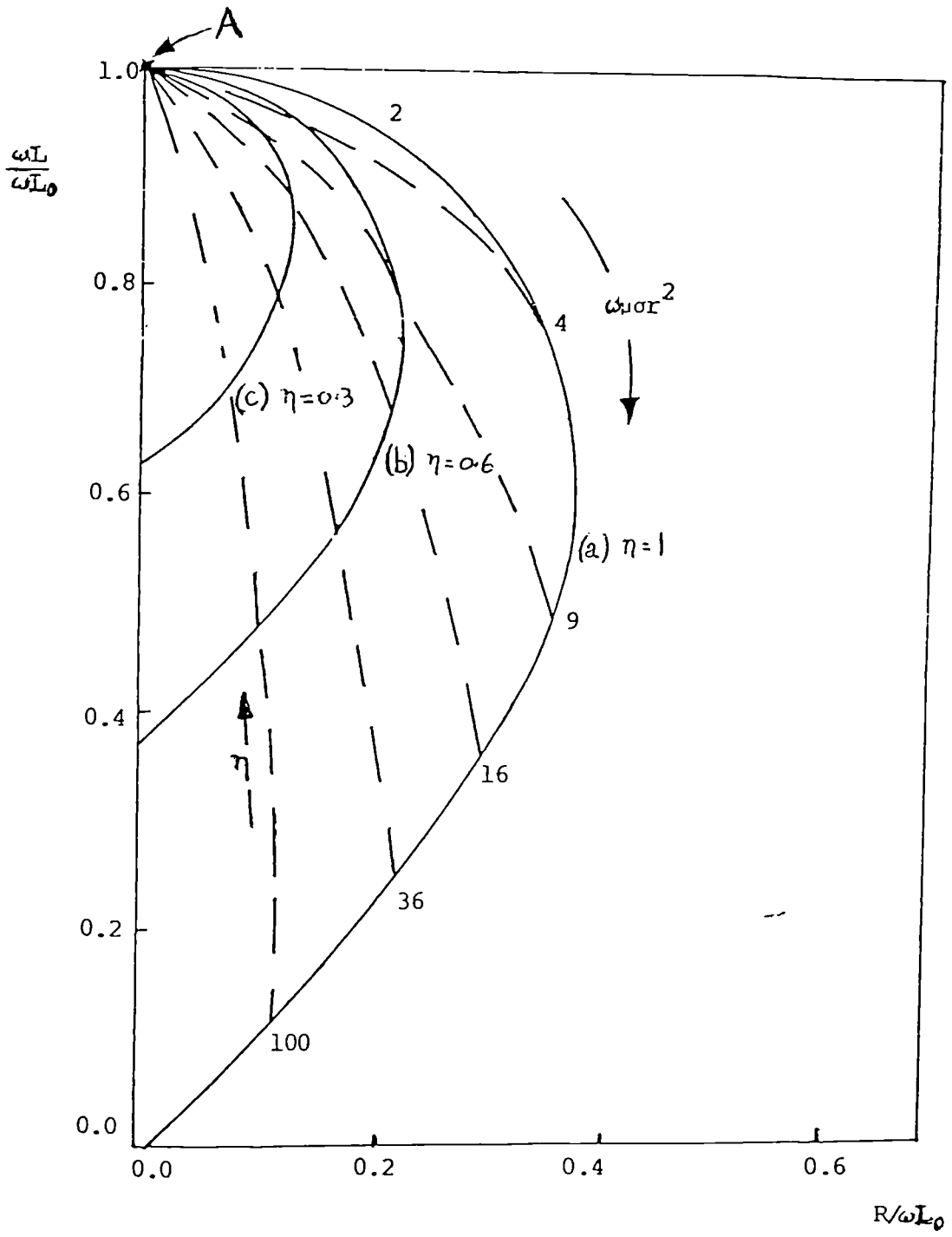

Figure 2.3: Variations of the normalised components of impedance with $k^2a^2 = \omega\mu_r\mu_0\sigma a^2$, for different values of fill-factor, η, for a coil encircling a non-ferromagnetic rod.

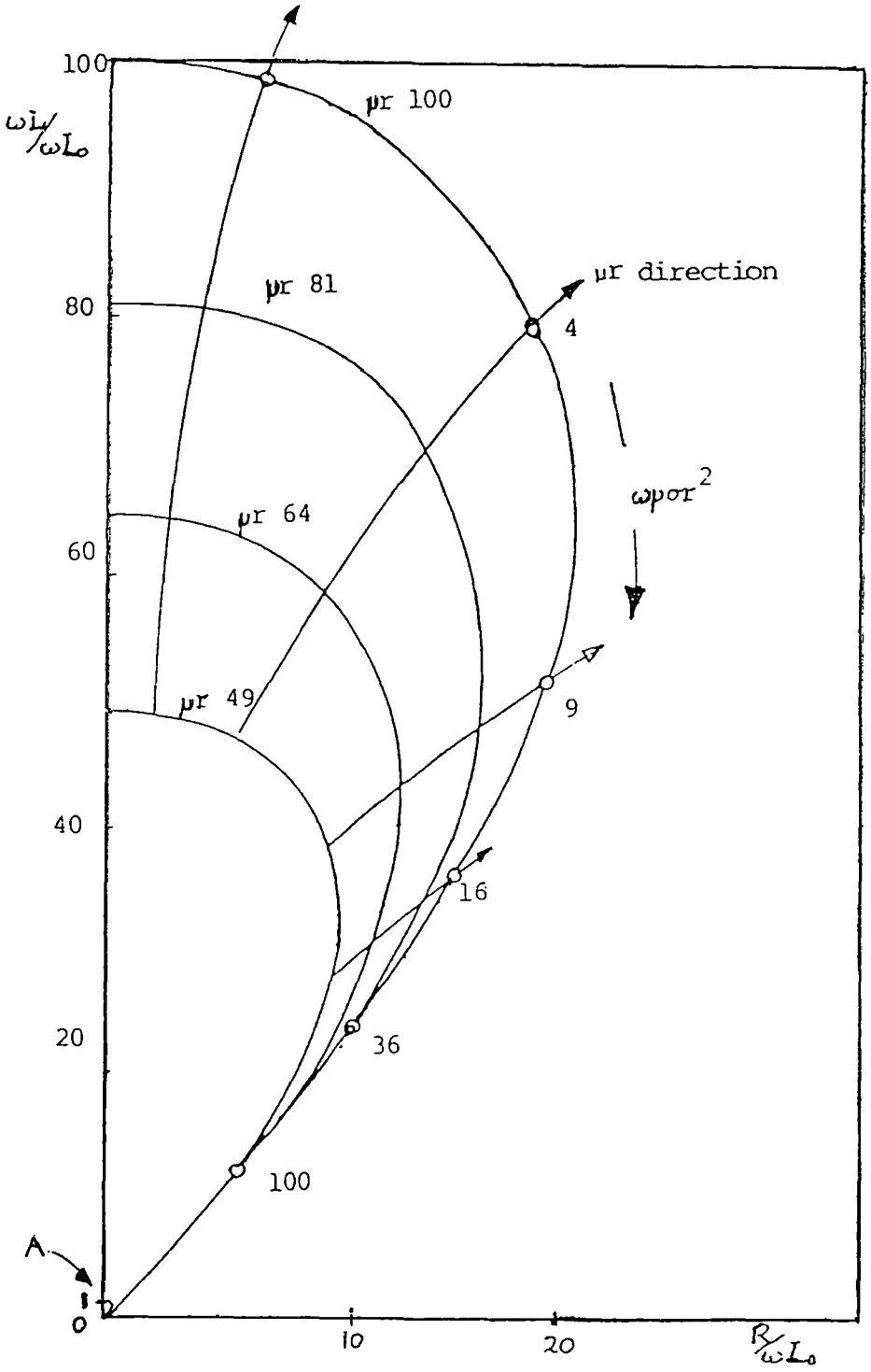

Figure 2.4: Variations in the components of impedance of a coil encircling ferromagnetic rods with different values of relative magnetic permeabilities, μ_r. Fill-factor $\eta = 1$.

2.2 Impedance Analysis for Surface-Scanning Coils Above Non-Ferromagnetic Metals

The analysis for a cylinder encircled by a coil is relatively straightforward because the system is symmetrical, but when considering a surface-scanning coil the symmetry is removed. Dodd and Deeds [5] resorted to numerical methods to analyse the behaviour of surface-scanning coils. They assumed an axial symmetry and used the vector potential $\underline{A}$ to get a single value function, where $\underline{B} = \nabla x \underline{A}$, to find expressions for the components of normalised impedance. For a conductor the electrical permittivity ε is negligible at all frequencies used for eddy current testing and when the medium is linear, isotropic and inhomogeneous, the differential equation for $\underline{A}$ due to an applied current density $\underline{J}_0$ in an air-cored coil, assuming conductivity σ and permeability μ to be constant, is given as

$$\nabla^2 \underline{A} = -\mu \underline{J}_0 + \mu\sigma \partial\underline{A}/\partial t + \mu.\nabla (1/\mu) \times (\nabla \times \underline{A}) \qquad (2.24)$$

Assuming that the coil is symmetrical about its axis, as shown in Fig. 2.5, $\underline{A}$ only has a component in the direction of θ and equation (2.24) can be written

$$\partial^2 A/\partial r^2 + (1/r)\,\partial A/\partial r + \partial^2 A/\partial z^2 - A/r^2$$

$$= -\mu \underline{J}_0 + \mu\sigma\, \partial A/\partial t - \mu[\{\partial(1/\mu)/\partial r\}\{(1/r)\partial rA/\partial r\} + \{\partial(1/\mu)/\partial z\}\partial A/\partial z] \qquad (2.25)$$

If $\underline{J}_0$, and therefore $\underline{A}$, are sinusoidal functions of time, $A = A'\exp(j(\omega t + \phi)) = A''\exp(j\omega t)$
To avoid confusion, the exponential term is cancelled and the suffixes dropped:

$$\partial^2 A/\partial r^2 + (1/r)\,\partial A/\partial r + \partial^2 A/\partial z^2 - A/r^2$$

$$= -\mu \underline{J}_0 + j\omega\mu\sigma A - \mu[\{\partial(1/\mu)/\partial r\}\{(1/r)\partial rA/\partial r\} + \{\partial(1/\mu)/\partial z\}\partial A/\partial z] \qquad (2.26)$$

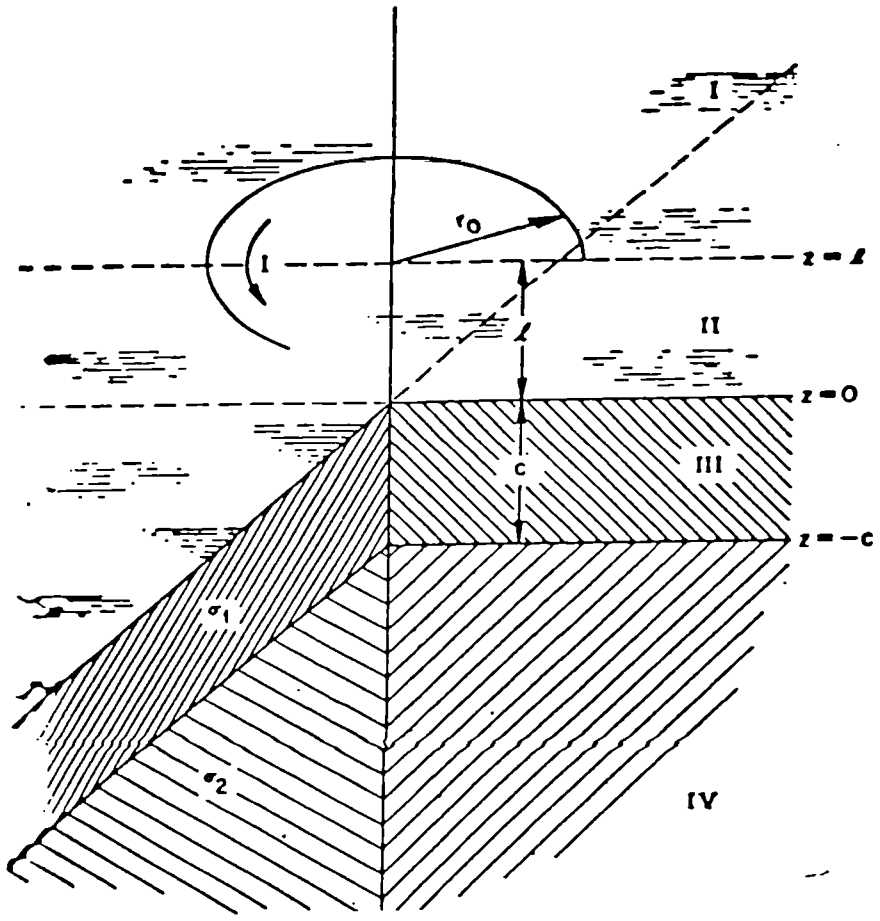

Figure 2.5: Single loop elementary coil above a two conductor plane, considered by Dodd and Deeds [5].

This is the general differential equation for the vector potential in a linear inhomogeneous medium with a sinusoidal driving current. If the medium is homogeneous, equation (2.26) can be written

$$\partial^2 A/\partial r^2 + (1/r)\,\partial A/\partial r + \partial^2 A/\partial z^2 - A/r^2 = -\mu J_0 + j\omega\mu\sigma A \qquad (2.27)$$

For an elementary coil positioned at (r_0, z_0), of rectangular cross-section $\delta(r - r_0)\,x$ $\delta(z - z_0)$, carrying a total driving current of $\dot{i}$, equation (2.27) becomes

$$\partial^2 A/\partial r^2 + (1/r)\,\partial A/\partial r + \partial^2 A/\partial z^2 - A/r^2 - j\omega\mu\sigma A + \mu i\delta(r - r_0)\delta(z - z_0) = 0 \qquad (2.28)$$

Dodd et al. [8-10] obtained finite solutions of this equation for six different arrangements of simple coils in the vicinity of layered conductors (Fig. 2.6). The analysis for a coil above a two-conductor plane is summarised below.

2.2.1 Coil above a Two-Conductor Plane of Non-Ferromagnetic Metal

The problem is divided into four regions (Fig. 2.5). In regions I and II (air), the differential equation for vector potential A is given as

$$\partial^2 A/\partial r^2 + (1/r)\,\partial A/\partial r + \partial^2 A/\partial z^2 - A/r^2 = 0 \qquad (2.29)$$

while in a conductor, in regions III and IV,

$$\partial^2 A/\partial r^2 + (1/r)\,\partial A/\partial r + \partial^2 A/\partial z^2 - A/r^2 - j\omega\mu\sigma A = 0. \qquad (2.30)$$

A is assumed to be a product of two independent functions, i.e, $A(r,z) = R(r).Z(z)$. By dividing by R.Z, equation (2.30) can be written as

$$[1/R]\partial^2 R/\partial r^2 + [1/r.R]\partial R/\partial r + [1/Z]\partial^2 Z/\partial z^2 - 1/r^2 - j\omega\mu\sigma = 0 \qquad (2.31)$$

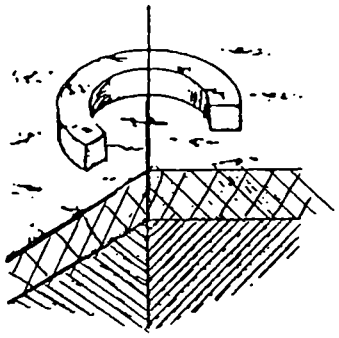

case 1:Coil above two-conductor plane.

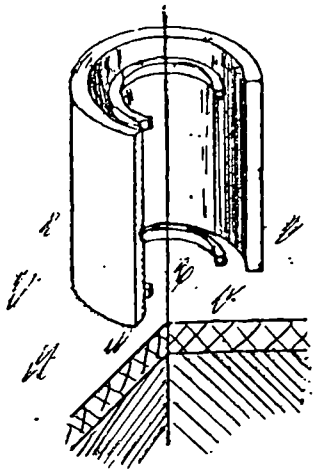

case 2:Reflection-type coil,as use in phase-sensitive instrument

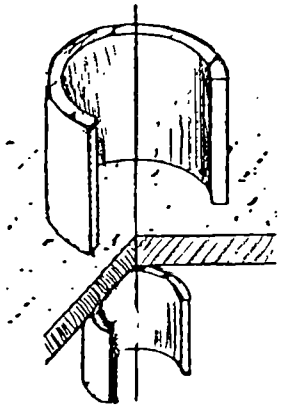

case 3:Through-transmission coils as used in phase-sensitive instrument.

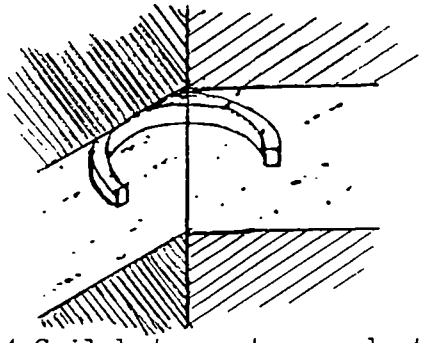

case 4:Coil between two-conducting planes;for spacing measurment.

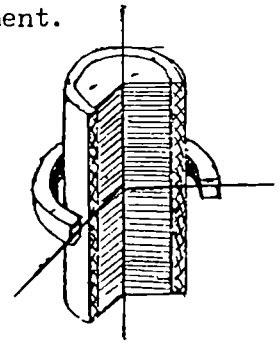

case 5:Coil encircling two-conductor.rod.

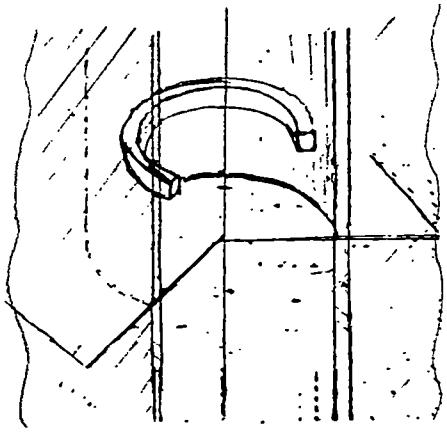

case 6:Coil inside two-conductor tube.

Figure 2.6: Eddy current problems treated by Dodd et al. [8-10]

The Z dependence is given by

$$[1/Z]\partial^2 Z/\partial z^2 = \text{"constant"} = k^2 + j\omega\mu\sigma$$

or
$$Z = A_i \exp[+(k^2 + j\omega\mu\sigma)^{1/2} z] + B_i \exp[-(k^2 + j\omega\mu\sigma)^{1/2} z] \qquad (2.32)$$

The R dependence can now be given as

$$[1/R]\partial^2 R/\partial r^2 + [1/r.R]\partial R/\partial r + k^2 - 1/r^2 = 0 \qquad (2.33)$$

This is a first order Bessel equation and has the solution

$$R = C_i J_1(kr) + D_i Y_1(kr) \qquad (2.34)$$

If $k' = (k^2 + j\omega\mu\sigma)^{1/2}$, on combining the solutions we have

$$A(r,z) = [A_i \exp(+k'z) + B_i \exp(-k'z)][C_i J_1(kr) + D_i Y_1(kr)] \qquad (2.35)$$

The constants A_i, B_i, C_i and D_i are functions of the separation "constant" k, and are usually different for each value of k. Because k is a continuous variable the complete solution for A is an integral over the entire range of k,;

$$A(r,z) = \int_0^\infty [A_i \exp(k'z) + B_i \exp(-k'z)]\,[C_i J_1(kr) + D_i Y_1(kr)]\,dk \qquad (2.36)$$

Setting $A_i = 0$ in region I (Fig. 2.5) where z goes to plus infinity, $B_i = 0$ in region IV where z goes to minus infinity, and $D_i = 0$ in all the regions due to the divergence of Y_1 at the origin, the vector potential in each region may be determined for a single delta function coil by applying the appropriate boundary conditions. From equation (2.36), the solutions for the vector potentials in the three regions are:

Region I $$A^{I}(r,z) = \int_0^{\infty} B_1.\exp(-kz)\, J_1(kr)\, dk \qquad (2.37)$$

Region II $$A^{II}(r,z) = \int_0^{\infty} [C_2.\exp(kz) + B_2.\exp(-kz)]\, J_1(kr)\, dk \qquad (2.38)$$

Region III $$A^{III}(r,z) = \int_0^{\infty} [C_3.\exp(kz) + B_3.\exp(-k'z)]\, J_1(kr)\, dk \qquad (2.39)$$

The constants in these equations were evaluated by applying the relevant boundary conditions at the interfaces of the regions.

For a multiple loop coil, the total vector potential is approximated by a number of co-axial elementary coils located at (r_i,z_i), assuming a rectangular cross-section as shown in Fig. 2.7, and that the phase and amplitude of the current in each loop is identical. The Vector potential A can be given by

$$A(r,z)_{total} \approx \int_r \int_{\ell} A(r,z,r_0,\ell)\, dr_0\, d\ell \qquad (2.40)$$

where $A(r,z,r_0,\ell)$ is the vector potential produced by a current density $J.(\ell,r_0)$, as calculated from regions I and II.

The integrals produced were difficult to solve analytically and a numerical solution was found using a large and complicated computer program. Fig. 2.8 shows the variations of normalised coil impedance when above the surface of a non-ferromagnetic metal, as calculated from the vector potential and found experimentally for coils of rectangular cross-section. The analysis could also be adapted for coils of circular cross-section.

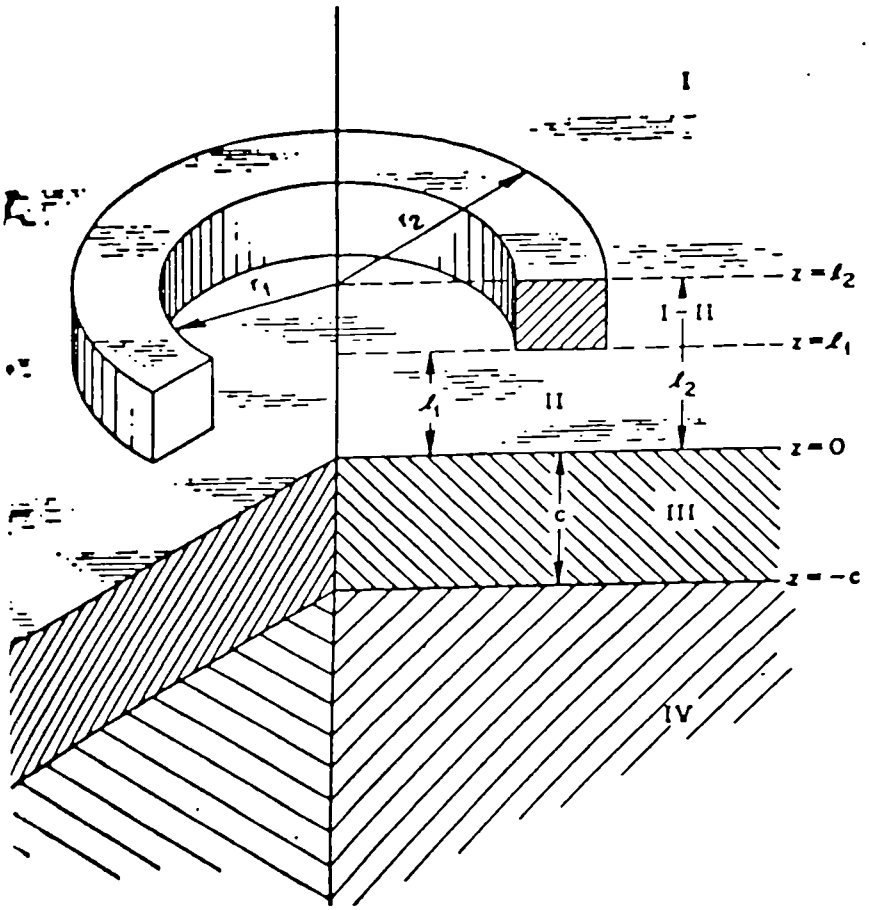

Figure 2.7: Coil with a rectangular cross-section above a two conductor plane [8]

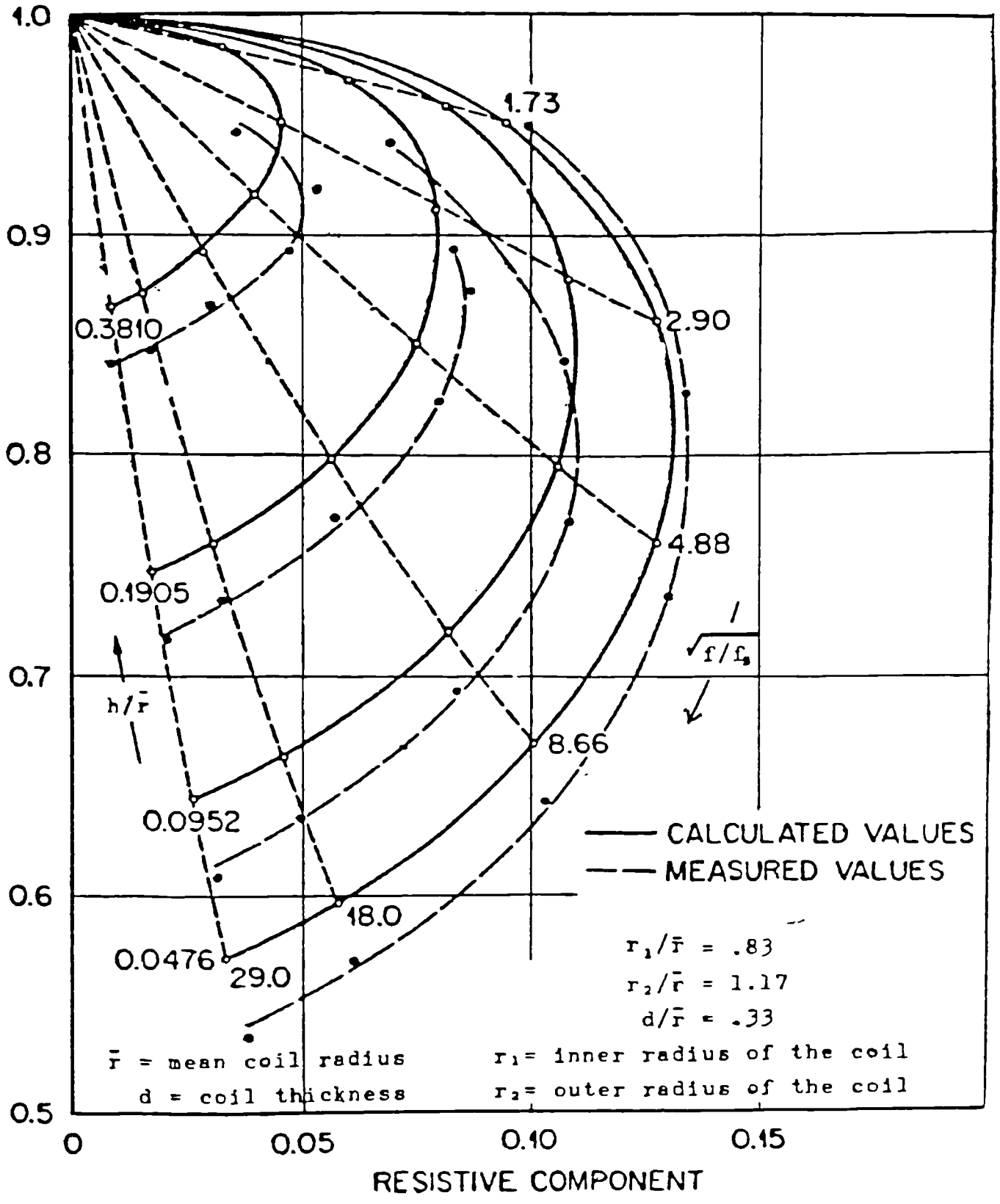

Figure 2.8: Variations of the theoretical and experimental values of impedance of a surface-scanning coil above a non-ferromagnetic plane [8], for different values of normalised lift-off, h/r and k^2a^2.

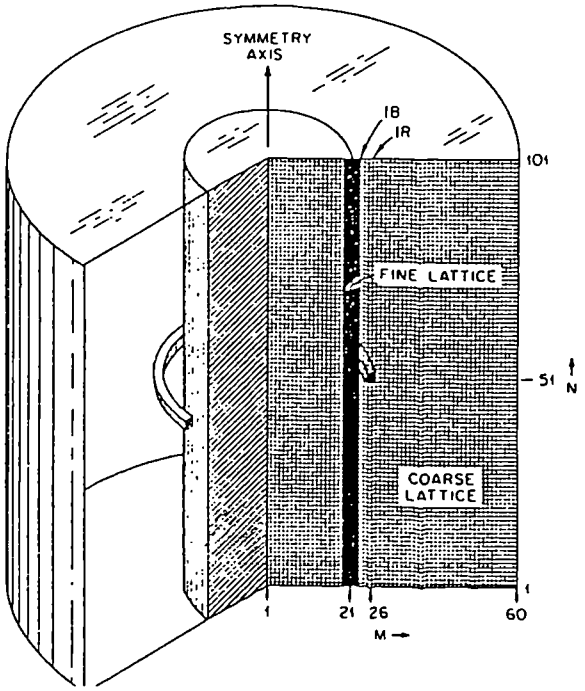

(a) Overall view of the lattice arrangement

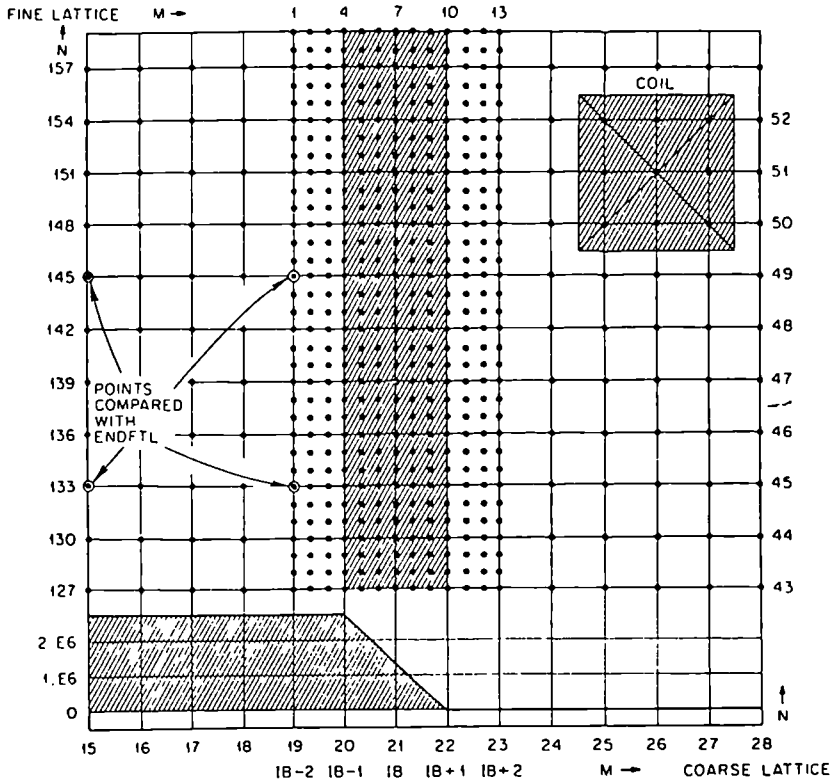

(b) Part of the fine and coarse lattices

Figure 2.9: Coarse and fine lattice arrangement used by Deeds and Dodd [16] to predict the impedance of an encircling coil around a ferromagnetic rod.

Deeds and Dodd [16] used a similar approach to find the solutions to the vector potentials of a coil encircling a ferromagnetic rod. For this they had to resort to using a numerical method of finite differences to calculate the vector potential at each point of a network of coarse and fine lattices (Fig. 2.9) for which a large and complex computer program was required. They suggested that the program might also be possible to modify for other arrangements of coils in the vicinity of ferromagnetic metals with axial symmetry.

In Chapter 3 an impedance analysis of the special case of an air-cored coil scanning the surface of both non-ferromagnetic and ferromagnetic metals is presented, based on the work of Dodd and Deeds [5]. It is shown how a solution can be found using a simple program written in BASIC, which can be run on a personal computer. The solution could also be applied to coils with ferrite cores, if an allowance is made for the change in the characteristics of the coil caused by a concentration of the magnetic flux by the ferrite core.

CHAPTER 3

ANALYTICAL SOLUTION FOR A COIL ABOVE THE SURFACE OF A FERROMAGNETIC METAL

The main object of this work is to obtain expressions for the real and imaginary components of normalised impedance of a surface-scanning coil above the surface of any ferromagnetic or non-ferromagnetic metal. Here the impedance of an air-cored coil is considered: for reasons to be given later, coils with ferrite cores are disregarded as being unsuitable (Section 5.3). The metal is assumed to be in the form of a flat plate of sufficient thickness to prevent through penetration of the eddy currents and a simplified model of the magnetic behaviour of a ferromagnetic metal is used. The approach used by Dodd and Deeds [5] is modified to obtain values of the components of normalised impedance $(R/\omega L_0)$ and $(\omega L/\omega L_0)$ for different values of normalised frequency and lift-off.

3.1 Impedance of an Air-Cored Probe above a Ferromagnetic Metal

It is shown in Section 2.2 that the general solution for the vector potential $\underline{A}$ of an elementary circular coil above a conducting plane may be represented by the equation

$$A(r,z) = \int_0^\infty [A_i \exp(k'z) + B_i \exp(-k'z)] . C_i J_1(kr)\, dk \qquad (3.1)$$

where $k'^2 = k^2 + j\omega\mu\sigma_i = [1/Z(z)][\partial^2 Z(z)/\partial z^2]$ (Section 2.2), σ is electrical conductivity, μ magnetic permeability, ω angular frequency and $j = (-1)^{1/2}$.

Following Dodd and Deeds (Section 2.2), consider three regions (Fig. 3.1) separated by plane parallel boundaries. The top two regions contain air, with electrical conductivity assumed to be zero and magnetic permeability $\mu = \mu_0 = 4\pi \times 10^{-7}\,Hm^{-1}$. The third region contains a semi-infinite plane of a ferromagnetic medium with values of electrical conductivity of σ and magnetic permeability $\mu = \mu_0 \mu_r$. The solutions for the vector potential in the three regions are

Region I
$$A^I(r,z) = \int_0^\infty B_1 \exp(-kz)\, J_1(kr)\, dk \qquad (3.2)$$

Region II
$$A^{II}(r,z) = \int_0^\infty [C_2 \exp(kz) + B_2 \exp(-kz)]\, J_1(kr)\, dk \qquad (3.3)$$

Region III
$$A^{III}(r,z) = \int_0^\infty [C_3 \exp(k'z)\, J_1(kr)\, dk \qquad (3.4)$$

Constants B_1 B_2 C_2 and C_3 may be found by applying the boundary conditions at the interfaces of the regions, for which a definition of the magnetic permeability is required.

The magnetic permeability μ of a ferromagnetic material, defined as $\mu = \underline{B} / \underline{H}$, where $\underline{B}$ is the magnetic flux density and $\underline{H}$ the applied field, normally varies non-linearly with applied field $\underline{H}$ (Fig. 3.2(a)) [14]. However, for the small alternating field $\Delta\underline{H}$ induced by an eddy current coil, the magnetic permeability μ can be assumed to be constant (Fig. 3.2(b)). Therefore, for a metal obeying Ohm's law, the problem can be simplified by assuming that the intensity of magnetisation $\underline{M}$ produced by the field from a magnetic material in excess of that produced in air by the same field, sometimes refered to as the ferric induction, is proportional to the magnetic flux density $\underline{B}$, such that [29]:

$$\underline{B} = \mu_0 (\underline{H} + \underline{M}) \qquad (3.5)$$

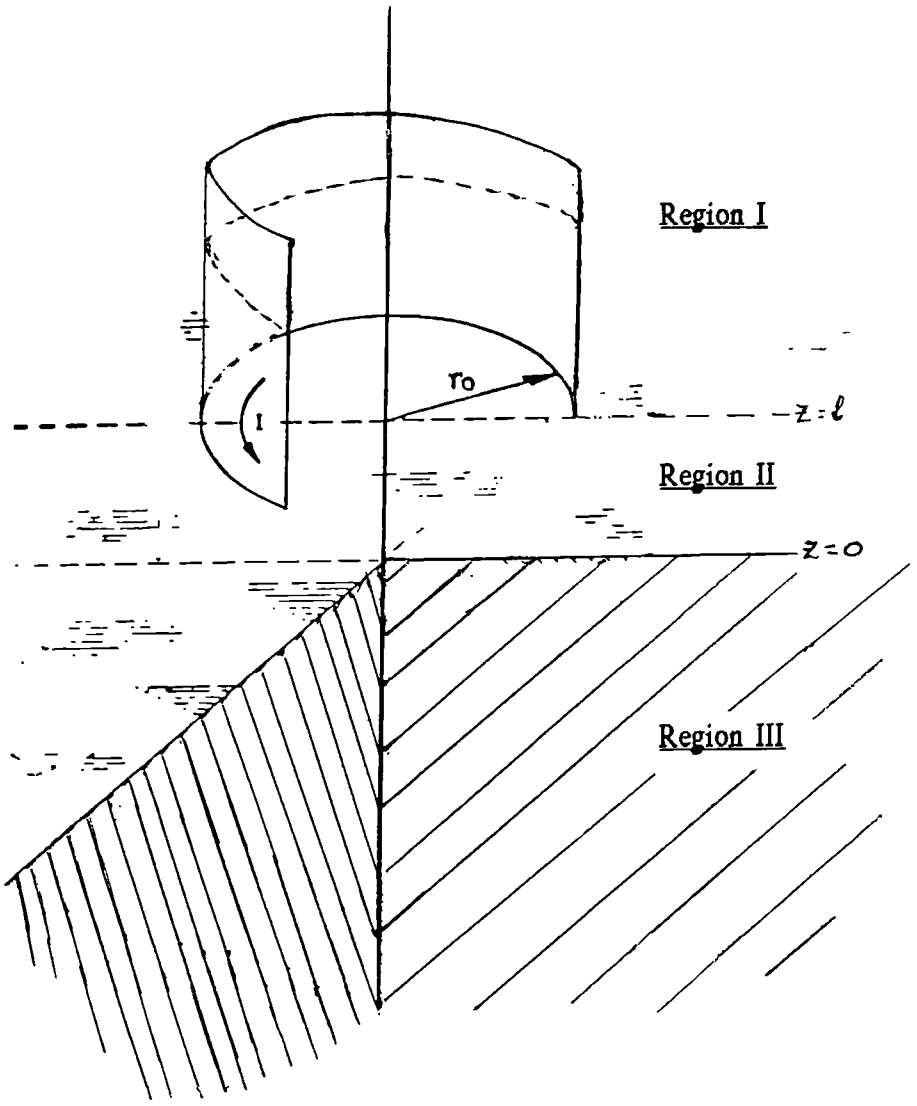

Figure 3.1: Solenoid coil above the surface of a metal.

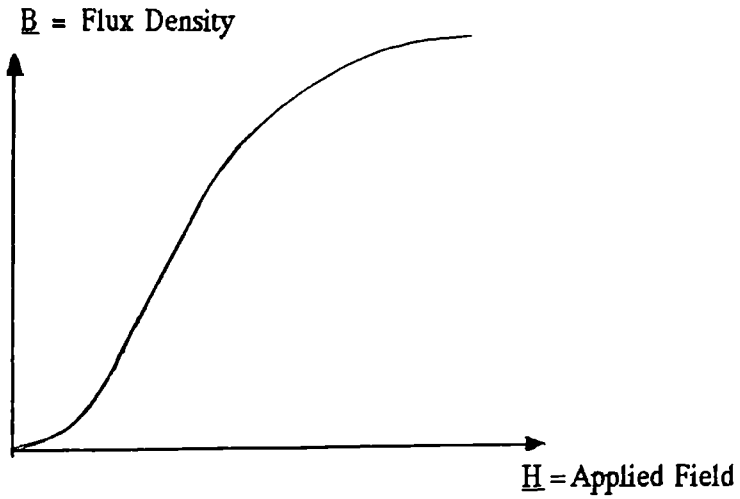

(a) Variation with a large change in H

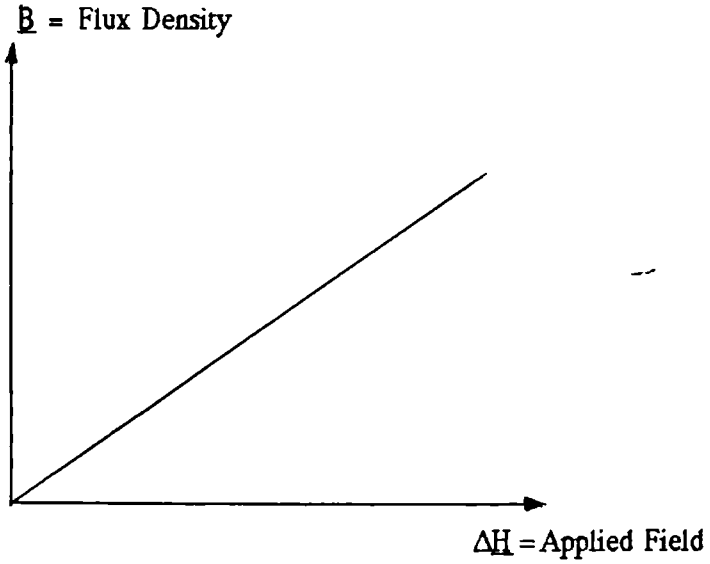

(b) Variation for a small change in H, ΔH

Figure 3.2: Variation of the magnetic flux density B and hence magnetic permeability μ of a ferromagnetic material with applied field H.

Here $\underline{M} = (\mu_r - 1).\underline{H}$, and the magnetic flux in a ferromagnetic metal $\underline{B}$(metal) is given by

$$\underline{B}(\text{metal}) = \mu_r \mu_0 . \underline{H}(\text{metal}) \qquad (3.6)$$

From Maxwell's equations, the normal component of $\underline{H}$ is continuous across the boundaries. The tangential component of $\underline{H}$ must also be continuous:

$$\underline{H}(\text{air}) = \underline{H}(\text{metal})$$

or $$\underline{B}(\text{air})/\mu_0 = \underline{B}(\text{metal})/\mu_r \mu_0,$$

hence $$\underline{B}(\text{air}) = (1/\mu_r).\ \underline{B}(\text{metal}) \qquad (3.7)$$

The boundary conditions can be obtained in terms of the vector potential $\underline{A}$, by using the relationship $\underline{B} = \nabla \times \underline{A}$. Assuming the coil is symmetrical about its axis as shown in Fig. 3.1, the normal and tangential components of $\underline{B}$, B_z and B_r respectively, can be written:

$$B_z = d(rA)/dr = A + r.dA/dr \qquad (3.8)$$

and $$B_r = -(1/r).d(rA)/dz = -dA/dz \qquad (3.9)$$

Therefore, the values of A given in equations 3.2 to 3.4 can be equated at $z = \ell$ and $z = 0$ (Fig. 3.1) to satisfy the boundary conditions as follows:

The normal component of A is continuous, and from equation (3.8),

at $z = \ell$, $$A^{I}(r,\ell) = A^{II}(r,\ell), \qquad (3.10)$$

and at $z = 0$, $$A^{II}(r,0) = A^{III}(r,0) \qquad (3.11)$$

The radial component of A is continuous at $z = 0$, but is discontinuous at $z = \ell$ by an amount equal to the current density of the coil. Therefore to satisfy the boundary conditions, from equations (3.9) and (3.7),

$$\text{at } z = \ell, \qquad (\partial/\partial z).A^{I}(r,z)|_{z=\ell} = (\partial/\partial z).A^{II}(r,z)|_{z=\ell} - \mu_0 i\, \delta(r-r_0) \tag{3.12}$$

$$\text{and at } z = 0, \qquad (\partial/\partial z).A^{II}(r,z)|_{z=0} = (1/\mu_r).(\partial/\partial z).A^{III}(r,z)|_{z=0} \tag{3.13}$$

From equations (3.2) and (3.3), equation (3.10) can be written

$$\int_0^\infty B_1 \exp(-kz)\, J_1(kr)\, dk = \int_0^\infty [C_2 \exp(kz) + B_2 \exp(-kz)]\, J_1(kr)\, dk \tag{3.14}$$

If both sides of equation (3.14) are multiplied by the operator $\int_0^\infty J_1(k'r).r.dr$, the expression can be simplified using a form of the Fourier-Bessel equation [31], i.e.,

$$F(k') = \int_0^\infty F(k) \int_0^\infty J_1(kr)\, J_1(k'r)\, kr\, dr\, dk, \text{ giving}$$

$$(B_1/k')\exp(-k'\ell) = (C_2/k')\exp(k'\ell) + (B_2/k')\exp(-k'\ell) \tag{3.15}$$

Therefore equation (3.12) can be written

$$-B_1.\exp(-k'\ell) = C_2.\exp(k'\ell) - B_2.\exp(-k'\ell) - \mu_0 i r_0\, J_1(k'r_0) \tag{3.16}$$

When considering the boundary conditions between regions II and III, equations (3.3) and (3.4) are substituted into equations (3.11) and (3.13) and treated in a similar manner to equations (3.10) and (3.12), giving:

$$C_2 + B_2 = C_3 \tag{3.17}$$

and

$$C_2 - B_2 = (k'/\mu_r k)C_3 \tag{3.18}$$

By solving equations (3.15) to (3.18) as four simultaneous equations the following values are obtained for the constants:

$$B_1 = (1/2)\mu i r_0 J_1(kr_0)[\exp(k\ell) + F'.\exp(-k\ell)] \tag{3.19}$$

$$B_2 = (1/2)\mu i r_0 J_1(kr_0) \,.\, F'.\exp(-k\ell) \tag{3.20}$$

$$C_2 = (1/2)\mu i r_0 J_1(kr_0) \exp(-k\ell) \tag{3.21}$$

$$C_3 = -\mu i r_0 J_1(kr_0) (k\mu_r/(k\mu_r + k')) \exp(-k\ell) \tag{3.22}$$

where $F' = \{(k\mu_r - k')/(k\mu_r + k')\}$.

The expressions for the vector potential in each region can now be written by *substituting the values of these constants into Equations (3.2) to (3.4).* $A^{I}(r,z)$ *and* $A^{II}(r,z)$ can be combined to form the equation

$$A(r,z,\ell) = (1/2)\mu i r_0 \int_0^{\infty} J_1(kr_0)J_1(kr)[\exp(\pm k.|\ell - z|) + F'.\exp(-k(\ell+z))]\, dk \tag{3.23}$$

Consider a coil of finite length ℓ_0, with n_0 turns per unit length, with its axis vertically above the surface of the sample at a lift-off h (Fig. 3.3). The current through the coil is $i_0 = i/n_0\ell_0$ and the current in an elementary length $\delta\ell$ at a distance $\ell = m - h$ from the sample surface is $\delta i = i_0 n_0 \delta\ell$. The number of turns in length δz of the coil is $n_0\delta z$, and the magnetic flux is given by

$$\Delta\Phi = 2\pi r_0 A(r,z,\ell) n_0 \delta z (i_0 n_0/i) \delta\ell \tag{3.24}$$

The total magnetic flux Φ_T through the coil must be the sum of the contributions from the coil length ℓ over the whole of z, hence

$$\Phi_T = \int_{\ell=h}^{m} \int_{z=h}^{m} \Delta\Phi$$

$$= t \int_0^{\infty} J_1^2(kr_0)\, dk \int_h^m d\ell \left[\int_{\ell}^{m} \exp(-k(\ell+z)) \left(\exp(2k\ell) + F'\right) dz + \int_h^{\ell} \exp(-k(\ell-z)) \left(1 + F'\exp(-2kz)\right) dz \right] \qquad (3.25)$$

where $t = \mu\pi r_0^2 i_0 n_0^2$.

Performing the integrations for z:

$$\Phi_T = t \int_0^{\infty} J_1^2(kr_0) dk \int_h^m d\ell \left[-(1/k)\exp(-k(\ell+m)) \left(\exp(2k\ell) + F'\right) - \left(-(1/k)\exp(-k2\ell)\right) \left(\exp(2k\ell) + F'\right) \right]$$

$$+ \left[(1/k) - (1/k).F'.\exp(-k2\ell) - \left\{ (1/k)\exp(-k(\ell-h)) - (1/k).F'.\exp(-k(\ell+h)) \right\} \right] \qquad (3.26)$$

By substituting $m = \ell_0 + h$, and integrating for ℓ, Φ_T may be written

$$\Phi_T = t \int_0^{\infty} J_1^2(kr_0) \left[2\ell_0/k - 2/k^2 + 2/k^2.\exp(-k\ell_0) + F'/k^2.\exp(-2kh)\left(\exp(-2k\ell) + 1\right) - 2F'/k^2.\exp(-k(\ell_0+2h)) \right] dk$$

$$= t \int_0^{\infty} J_1^2(kr_0) \left[2\ell_0/k - 2/k^2.(1 - \exp(-k\ell_0)) + F'/k^2.\exp(-2kh)\left(1 - \exp(-k\ell_0)\right)^2 \right] dk \qquad (3.27)$$

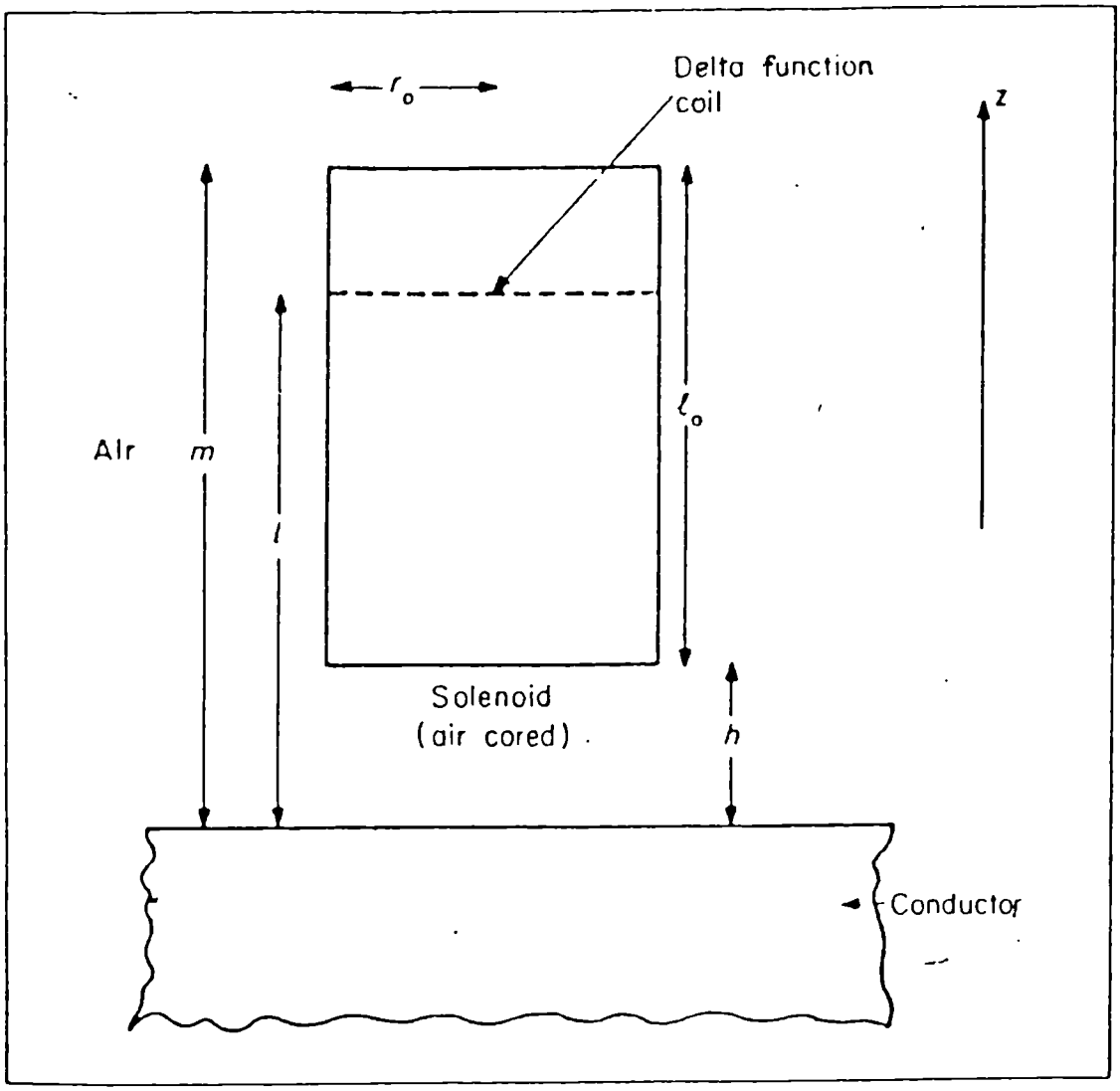

Figure 3.3: Schematic diagram of a coil above the plane surface of a conductor.

The lift-off and length of coil should be normalised with respect to coil radius, hence substituting $Y = h/r_0$ and $Y_0 = \ell_0/r_0$ respectively, and also changing the variables $kr_0 = X$ and $k'r_0 = X'$, so that

$$X'^2 - X^2 = j\beta^2 = j\omega\sigma\mu r_0^2, \tag{3.28}$$

then

$$\Phi_T = t.r_0\left[\int_0^\infty J_1^2(X)/X.dX.2Y_0 + \int_0^\infty J_1^2(X)/X^2.dX\{-2(1-\exp(-Y_0X)) + [X\mu_r - X']/[X\mu_r + X'].\exp(-2YX)\,(1 - \exp(-Y_0X)^2\}\right] \tag{3.29}$$

$$= \mu\pi\, r_0^3 i_0 n_0^2 [2Y_0 I_1 - 2I_2 + 2I_3 + I_4] \tag{3.30}$$

where $I_1 = \int_0^\infty J_1^2(X)/X\, dX$ (3.31)

$$I_2 = \int_0^\infty [J_1(X)/X]^2\, dX \tag{3.32}$$

$$I_3 = \int_0^\infty [J_1(X)/X]^2 \exp(-Y_0X)\, dX \tag{3.33}$$

and $I_4 = \int_0^\infty [J_1(X)/X]^2 \exp(-2YX)(1 - \exp(-Y_0X))^2\, [X\mu_r - X']/[X\mu_r + X']\, dX.$ (3.34)

The integrals I_1 and I_2 are standard integrals [31] having solutions 1/2 and $4/3\pi$ respectively. I_3 and I_4 have to be calculated numerically using Simpson's rule.

From Faraday's law the EMF induced in the coil is equal to $-\partial\Phi_T/\partial t$. Because current i varies sinusoidally with time, Φ_T varies in a similar manner, hence

$$-\partial\Phi_T/\partial t = -j\omega\Phi_T = Zi = i(R + j\omega L) \tag{3.35}$$

and $$R + j\omega L = -j\omega\Phi_T / i = -T / i . [Y_0 - 8/3\pi + 2I_3 + I_4] \tag{3.36}$$

where $T = j\omega\mu\pi r_0^3 i_0 n_0^2$ and $Y_0 = \ell_0 / r_0$

For infinite lift-off h, for which $Y = h/r_0 = \infty$, the impedance of the coil is purely inductive, i.e, $Z_\infty = j\omega L_0$, if we assume that the inherent coil resistance R_0 is zero. Also $\exp(-2YX) = 0$ therefore $I_4 = 0$, and the normalised impedance $Z/j\omega L_0$ can be written

$$\omega L / \omega L_0 + jR / \omega L_0 = 1 + I_4 / S \tag{3.37}$$

where . $S = (Y_0 - 8/3\pi + 2I_3)$.

The integrals I_3 and I_4 can be evaluated using Simpson's rule, if an upper limit is set above which the integral becomes insignificant:

$$\int_a^b f(x)dx = (w/3)\,[y_0 + 4(y_1 + y_3 + \ldots + y_{n-1}) + 2(y_2 + y_4 + \ldots + y_{n-2}) + y_n]$$

where the interval from a to b is divided into (n-1) equal strips, each of width w. The negative exponential factor in I_3 makes the integral approach zero with increasing

values of X and it can be shown that I_3 diminishes to zero well before X = 10 (Fig. 3.4) for typical values of $Y_0 = \ell_0/r_0$ found in practice, between 0.2 and 5.0. The integral I_4 contains an expression F' which includes X', a complex function of X given by

$$X'^2 = j\beta^2 + X^2 \tag{3.38}$$

where $\beta^2 = \omega\mu_r\mu_0\sigma r^2$, the normalised frequency. The real and imaginary components of this expression can be found through conversion into polar coordinates, where $\tan\theta = \beta^2/X^2$, such that

$$X'^2 = g(\cos\theta + j\sin\theta)$$

and

$$X' = g^{1/2}(\cos\theta/2 + j\sin\theta/2) \tag{3.39}$$

where $g = (\beta^4 + X^4)^{1/2}$.

The real and imaginary components of X' become respectively

$$\mathrm{Re}(X') = g^{1/2}\cos\theta/2 \tag{3.40}$$

and

$$\mathrm{Im}(X') = g^{1/2}\sin\theta/2. \tag{3.41}$$

Putting $\{F'\} = [X\mu_r - X'/X\mu_r + X']$, we have from equation (3.39)

$$\{F'\} = [(X\mu_r)^2 - g - j\,2X\mu_r g^{1/2}\sin\theta/2] \,/\, [(X\mu_r)^2 + g + 2X\mu_r g^{1/2}\cos\theta/2] \tag{3.42}$$

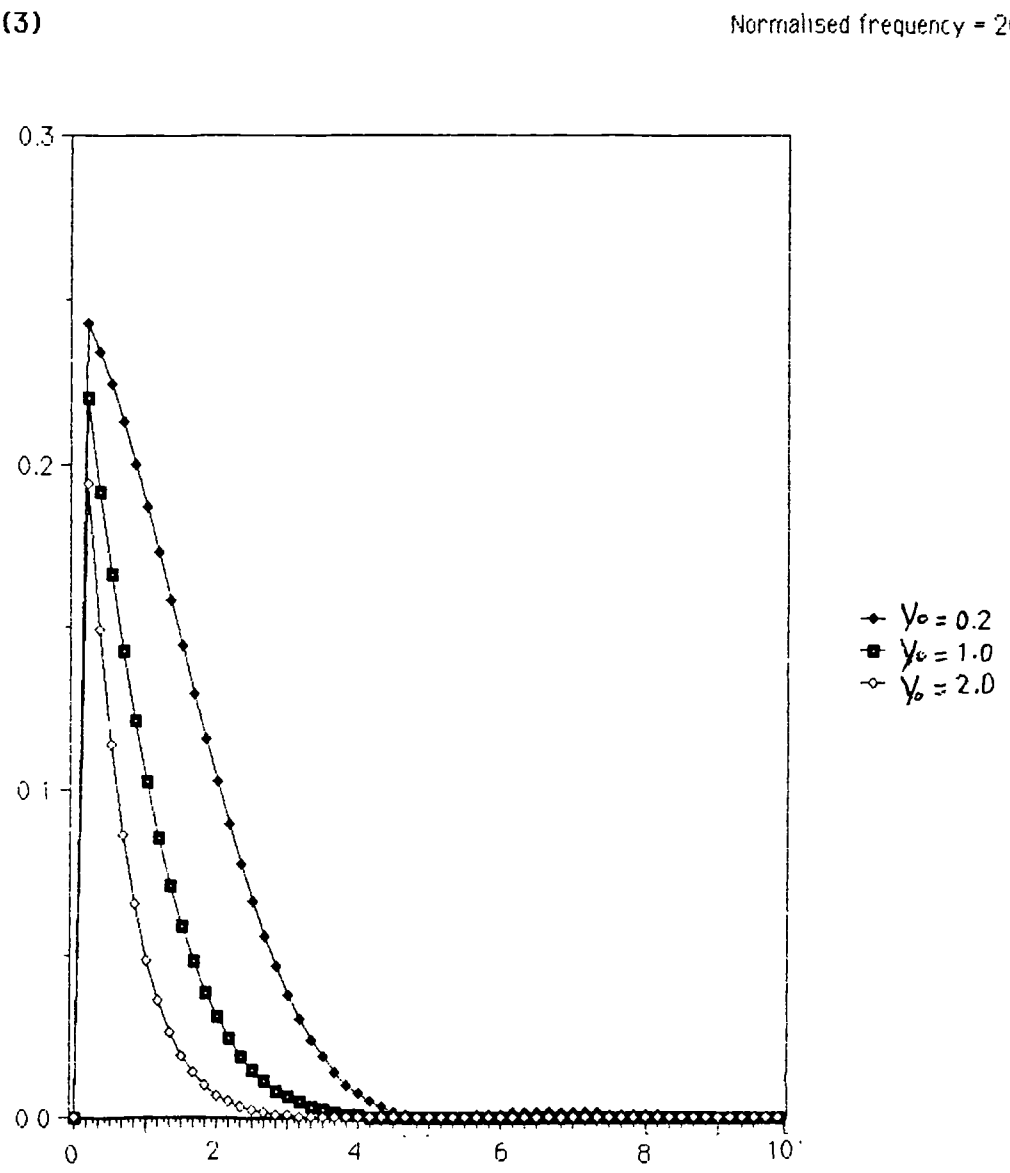

Figure 3.4: Variation of the integral I_3 with X, for different values of normalised coil length, Y_0, where normalised frequency $\beta^2 = 200$.

Equation (3.42) may be simplified by substituting

$$\cos \theta/2 = [(1/2)(1 + \cos \theta)]^{1/2} = [(1/2)(1 + X^2/g)]^{1/2} \quad (3.43)$$

and

$$\sin \theta/2 = [(1/2)(1 - \cos \theta)]^{1/2} = [(1/2)(1 - X^2/g)]^{1/2} \quad (3.44)$$

Thus the real and imaginary components of F' can be written

$$\mathrm{Re}(F') = [(X\mu_r)^2 - g]/n \quad (3.45)$$

$$\mathrm{Im}(F') = X\mu_r[2\{g - X^2\}]^{1/2}/n \quad (3.46)$$

where $n = (X\mu_r)^2 + g + X\mu_r[2\{g + X^2\}]^{1/2}$ and $g = (\beta^4 + X^4)^{1/2}$.

The normalised components of impedance can be found by substituting these values of the expression into equations (3.34) and (3.37):

$$\omega L/\omega L_0 = 1 + \mathrm{Re}(I_4)/S \quad (3.47)$$

$$R/\omega L_0 = \mathrm{Im}(I_4)/S \quad (3.48)$$

where $S = (Y_0 - 8/3\pi + 2I_3)$.

The integrals I_3 and I_4 cannot be evaluated by an analytical method and a numerical method is necessary.

3.2 Predicted Changes of the Components of Impedance with μ_r.

A simple program written in BASIC (Appendix 1) was run on a personal computer, using values of normalised frequencies β^2 between 10 and 100,000 and values of normalised lift-off Y varying from 0 to 3.0. The program was run using normalised coil lengths Y_0 between 0.2 and 5.0 for different values of the product $\mu\sigma$. For a given value of Y_0 the integral I_3 (Fig. 3.4) is independent of magnetic permeability μ_r and normalised frequency β^2. Figs. 3.5 to 3.7 show how the integral I_4 are changed with μ_r, β^2 and Y_0.

Fig. 3.8 shows the variations of the components of impedance with normalised frequency, for a coil of normalised length 0.2 touching the surface of metals with different values of relative magnetic permeability μ_r. Fig. 3.9 shows how the components of impedance vary at a given normalised frequency with lift-off for different values of μ_r. As expected, the reactive component of impedance is increased when the coil is above a ferromagnetic metal as compared with a non-ferromagnetic metal. However, because there are large leakages of flux associated with surface-scanning coils, the reactive component of impedance does not increase beyond 2.5 for any value of μ_r. For a given value of normalised frequency, there is a marked change in phase of the normalised lift-off vector with μ_r (Fig. 3.9), similar to that caused by a change of normalised frequency. There is very little change in the direction of changes in the normalised lift-off, unlike that of the encircling coil predicted by Förster [3] (Fig. 2.4).

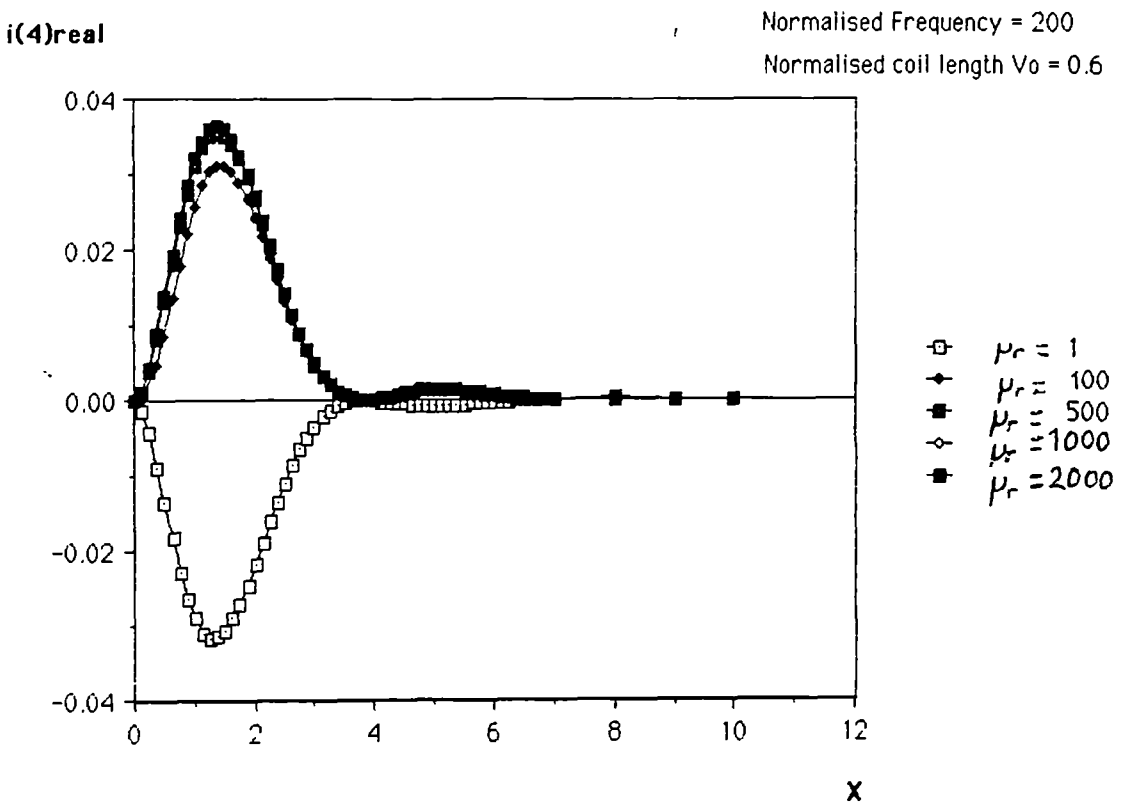

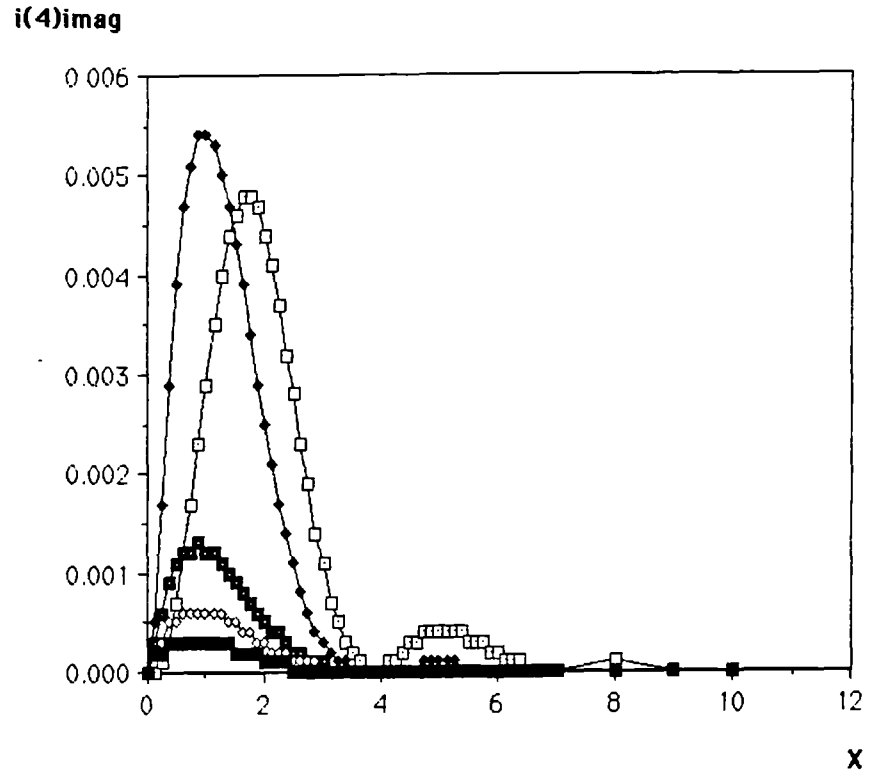

Figure 3.5: The real and imaginary components of the integral I_4 with X for different values of μ_r. $\beta^2 = 200$, $Y_0 = 0.6$.

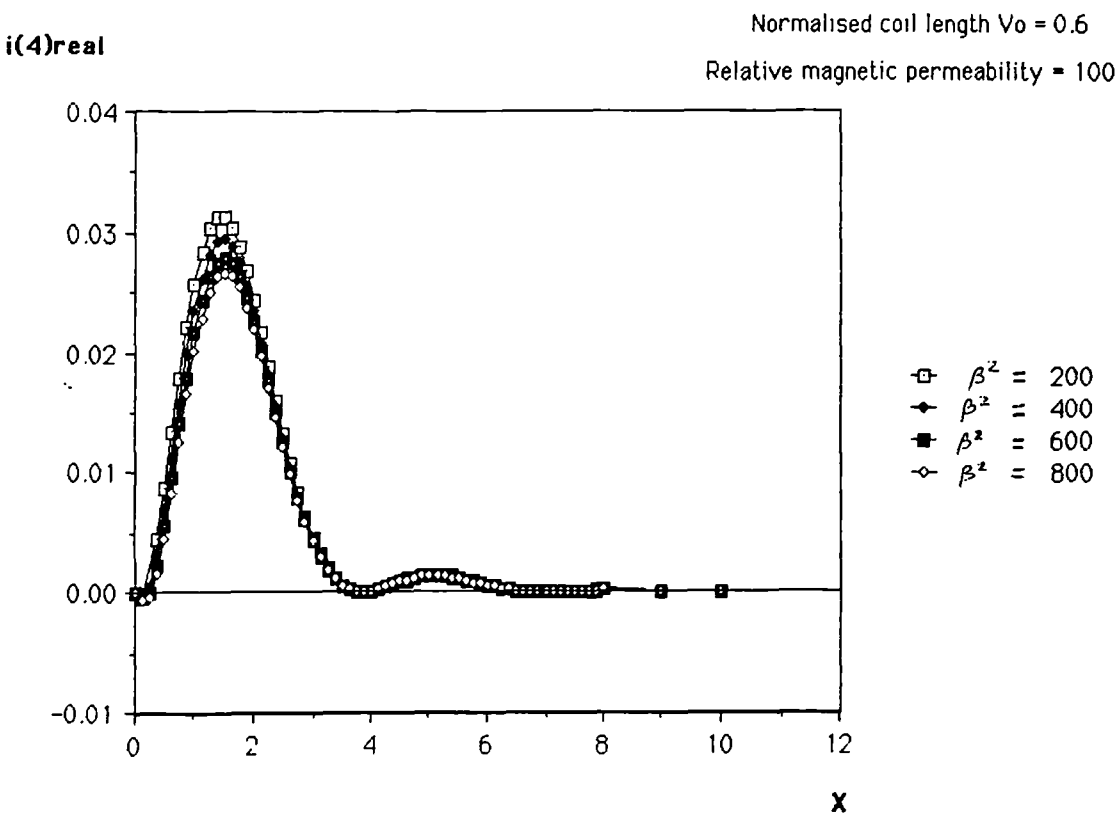

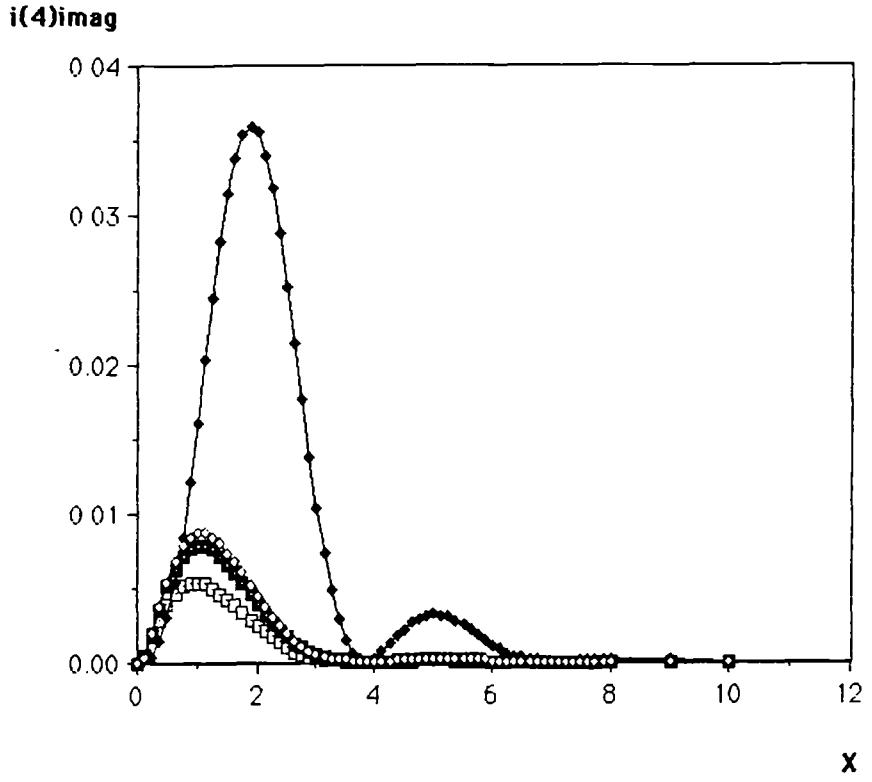

Figure 3.6: The real and imaginary components of the integral I_4 with X for different values of β^2. $\mu_r = 100$, $Y_0 = 0.6$.

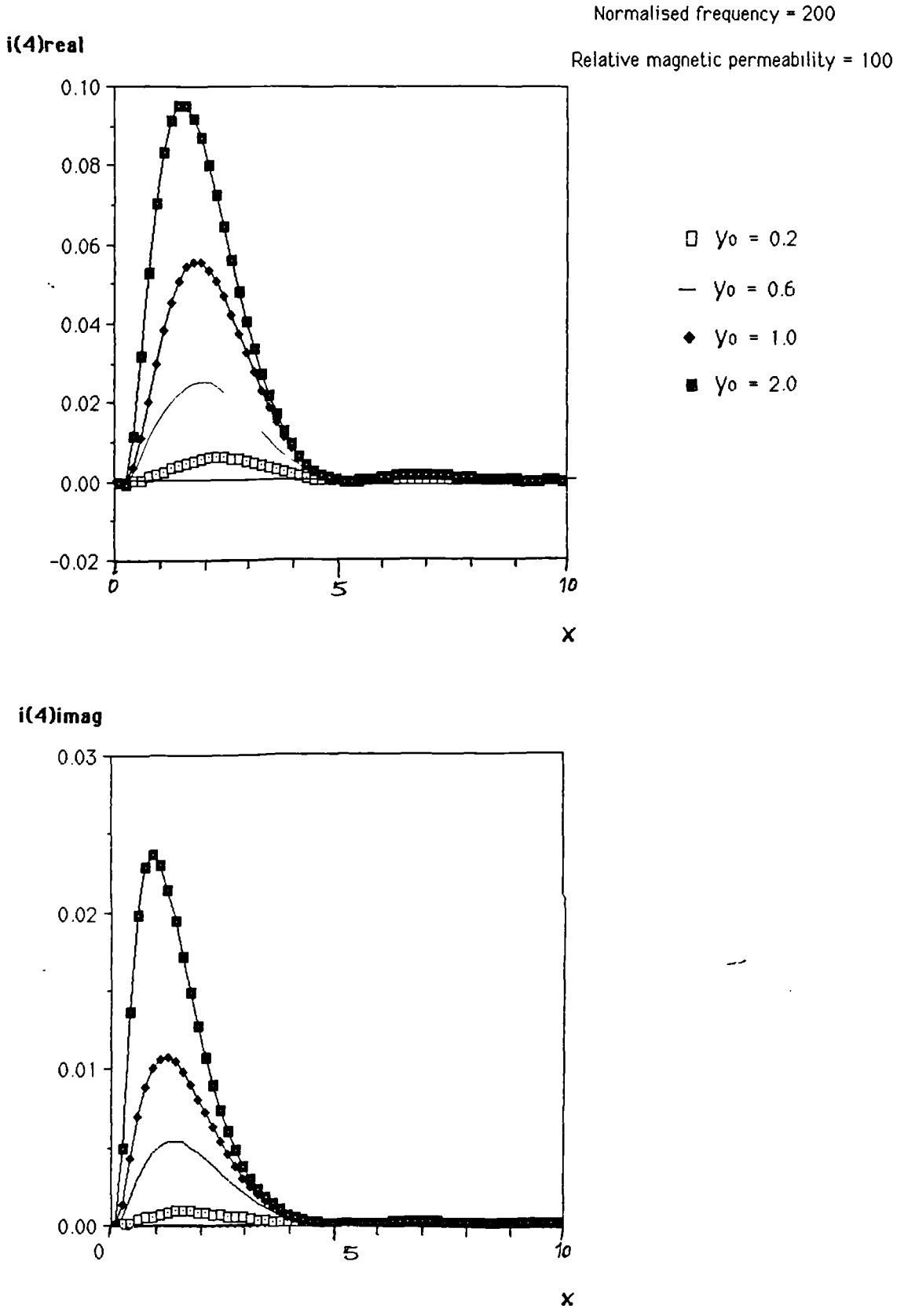

Figure 3.7: The real and imaginary components of the integral I_4 with X for different values of Y_0 $\mu_r = 100$, $\beta^2 = 200$.

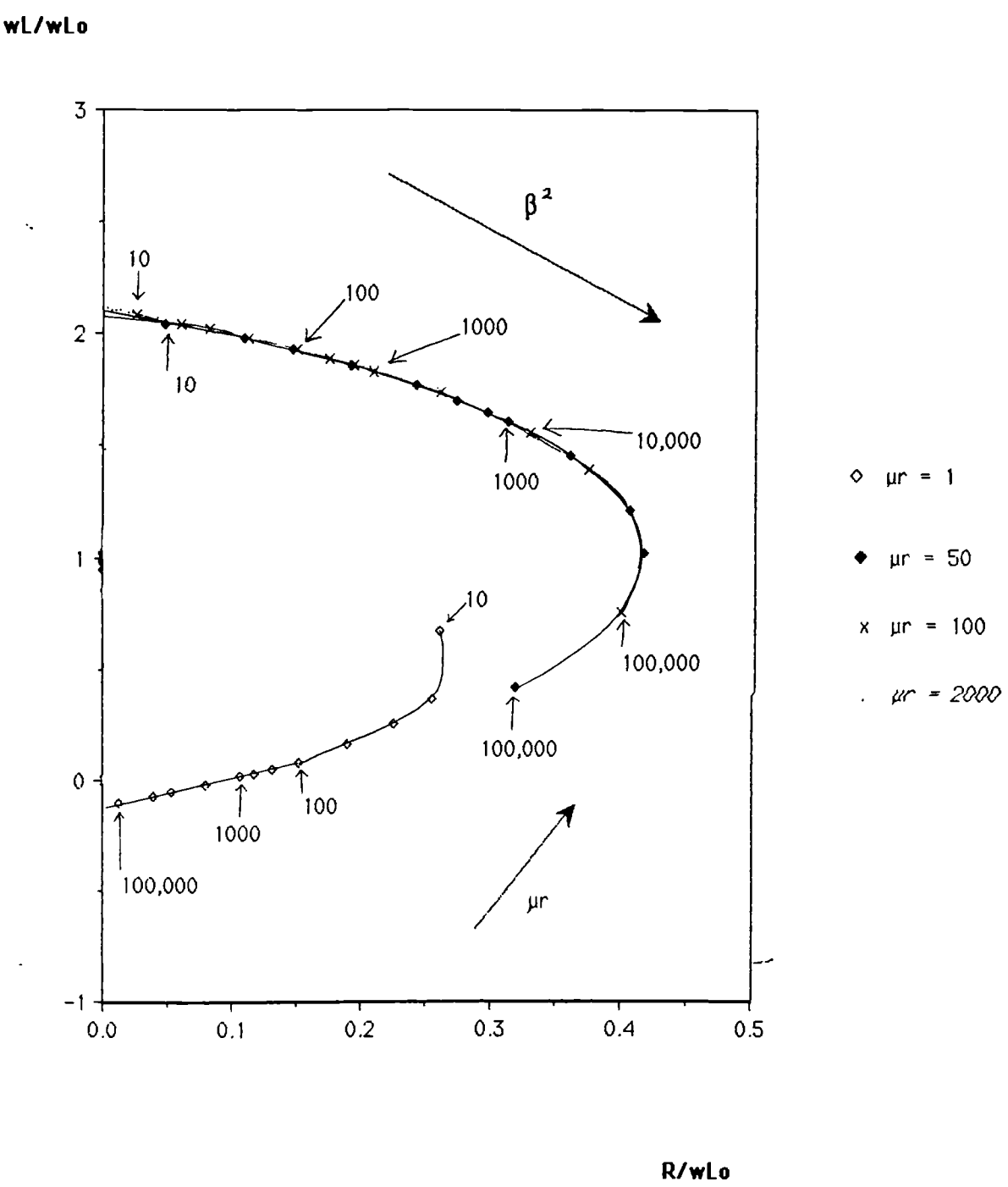

Figure 3.8: Variations in the components of impedance with normalised values of frequency β^2 of a coil with normalised length $Y_0 = 0.2$, above the surface of metals with values of μ_r between 1 and 2000.

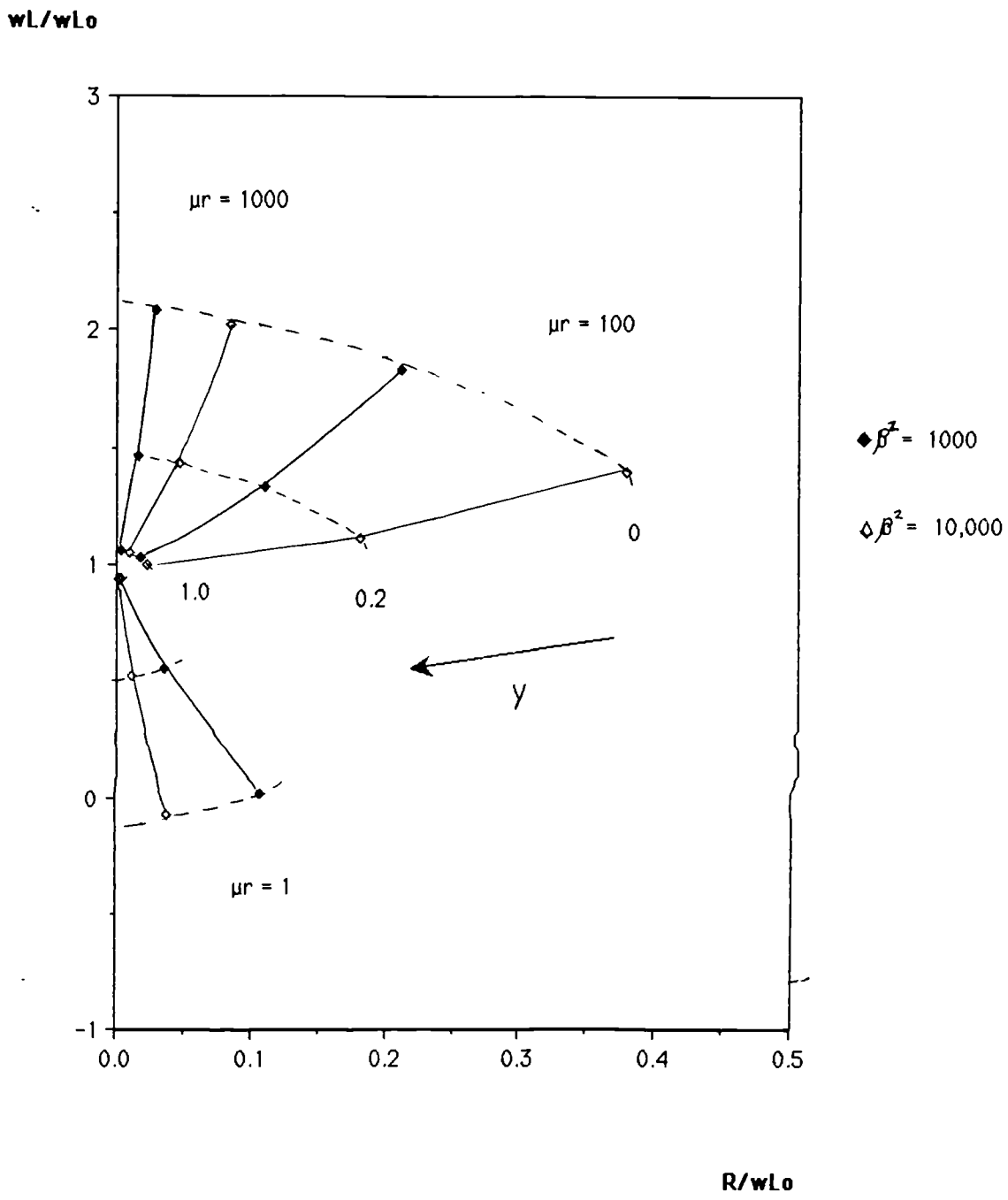

Figure 3.9: Variations in the components of impedance with normalised values of lift-off Y of a coil with normalised length $Y_0 = 0.2$, above the surface of metals with values of μ_r of 10, 00 and 1000. $\beta^2 = 1000$ and 10,000.

Fig. 3.10 shows how an increase in the normalised coil length Y_0 affects the normalised components of impedance for different values of μ_r. As expected, an increase in the value of Y_0 has a similar effect to an increase in the value of normalised lift-off (Fig.3.10(b)), because the end of a long coil is more remote from the surface of the metal as compared with a shorter coil, hence there is a decrease in the relative amount of eddy current induction. Theoretical values are compared with experimental measurements in Section 6.2.

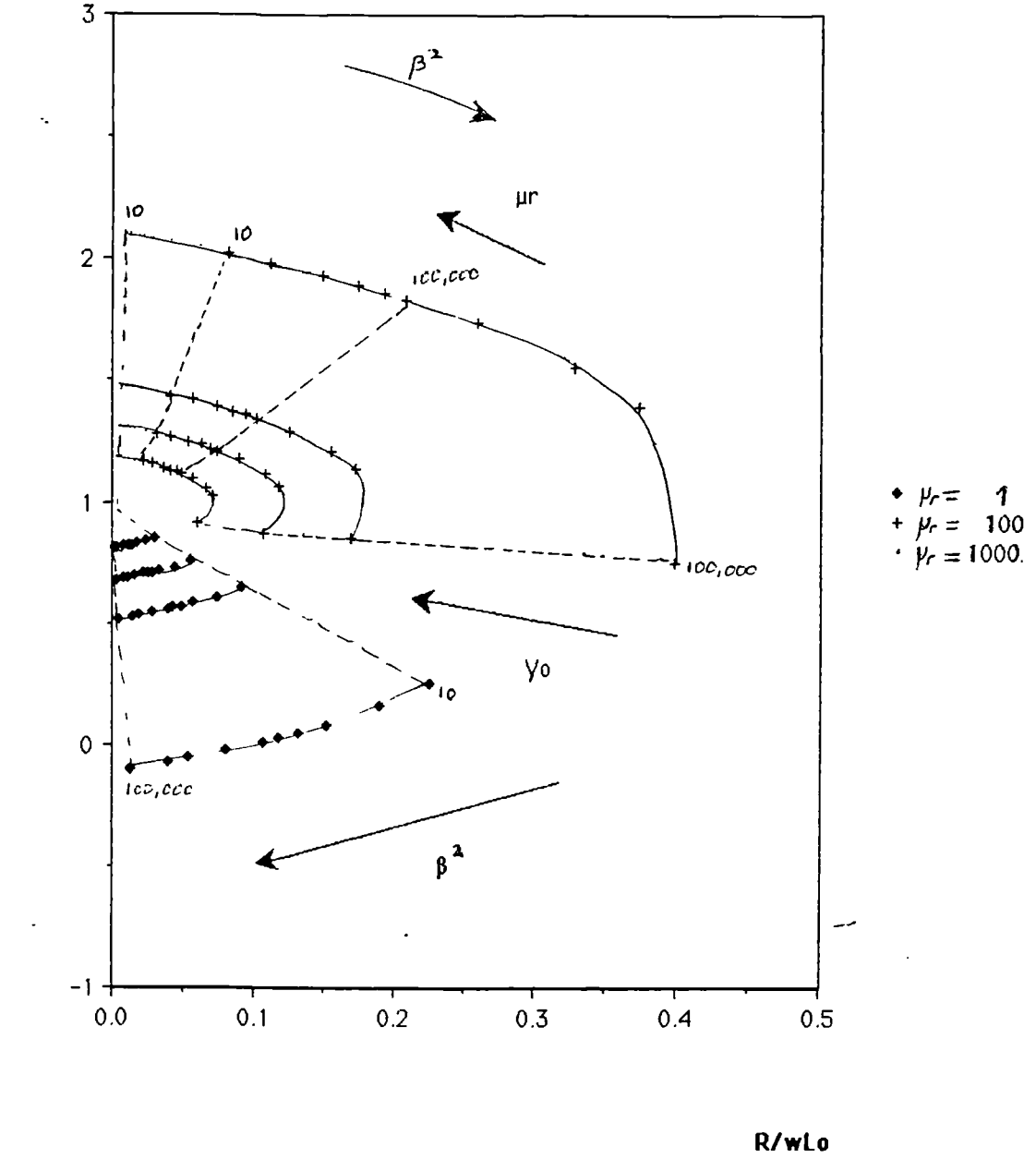

Figure 3.10(a): Variations in the components of impedance with normalised values of coil length Y_0 and frequency β^2. $Y = 0$, $\mu_r = 1$, 100 and 1000.

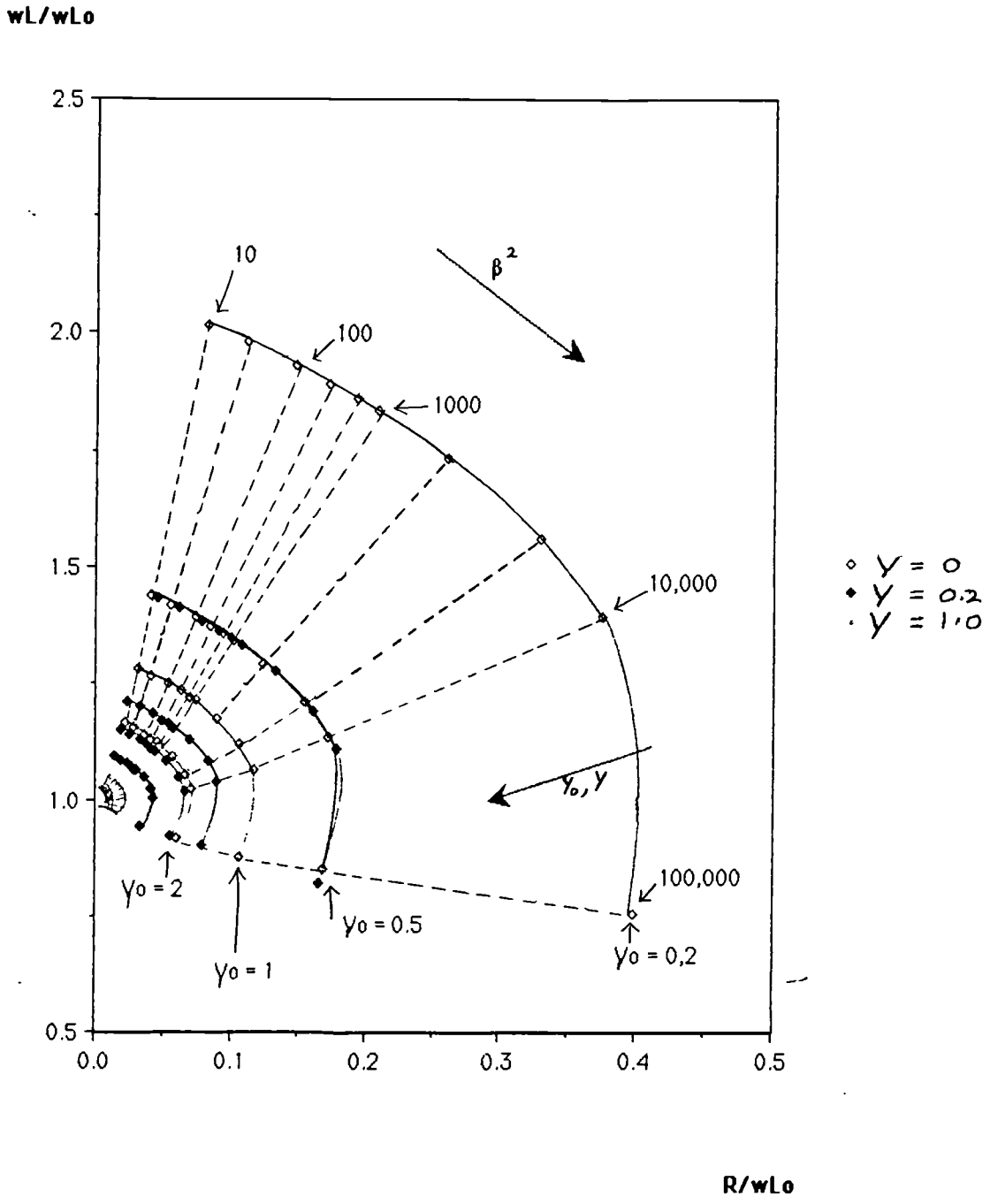

Figure 3.10(b): Variations in the components of impedance with normalised values of coil length Y_0, and lift-off Y at different values of β^2. $\mu_r = 100$.

CHAPTER 4

EXPERIMENTATION

In this chapter the basic equipment is described for the measurement of the impedance of coils used:-

a) to verify the theoretical conclusions obtained in Chapter 3, and

b) to measure the changes of impedance used for the lift-off method of flaw detection as described in Chapters 7 and 8.

Real and simulated defects in homogeneous and welded steel samples were studied to determine the effects of magnetic permeability on the identification and sizing of surface-breaking flaws.

A multifrequency flaw detector (Section 4.1.2) was used to detect the changes in the components of impedance of three different types of surface-scanning probe (Section 4.3) above samples of Aluminium and Mild Steel (Section 4.4). The output of the flaw detector was calibrated by inserting a small, non-inductive resistance in series with the detecting coil of the probe, as described in Section 4.5. Absolute values of the components of impedance of the coils were measured with an impedance bridge analyser (Section 4.1.1). The position of the coils above the surface of the metal samples was controlled using a scanning rig and sample levelling device (Section 4.2).

4.1 Instrumentation

4.1.1 Measurement of Impedance

Absolute measurements of the reactive and resistive components of impedance of the coils were made either with a Sullivan and Griffiths Universal Inductance Bridge,

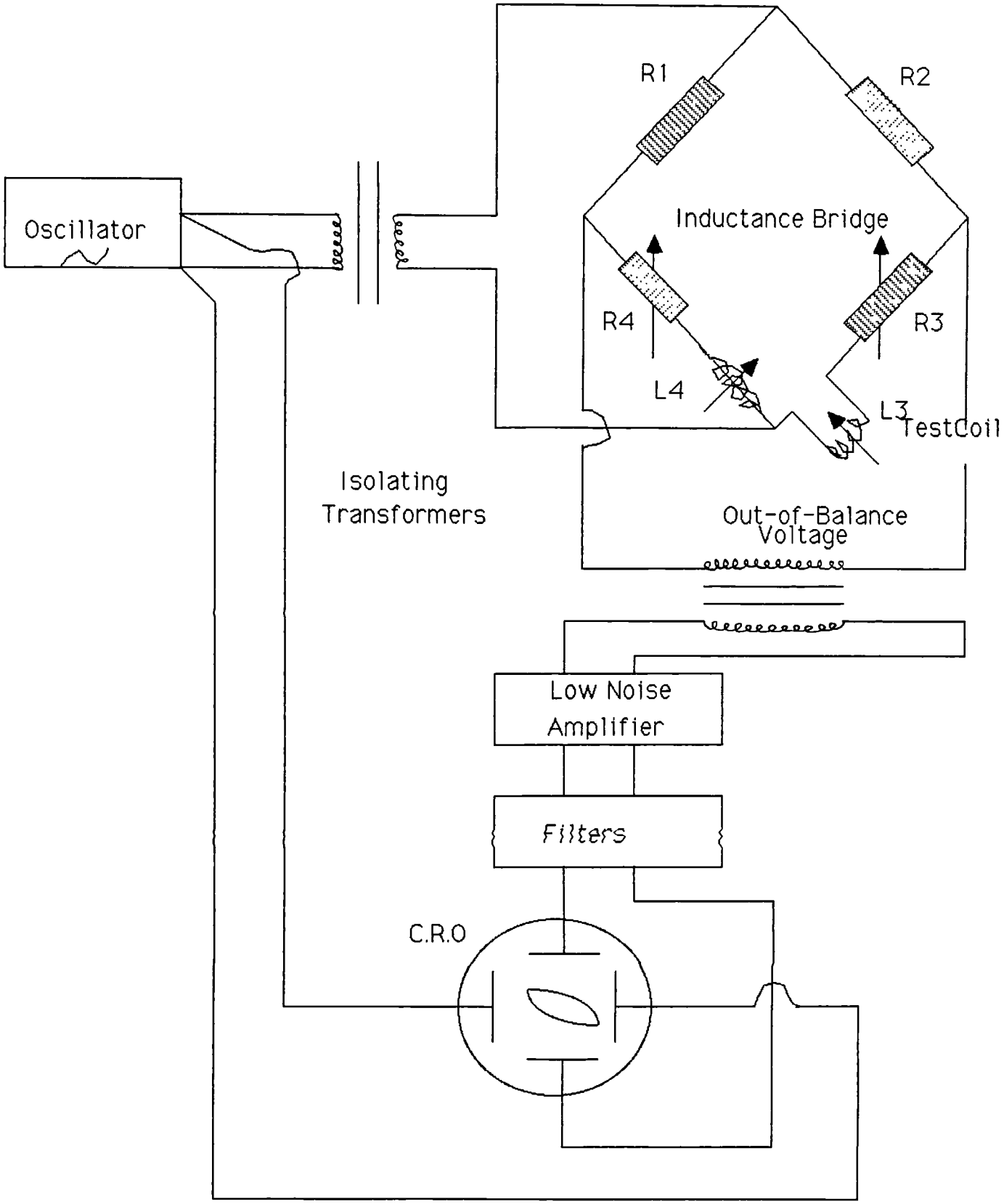

Figure 4.1: Schematic diagram of an impedance bridge

type AC1100, or with a Hewlett Packard LF Automatic Impedance Analyser, model 4192A. The Sullivan and Griffiths Universal Inductance Bridge (Fig. 4.1) was capable of measuring inductances from 1μH to 100H and resistances from 0.1 ohm to an accuracy of ±1 per cent, for frequencies between 200 Hz and 20 kHz. The Hewlett Packard LF Impedance Analyser can measure impedances between 0.1 milliohms and 1.2 Megaohms automatically at frequencies from 5 Hz to 13 MHz with an accuracy of 0.1 per cent. The instrument can display the impedance measured as either the total impedance of the sample, or the separate components of inductance, resistance and capacitance of the impedance.

4.1.2 The Hocking Eddy Current Flaw Detector

Generally, for the measurement of eddy current phenomena, better sensitivity is achieved by measuring the changes of the components of impedance, rather than the absolute values. In these investigations a *Hocking Electronics Vector S900* multichannel flaw detector was used. The main component of the instrument is an a.c. bridge, which can be balanced automatically at any frequency between 1kHz and 1MHz. The output potential difference of the bridge can be displayed on the screen of an integral storage oscilloscope, either as a vector displacement on an x-y plane, or as a function of time. The Vector S900 can be operated simultaneously on three channels at different frequencies, the outputs of which can be mixed to eliminate unwanted signals, such as those caused by changes in the values of lift-off or magnetic permeability, from the display. In these investigations this facility was not found useful.

The output from the oscillator (Fig. 4.2) passes through an automatic gain control to a potentiometer, which controls the voltage input to the bridge and thus regulates the sensitivity of the instrument. The detecting coil is connected to one arm of the

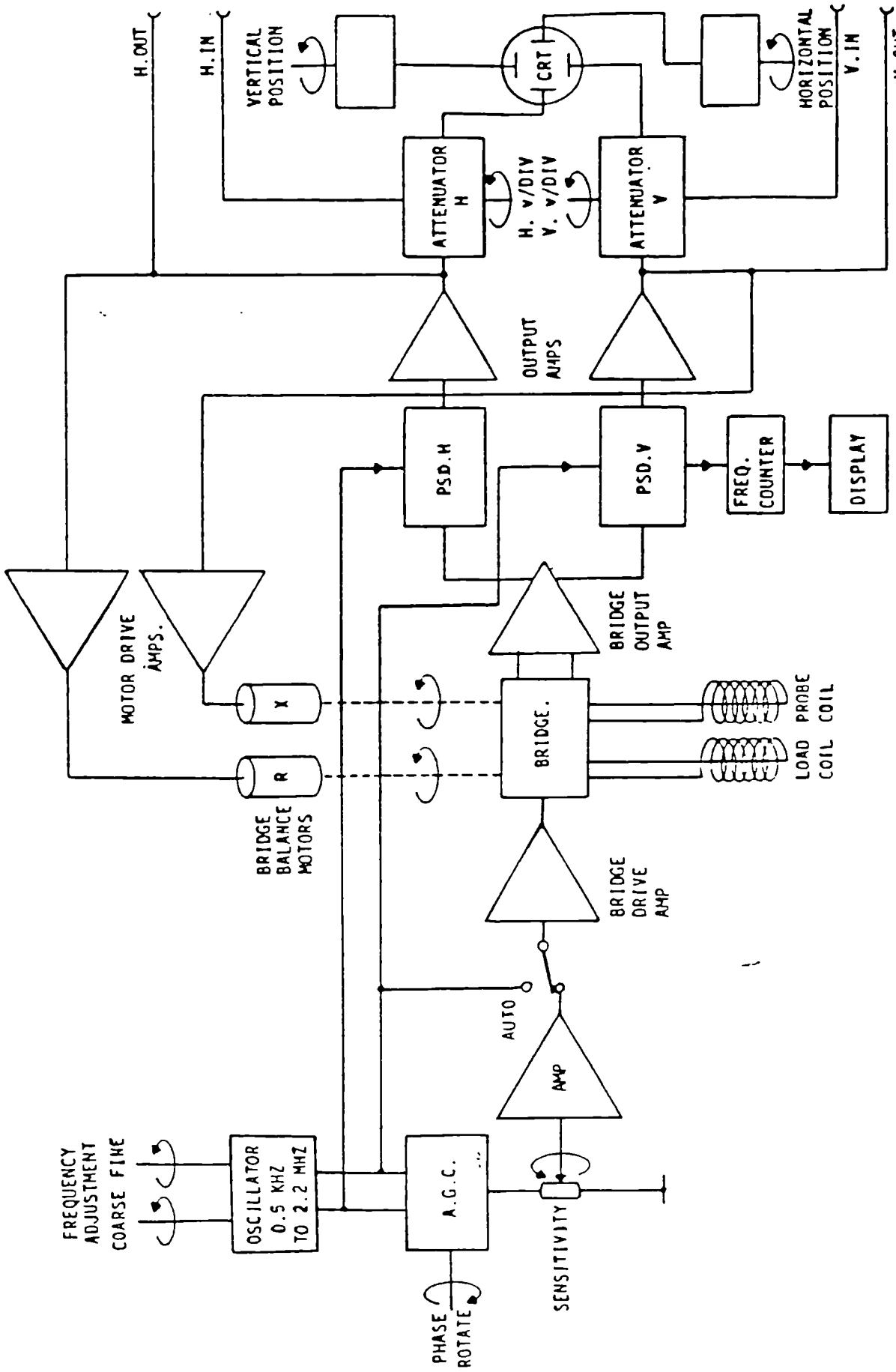

Figure 4.2: Schematic diagram of the bridge circuit of a Hocking Electronics phase-sensitive eddy current flaw detector.

bridge circuit and a balancing load coil of similar impedance to an adjacent arm. For a single-coil probe, a separate load coil is required to balance the bridge circuit, but for multiple-coil probes the load coil forms part of the probe (Section 4.3). The remaining two arms of the bridge circuit contain potentiometers to reduce the output potential difference of the bridge to zero. The output of the bridge is amplified and passed to two phase sensitive detectors in quadrature, each of which is provided with a reference signal from the oscillator, and then to the oscilloscope to be displayed as a function of the two perpendicular components of voltage. An additional potentiometer rotates the trace on the oscilloscope through any angle.

In Section 4.5 it is shown possible to express the output signal in terms of changes in the real and imaginary components of impedance of the test coil.

4.2 The Scanning Rig

The position of the detecting coil above the surface of a metal sample was controlled using a scanning rig. The scanning rig (Fig. 4.3) allows samples to be scanned at constant speeds and constant known values of lift-off, without introducing either any electrical noise or mechanical vibrations. The probe holder fixes the probe normal to the surface of the sample under test, but remote from any other metal which could affect the eddy current response. The lift-off distance can be altered and measured by means of a travelling micrometer. The probe is scanned across the surface of the sample by using a small d.c. motor to turn a threaded bar on which the probe holder assembly travels. To ensure that the probe is kept normal to the test surface during the scan, the sample is mounted on a perspex levelling device (Fig. 4.4).

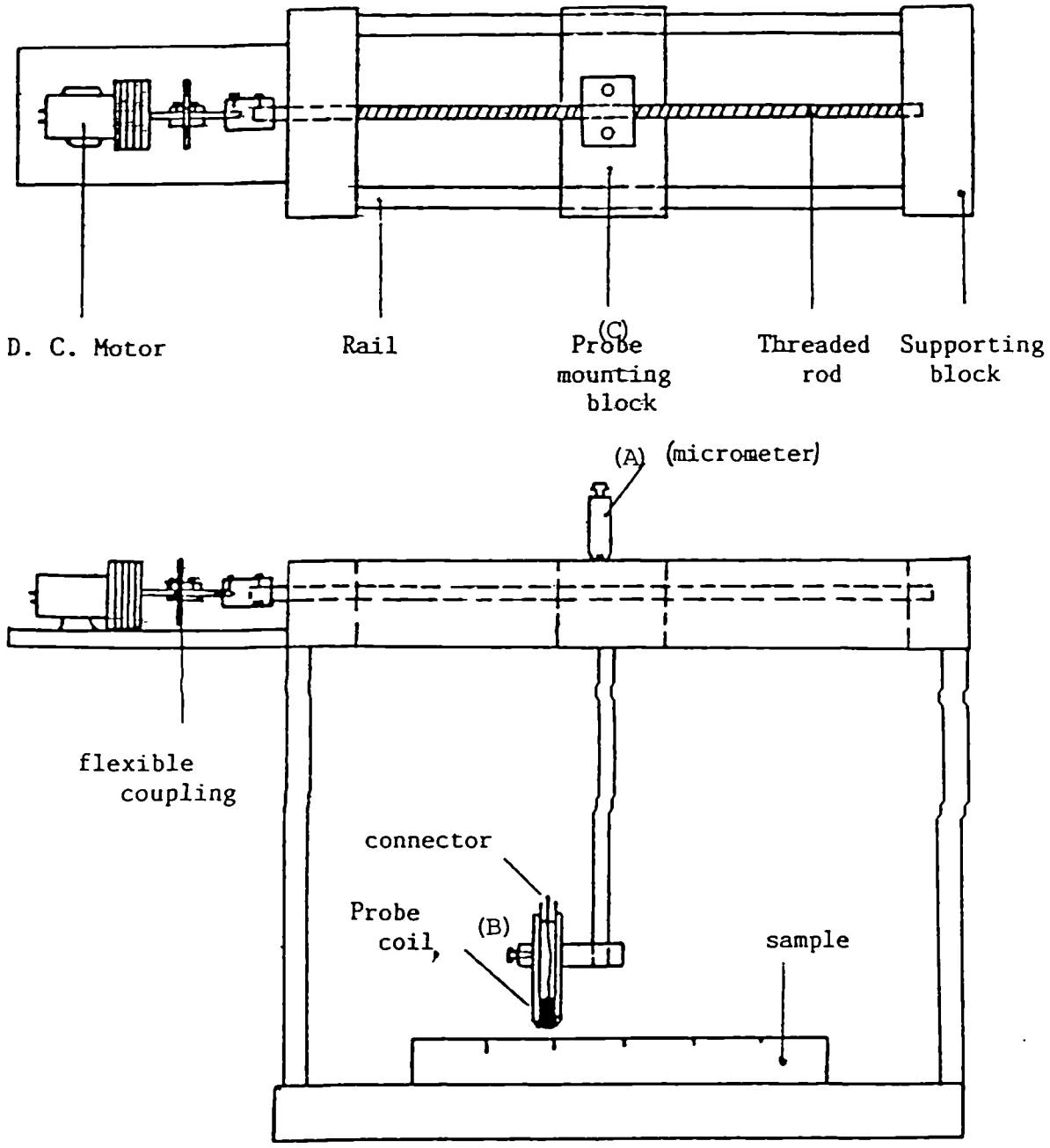

Figure 4.3: Scanning rig for precise positioning of the probe when scanning a sample.

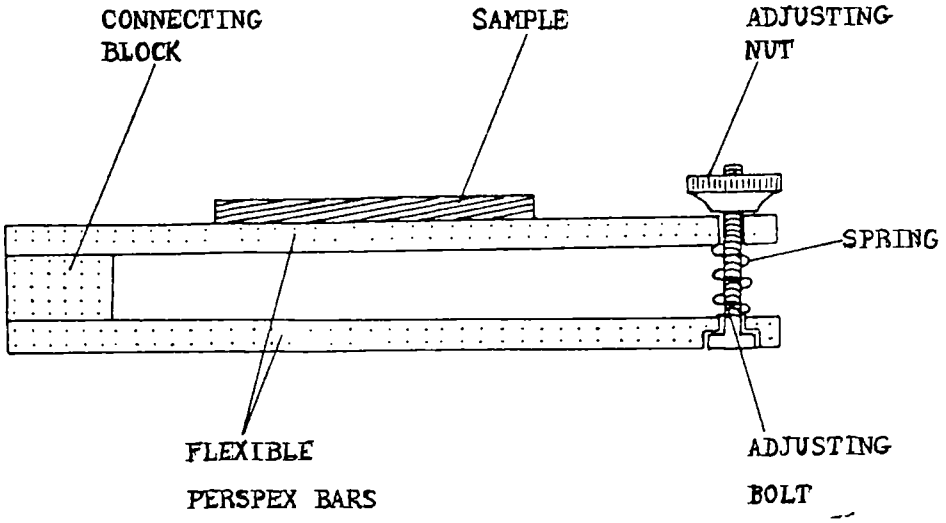

Figure 4.4: Levelling mechanism for a sample in the scanning rig.

4.3 Design and Construction of Probes

When designing a probe for flaw detection, it is important to consider the radius and inductance of each coil: A coil having a small radius has a greater ability to resolve individual flaws than a larger one, but the smaller the coil the lower its inductance. The inductance may be increased by the use of a ferrite core, which increases the magnetic flux within the coil. Three main designs of surface-scanning probe (Sections 4.3.1 to 4.3.3) are used in these investigations, some with Perspex cores and others with ferrite cores. The Perspex cores serve only as support for the coils, since, for the purposes of eddy current testing, Perspex may be regarded as having an electrical conductivity $\sigma = 0$ and magnetic permeability $\mu_0 = 4\pi \times 10^{-7}$ H/m, which is similar to air. The ferrite cores are made from *F14* ferrite, a nickel-zinc ceramic containing approximately 50 percent ferrous oxide, compressed and sintered in the shape of a solid cylinder. The manufacturers quote [33] an intrinsic relative magnetic permeability of 220 at 1 MHz, and an electrical resistivity of 10^3 ohm-m. Eddy current induction in the core is negligibly small because of its relatively high resistivity, although there are some minor power losses as a result of magnetic hysteresis, approximately proportional to the frequency of applied field. The value of magnetic permeability quoted by the manufacturers was obtained using a toroid of ferrite. This value is higher than the effective permeability measured from a ferrite rod, because there is a greater leakage of flux from a rod. However, the exact value is not important here, because only normalised values of impedance of the coil are considered.

The coils were wound uniformly about the axis of the core using fine gauge copper wire, taking care not to overlap the turns on any one layer (Fig. 4.5). They were then secured in a perspex probe body with cyanoacrylate adhesive, with the ends of the coil threaded through the centre of the body (Fig. 4.6). The ends were scraped

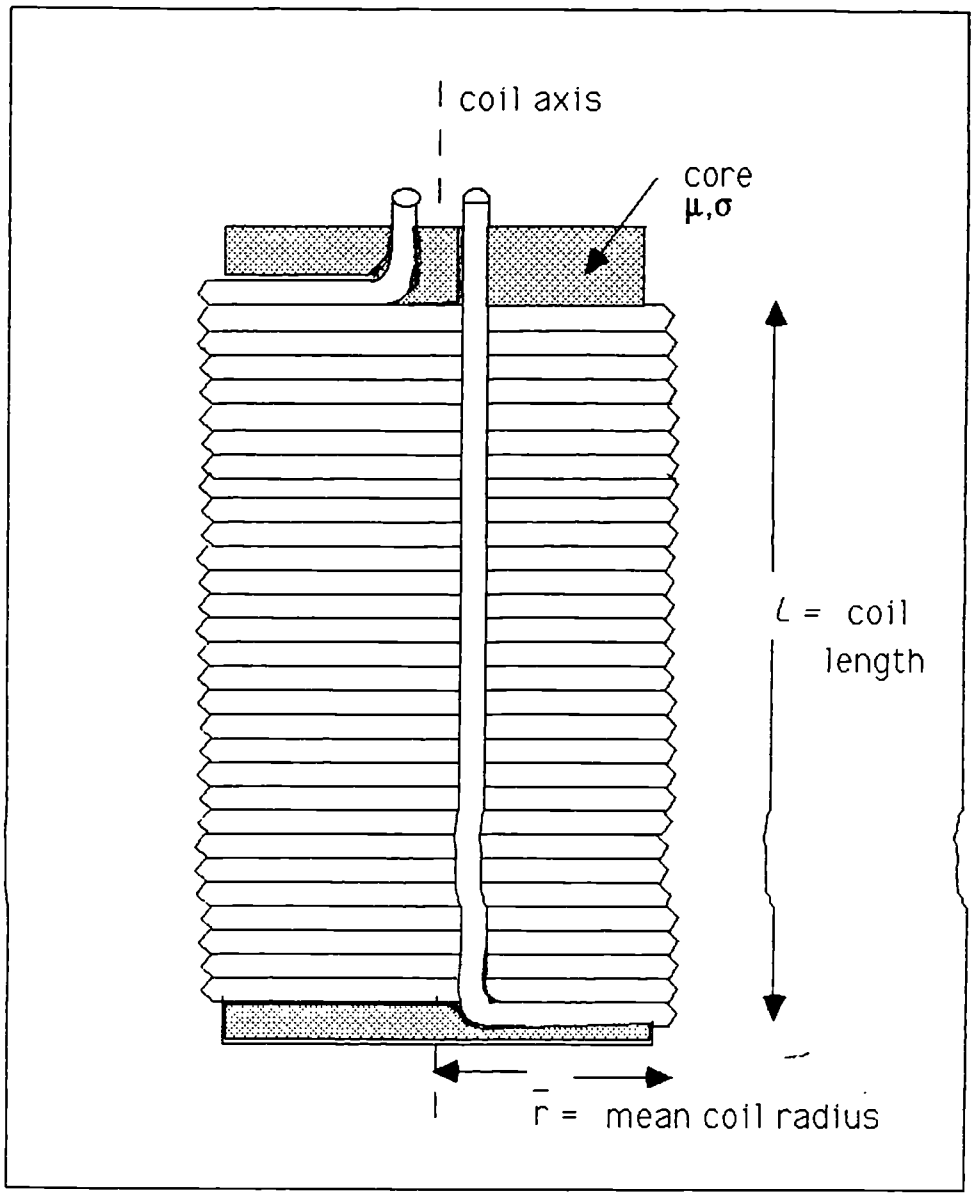

Figure 4.5: Winding of a single solenoid coil.

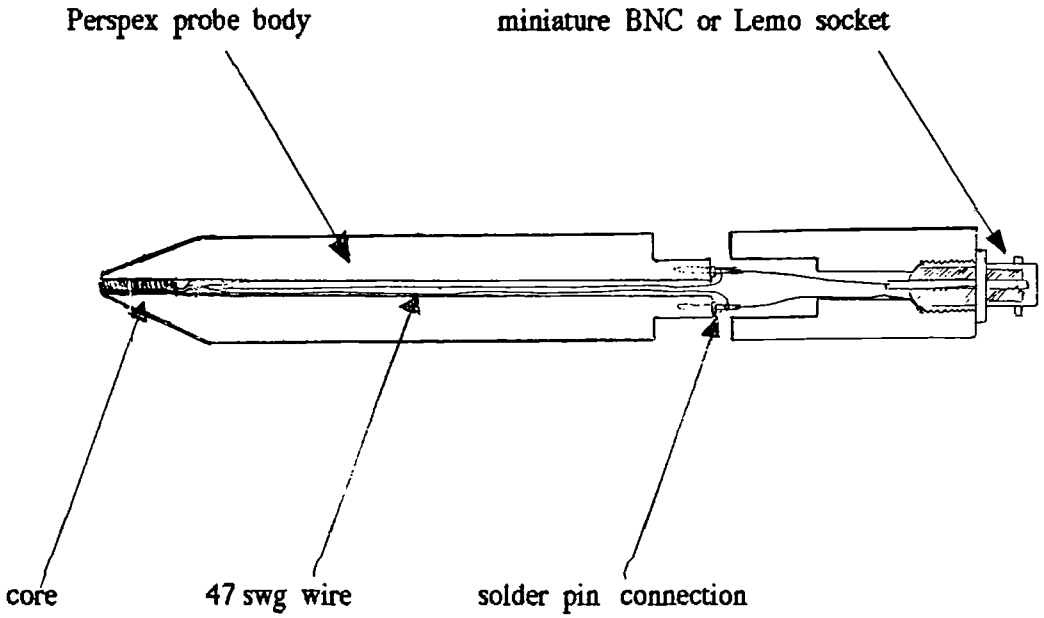

Figure 4.6: Cross-section of an eddy current probe.

clean of insulator coating and soldered to steel pins fixed in the bottom half of the probe body, so that no strain was applied to the fine wire of the coil, either during assembly or through rough treatment when connecting the probe to the instrument. A thicker plastic-coated wire was used to connect the coils to a miniature BNC terminal for the single coils, or a miniature 4 pin LEMO connector for the multi-coil probes. The mean radii and lengths of the coils were measured with a micrometer (Tables 4.1 to 4.3).

4.3.1 Single Coil Probes

The simplest type of eddy current probe, used extensively in these investigations, is the single coil probe (Fig. 4.7). The inductance L of the coil is related to the number of turns N (Fig. 4.8), radius r, length ℓ and magnetic permeability μ_c of the core by the equation [29]

$$L = N\Phi / i = N^2 \mu_c \pi r^2 / \ell \qquad (4.1)$$

where

$$\Phi = \underline{B}.A = N \mu_c \pi r^2 i / \ell \qquad (4.2)$$

Here Φ is the total magnetic flux due to current i passing through the coil, assuming all the flux passes through the whole solenoid and the internal magnetic field is uniform. The effect of the flux diverging at the ends of the coils has been neglected here, although in practice this would reduce the value of inductance.

A set of four single coil probes were built with Perspex cores, together with matching load coils to balance the bridge circuit in the flaw detector (Section 4.1.2). A suitable impedance match with the Vector S900 Eddy Current Flaw Detector was provided for frequencies in the range 100 kHz to 1 MHz. In addition, a set of four

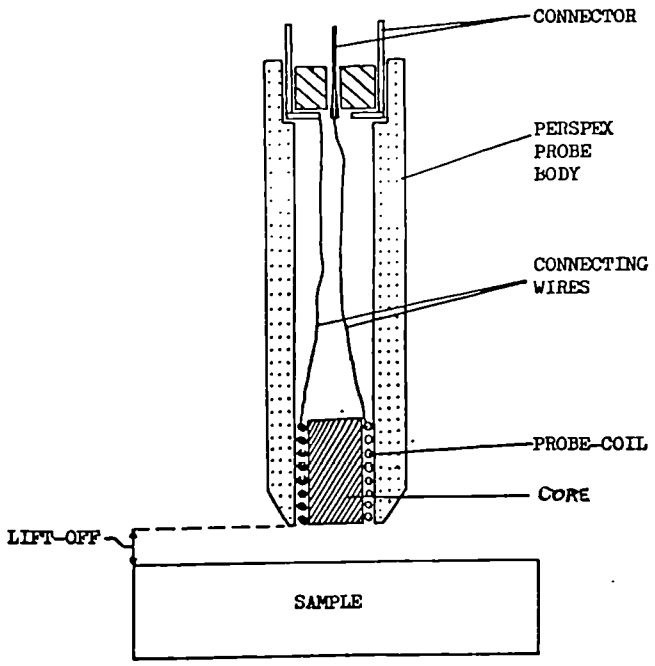

Figure 4.7(a): Cross-section of a single coil probe

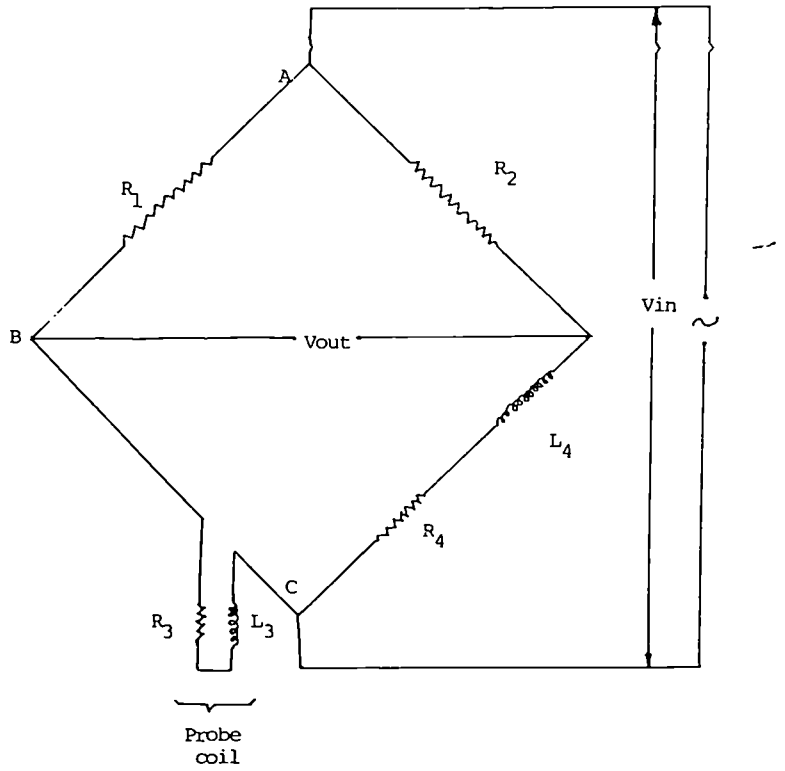

Figure 4.7(b): Connection of a single coil to an inductance bridge

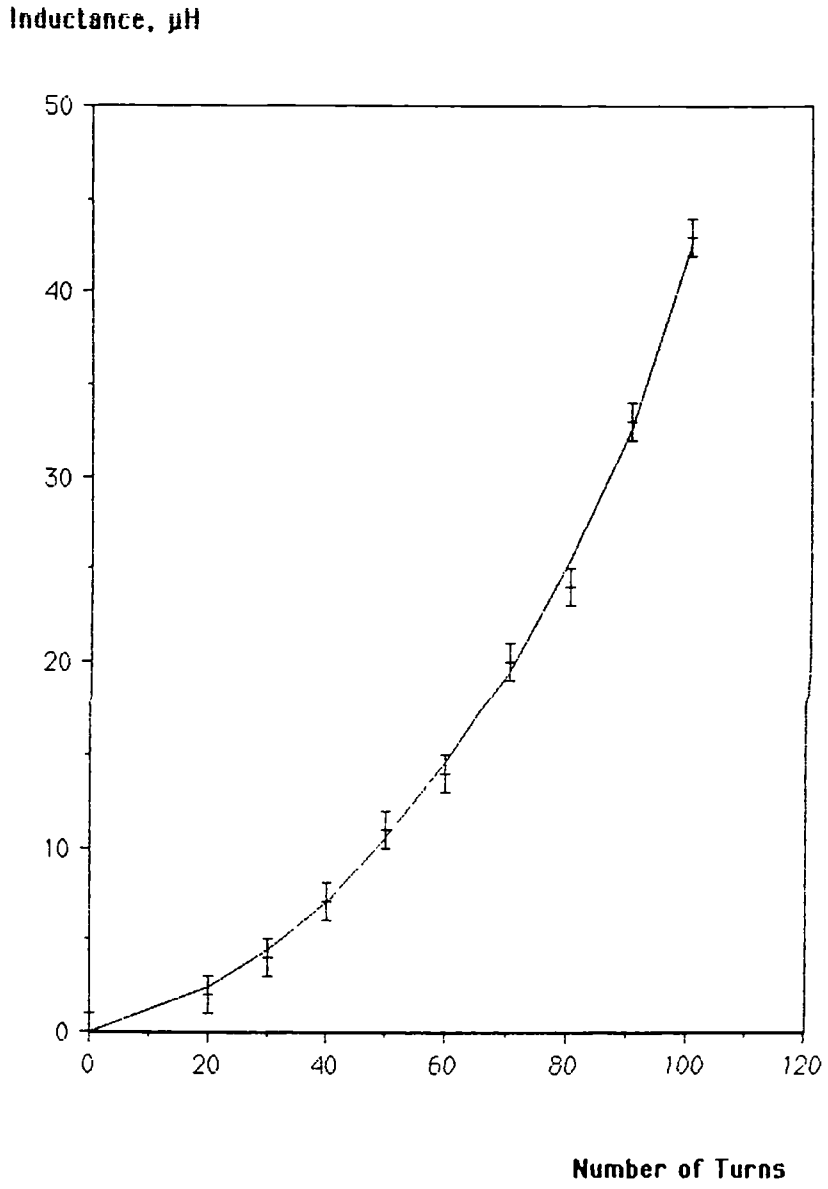

Figure 4.8: Variation of inductance with number of turns of a coil

single coil probes were built with low inductances, two air-cored and two ferrite-cored, for which the core diameters were determined by the limited availability of suitable ferrite cores. Table 4.1 lists the coil sizes and inductances of all the single coil probes.

4.3.2 Differential Probes

Differential probes were designed to minimise the effects of lift-off without undue loss in sensitivity to flaw detection. They were built with two identical coils wound in opposition, set parallel to each other and as near as possible at identical distances from the base of the probe (Fig. 4.9). On scanning a sample with the axis of the probe held perpendicular to the surface, each coil should contribute to the output signal with equal amplitude and opposing phase. Thus, over a defect-free area no out of balance output signal should be observed. On meeting a discontinuity the coils would not be affected simultaneously, hence producing an output signal with each coil contributing to half of the signal. Three air-cored differential probes were built with the dimensions given in Table 4.2, to form a set with single coil probes 1S to 3S (Table 4.1), in order to compare the characteristics of similar single and differential type probes. One coil of each differential probe was built eccentrically into an axially revolvable cylinder, such that the distance between the two coils could be varied (Fig.4.10). The optimum distance apart of the coils with 1.5 mm radius was 5 mm.

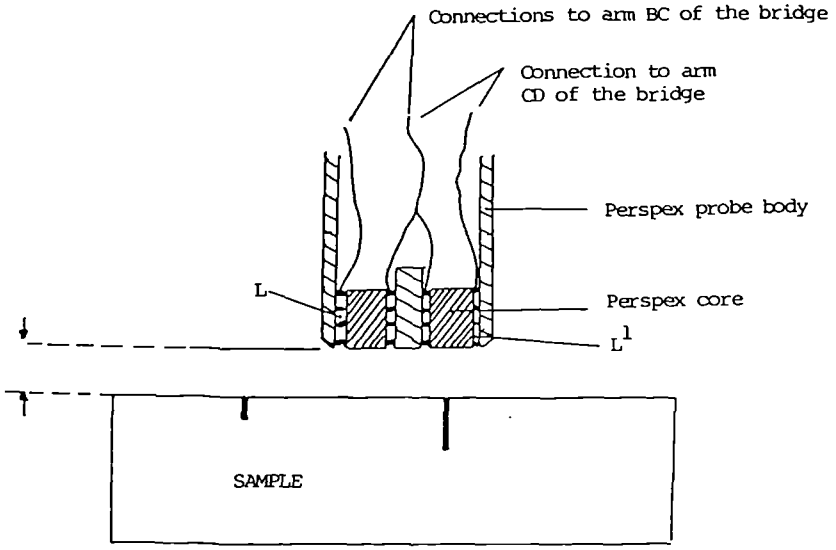

Figure 4.9(a): Cross-section of a differential probe

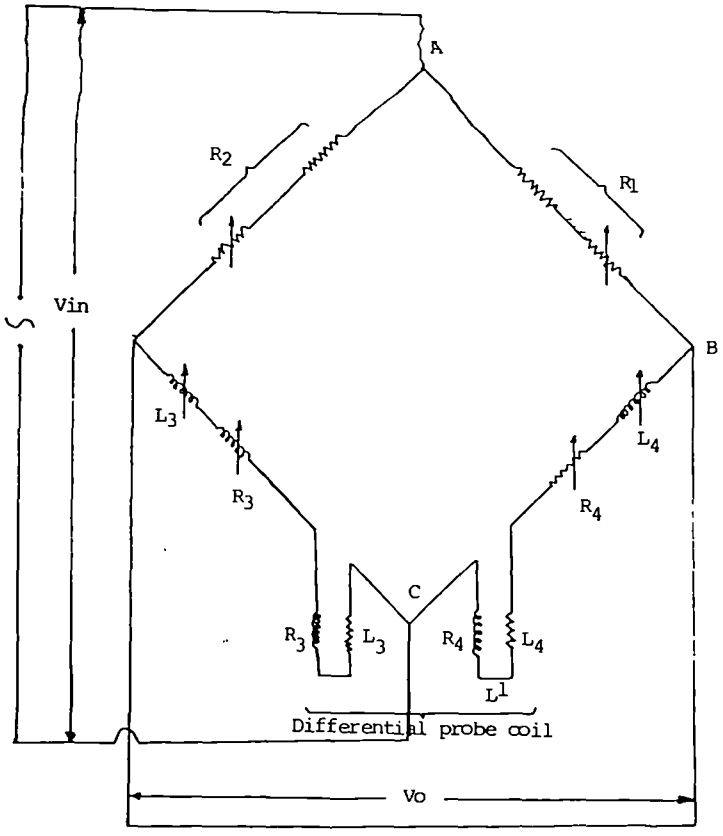

Figure 4.9(b): Connection of a differential probe to an inductance bridge.

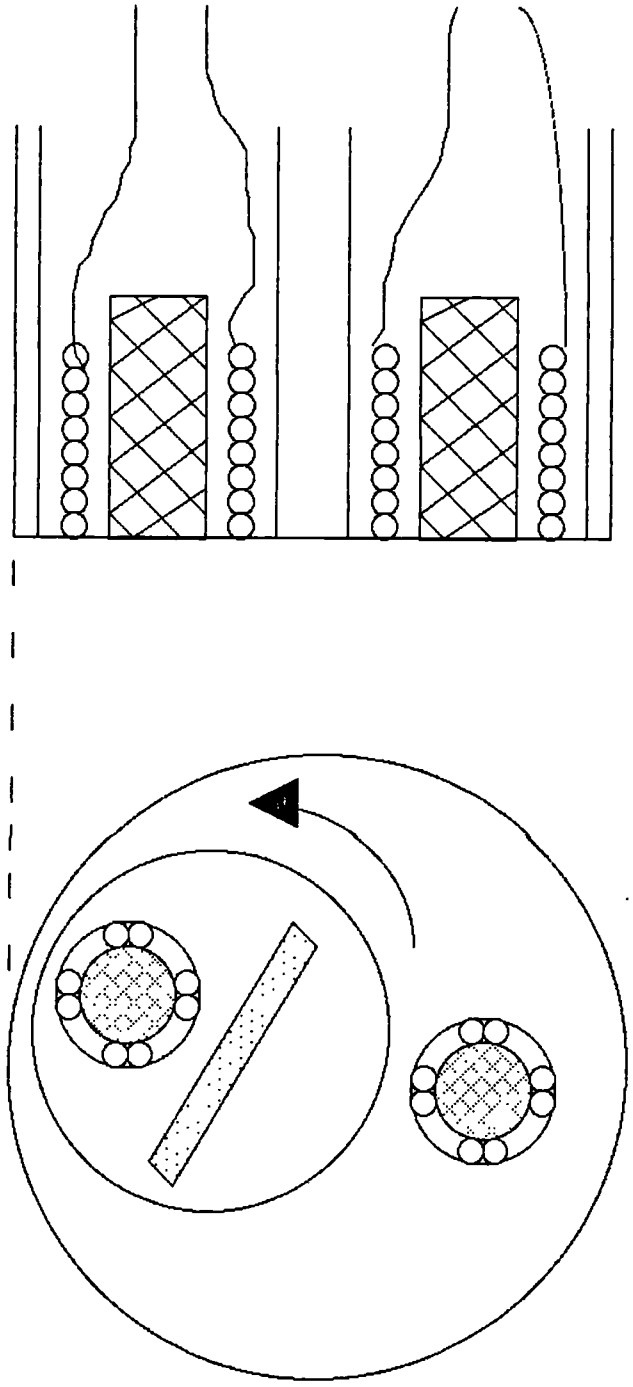

Figure 4.10: Revolvable cylinder in the base of the differential probes, used to optimise the distance apart of the two coils.

Table 4.1 Sizes and Inductances of Single Coil Probes

r = mean radius,

ℓ = coil length,

n = number of turns,

swg = standard wire gauge,

L = coil inductance, measured remote from the sample

Core material: f = ferrite F14; a = "air" (Perspex)

Probe	r (mm)	Core	ℓ (mm)	n	Wire swg	L (μH)
1S	1.25	a	9.0	112	45	9
2S	1.25	a	4.1	112	45	13
3S	2.65	a	2.0	50	45	17
4S	3.90	a	3.2	315	45	170
AS1	2.05	a	2.2	30	47	5
AS2	2.05	a	6.2	90	47	17
FS1	2.05	f	2.2	30	47	15
FS2	2.05	f	6.2	90	47	140

Table 4.2 Characteristics of the Differential Probe Coils

r = mean radius,

l = coil length,

n = number of turns,

swg = standard wire gauge,

L = coil inductance, measured remote from the sample

Core material : f = ferrite F14; a = "air" (Perspex)

Probe	r (mm)	Core	l (mm)	n	Wire swg	L_1 (μH)	L_2 (μH)
1D	1.25	a	9	112	45	9	9
2D	1.25	a	4	112	45	14	16
3D	2.65	a	2	50	45	17	18

4.3.3 Transformer Probes

The Transformer probes [34] used here were designed to enable eddy current measurements to be made with the Vector S900 flaw detector at frequencies below 100kHz., thus increasing the range of frequencies at which measurements were possible to between 10 kHz and 1MHz. It was considered that testing with frequencies lower than 100 kHz would allow greater penetration of the eddy currents in a ferromagnetic material, to counteract the effect of diminishing depth of eddy current penetration ∂ when magnetic permeability μ is increased, where [2]

$$\partial = (2/\omega\mu\sigma)^{1/2}. \qquad (4.3)$$

Transformer probes have been described by Dodd et al [35] and Bains [36], who called them reflection probes. The probe is designed with separate exciting and detecting coils, which form the primary and secondary windings respectively of a transformer. This arrangement allows the excitation current to be increased and the detection sensitivity of the probe to be optimised at the chosen frequency. A large turn-ratio of the secondary to primary windings is preferable for good defect sensitivity.

The transformer probes used here were built using three coils (Figs.4.11 and 4.12). Two similar coils acting as detecting coils were wound in opposition on a ferrite core to obtain good sensitivity, with a separate driver coil wound around them. A simple modification to the impedance bridge of the eddy current flaw detector was necessary to allow the input voltage to be connected directly across the primary windings of the transformer probe (Fig. 4.12(b)). Four probes with ferrite cores were used, for which the dimensions are given in Table 4.3.

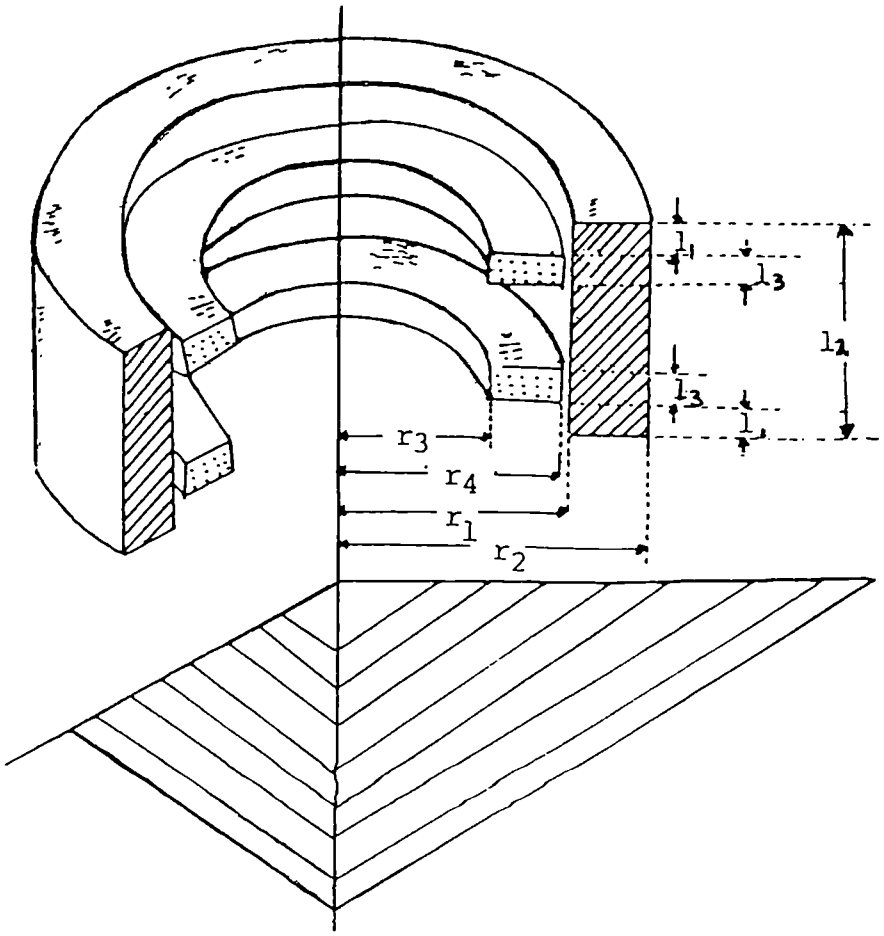

r_1 = the driver coil inner radius
r_2 = the driver coil outer radius
r_3 = the pick-up coil inner radius
r_4 = the pick-up coil outer radius
l_1 = the minimum amount of lift-off of the pick-up coil
l_2 = the length of the driver coil
l_3 = the length of each pick-up coil
n_1 = number of turns of the driver coil
n_2 = the number of turns on each pick-up coil

Figure 4.11: Sectional view of the coil arrangement of a transformer probe.

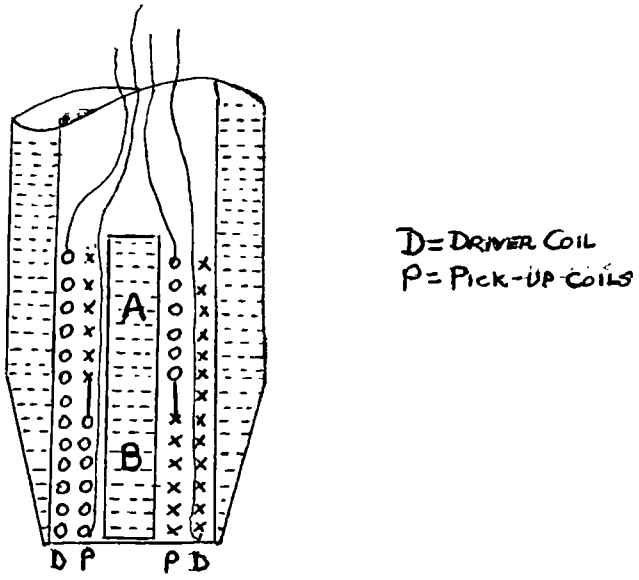

Figure 4.12(a): Cross-section of a transformer probe

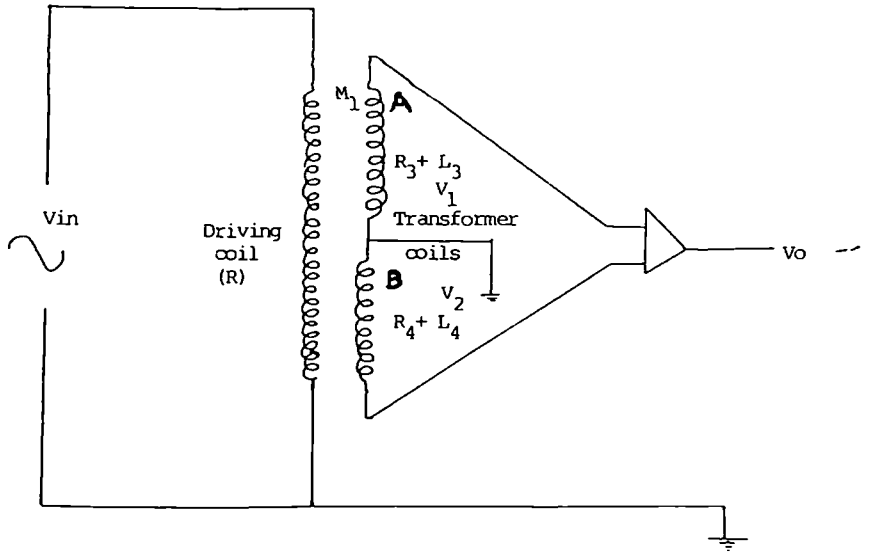

Figure 4.12(b): Circuit of an inductance bridge which has been modified to measure the impedance of a transformer probe.

Table 4.3 Transformer Coil Dimensions and Inductances

r = mean radius (pick-up coil),

ℓ = coil length,

n = number of turns,

swg = standard wire gauge,

L = coil inductance, measured away from the sample

Core material : f = ferrite F14.

			Driver coil				Pick-up coils			
Probe	r	Core	ℓ	n	Wire	L	ℓ	n	Wire	L
	(mm)		(mm)		swg	(μH)	(mm)		swg	(μH)
1T	1.40	f	8.2	75	45	36	4.1	50	47	31
2T	1.42	f	9.4	250	47	360	4.7	200	47	300
3T	1.20	f	10.6	125	45	135	5.3	90	47	29
4T	1.42	f	13.8	313	45	997	6.9	220	47	515

4.4 Calibration Samples

Slots were cut in samples of Aluminium alloy and mild steel, to use for testing the performance of the probes for defect detection (Chapter 7). Two B.S. 970 mild steel blocks 25mm x 38mm x 240mm were machined, block 1 containing 5 slots of depths 0.5, 1, 2, 3 and 4 mm with widths of 0.1 mm, and block 2 containing 6 slots 0.2mm wide with depths from 5mm to 10mm in 1mm increments (Fig. 4.13). The thinnest available slitting saw capable of cutting to the desired depth was used to cut each slot. The slots were positioned such that each slot could be tested without influence from edges or neighbouring slots. The thickness of the samples was sufficient to avoid any through penetration of the eddy currents. A similar mild steel sample was also produced with 5 slots of equal depth of 1.5mm, cut at angles between 90° and 30° to the sample surface, to study the effect of crack inclination (Section 7.5). Smaller blocks 12mm x 38mm x 50mm of both aluminium alloy and mild steel, each containing a saw cut of a depth between 0.5mm and 2.5mm and width 0.1mm, were compressed and machined flat to simulate tight cracks [34]. Compression of each sample was maintained until the saw cut just ceased to be visible to the naked eye. Further mild steel blocks containing similar saw cuts were left uncompressed. The degree of compression necessary to close each slot is given in Table 4.4.

Two BS.5436 50D steel samples containing the heat affected zone of a weld (HAZ) were also prepared for a study of the effect of changing magnetic permeability on crack detection (Sections 7.2 to 7.4). Two 175mm x 85mm x 12mm plates were prepared by laying a weld bead down the centre of the short side (Fig. 4.14), which was then machined off flat to leave the heat affected zone. One plate contained a fatigue-type crack, while the other was defect-free. A further plate of 50D steel was left unwelded and was machined with a slot 3.3mm deep at its centre and elliptical in shape (Fig. 4.15).

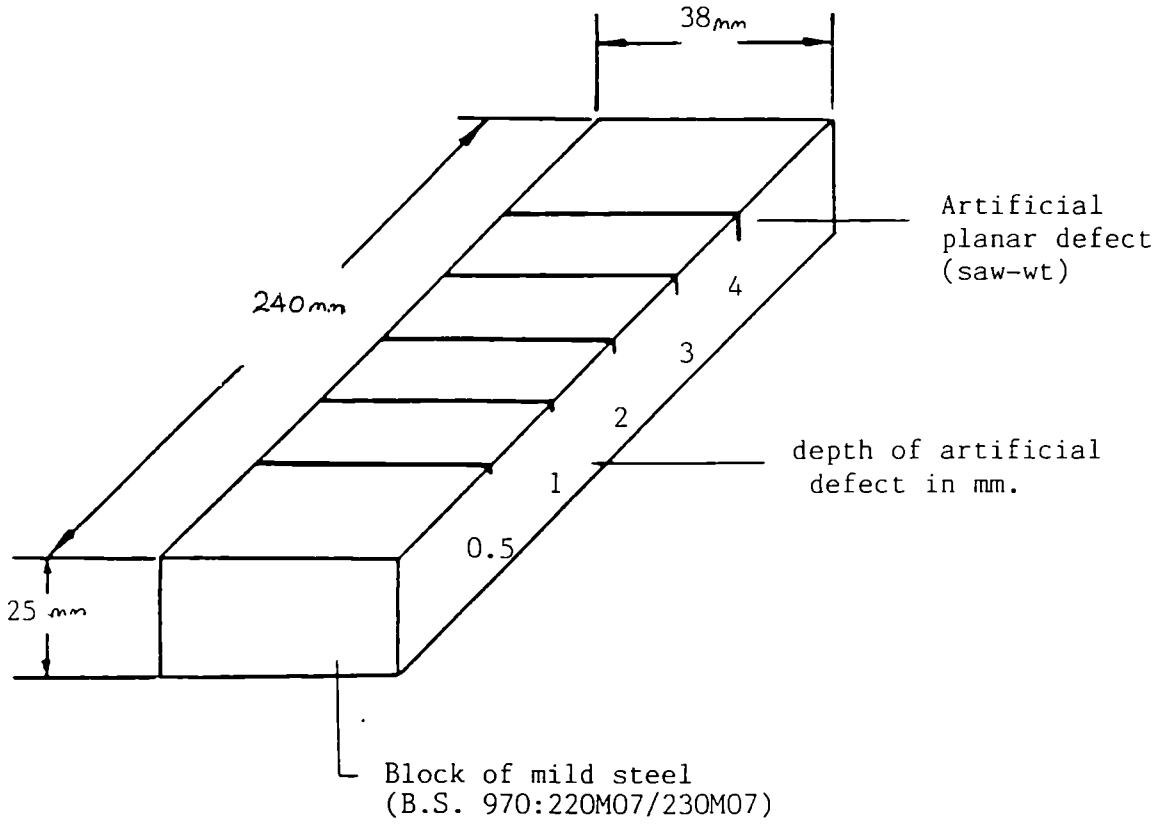

Figure 4.13: Mild steel calibration sample block 1, containing saw cuts 0.5mm to 4mm deep. Block 2 contains saw cuts 5mm to 10mm deep.

Table 4.4 Compression of Aluminium and Mild Steel Samples

Depth of saw cut (mm)	Compression (KN)		Sample Size (mm)	
	Aluminium	Mild steel	Aluminium.	Mild steel
0.5	225	285	12 x 38 x 76	12 x 38 x 50
1.0	216	262	12 x 38 x 76	12 x 38 x 50
1.5	206	257	12 x 38 x 76	12 x 38 x 50
1.75	198	255	12 x 38 x 76	12 x 38 x 50
2.0	193	253	12 x 38 x 76	12 x 38 x 50
2.5	186	250	12 x 38 x 76	12 x 38 x 50
1.0	---	none	----	12 x 38 x 50
1.75	---	none	----	12 x 38 x 50

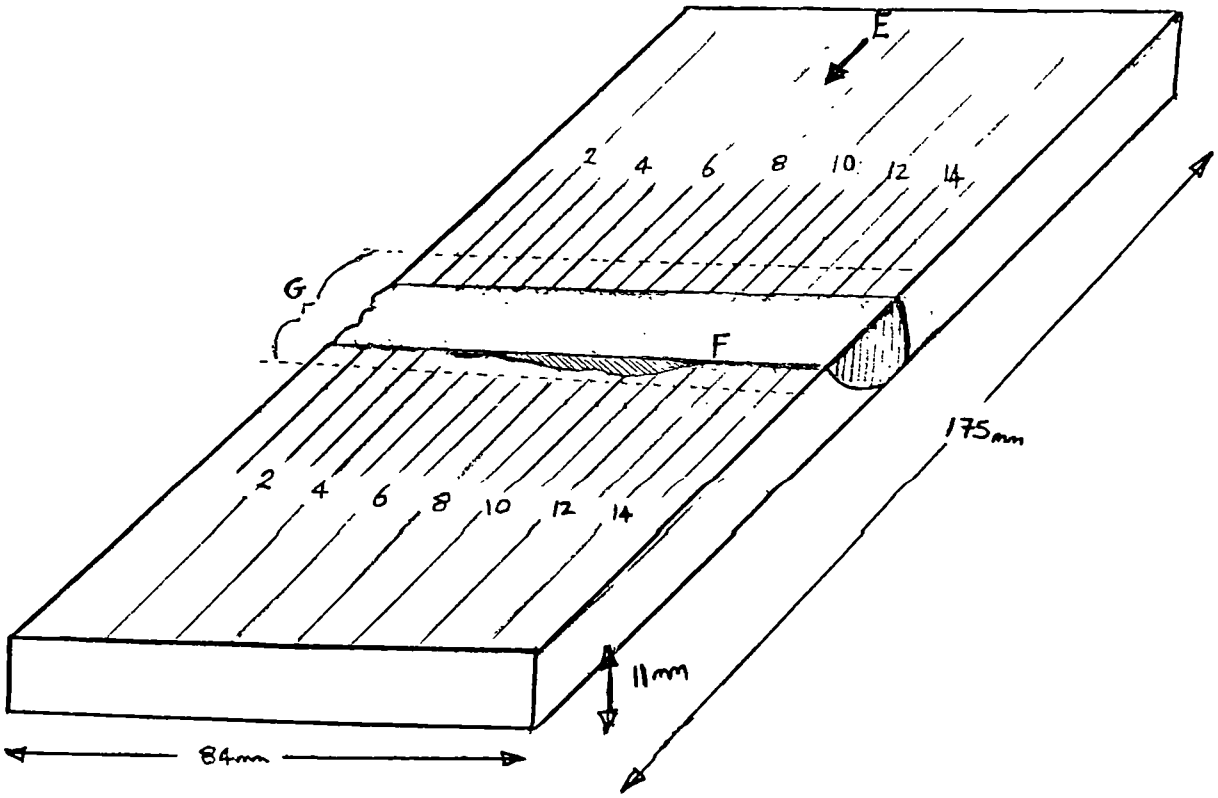

Figure 4.14: 50D steel plate containing a fatigue crack in the heat affected zone (HAZ) of a weld.

E = Direction of scanning
F = Crack, revealed with magnetic particle inspection
G = Weld and heat affected zone

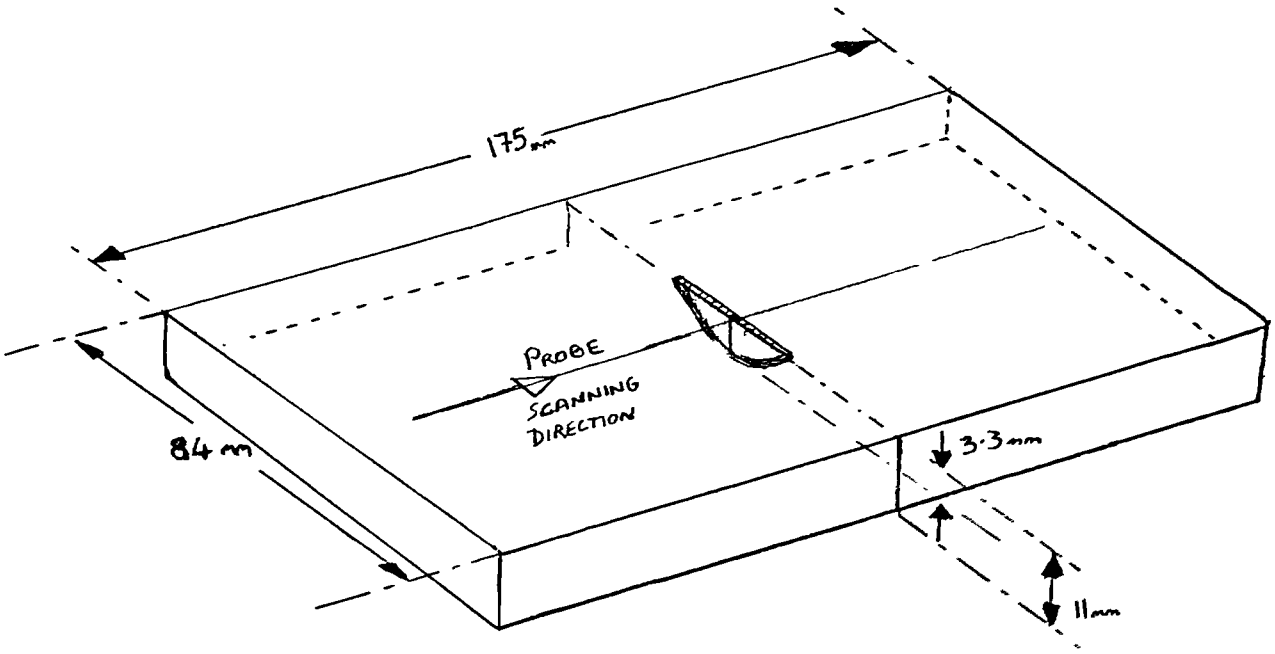

Figure 4.15: 50D steel plate containing a saw cut of maximum depth 3.3mm.

4.5 Calibration of the Flaw Detector

To convert the output voltages of the flaw detector to measurements of the components of impedance of a coil, the flaw detector should be calibrated for each probe over the frequency range used. In this way normalisation can be performed. Blitz, Williams and Tilson [37] have shown that the out-of-balance voltage of the bridge circuit of a flaw detector is related directly to any change in impedance of the coil from its balanced value by:

$$\Delta V_L = K.\Delta(\omega L) \qquad (4.4)$$

$$\Delta V_R = K.\Delta R \qquad (4.5)$$

where ΔV_L and ΔV_R are changes in the components of output voltage caused by changes in the components of coil impedance $\Delta(\omega L)$ and ΔR of the coil. Here K is a constant. They also showed that the components of the output voltage ΔV_L and ΔV_R were 90° out of phase with each other and in phase with the corresponding components of impedance.

The output of the flaw detector was calibrated by connecting a variable non-inductive resistance in series with the probe coil. The bridge circuit was balanced with the probe over a continuous part of the sample and the resistance was changed by a small amount. The displacement on the screen of the oscilloscope was proportional to the known resistance and at an angle $\varnothing_R$ to the x-axis of the screen (Fig. 4.16). The sensitivity S of the instrument was calculated from the change in voltage of the flaw detector per ohm change in resistance:

$$S = 1/C_f = \Delta V_R / \Delta R \qquad (4.6)$$

Here C_f is the calibration factor used to calculate the changes in the components of impedance caused by a defect, as follows:

$$\Delta R_d = V_d.C_f . \cos \emptyset \qquad (4.7)$$

and

$$\Delta wL_d = V_d.C_f . \sin \emptyset \qquad (4.8)$$

where $\emptyset$ is the angle between the outputs from ΔR and the defect.

A decade non-inductive resistance box was used mainly, but for more accurate measurements a small known resistance was produced by controlled heating of a conducting material in the form of a non-inductive coil with a predetermined temperature coefficient (Fig. 4.17). The coil was made from a length of 46 swg copper wire, doubled over and wound non-inductively around a hollow non-ferromagnetic metal cylinder. A Nichrome heating wire was wound around it, regulated by a low voltage d.c. supply. The temperature was monitored by placing the probe of a Comark thermocouple electronic thermometer inside the central cylinder. The whole was mounted firmly in a draft-free area with solder pin connectors for the electrical connections. A change of current of 0.20 amps was found to be sufficient to produce a resistance change of 0.25 Ω, calibrated using the Sullivan and Griffiths impedance bridge and allowing for stabilisation of the temperature. Typical variations of the components of impedance of the calibration coil with applied current to the heating wire are given in Table 4.5.

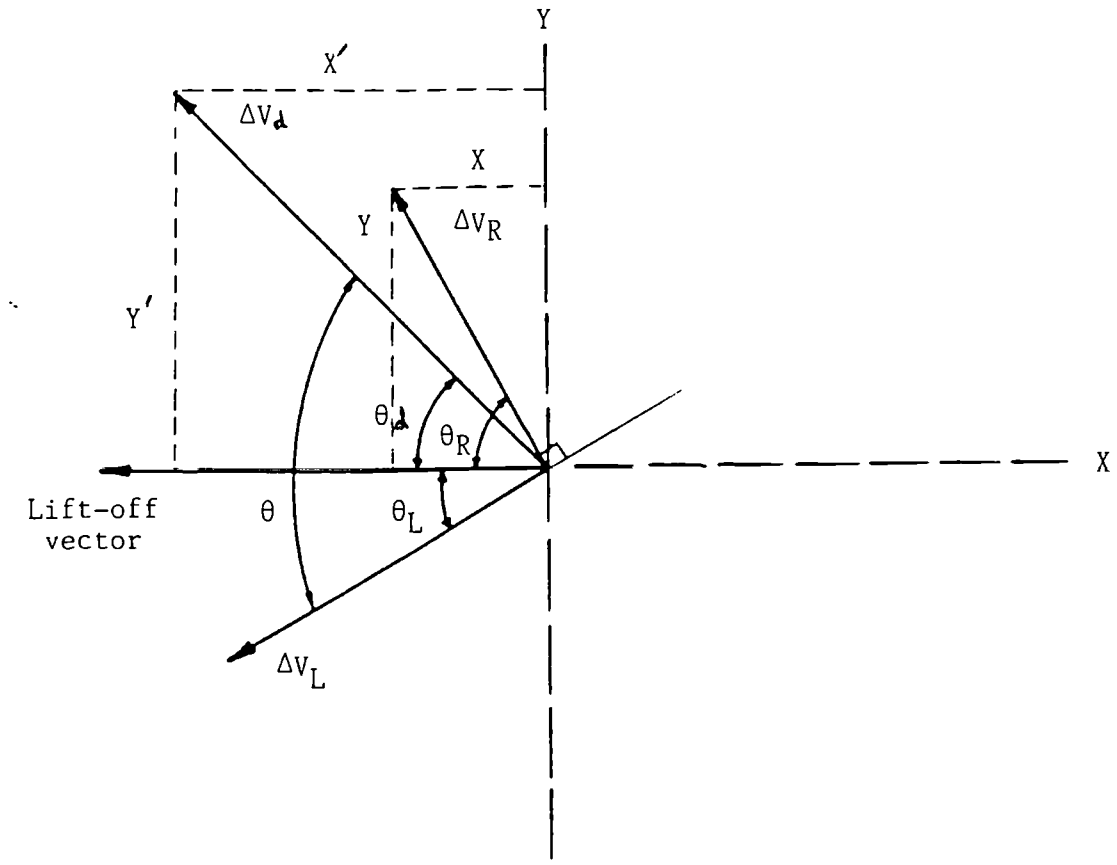

Output Voltage ΔV_R due to change of Resistance ΔR_o: $\Delta V_R = (x^2 + y^2)^{\frac{1}{2}}$

Output Voltage ΔV_d due to defect: $\Delta V_d = (x'^2 + y'^2)^{\frac{1}{2}}$

Sensitivity: $s = \Delta R_o / \Delta V_R$ (ohm/volt)

Calibration Factor: $C_f = 1/s = \Delta V_R / \Delta R_o$ (volt/ohm)

Phase Angles: $\theta_R = \tan^{-1}(y/x)$
$\theta_d = \tan^{-1}(y'/x')$
$\theta = 90 - (\theta_R - \theta_d)$

Resistive Component of change of Impedance: $\Delta R = \Delta V_d \times \sin\theta / C_f$ (ohm)

Inductive Component of change of Impedance: $\Delta wL = \Delta V_d \times \cos\theta / C_f$ (ohm)

Figure 4.16: **Typical voltage vectors produced when calibrating the flaw detector to display the components of impedance of a coil above a ferromagnetic metal.**

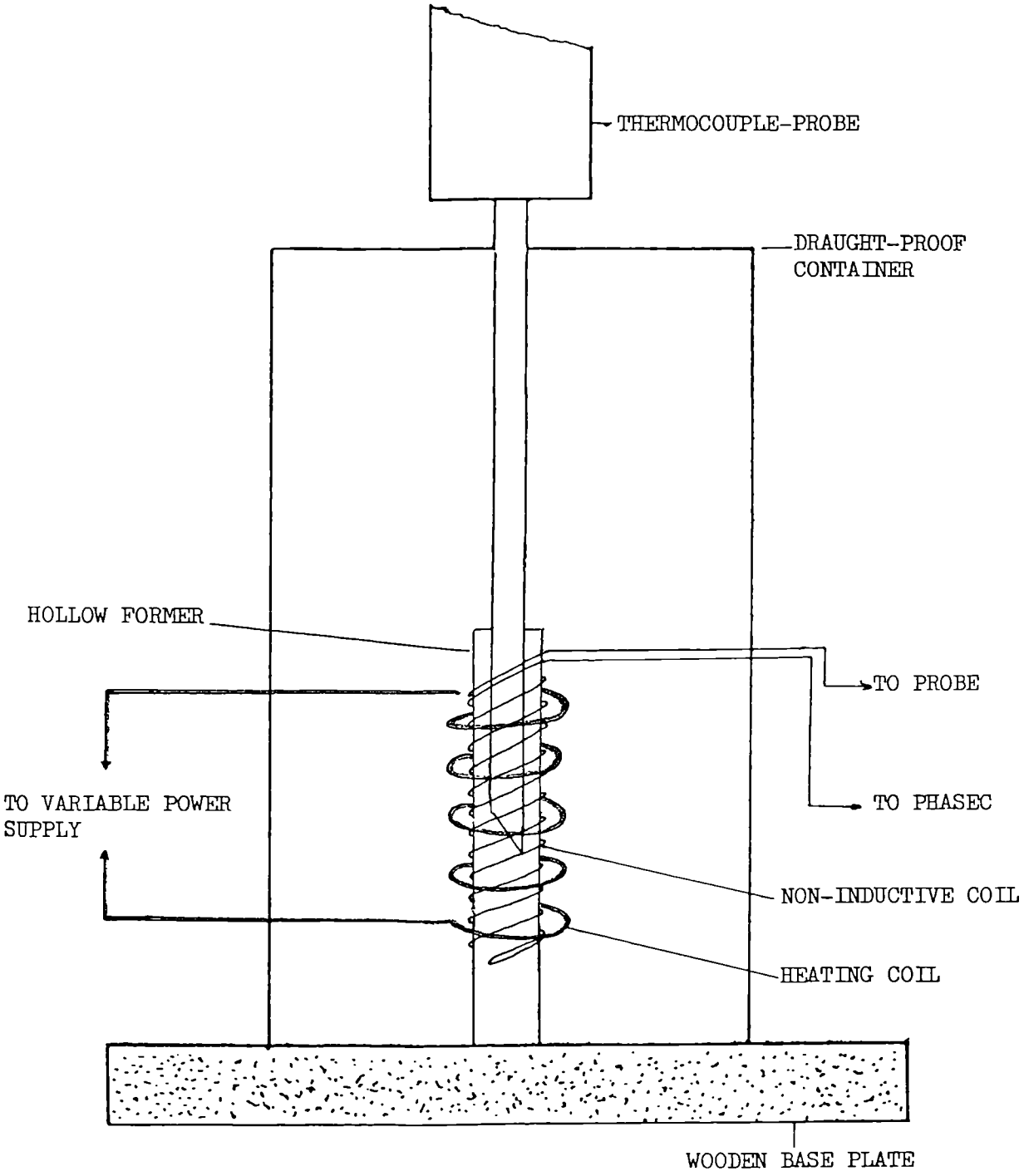

Figure 4.17: Device for producing a known small change of non-inductive resistance for calibration purposes.

Table 4.5 Typical Impedance Changes of a Calibration Coil Produced by Varying the Temperature, using a Separate Heater Coil

HEATER COIL			IMPEDANCE CHANGE OF CALIBRATION COIL (±0.001)	
Current. (A)±0.02	EMF (V)± 0.02	Temperature (°C)±0.05	R (Ω)	L (μH)
0	0	26.5	8.433	1.133
0.10	0.5	27.2	8.495	1.133
0.20	0.5	35.0	8.685	1.133
0.25	0.5	40.5	8.825	1.133
0.30	0.5	45.1	8.960	1.132

4.6 Estimation of Errors

Although all measurements were repeated several times where applicable, several experimental difficulties existed, giving rise to possible sources of error. The following precautions were taken to limit the propagation of errors:

i) The coils were wound to produce an impedance to match the impedance of the flaw detector oscillator.

ii) The dimensions of the probes were made as similar as possible to other probes in any set.

iii) The coils were wound to be axially symmetrical and with no turns overlapping on any layer.

iv) The end of each coil was as close to the end of the former as possible without damaging the coil. Any resulting lift-off was kept as near constant as possible.

v) For differential probes the two coils were wound as similarly as possible to one another, and set parallel to each other and at the same distance from the end of the probe.

vi) The probe coils were kept perpendicular to the surface.

vii) Voltage changes of the flaw detector were read only when within the range of linearity of voltage of the CRO display.

viii) Impedance changes caused by changes in temperature were minimised by keeping all the equipment at a constant temperature and cooling the coils with a flow of air when high values of current were applied.

ix) The calibration resistance was non-inductive and of an order of magnitude similar to that produced by a small defect. When using temperature controlled resistance changes for calibration (Section 4.5), the temperature and resistance were stable at the time of measurement.

Errors in the measurement of the components of impedance were contributed to by measurements of the calibration resistance R, potential difference of the bridge V and also phase angle Ø between V_R and V_d. The error in the calibration factor was calculated as a vector addition of the errors in resistance and voltage as 1.3 percent. Potential differences were read from the screen of the oscilloscope to an accuracy of ±0.05 V, and for a signal of the order of 2.0 V, the percentage error was ±2.5 per cent. The phase angle Ø was measured to ±0.5°, indicating percentage errors of the order of 0.03 to 0.17. Therefore estimated errors in R and wL were of the order of 2.8 percent. The value of lift-off at any point was measured with reference to the point at which the probe touched the surface of the sample, to an accuracy of ±0.01 mm, giving percentage errors typically less than ±0.5 percent. An additional systematic error in the measurement of lift-off was also present, typically of about 0.25mm, caused by the distance of the coil end from the base of the probe. Errors caused by normalisation of results should be systematic, depending on the values of electrical conductivity and magnetic permeability used. The coil length was measured to ±3 percent. The coil radii used were the mean values, obtained from the measured core and outer coil diameters of each probe.

CHAPTER 5

MEASUREMENT OF MAGNETIC PERMEABILITY

To predict the components of impedance of a coil used to test a ferromagnetic material, it was necessary to determine the value of relative magnetic permeability μ_r and electrical conductivity σ of that material. The electrical conductivity was measured by a Kelvin double bridge using a 1m length of the material. To determine the magnetic permeability, the definition of permeability required and the exact state of the metal must be specified, e.g., the point of the hysteresis curve under consideration (Section 5.1). In these investigations the relative recoil permeability was considered.

The magnetic permeability of a sample of BS 970 mild steel was estimated by comparing the eddy current depth of penetration of similar samples of mild steel and aluminium alloy (Section 5.2). The effect of changing magnetic permeability on the components of impedance of single coil surface-scanning probes was also investigated experimentally (Section5.3).

5.1 Definition of Magnetic Permeability

Magnetic permeability μ is the magnetic flux density $\underline{B}$ produced in a medium per unit applied magnetic field strength $\underline{H}$. It is dependent on on the magnetic state and composition of the material and may be written

$$\mu = \underline{B} / \underline{H} \qquad (5.1)$$

For non-ferromagnetic conductors the magnetic permeability is very nearly equal to the free space value, $\mu_0 = 4\pi \times 10^{-7}$ H/m, whilst that of a ferromagnetic material is far greater.

For a ferromagnetic material the presence of a magnetic field causes atomic magnetic elements within the material to try and align themselves with the inducing field [14], increasing the flux density. As the magnetic field strength is increased the rate of alignment varies, thus the magnetic flux density $\underline{B}$ varies hysteretically with changing magnetic field $\underline{H}$ (Fig. 5.1), cutting the $\underline{H}$ and $\underline{B}$ axes at H_c and B_r respectively. H_c is known as the coercive force and B_r the magnetic remenance of the material. The energy loss of the hysteresis loop acts as a source of electrical resistance, however this effect is always small in comparison with the components due to the eddy currents, so may be neglected.

Magnetic permeability may be defined in one of several ways, e.g., initial, differential or recoil permeability (Fig. 5.1). The initial permeability is that of a completely demagnetised sample before any field is applied. The slope of the $\underline{B}$-$\underline{H}$ curve at any

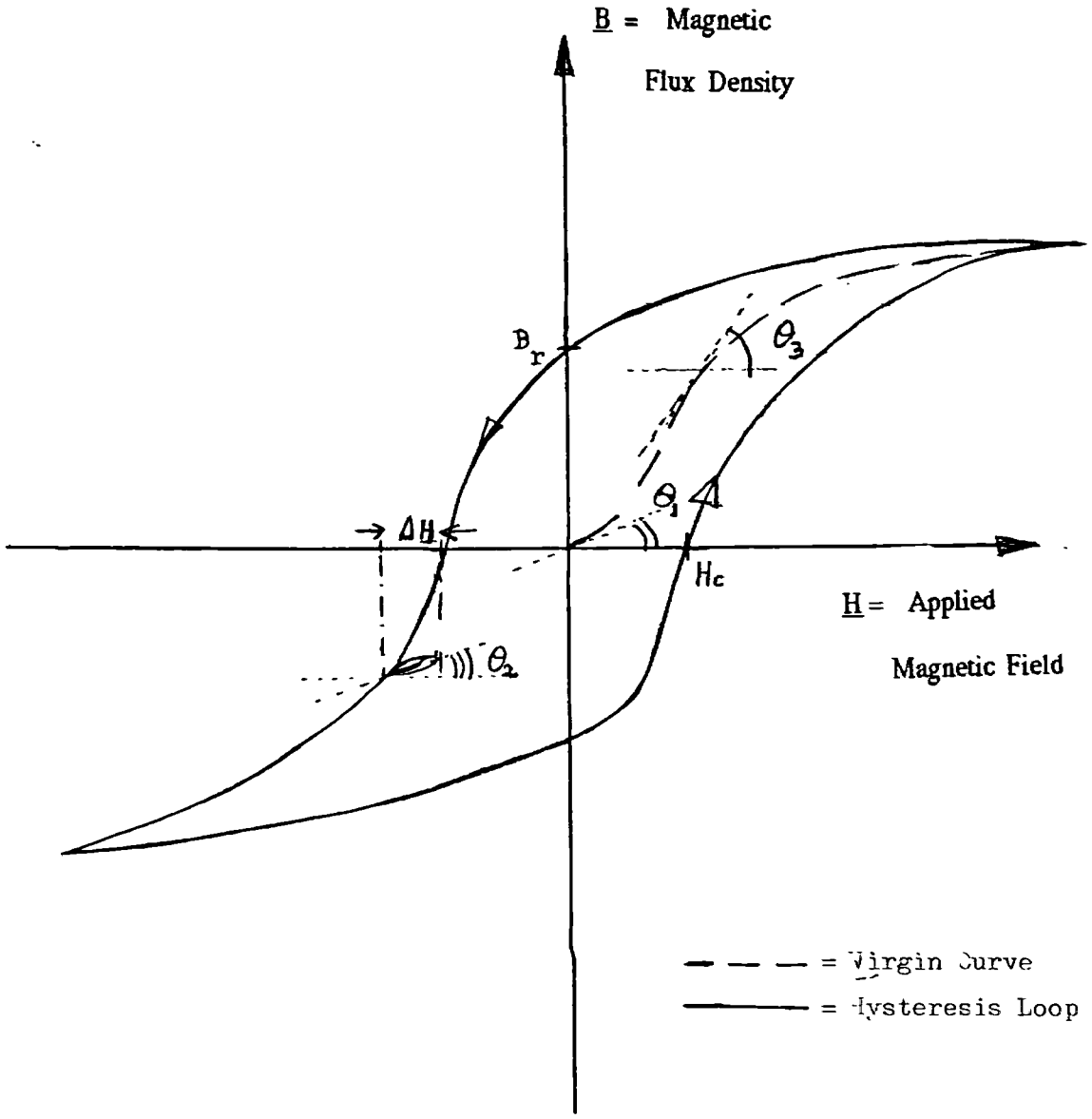

Figure 5.1: A typical B-H hysteresis loop of a magnetic material.

$\tan^{-1} \Theta_1 = \mu_{init}$ = initial permeability

$\tan^{-1} \Theta_2 = \Delta\mu$ = recoil permeability

$\tan^{-1} \Theta_3 = \mu_\Delta$ = differential permeability

point is known as the differential permeability, $\mu_\Delta = d\underline{B} / d\underline{H}$. As $\underline{H}$ is increased, μ_Δ approaches the free space value μ_0 at which point the material is considered to be magnetically saturated. Magnetic saturation is one way to remove the influence of magnetic permeability when testing ferromagnetic materials, however, it is often impractical to produce a high enough magnetic field to saturate the area under inspection, and the influence of the magnetic permeability cannot be removed from samples of complicated shape by driving the material towards saturation. If $\underline{H}$ is varied by a small amount $\Delta\underline{H}$ at any point along the hysteresis curve, a small reversible change of permeability occurs, the slope of which is defined as the recoil permeability $\Delta\mu$. $\Delta\mu$ does not appear to vary significantly with the value of $\underline{H}$ for constant values of $\Delta\underline{H}$. However as $\Delta\underline{H}$ is decreased, the value of $\Delta\mu$ tends towards μ_0 (Fig. 5.2). *In these investigations the recoil permeability was considered* to be the important value, because the small alternating current carried by an eddy current coil would induce a magnetic field with low-amplitude hysteresis within the metal. To confirm this hypothesis, the current in an eddy current air-cored scanning coil was calculated by measuring the voltage across the coil with an oscilloscope, and the resulting magnetic field was estimated as less than $1 Am^{-1}$. This value is very low when compared with the fields needed to magnetise a steel sample (Fig. 5.3).

Permeability values quoted are usually values of magnetic permeability relative to the value in air, $\mu_0 = 4\pi \times 10^{-7}$ H/m, known as the relative permeability, $\mu_r = \mu / \mu_0$. Non-ferromagnetic metals have relative permeability values of $\mu_r = 1$, while for ferromagnetics $\mu_r >> 1$, typically by 50 to 10,000 times. Mild steel has a relative permeability between 200 and 800, and an initial permeability in the region of 100 (Fig. 5.3).

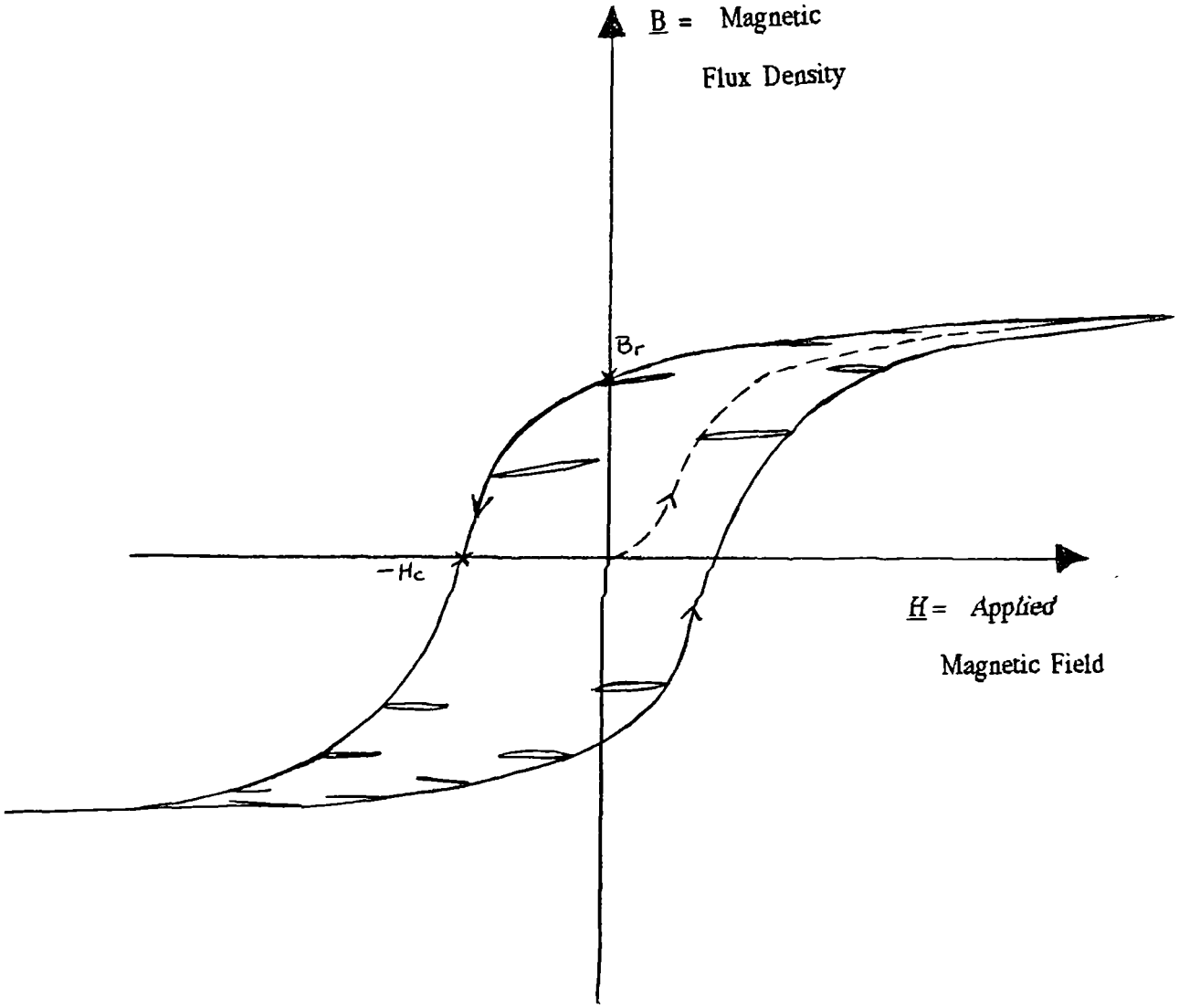

Figure 5.2: B-H hysteresis loops of a pipe-steel, with reversible loops of recoil permeability, drawn using an automatic Permeameter [32].

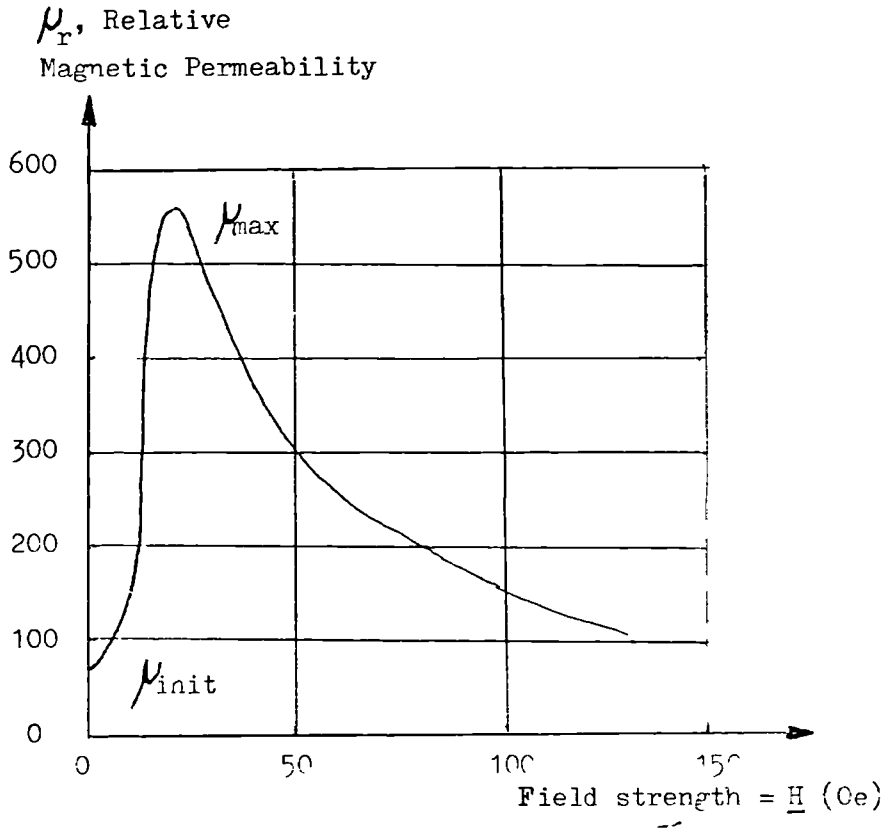

Figure 5.3: Relative magnetic permeability μ_r of a carbon steel as a function of applied field strength H.

5.2 Measurement of Magnetic Permeability.

Different eddy current methods were considered for the measurement of magnetic permeability μ_r of a sample of BS 970 mild steel. For one method, the use of a coil encircling a mild steel rod was considered, to which Forster's impedance analysis could be applied (Section 2.1). In theory, by taking the ratio of the real and imaginary components of impedance defined by Förster (Equations 2.23, Section 2.1), for a given value of normalised frequency $k^2a^2 = \beta^2 = \omega\mu_r\mu_0\sigma a^2$, a ratio of the components of effective permeability is obtained:

$$(\mu_{eff})_{real} / (\mu_{eff})_{imag} = \{(\omega L/\omega L_0) + \eta - 1\} / (R/\omega L_0) \qquad (5.2)$$

where η is the fill-factor, ωL_0 is the impedance of the coil measured away from any metal, and μ_{eff} is the effective permeability, a complex quantity related to β^2 (Table 5.1), accounting for the uneven distribution of magnetic field within a sample.

Therefore in theory, by measuring the normalised components of impedance at a certain normalised frequency, μ_r could be calculated, knowing the values of η and σ. In practice, Forster s analysis does not allow for any leakage of flux from the ends of a rod and the method could only be used with rods of infinite length-to-diameter ratios, or a toroidal sample.

The method used to estimate the value of μ_r, by comparing the penetration of eddy currents in similar samples of mild steel and aluminium alloy, is described below

Table 5.1: Values of Förster's Effective Permeability μ_{eff} at Different Values of Normalised Frequency β^2, and Corresponding Values of the Ratio $(\mu_{eff})_{real}/(\mu_{eff})_{imag}$

(f/fg)	$\mu_{eff(real)}$	$\mu_{eff(imag)}$	$\mu_{eff(real)}/\mu_{eff(imag)}$
0.00	1.0000	0.0000	
0.25	0.9989	0.0311	32.119
0.50	0.9948	0.06202	16.040
1	0.9798	0.1216	8.057
2	0.9264	0.2234	4.1478
3	0.8525	0.2983	2.8579
4	0.7738	0.3449	2.2435
5	0.6992	0.3689	1.8957
6	0.6360	0.3770	1.6870
7	0.5807	0.3757	1.5456
8	0.5361	0.3692	1.4520
9	0.4990	0.3599	1.3865
10	0.4678	0.3494	1.3388
12	0.4202	0.3284	1.2795
15	0.3701	0.3004	1.2320
20	0.3180	0.2657	1.1968
50	0.2007	0.1795	1.1181
100	0.1416	0.1313	1.0784
150	0.1156	0.1087	1.0635
200	0.1001	0.09497	1.0540
400	0.07073	0.06822	1.0368
1,000	0.04472	0.04372	1.0229
10,000	0.01414	0.01404	1.0071

From Maxwell's equations it can be shown that, for a coil above the flat surface of a metal with electrical conductivity σ and magnetic permeability μ, (Equation 2.9, Section 2.1)

$$d^2B / dz^2 - k^2 B = 0 \qquad (5.3)$$

where $k^2 = j\omega\mu\sigma$, and B is the magnetic flux density. Here $j = (-1)^{1/2}$ and $\omega = 2\pi f$ is the angular frequency.

The solution to this equation is

$$B = B_0 \exp(-kz) \qquad (5.4)$$

where B_0 is the flux at the surface of the metal.

Because from Maxwell's equations for a conductor $\nabla x \underline{B} = \underline{J}$, the current density J has a solution of the same form and it can be shown that the eddy currents are attenuated exponentially with depth of metal penetrated. The depth at which the current density is reduced to $1/e^{th}$ of the surface value is known as the standard depth of penetration or skin effect, δ, where

$$\delta = (2/\omega\mu\sigma)^{1/2} \qquad (5.5)$$

The eddy currents are attenuated by about 8dB for every standard depth of penetration; therefore the maximum depth d that eddy currents are able to penetrate is approximately 12 δ. The value of d was measured for samples of mild steel and aluminium alloy, by scanning metal wedges with an air-cored single coil eddy current probe of diameter 2 mm, connected to a Hocking Electronics Vector S900 multi-frequency flaw detector (Fig. 5.4).

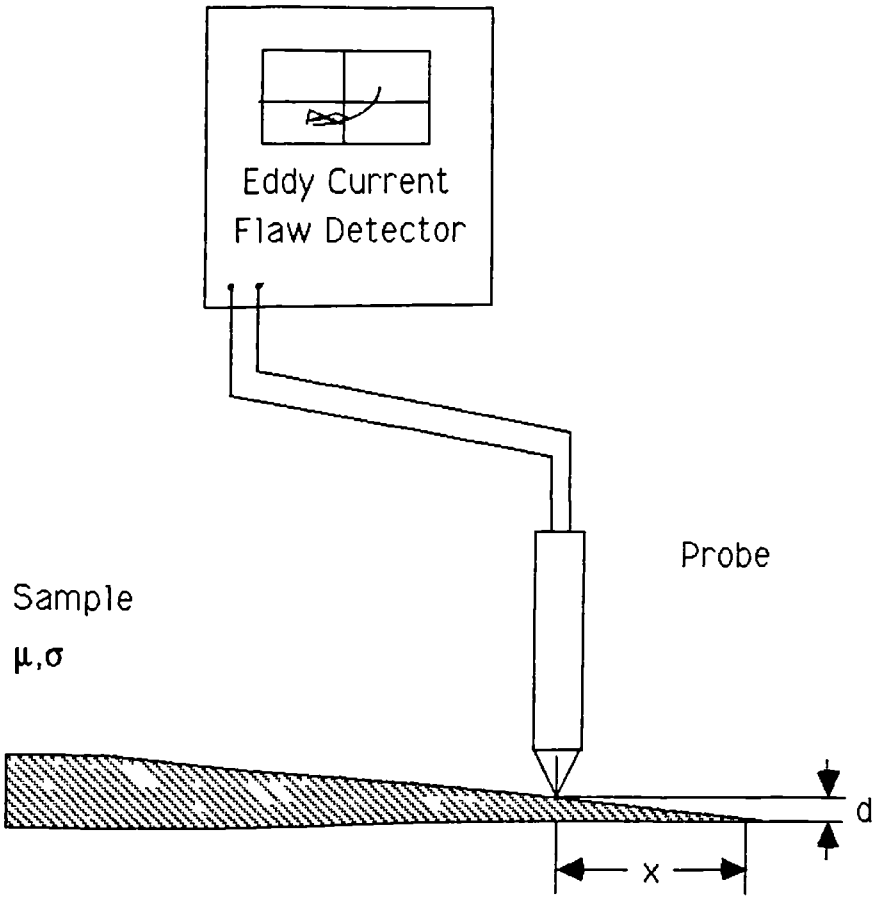

Figure 5.4: Measurement of relative magnetic permeability with the penetration depth method

There was no change in the output of the instrument as long as the metal was continuous, but as soon as the eddy currents were able to penetrate through the metal the continuity was lost and a change in output occurred. Two shallow wedges were made, one of annealed and demagnetised BS 970 mild steel of 2.5 degree incline with a value of electrical conductivity of 6.8 MS m^{-1}, and the other from an annealed aluminium alloy which had an angle of 10 degrees and an electrical conductivity of 21.7 MS m^{-1}. Conductivities were measured from a metre length of a rod of the same material as that used for the wedges with the Kelvin double bridge. The aluminium, being non-ferromagnetic, had a relative permeability of 1. The relative permeability of the steel sample was calculated from the ratio of d for the steel and aluminium samples, as follows:

$$d_1^2 / d_2^2 = \mu_2\sigma_2 / \mu_1\sigma_1 \qquad (5.6)$$

where subscripts of 1 denote Aluminium alloy and subscripts of 2 mild steel.

The surface of each wedge was scanned in turn from the thin end, with a constant lift-off of 0.1 mm at frequencies ranging from 800 to 1500 Hz, until a point was reached beyond which the output of the instrument remained constant. The mean value of μ_r obtained in this way for the steel sample was 97 ± 3.

5.3 Variations of Impedance of Single Coil Scanning Probes with μ_r.

The changes of the components of impedance as a result of changes in μ_r and σ alone were monitored, to optimise the conditions under which the effect of a change in μ_r could be minimised. Generally it is impractical to measure variations

of σ of a metal independently, but percentage changes of electrical conductivity are small compared with those of magnetic permeability. The following method was used to establish the effect of changing μ_r alone on the components of impedance of a surface-scanning coil: 30 and 90 turn ferrite- and air-cored single coils of 2 mm diameter, numbers AS1, AS2, FS1 and FS2 (Table 4.1, Section 4.3.1), were clamped in turn touching, and with their axes perpendicular to, the flat end of a mild steel rod, of length 130 mm and diameter 12.7 mm, which was encircled by a d.c. magnetising coil (Fig. 5.5). The voltage output of each scanning coil was observed using the Vector S900 flaw detector (Section 4.1.2), for different values of lift-off, over a frequency range of 100kHz to 1MHz, while the degree of magnetisation of the rod was increased progressively. The latter was achieved by applying increasing values of direct current through the magnetising coil, supplied by a heavy duty car battery and controlled with variable carbon resistors. The magnetic field was increased to 13 kA m^{-1} with no changes observed above these limits. Care was taken to ensure that initially the rod was demagnetised to the same degree for each test. It was found that when using the ferrite-cored coils there was a straight line deflection on the C.R.O. of the flaw detector, which did not follow a linear relationship with increases of applied field. There was a far less significant change in output when using air-cored coils for applied fields up to 13kAm^{-1}. The ferrite-cored coils were also adversely affected by temperature variations, which were minimised by directing a flow of cool air over the field coil and probe. To eliminate the possibility of the ferrite core of the probe being magnetised by the applied field, the sample was removed and the ferrite-cored coil was monitored with changes in the d.c. field alone. The out of balance signal of the Vector S900 was insignificant, being approximately 6% of the signal with the sample in situ. It was concluded that air-cored coils should be used in preference to ferrite-cored coils for testing ferromagnetic metals.

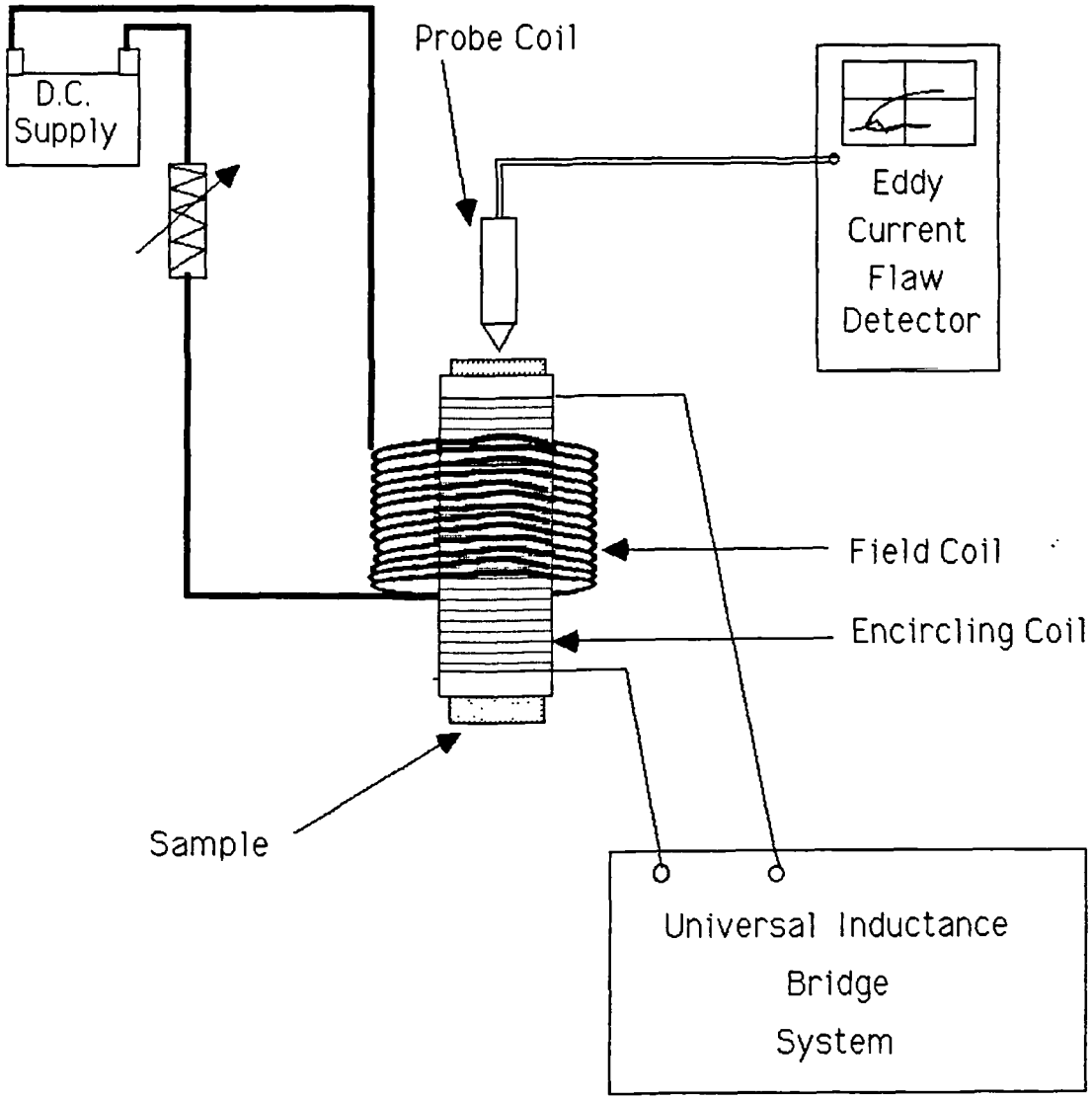

Figure 5.5: Equipment for measuring the effect of changes in magnetic permeability on surface-scanning eddy current probes

It was also found that the effect of a change in μ_r could be minimised by using high values of frequency and lift-off [38]. Both the air-cored and ferrite-cored coils were found to be less sensitive to changes in μ_r when using values of lift-off exceeding twice the radius of the coil at a frequency of 100kHz and one times the coil radius at a frequency of 500kHz.

The change in impedance of both the air- and ferrite-cored probe coils were evaluated when scanning a flaw in a ferromagnetic sample under the influence of a changing applied magnetic field. Ferrite block magnets 25mm x 25mm x 10mm were used to complete a magnetic circuit between two mild steel plates, one of which contained a simulated defect of 1 mm depth (Fig. 5.6). The defect was scanned by each probe at frequencies ranging from 100 kHz to 1 MHz, while the number of block magnets in the circuit was increased. The air-cored probes showed no change in the defect signal but the ferrite-cored probes indicated small variations in signal with the addition of block magnets, of the order of 8% of the defect signal for the limited change in magnetic field produced in this experiment.

From these results it would appear that ferrite-cored coils, although generally considered more sensitive to defects than air-cored coils, are less suitable for testing samples with varying magnetic permeability than air-cored coils. However, the effects of a change in μ_r on a ferrite-cored coil can be minimised by using high values of frequency and lift-off. This is confirmed experimentally in Section 7.3.

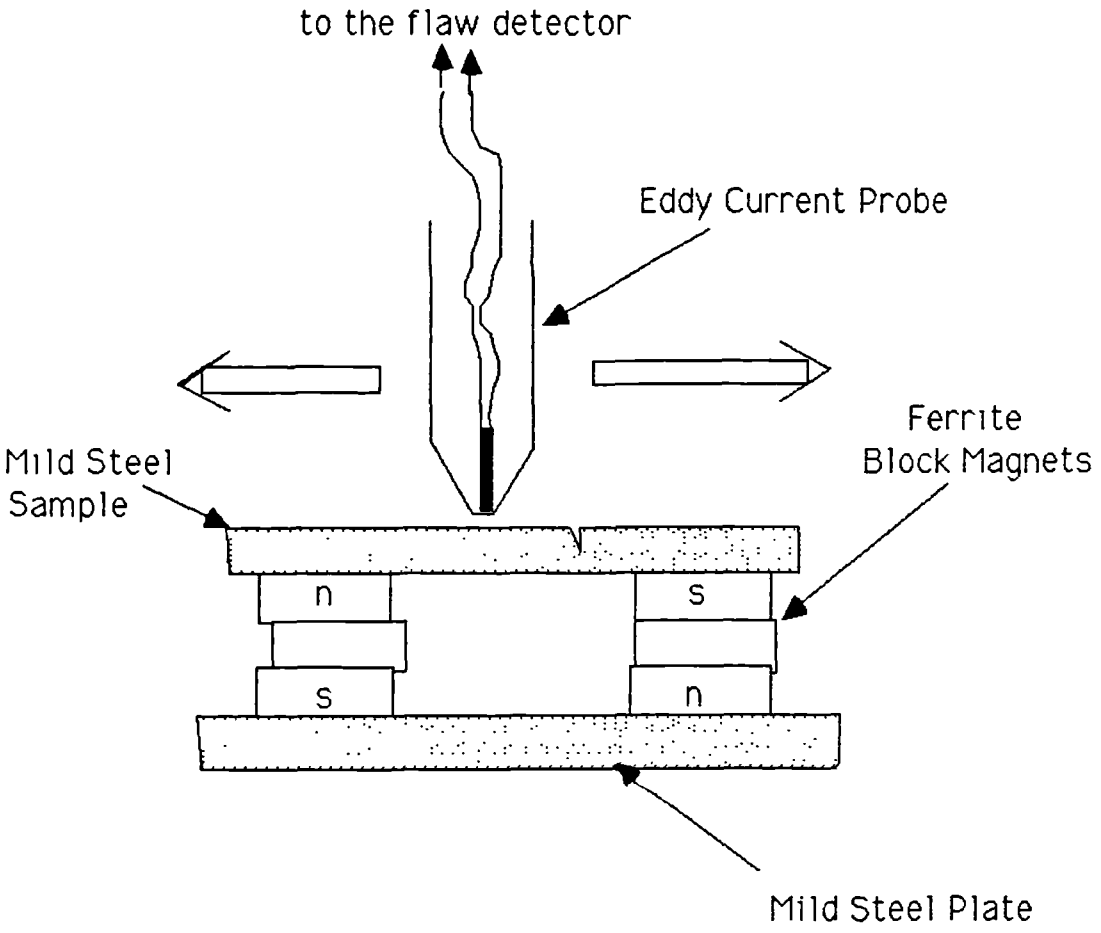

Figure 5.6: Magnetic circuit used to measure the impedance of an eddy current probe when scanning a defect under the influence of a changing magnetic field

CHAPTER 6

EXPERIMENTAL VERIFICATION OF THE IMPEDANCE ANALYSIS OF A COIL ABOVE A FERROMAGNETIC METAL

In this chapter experiments to verify the impedance analysis developed in Chapter 3, for a solenoid above the surface of a thick metal plate, are described. The components of impedance of three air-cored surface-scanning coils were measured at different frequencies, while the probes were lifted progressively from a position touching the surface of a flaw-free sample of aluminium alloy or BS 970 mild steel, to a point out of the influence of the metal. The aluminium sample was a block 24.5mm x 40.0mm x 26.0mm of electrical conductivity $\sigma_{AL} = 21.7$ MS/m and relative magnetic permeability $\mu_{r.AL} = 1$. The mild steel block was 25.0mm x 25.0mm x 25.0mm with an electrical conductivity $\sigma_{MS} = 6.8$ MS/m. The relative recoil magnetic permeability $\mu_{r.MS}$ of the mild steel was assumed to be 97, as calculated in Section 5.2. The experimental procedure is described in Section 6.1.

The normalised components of the impedance of each of the coils used experimentally were determined, and are compared with the theoretical predictions (equations 3.47 and 3.48, Section 3.1), calculated using the computer program described in Appendix 1, in Section 6.2.

6.1 Experimental Values of Coil Impedance

A Hewlett Packard LF 4192A Impedance analyser was used to measure absolute values of the resistive R and inductive ωL components of impedance of three air-cored coils 2S, 3S and 4S (Table 4.1, Section 4.3.1), at different values of normalised frequency and lift-off as indicated below, for aluminium or mild steel samples. The three coils were positioned in turn perpendicular to the surface of a sample and at different fixed heights, using a scanning rig (Section 4.2). The components of impedance of each coil were recorded as lift-off was increased from zero, i.e., when touching the sample surface, to 4mm in steps of 0.5mm, at normalised frequencies between 100 and 1000. For values of lift-off above 4mm the change in the components of impedance reduced to zero. To obtain the normalised values $\omega L/\omega L_0$ and $R/\omega L_0$, a measurement was taken with no sample present, i.e., infinite lift-off, and this value of impedance was used for normalisation. Both measured and normalised values of the components of impedance are given in Tables A2.1 to A2.6, Appendix 2. Typical variations of $R/\omega L_0$ and $\omega L/\omega L_0$ with normalised lift-off Y for coil 3S when located above aluminium alloy and mild steel are shown in Figs. 6.1 and 6.2 respectively, for different normalised frequencies. In Fig. 6.3 the variations are compared for the three coils at a normalised frequency of 200. Figs. 6.4 to 6.6 show the normalised impedance-plane diagrams for each coil when above the surface of both aluminium and mild steel samples, for different values of normalised lift-off Y, and normalised frequency β^2.

Fig. 6.1 shows that, when scanning a non-ferromagnetic sample, $\omega L/\omega L_0$ increases where $R/\omega L_0$ decreases with increasing lift-off at all the frequencies, and both $R/\omega L_0$ and $\omega L/\omega L_0$ decrease with increasing frequency. For a ferromagnetic sample (Fig. 6.2), both $\omega L/\omega L_0$ and $R/\omega L_0$ decrease with increasing lift-off and frequency, as predicted. In Fig. 6.3 it is seen how an increase in the normalised coil length Y_0 decreases both components of normalised impedance. The value of $\omega L/\omega L_0$ never exceeds 1.3, because of high losses caused by the poor magnetic flux linkage of a surface-scanning probe with a metal sample. Figs. 6.4 to 6.6 show the marked change in phase of the lift-off vectors for the two different metals. The impedance changes in the direction of Y are negligible compared with the changes in the direction of β^2 when the values of magnetic permeability and electrical conductivity are changed.

Fig. 6.7 shows the effect of increasing normalised coil length Y_0 on $\omega L/\omega L_0$ and $R/\omega L_0$. For both aluminium and mild steel, increasing values of Y_0 and Y cause the components of impedance to converge on a value of $\omega L/\omega L_0 = 1$ and $R/\omega L_0 = 0$, with no apparent change in β^2, as expected.

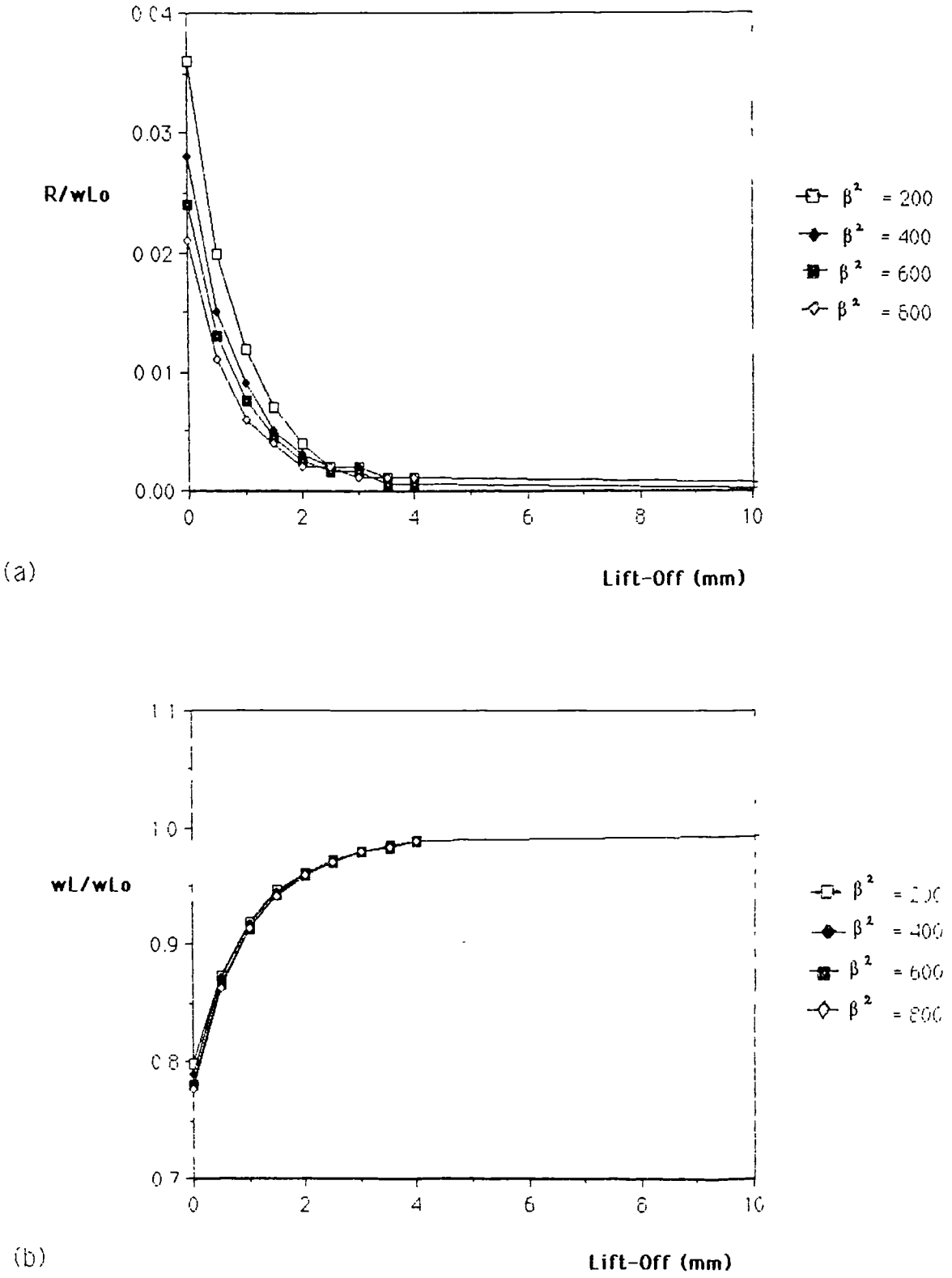

Figure 6.1: Normalised (a) resistive and (b) inductive components of impedance of coil 3S above aluminium alloy. L_0= 17μH, Y_0= 0.74.

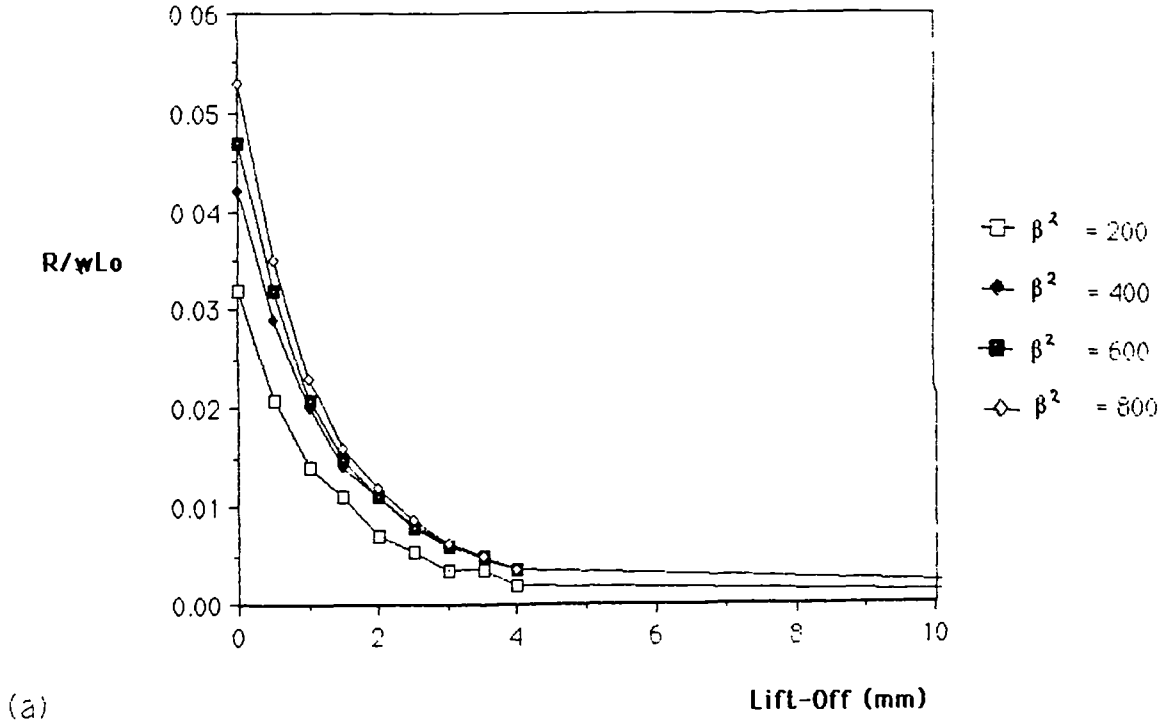

(a)

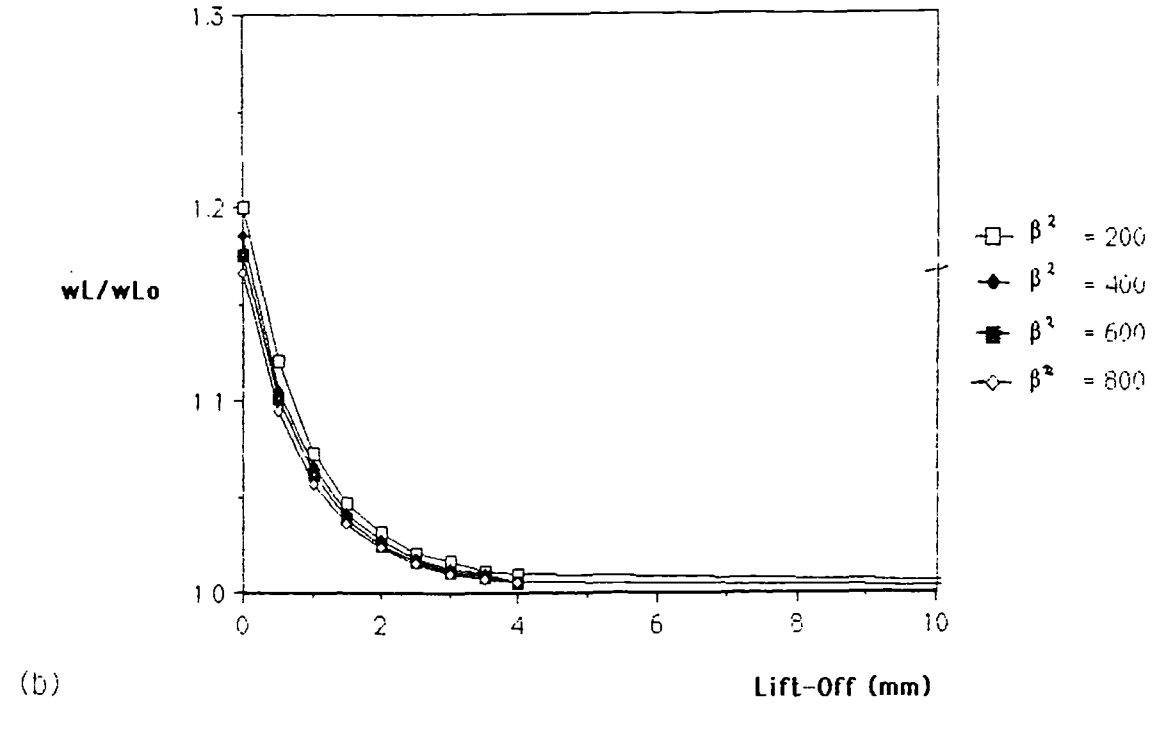

(b)

Figure 6.2: Normalised (a) resistive and (b) inductive components of impedance of coil 3S above mild steel. $L_0 = 17\mu H$, $Y_0 = 0.74$.

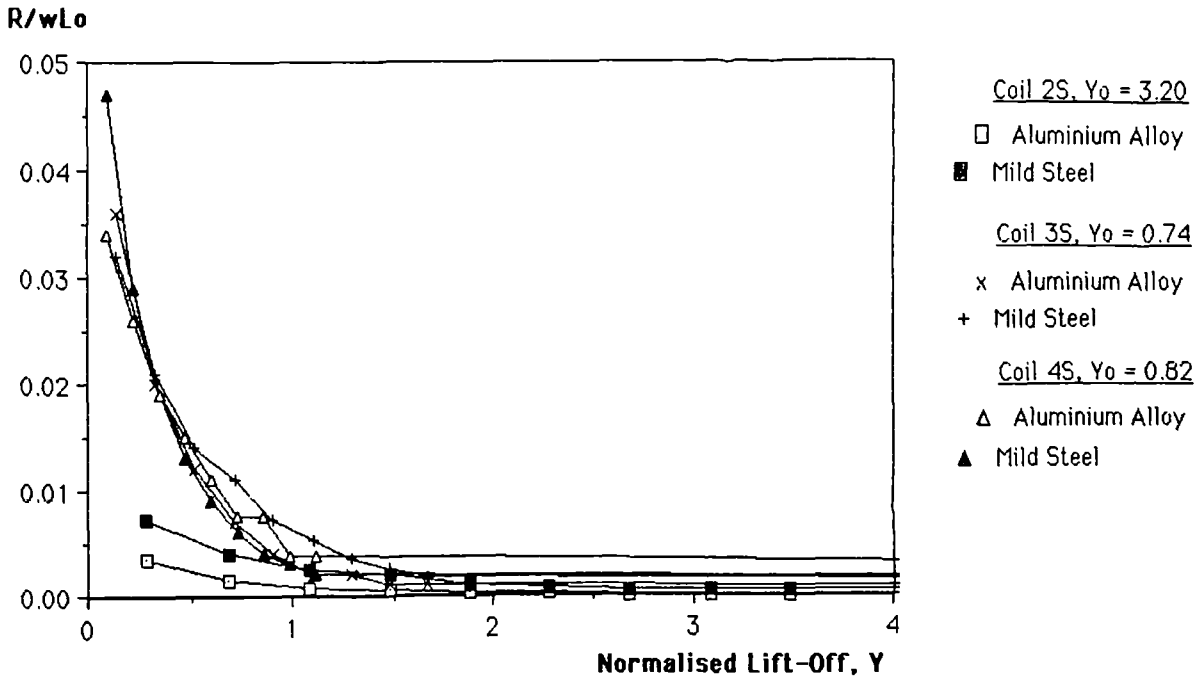

(a)

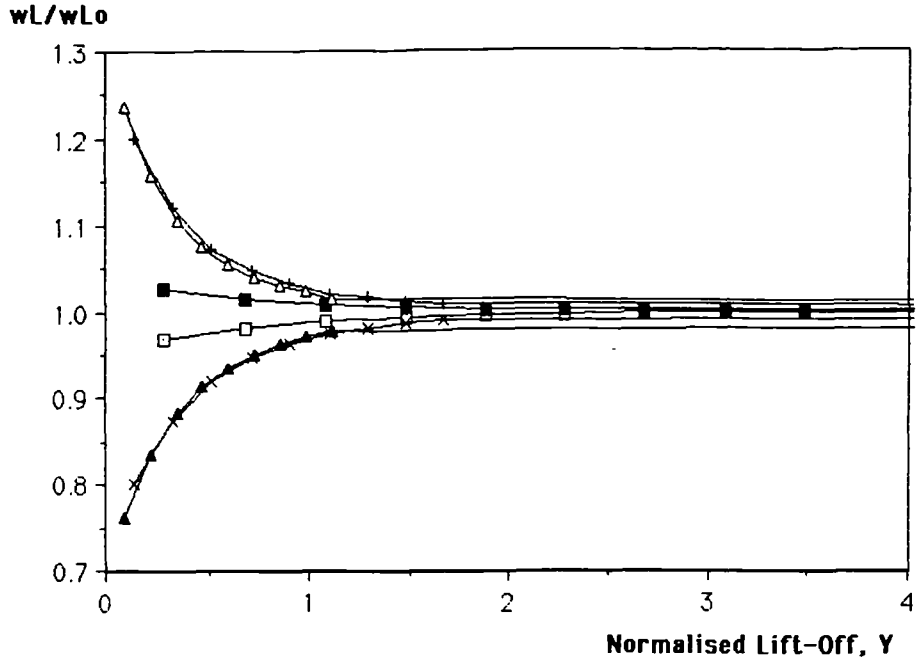

(b)

Figure 6.3: Normalised (a) resistive and (b) inductive components of impedance of coils 3S, 4S and 2S above aluminium alloy and mild steel.

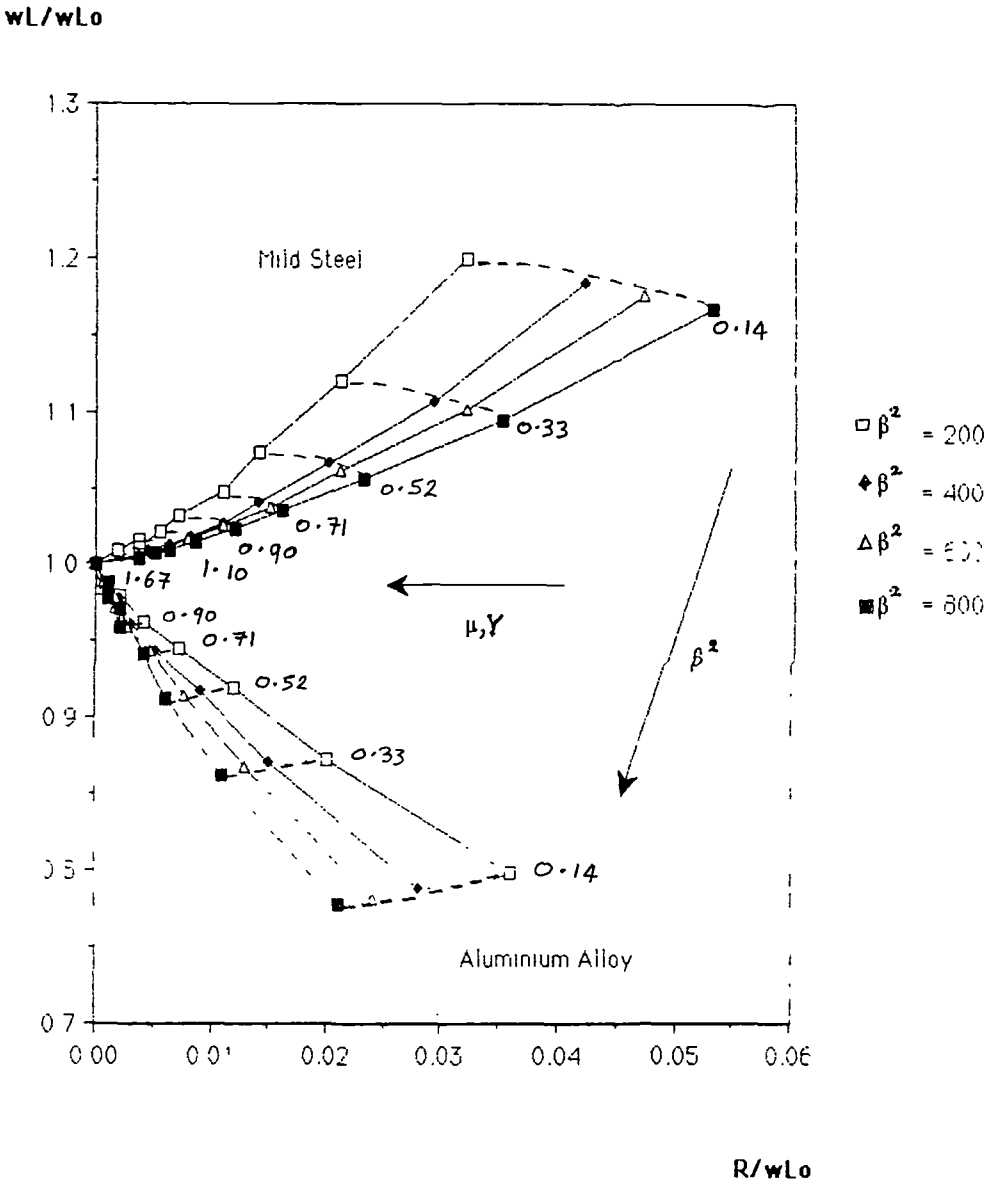

Figure 6.4: Variations in $R/\omega L_0$ versus $\omega L/\omega L_0$ of coil 3S above aluminium and mild steel, where $\sigma\mu = 27.2$ and 831.5 respectively. $L_0 = 17\mu H$, $Y_0 = 0.74$.

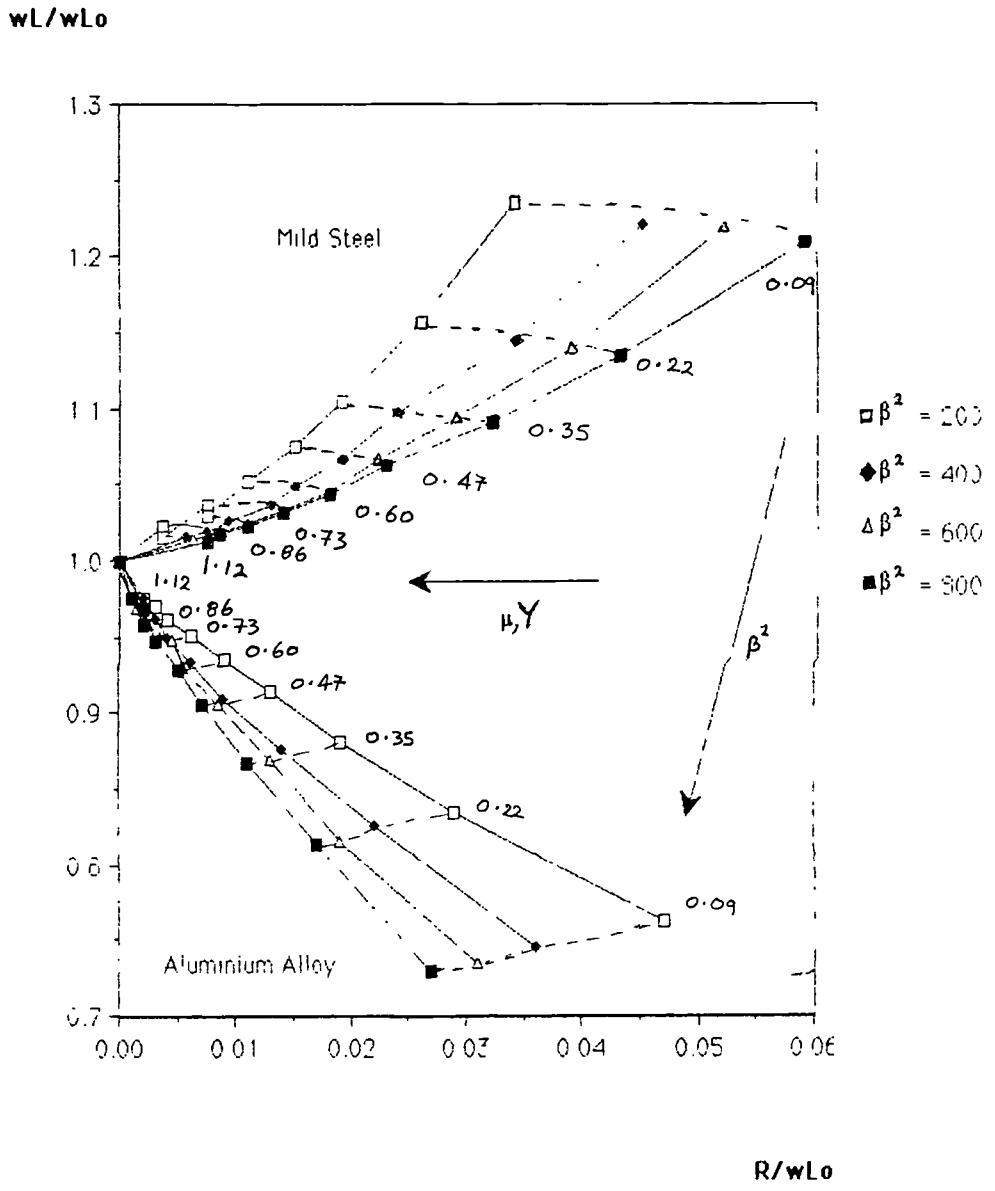

Figure 6.5: Variations in $R/\omega L_0$ versus $\omega L/\omega L_0$ of coil 4S above aluminium and mild steel, where $\sigma\mu$ = 27.2 and 831.5 respectively.

L_0 = 170μH, Y_0 = 0.82.

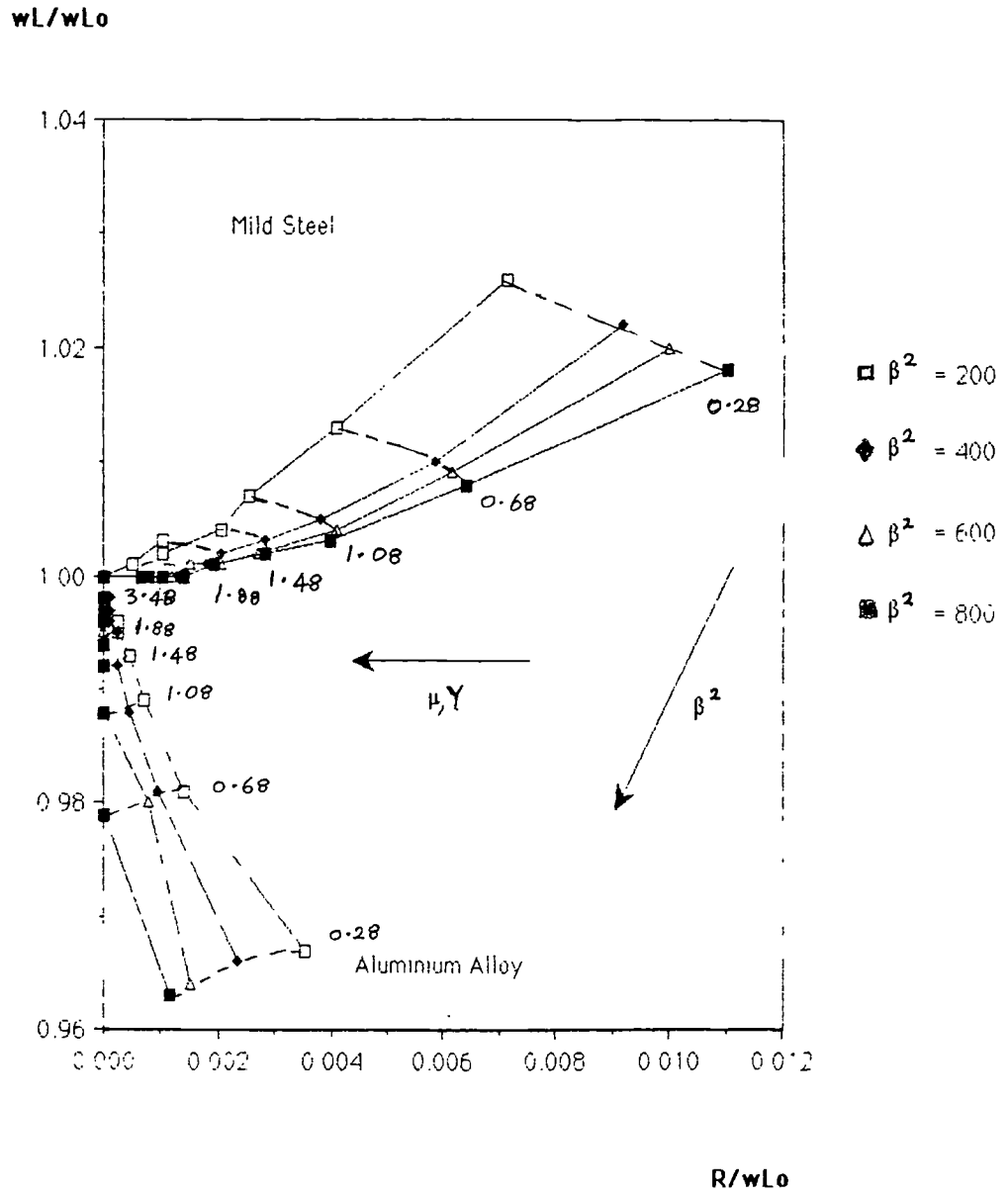

Figure 6.6: Variations in $R/\omega L_0$ versus $\omega L/\omega L_0$ of coil 2S above aluminium and mild steel, where $\sigma\mu = 27.2$ and 831.5 respectively.

$L_0 = 13\mu H$, $Y_0 = 3.20$.

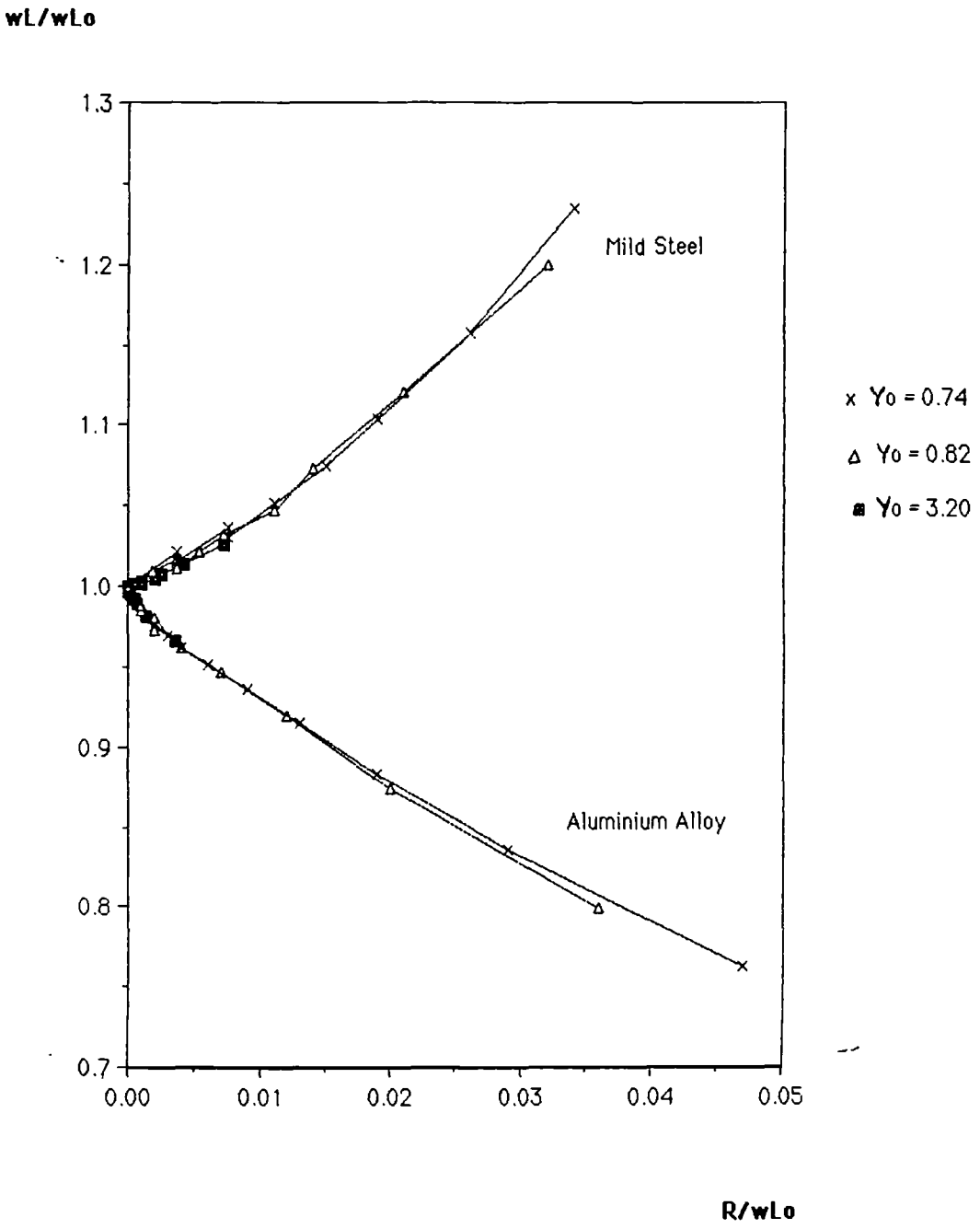

Figure 6.7: The Effect of Y_0 on the variations of $R/\omega L_0$ versus $\omega L/\omega L_0$ for both ferromagnetic and non-ferromagnetic metals.

6.2 Comparison of Theoretical and Experimental Results

The values of $R/\omega L_0$ and $\omega L/\omega L_0$ for each coil for both aluminium and mild steel were predicted to 4 decimal places from equations 3.47 and 3.48 (Section 3.1), using the computer program given in Appendix 1. A correction of 0.35mm was added to all experimental values of lift-off, because the probes had to be built with the core-former slightly longer than the coil. An initial lift-off of about 0.35mm was assumed at the "zero" position. Also it has been shown [12] that a solenoid coil has an effective coil length which is shorter than the actual coil length, as a result of the divergence of the magnetic flux at the ends of the coil. A coil length correction factor of 20% was used for the predictions. The values of Y_0 fed into the program were 0.60 for the 17μH coil 3S, 0.66 for the 170μH coil 4S and 2.56 for the 13μH coil 2S, using values of $\sigma_{AL} = 21.7\ MSm^{-1}$ and $\mu_r = 1$ for the aluminium sample, or $\sigma_{MS} = 6.8\ MSm^{-1}$ and $\mu_r = 97$ for the mild steel sample. The components of impedance predicted are listed in Tables A3.1 to A3.6, Appendix 3, and shown in Figs. 6.8 to 6.10, together with corresponding experimental results.

There was good agreement between the experimental and theoretical results for both aluminium and mild steel, for coils 3S and 4S (Figs. 6.11 and 6.12). For coil 2S (Fig. 6.13) the predicted values of both components of normalised impedance were twice those found experimentally. The majority of the discrepencies were in the direction of increasing Y, suggesting that there were small errors in the estimation of coil radius, lift-off and/or effective coil length (Fig.6.7): If there were errors of 0.05mm in the measurement of coil radius r and length ℓ, the error in Y_0 would be ± 0.173 for coil 2S. An error of 0.05mm in r would also generate a discrepency in β^2 of about ±8.

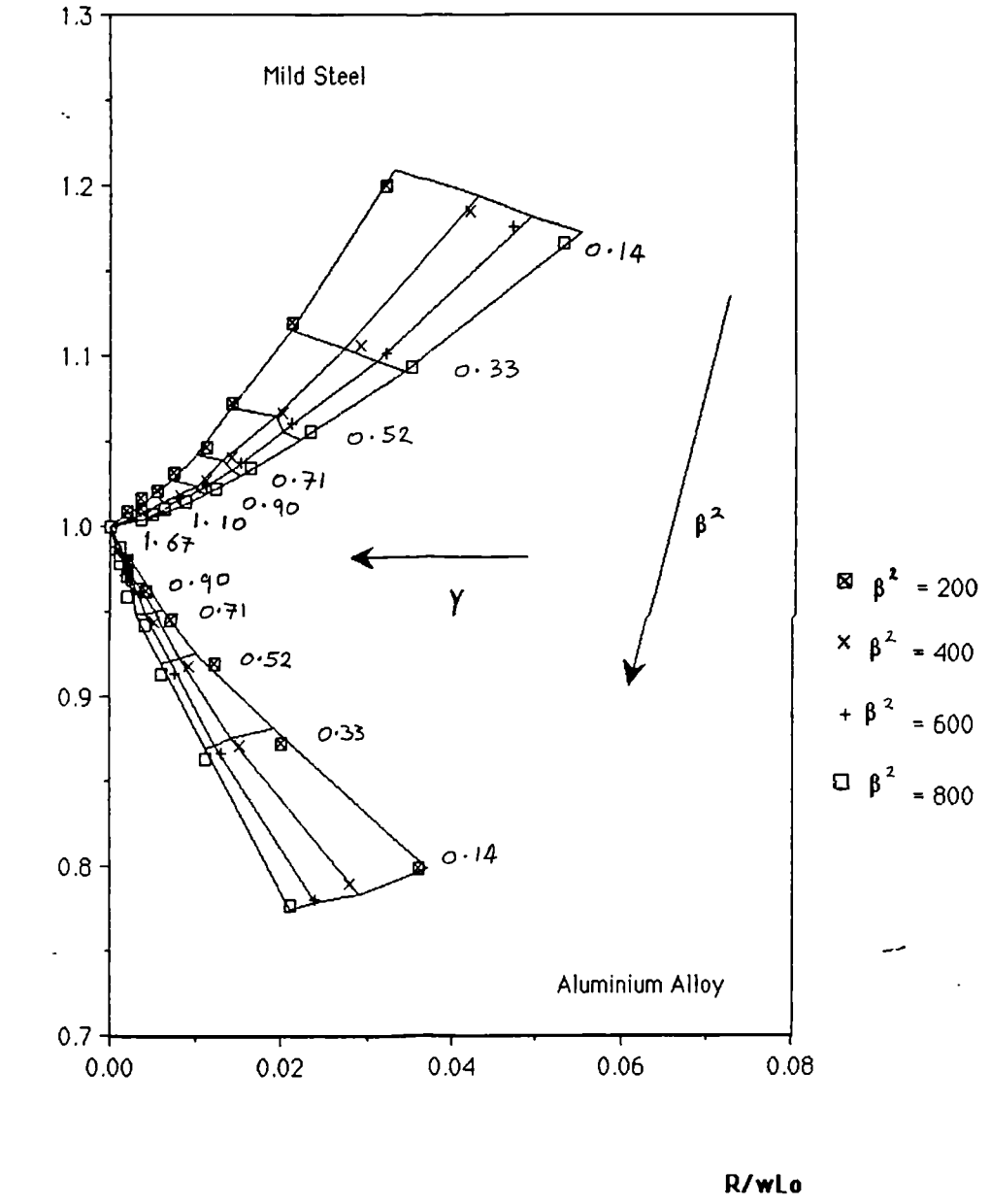

Figure 6.8.: Predicted and experimental values of the components of impedance of coil 3S above aluminium and mild steel. $L_0 = 17\mu H$, $Y_0 = 0.6$.

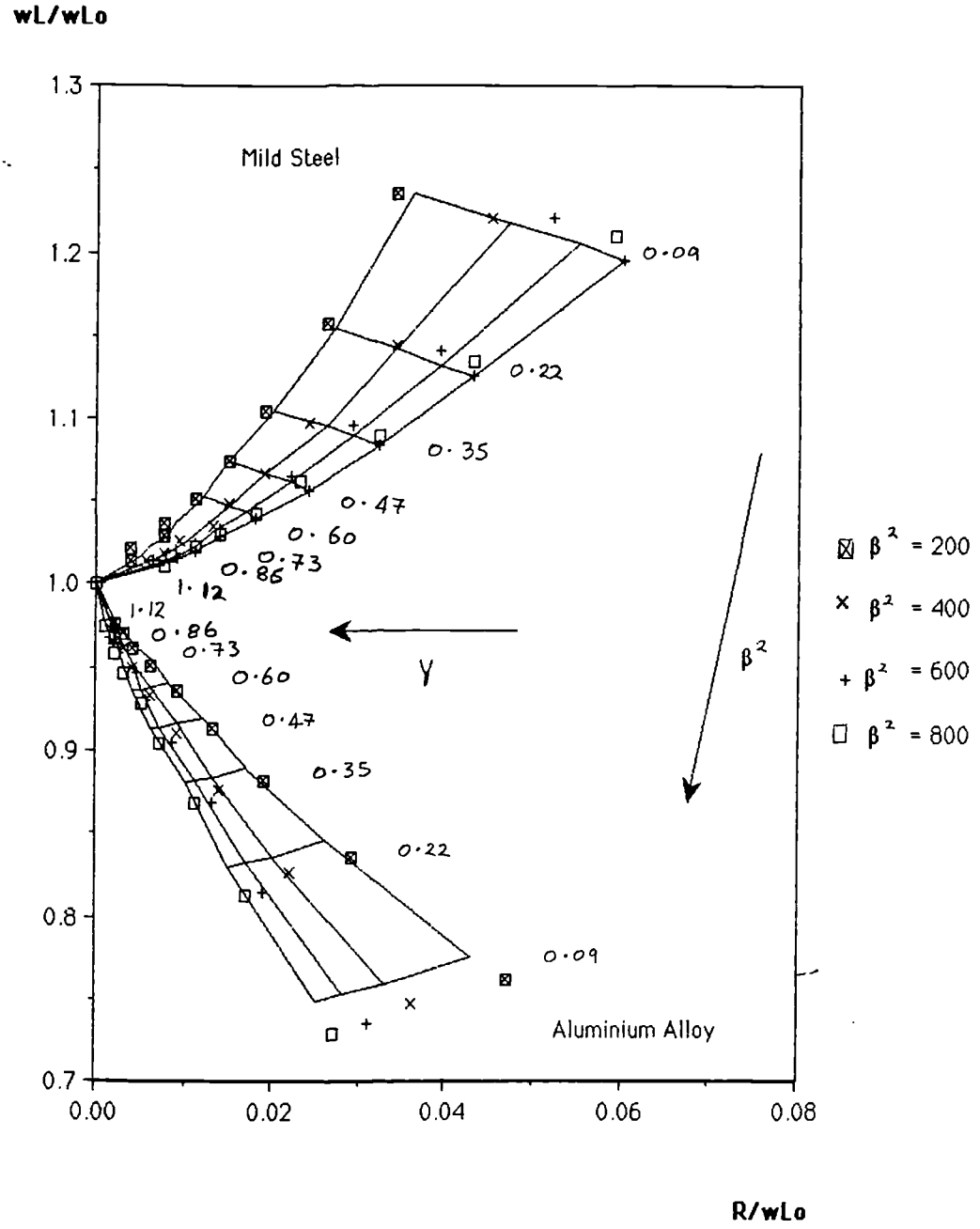

Figure 6.9 : Predicted and experimental values of the components of impedance of coil 4S above aluminium and mild steel. $L_0 = 170\mu H$, $Y_0 = 0.66$

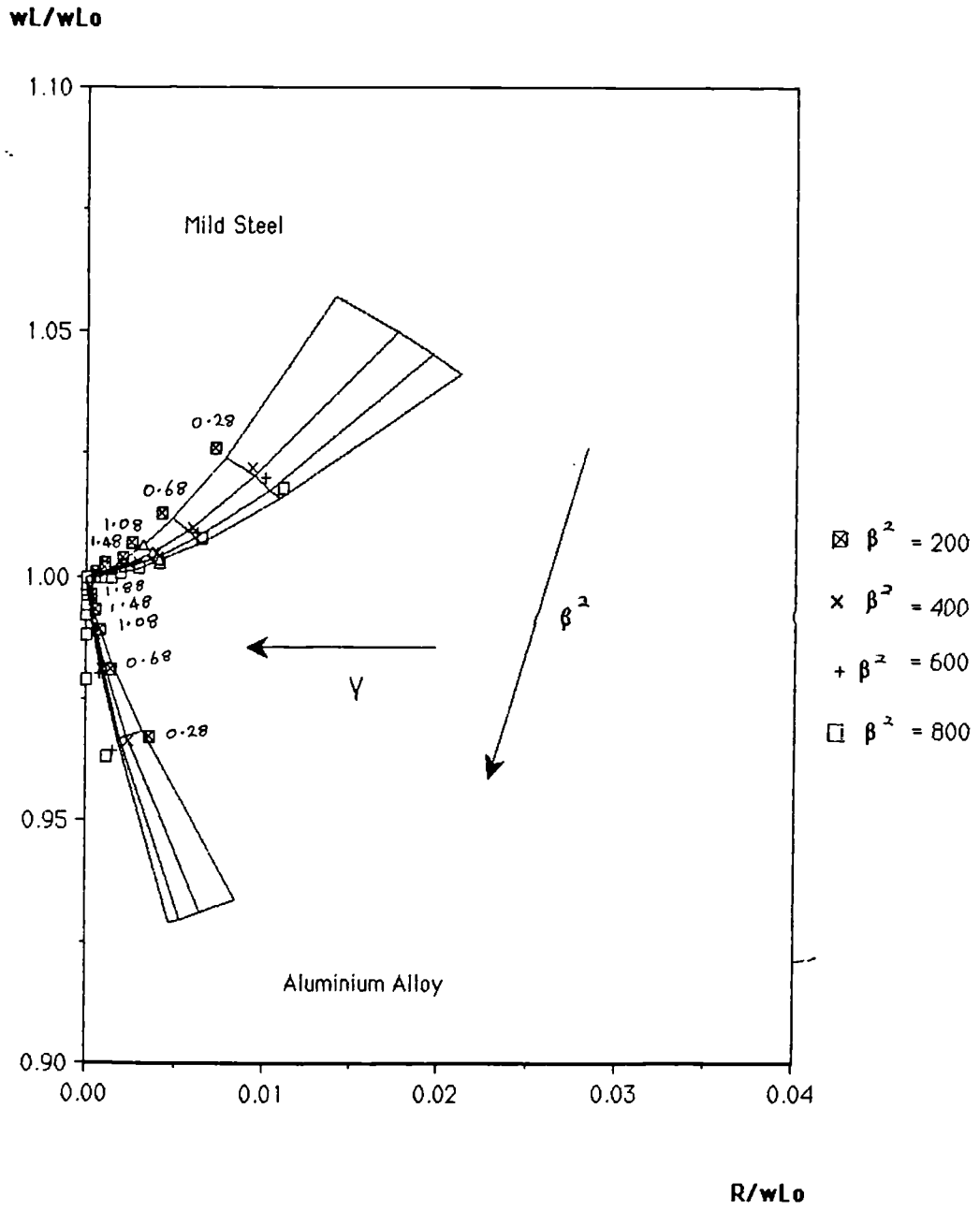

Figure 6.10: Predicted and experimental values of the components of impedance of coil 2S above aluminium and mild steel. $L_0 = 13\mu H$, $Y_0 = 2.56$.

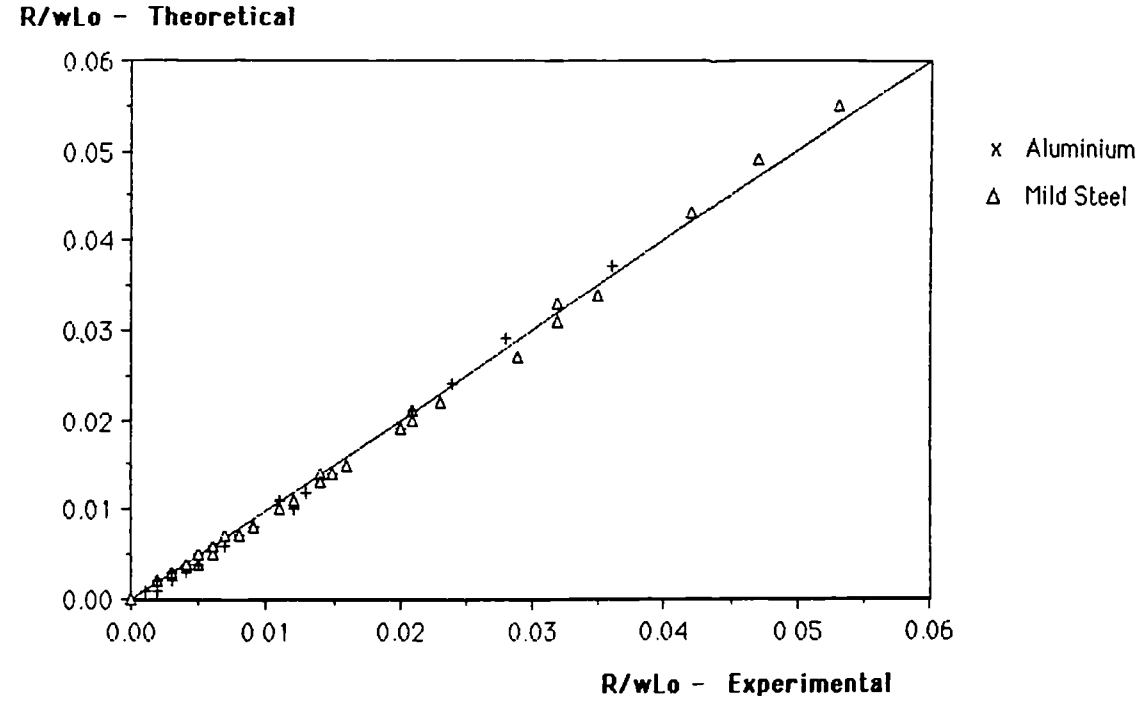

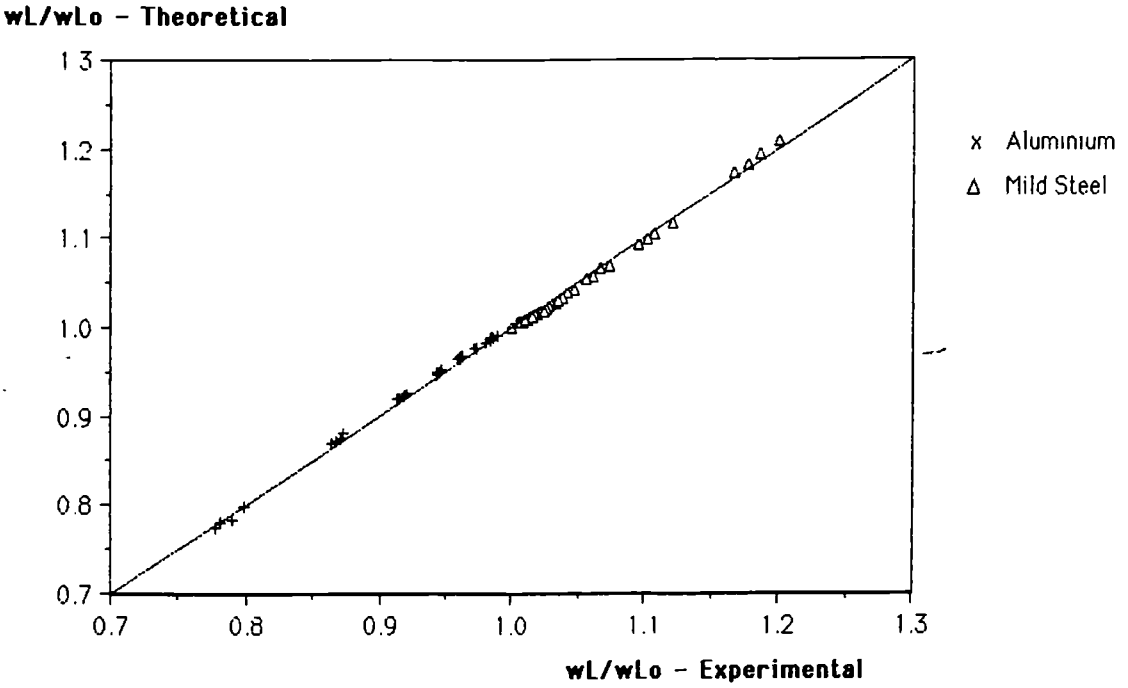

Figure 6.11: Correlation of predicted and experimental values of the components of impedance of coil 3S. $L_0 = 17\mu H$, $Y_0 = 0.6$.

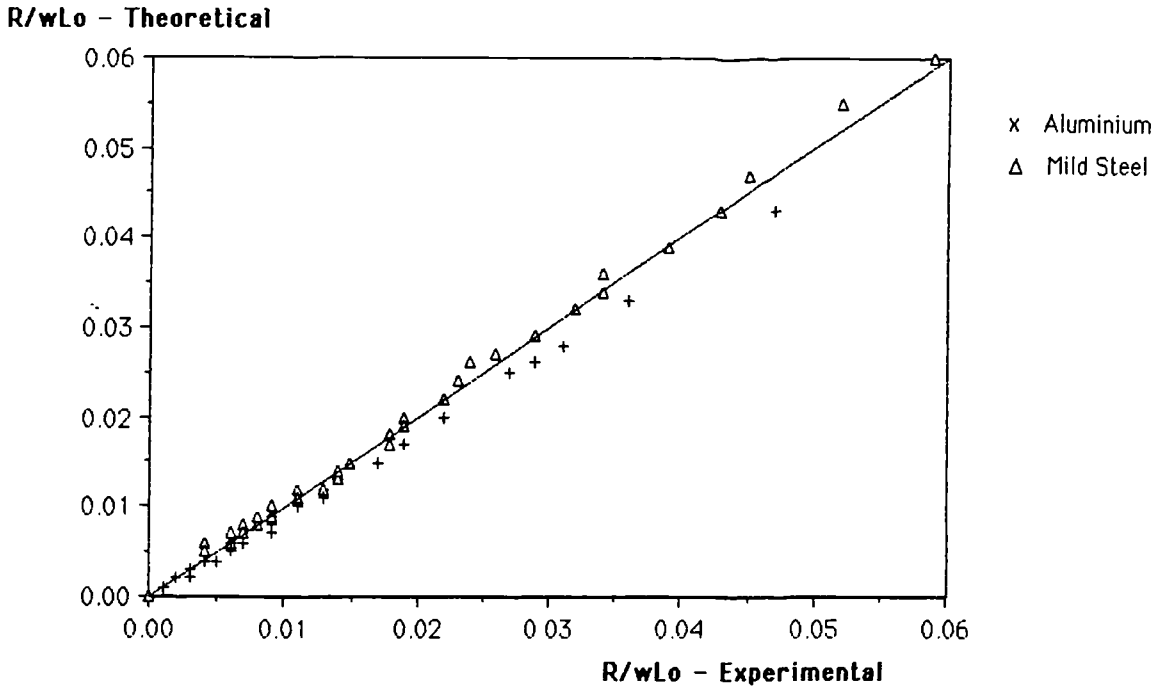

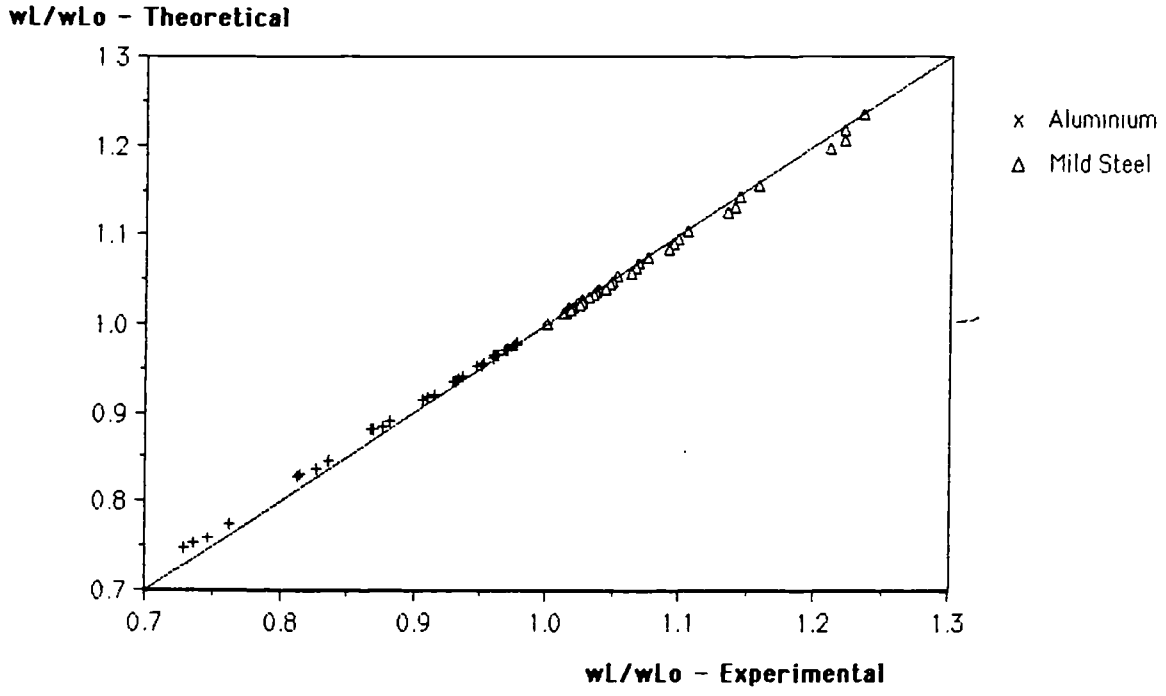

Figure 6.12: Correlation of predicted and experimental values of the components of impedance of coil 4S. $L_0 = 170\mu H$, $Y_0 = 0.66$

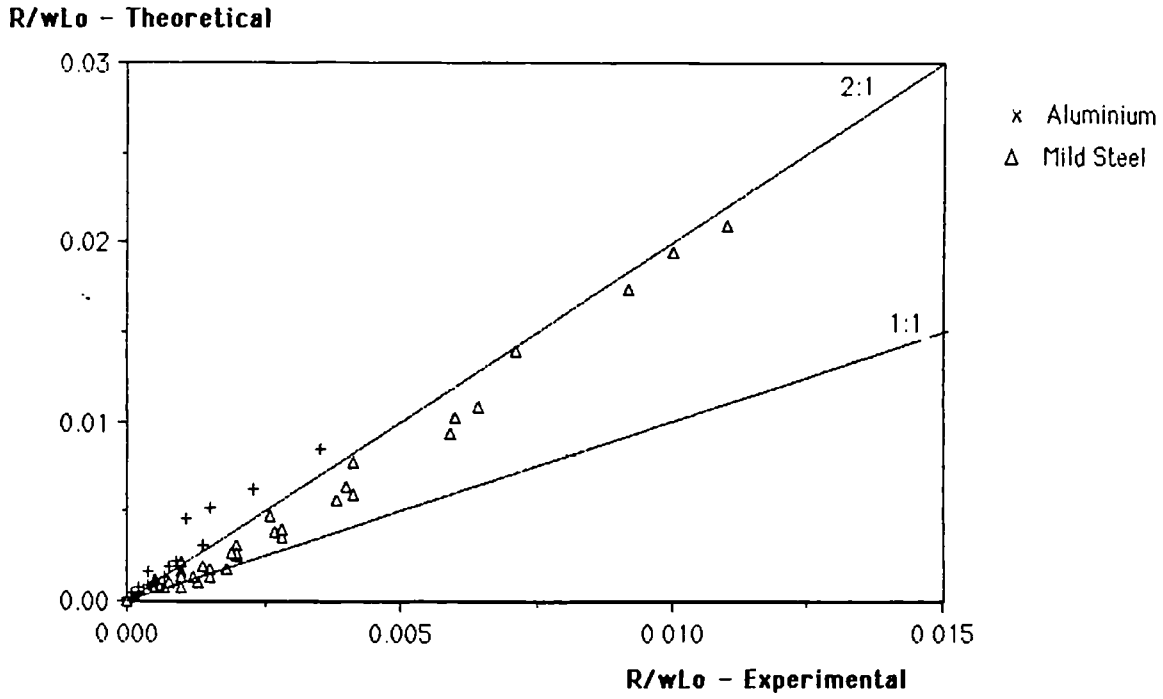

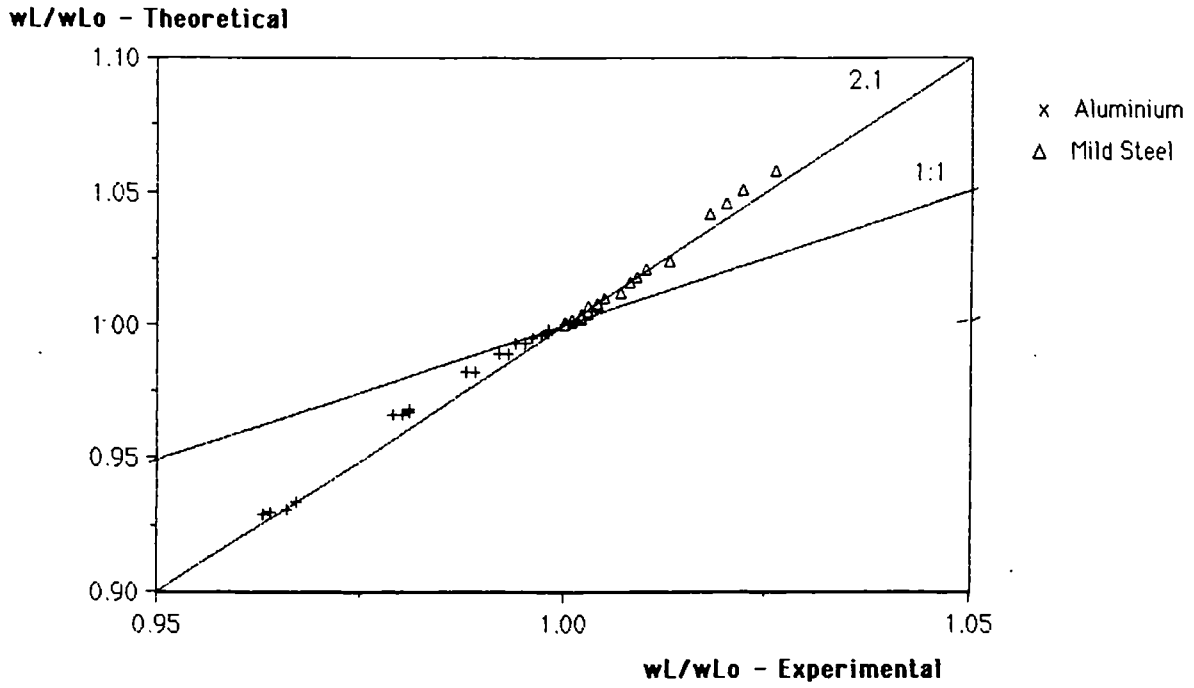

Figure 6.13: Correlation of predicted and experimental values of the components of impedance of coil 2S. $L_0 = 13\mu H$, $Y_0 = 2.56$.

To evaluate the causes for any discrepencies in the direction of β^2, errors in the estimation of σ, μ and r must be considered. An error of $1MSm^{-1}$ in σ could alter the value of β^2 by $\pm$ 15 percent for normalised frequencies between 200 and 1000. About $\pm$ 20 percent change is apparant for a change of $\pm$ 10 in the value of μ_r (Fig. 6.14). This infers that a small change in μ_r has approximately twice the effect of a small change in σ of the same order. From the results predicted it appears that the estimation of $\mu_r = 97$ was reasonable.

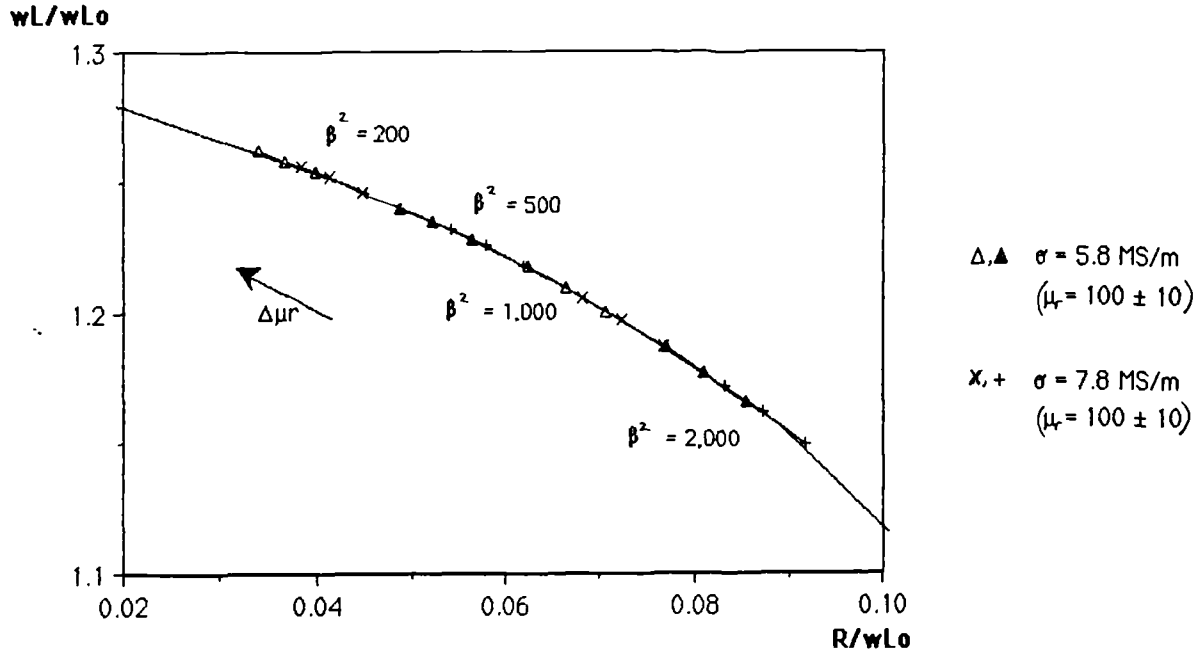

(a) Normalised frequencies between 200 and 2,000

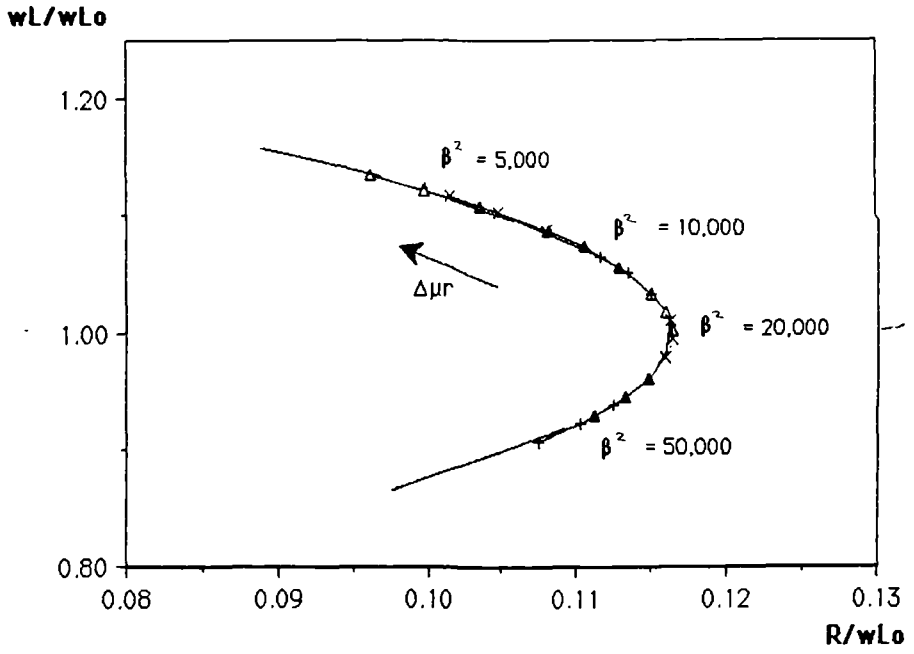

(b) Normalised frequencies between 5,000 and 50,000

Figure 6.14: The effects of small changes in the values of μ_r and σ on the normalised components of impedance.

$\mu_r = 100 \pm 10$, $\sigma = 6.8 \pm 1$ MS/m .

CHAPTER 7

ASSESSMENT OF THE SIZE OF CRACKS WITH EDDY CURRENTS

Any flaw, such as a crack, affects the impedance of an eddy current coil in a manner differing from the impedance variations caused by a change in either normalised frequency, lift-off or sample shape. Förster [3] investigated the effect of cracks experimentally in non-ferromagnetic cylinders, using an encircling coil. He plotted the changes in the components of normalised impedance when the coil was scanned from defect-free to defective parts of the sample for different values of normalised frequency β^2 (Fig. 7.1). He found that optimum flaw detection occurred when β^2 was equal to 15. In this chapter the effects of cracks, simulated by saw cuts, on the impedance of a detecting coil above a ferromagnetic plate are considered: The influence of an edge is studied in Section 7.1 and the measurements of changes in impedance with slot depth of three different types of probe are described in Sections 7.2 to 7.4. The effect of crack inclination is described briefly in Section 7.5

The changes in the components of impedance of each probe were measured using the Vector S900 flaw detector (Section 4.1.2), while the probe was scanned normal to each saw cut and away from any edges, at frequencies between 10kHz and 1MHz and values of lift-off up to 10mm. A scanning rig (Section 4.2) was used to keep the probe perpendicular to and at a fixed height from the surface of the sample. Initially cracks were simulated by compressed saw cuts [34], but the act of compression of the saw cuts caused changes in the eddy current response (Section 7.2), because of local changes in magnetic permeability around the base of the crack, where high stresses are induced. Subsequent saw cuts were left uncompressed.

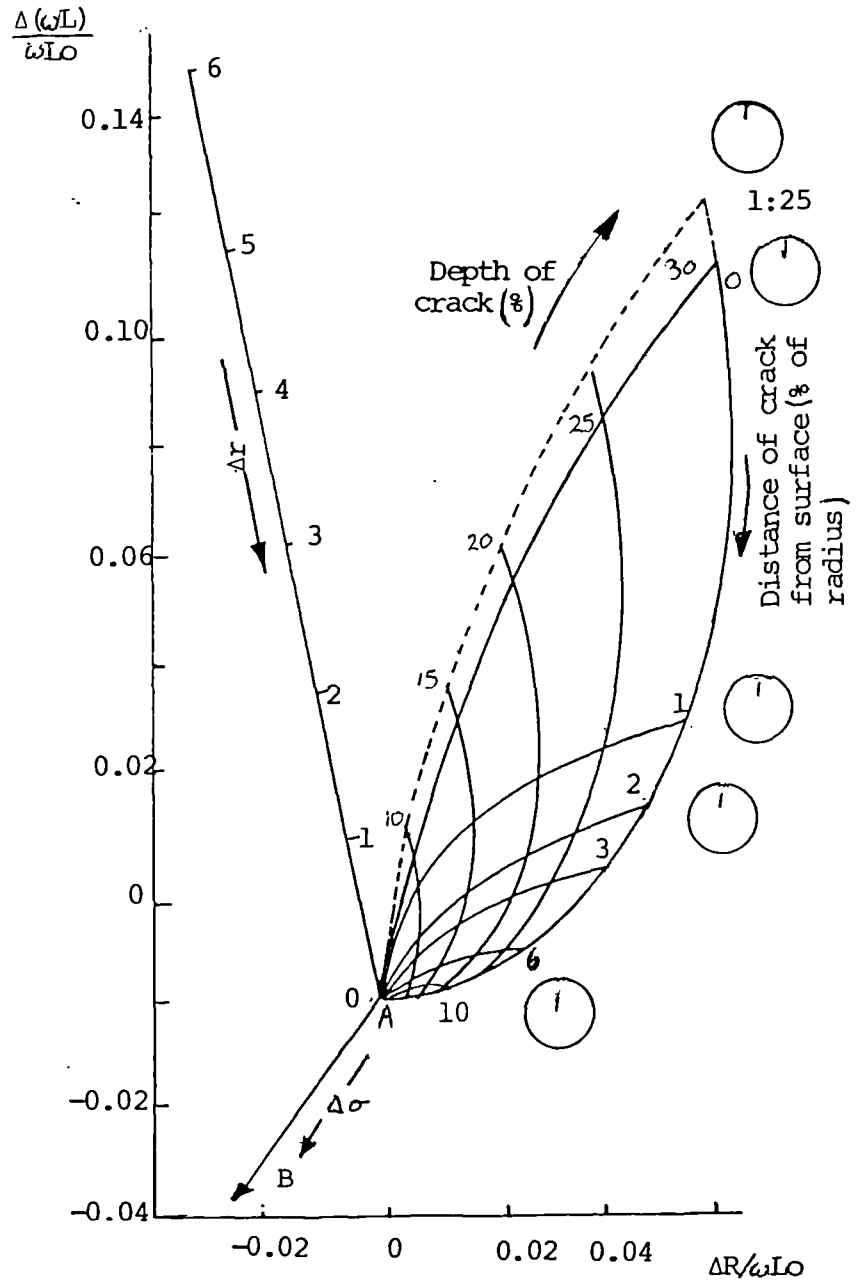

Institut Dr Foerster

Figure 7.1: Variations of impedance caused by surface and subsurface cracks in non-ferromagnetic cylinders. $\beta^2 = 15$.

7.1 The Influence of an Edge

When investigating the effects of defects on the impedance of an eddy current coil it is important to eliminate unwanted signals, caused by effects such as those from lift-off and the vicinity of a boundary such as an edge. The lift-off was kept constant by means of a scanning rig (Section 4.2). On approaching an edge, the signal caused by a change in lift-off displayed on the screen of the flaw detector (Section 4.1.2) changed in phase. The nature of the change and the distance of the probe from the sample edge at which the edge-effects started to occur was found using probe 1T (Table 4.3, Section 4.3.3), of nominal inductance 31μH and radius 1.4mm, by scanning from the middle of a defect-free plate of mild steel to the edge and beyond. With the probe positioned and balanced over the centre of the plate the lift-off signal was made to coincide with the negative x-axis of the screen as a reference. The change in phase of the lift-off signal was monitored with respect to the reference at intervals of 0.25mm across the plate.

Blitz, Tilson and Williams [34] investigated the effects of edges in aluminium and found that the distance from the edge at which edge-effects first occured was approximately proportional to the penetration depth δ at any frequency. The phase angle of the signal changed as shown in Fig. 7.2(a), using a 30μH coil of 1mm radius. For mild steel, when using a 31μH, 1.4mm radius probe, it was found that over the frequency range of interest, i.e., 10 to 200 kHz, there seemed to be no change in the distance from the sample edge at which edge-effects first occurred, remaining approximately 2.7 times the coil radius. The phase angle changed in the manner shown in Fig.7.2(b). The reason for the difference in phase response may be explained by the influences of electrical conductivity σ and magnetic permeability μ, which change from $\sigma\mu$ of the sample to $\sigma_o\mu_o$ of air as the probe is moved from the sample edge, causing a change in phase of the lift-off vector (Fig.6.14, Section 6.2).

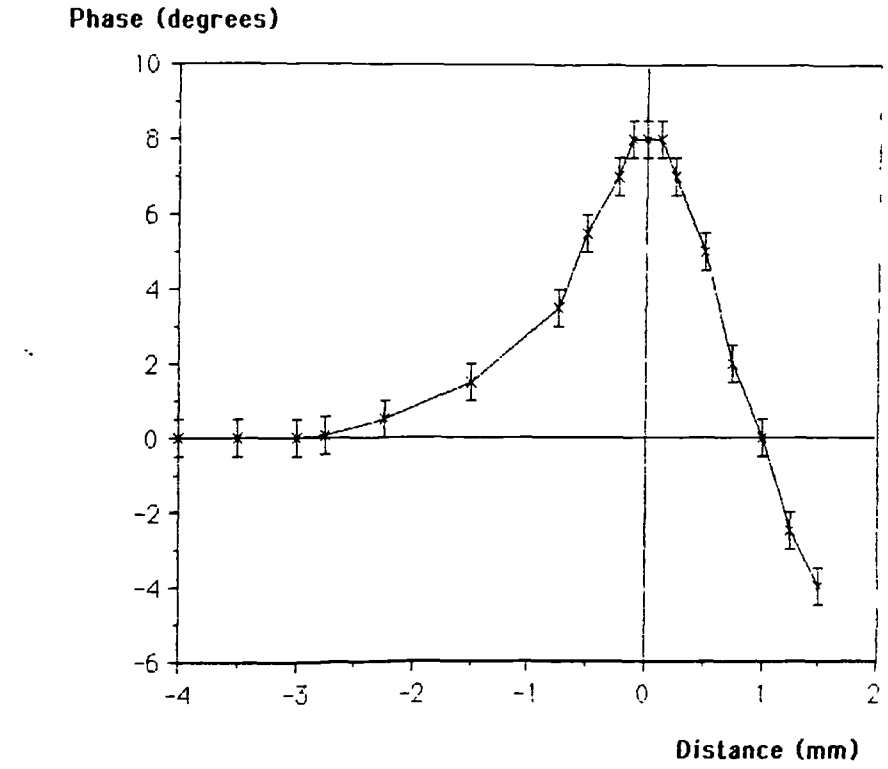

(a) Non-Ferromagnetic Sample

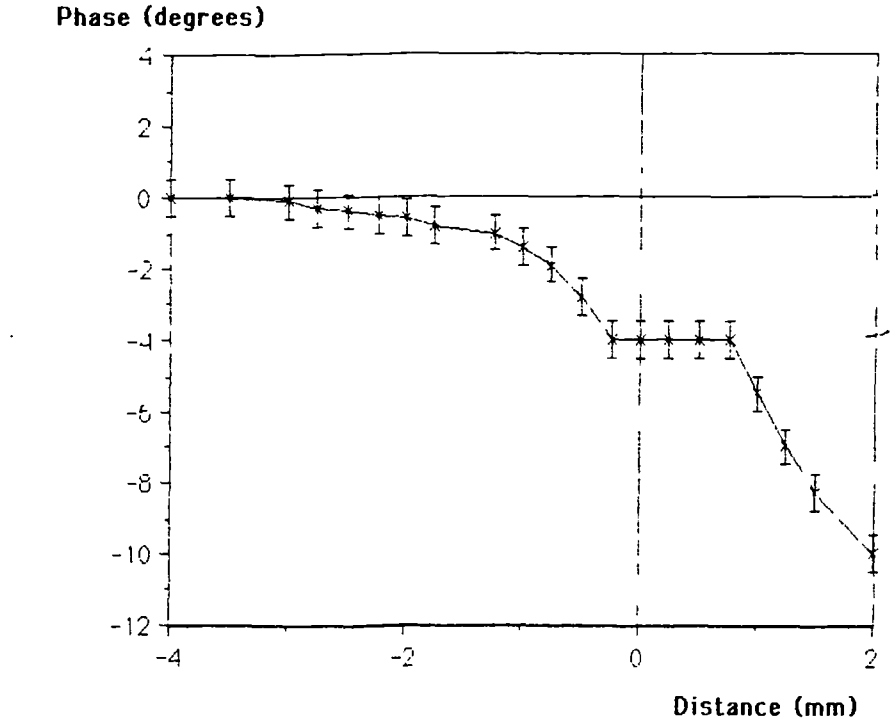

(b) Ferromagnetic Sample

Figure 7.2: The influence of an edge.

With non-ferromagnetic metals, only changes in σ have any influence. Directly above the sample the magnetic field induced by the probe is reduced by the opposing field generated by the induced eddy currents. On moving away from the sample, the opposing eddy current field becomes progressively weaker because eddy currents are generated only in the metal, and the conductivity changes to the air value of $\sigma_a = 0$, causing an abrupt negative change in phase of the lift-off vector (Fig.6.14). When the probe is positioned over the edge of the metal, the field from the induced eddy currents is effectively concentrated at the edge as if at a defect, resulting in a positive change in phase. The magnetic permeability of a ferromagnetic sample has the effect of magnifying the magnetic field generated by the eddy currents. On moving away from the metal, both σ and μ change abruptly to the air values, with an associated negative change in phase of the lift-off vector. When the coil is directly over the edge of the metal, the field induced by the eddy currents is concentrated, the value of μ is changed, and the phase of the lift-off vector is altered by the influence of μ in the same direction as a negative change in conductivity (Fig.6.14)

7.2 Slot Detection with Transformer Probes

The depth of eddy current penetration is inversely dependent on frequency $f = \omega/2\pi$, and the electrical conductivity σ and magnetic permeability μ of the sample (Section 5.2):

$$\delta = (2/\omega\mu\sigma)^{1/2} \qquad (7.1)$$

where δ is the depth at which the eddy current density falls to a fraction 1/e of the surface value. The transformer probes 1T to 4T (Table 4.3, Section 4.3.3) were designed to operate at low frequencies, i.e. from 10kHz to 100kHz. The sensitivity and

phase of the responses to a small change in resistance of these probes (Section 4.5) are shown in Fig. 7.3. Compressed saw cuts, ranging in depth from 0.5mm to 2.5mm in samples of both aluminium and mild steel (Table 4.4, Section 4.4), were scanned at frequencies between 10kHz and 100kHz, with values of lift-off from 0.05mm to 0.25mm. Two mild steel samples containing uncompressed saw cuts 0.2mm wide and with depths 1mm and 1.75mm respectively were also scanned. Fig.7.4 and Table 7.1 compare the responses from mild steel and aluminium samples containing compressed saw cuts 1mm deep.

It was noted while scanning the mild steel samples that the phase of impedance changes caused by the defect varied from sample to sample for the compressed samples, but not for the uncompressed samples. Fig. 7.5 demonstrates the different responses of the compressed and uncompressed mild steel samples. Also the compressed defects of depths 0.5mm and 1.0mm could be detected from the opposite surfaces of the samples. X-ray and magnetic particle inspection revealed nothing peculiar to these samples. It was concluded that the act of compression of the mild steel samples had influenced the magnetic properties of the material and that no direct comparisons could be made. Fig. 7.6 shows the response, at a frequency of 50 kHz, of probe 1T to uncompressed saw cuts with depths from 0.5mm to 10mm, cut into two blocks of mild steel (Section 4.4).

The impedance changes caused by variations in permeability were also investigated briefly. A mild steel plate containing a defect-free weld with a heat affected zone was scanned normally to the weld bead. It was found that impedance variations caused by the weld bead were approximately 180° out of phase with a signal produced by a crack in the same material, over the whole frequency range applied. This suggested that a defect in the form of a crack could be characterised by a change in the material properties of the metal, indicated by the parameter $\sigma\mu$.

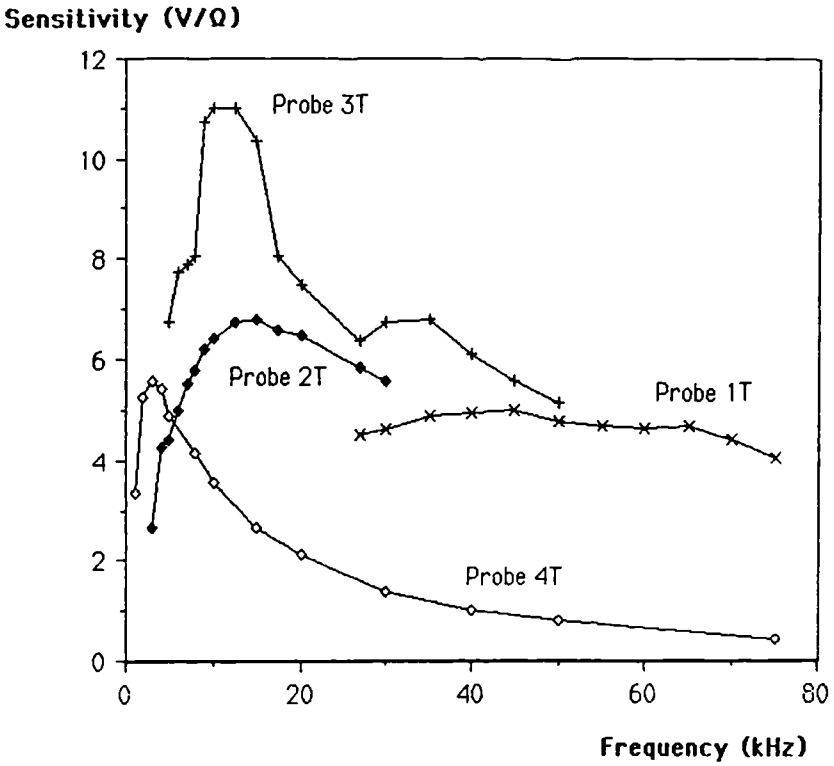

(a) Sensitivity

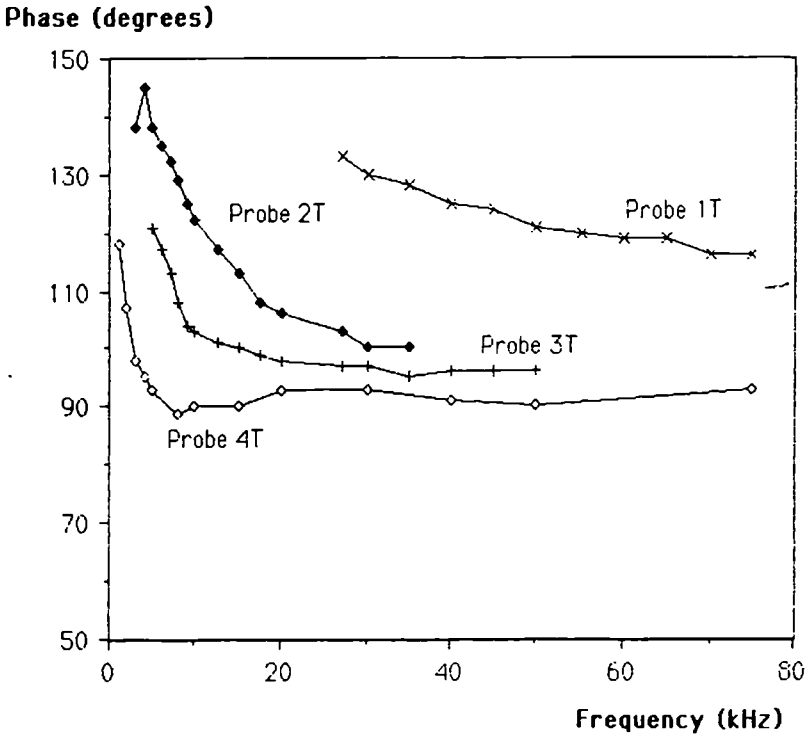

(b) Phase

Figure 7.3: Sensitivity and phase of transformer probes 1T to 4T, measured on the addition of a calibrating resistance.

Table7.1 **Changes in voltages and impedance magnitudes of probes 1T to 4T produced when scanning defects of 1mm in aluminium alloy and mild steel.**

At 10 KHz;

	Mild Steel				Aluminium Alloy		
PROBE	1T	2T	3T	4T	1T	3T	4T
V_d (volt)	2.04	5.09	2.53	2.69	1.49	2.85	4.39
C_f (Ω/V)	0.40	1.43	1.88	5.59	1.63	0.30	0.90
ωL_0 (Ω)	1.95	18.85	1.82	32.36	1.95	1.82	32.36
$\frac{\Delta Z}{\omega L_0}$ ($\times 10^{-1}$)	0.42	0.38	2.61	0.46	1.23	0.47	0.12

At 30 KHz;

	Mild Steel				Aluminium Alloy		
PROBE	1T	2T	3T	4T	1T	3T	4T
V_d (volt)	4.82	6.09	5.46	3.22	3.23	4.65	3.49
C_f (Ω/V)	0.28	3.66	2.11	18.11	0.71	0.30	2.02
ωL_0 (Ω)	5.84	56.55	5.47	97.08	5.84	5.47	97.08
$\frac{\Delta Z}{\omega L_0}$ ($\times 10^{-1}$)	0.23	0.40	2.11	0.60	0.39	0.26	0.07

At 100 KHz;

	Mild Steel				Aluminium Alloy		
PROBE	1T	2T	3T	4T	1T	3T	4T
V_d (volt)	8.77	3.61	8.43	1.95	3.84	3.83	1.03
C_f (Ω/V)	0.49	6.39	2.70	29.81	0.84	0.72	5.72
ωL_0 (Ω)	19.48	188.50	18.22	323.58	19.48	18.22	323.58
$\frac{\Delta Z}{\omega L_0}$ ($\times 10^{-1}$)	0.22	0.12	1.25	0.18	0.17	0.15	0.02

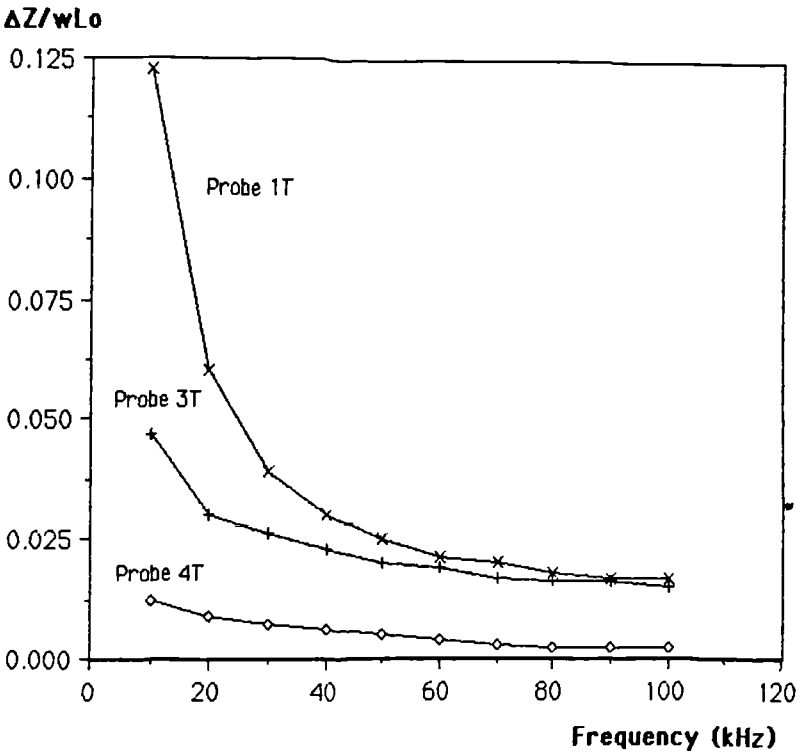

(a) Aluminium Alloy

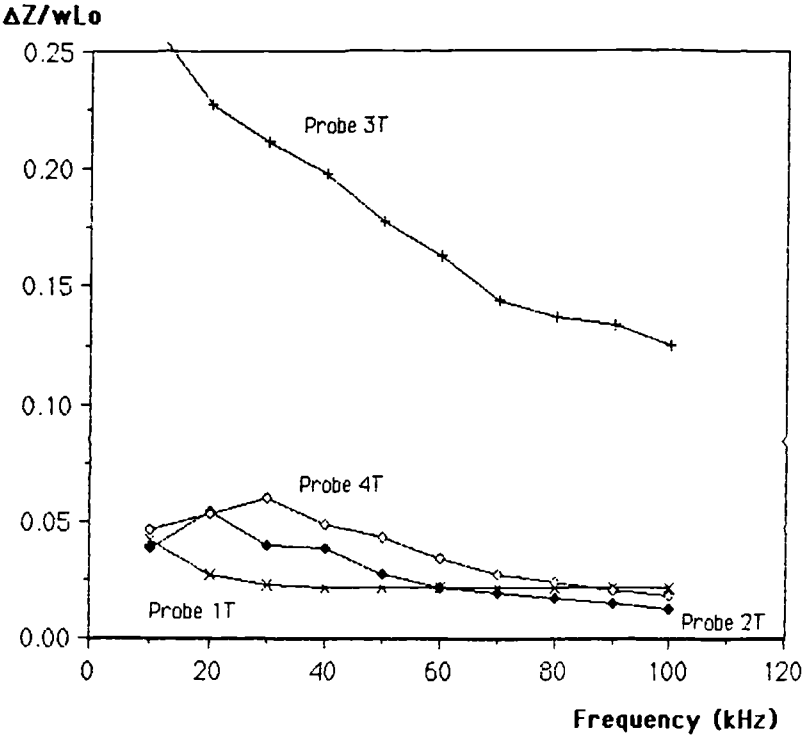

(b) Mild Steel

Figure 7.4: Changes in impedance magnitude of coils 1T to 4T with frequency when scanning compressed saw cuts 1mm deep in (a) aluminium alloy and (b) mild steel.

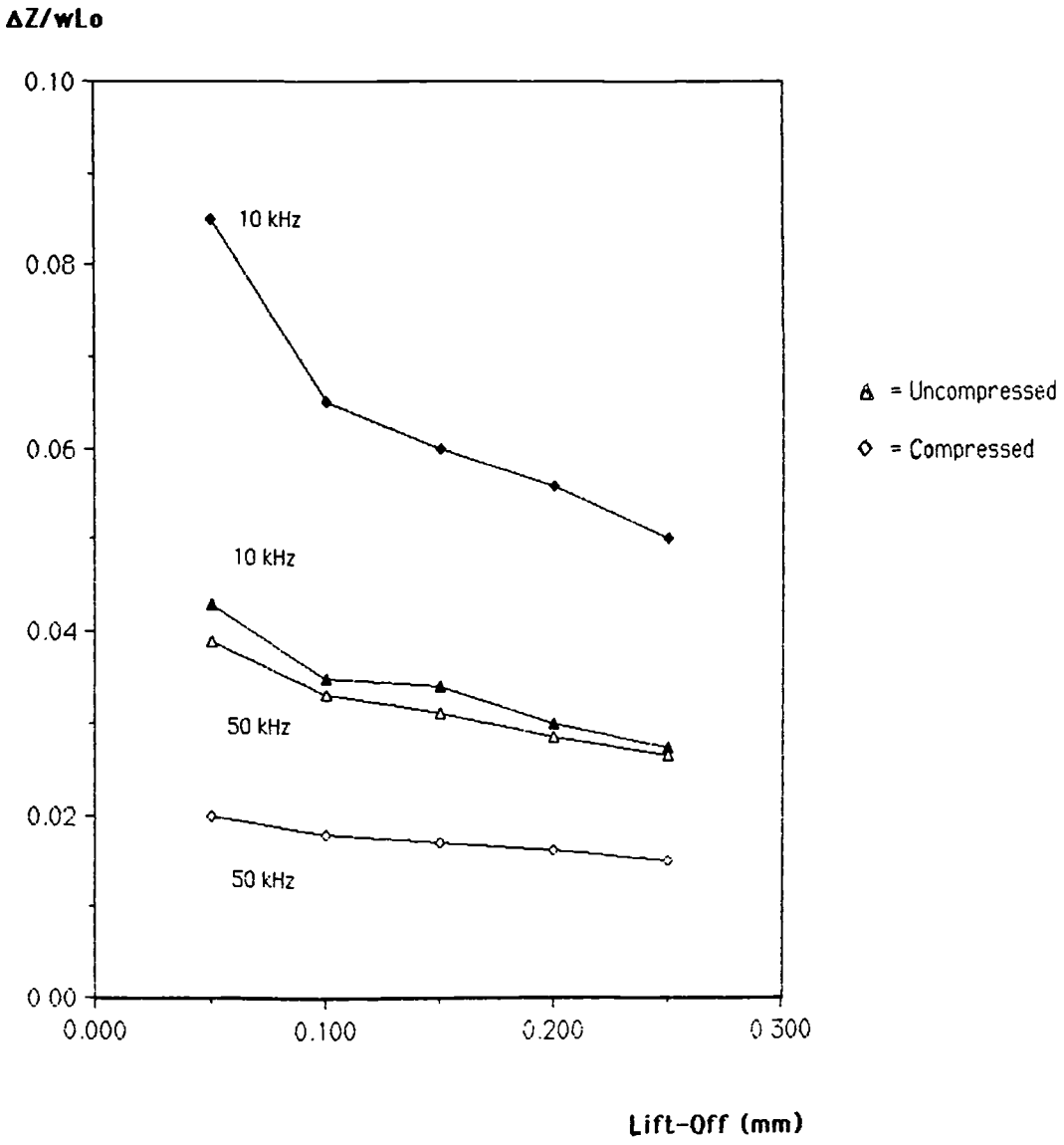

Figure 7.5: Comparison of the response of probe 1T to compressed and uncompressed saw cuts 1.75mm deep in mild steel at frequencies of 10 and 50 kHz.

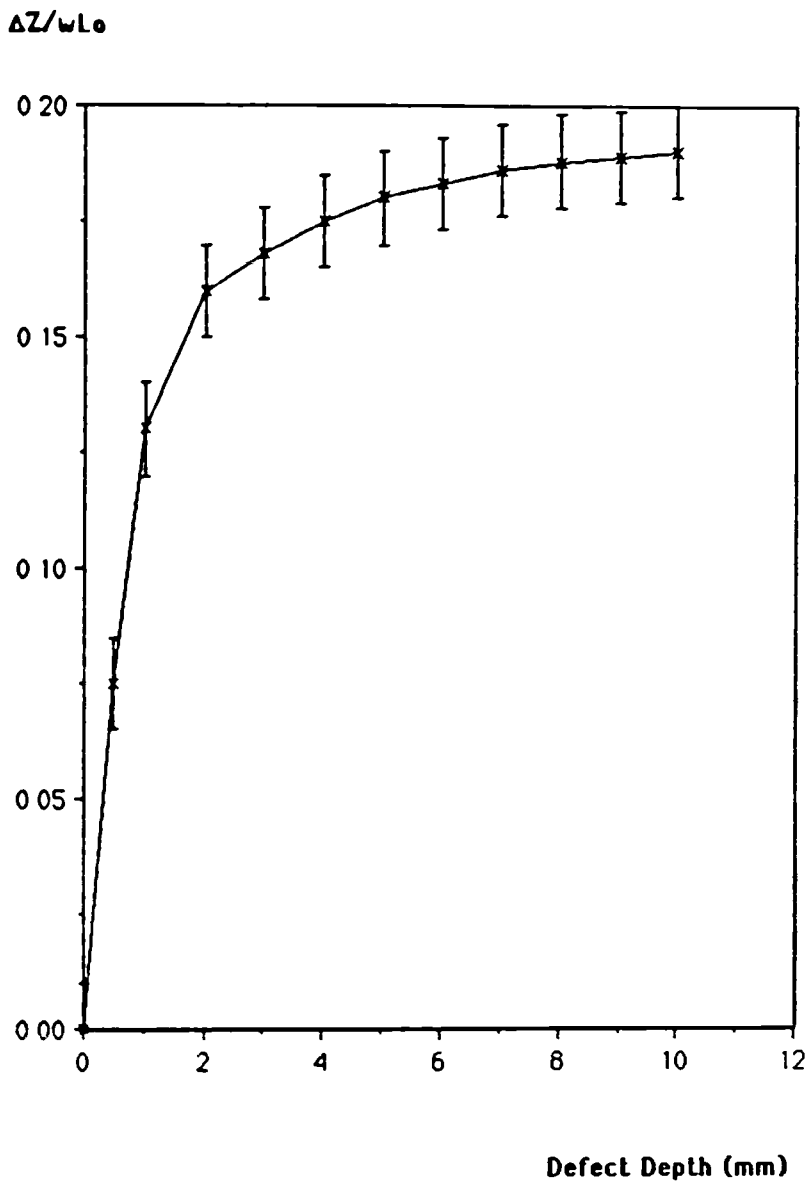

Figure 7.6: Changes in impedance magnitude with defect depth of coil 1T when scanning uncompressed saw cuts in mild steel at a frequency of 50kHz and lift-off of 0.1mm.

7.3 Slot Detection with Single Coil Probes

Air-cored coil AS2 and ferrite-cored coil FS1 (Table 4.1, Section 4.3.1), having impedances of 17μH and 15μH respectively when measured in air, were used to scan the mild steel blocks 1 and 2 (Section 4.4) at frequencies between 50kHz and 1MHz, and values of lift-off from a nominal zero to infinity. The optimum frequency for these probes was found to be 600kHz, for which the defect signals were large and at angles approaching 90° with respect to the lift-off signal. Fig. 7.7 shows the response of probe AS2 to defects at this frequency. Fig. 7.8 shows the maximum degree of lift-off attainable for different depths of slot while still being able to detect the slot. Maximum values of lift-off of up to 3 and 5 times the coil radius could be used for air- and ferrite-cored probes respectively.

The ferrite-cored probe was about five times more sensitive to defects than the air-cored coil, but it was found that the ferrite-cored coil was also sensitive to variations in temperature and magnetic permeability (Section 5.3). The work was thus confined to using air-cored probes. Probes 1S, 2S and 3S were scanned across the saw cuts in block 1 (Figs. 7.9 to 7.11). It would appear from a comparison of these figures that a decreased value of normalised coil length Υ_0 is not particularly advantageous for flaw detection.

Probe AS2 was used to scan the heat affected zone (HAZ) of two welded BS.5436 50D steel plates (Section 4.4). The two 175 x 85 x 12 mm plates were prepared by laying a weld bead down the centre of the short side, which was then machined off flat to leave the heat affected zone. One plate contained a fatigue-type crack, whilst the other was defect-free. A third plate of 50D steel, left unwelded and machined with a slot 3.3mm deep at its centre and elliptical in cross-section (Section 4.4) was also scanned.

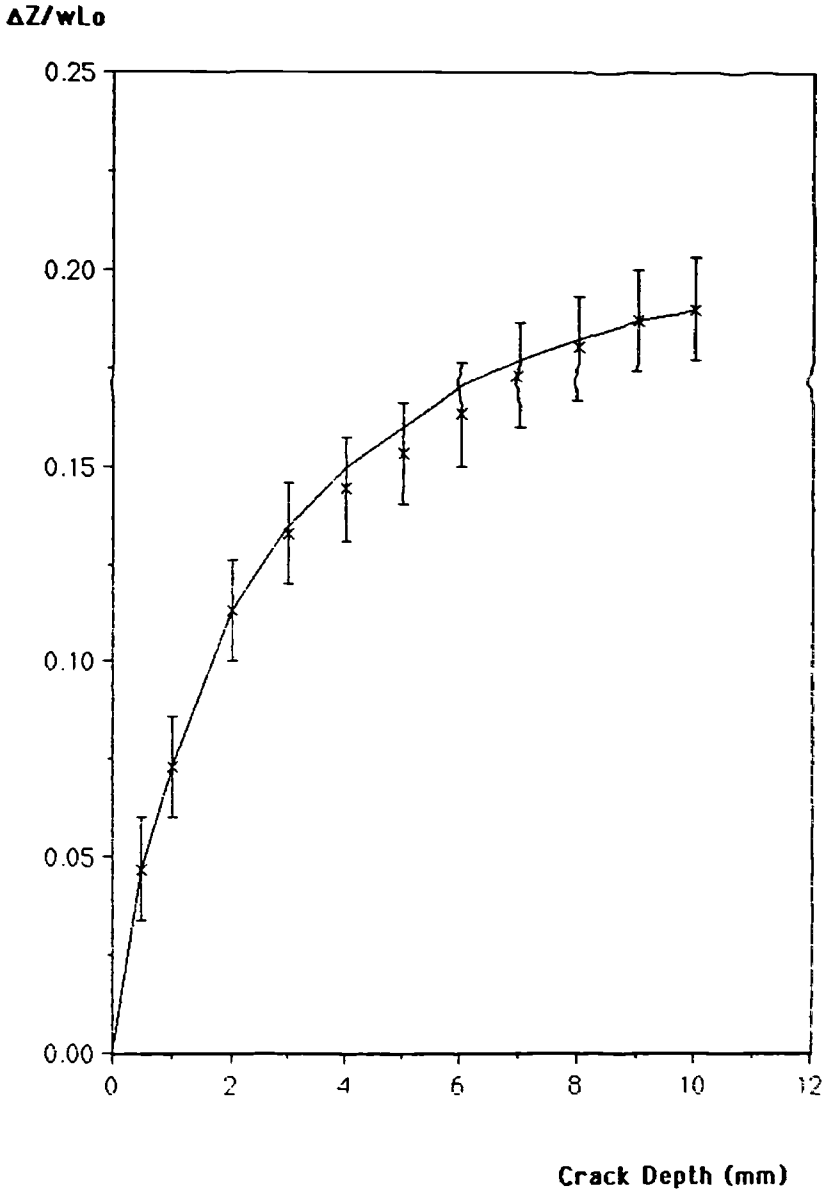

Figure 7.7: Response of probe AS2 to defects of different depths in mild steel at a frequency of 600kHz and lift-off of 0.1mm.

$Y = 0.05$, $L_0 = 17\mu H$, $Y_0 = 3.0$.

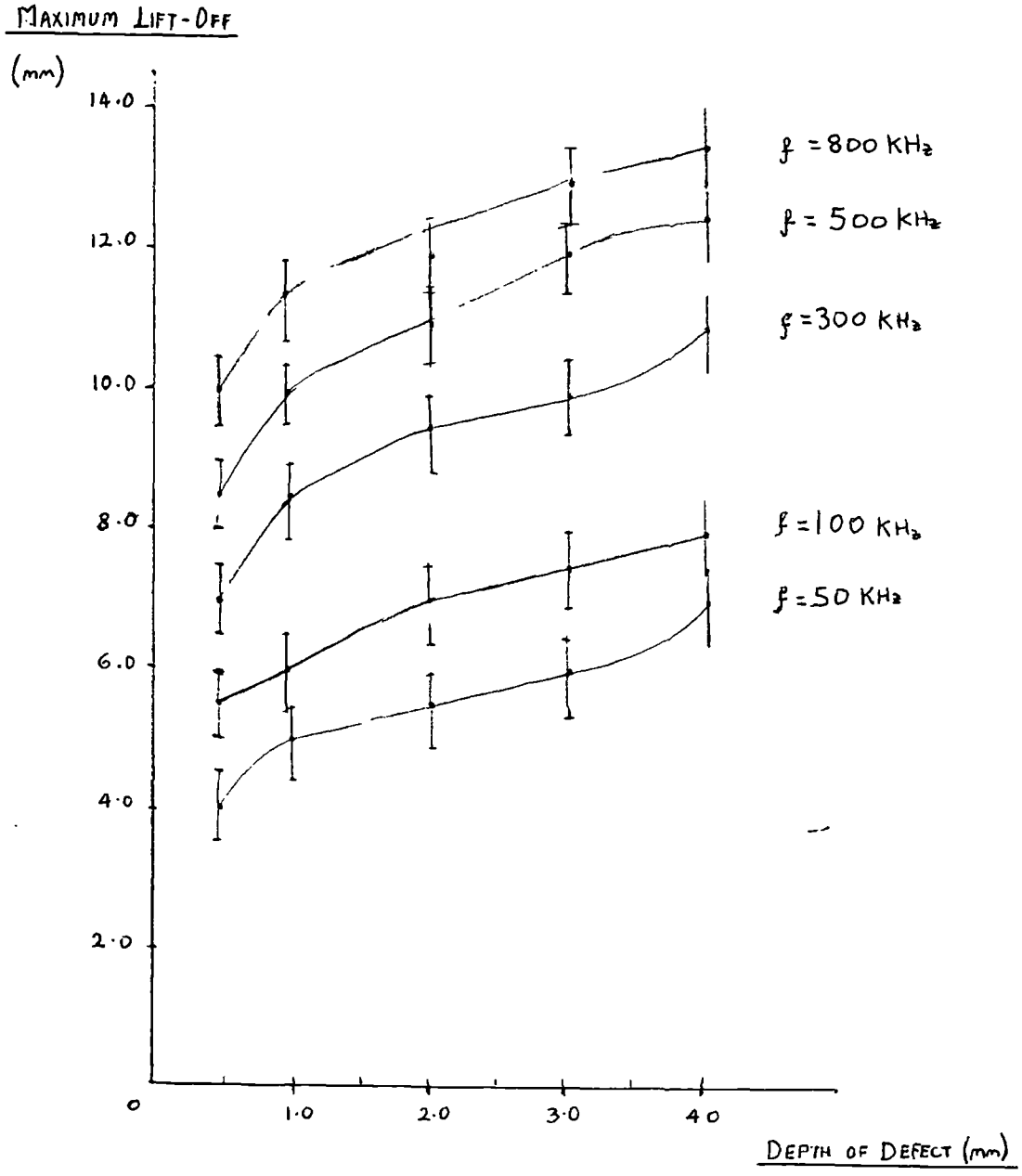

Figure 7.8: Maximum values of lift-off at which defects caused a *minimum* change in impedance of $1x10^{-3}\Omega$, using probe AS1.

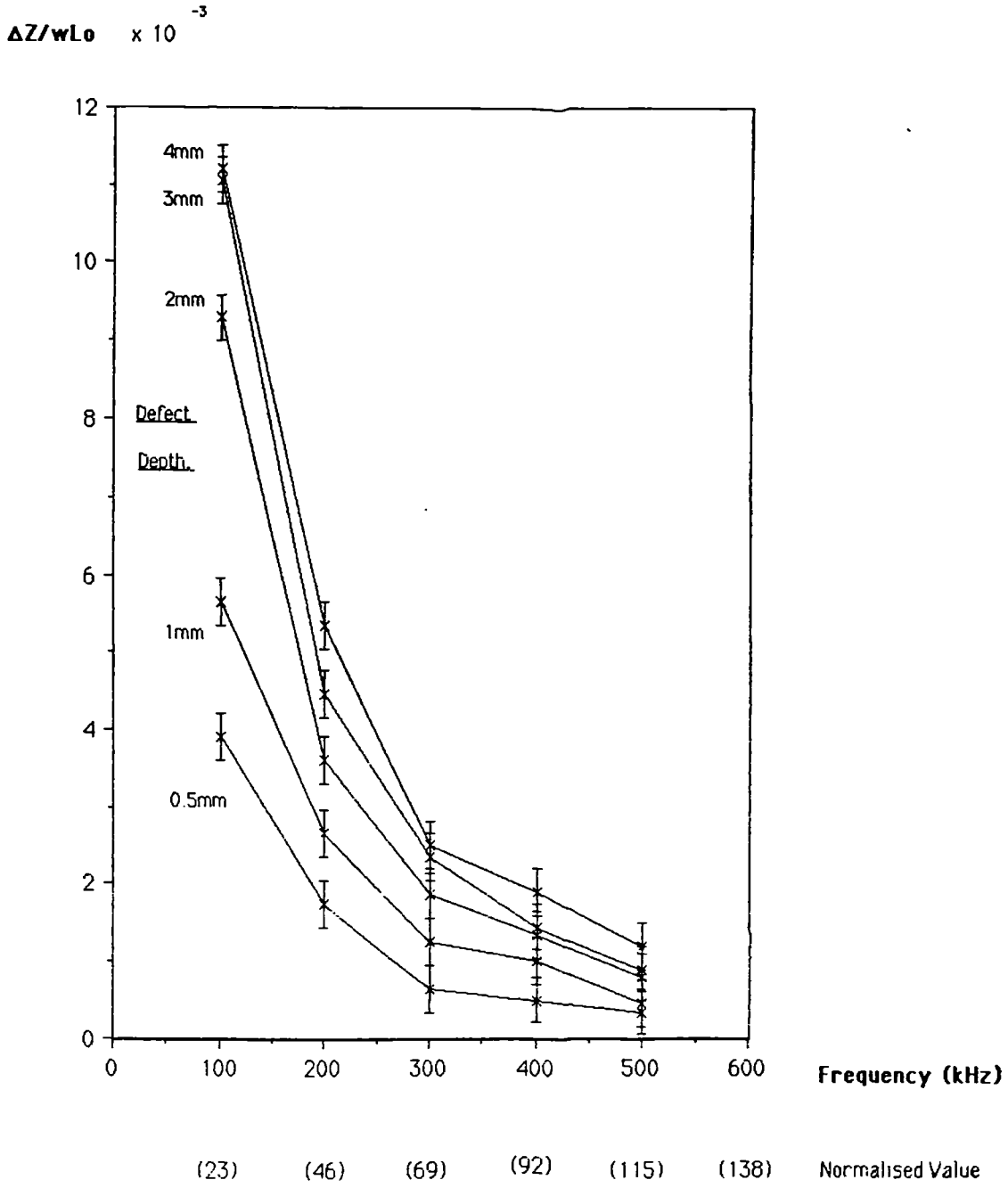

Figure 7.9: Response of probe 1S to defects of different depths in mild steel at a lift-off of 0.1mm, $Y = 0.67$. $L_0 = 9\mu H$, $Y_0 = 6.0$.

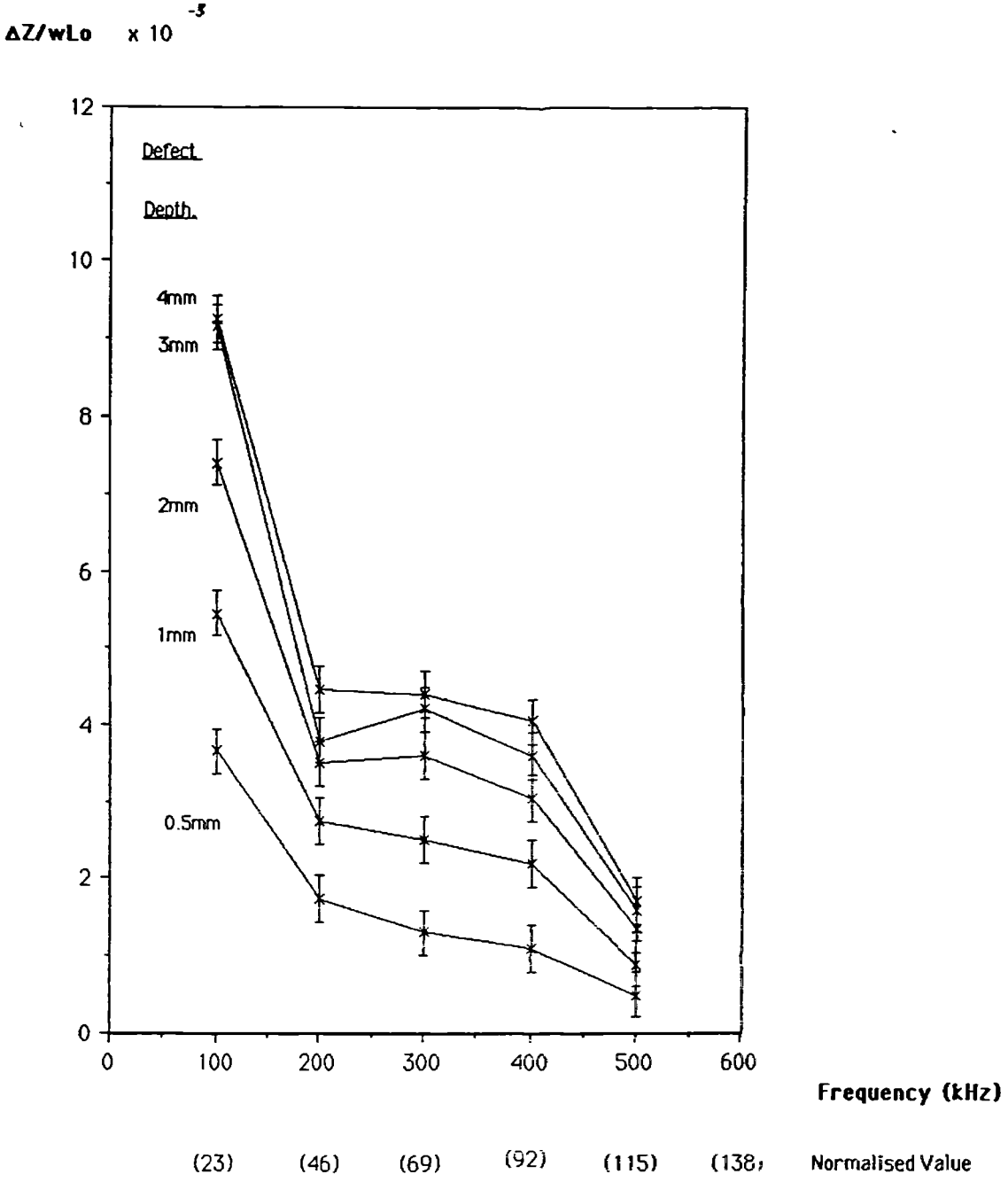

Figure 7.10: Response of probe 2S to defects of different depths in mild steel at a lift-off of 1mm, $Y = 0.67$. $L_0 = 13\mu H$, $Y_0 = 2.6$.

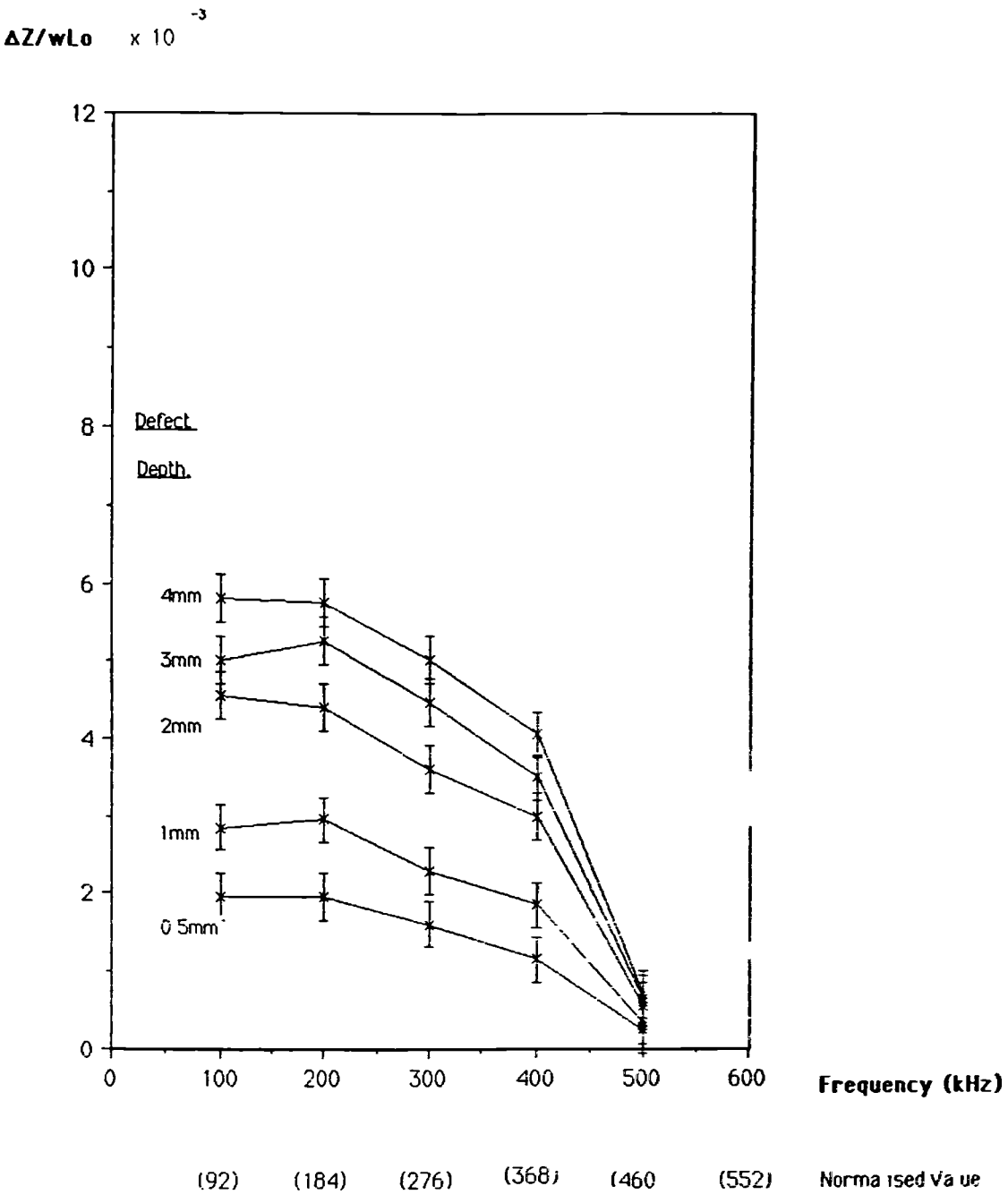

Figure 7.11: Response of probe 3S to defects of different depths in mild steel at a lift-off of 2mm, $\Upsilon = 0.67$. $L_0 = 17\mu H$, $\Upsilon_0 = 0.6$.

Each plate was scanned along the centre of the longest side, and the impedance of the coil was monitored at 9 points across the HAZ and surrounding plate (Fig. 7.12). Frequencies from 10kHz to 1MHz were used, with values of lift-off from 0.1 to 10.0mm. Fig. 7.13 shows how the amplitude of the out-of-balance voltage of the probe varied with lift-off when scanning the HAZ alone, at frequencies of 200, 400 and 800 kHz, and Fig. 7.14 shows typical vector diagrams of the changes in impedance caused by the HAZ alone and the slot alone at the same frequencies. The impedance changes from the cracked plate with HAZ are shown in Fig. 7.15. It was clear that the effects of the HAZ were limited at higher values of frequency and lift-off, whilst the ability to detect defects remained [38].

The impedance of a coil is influenced by variations of lift-off, which could mask other indications such as the impedance changes caused by a defect, when scanning samples which are not completely flat, such as a weld bead. Therefore an attempt was made to phase out the components of impedance caused by lift-off by using a multifrequency method [1]. This approach was not successful when testing mild steel, because the phase of the lift-off vector changed with the value of lift-off, and the degree of change in phase was different for different frequencies. Differential probes (Section 4.3.2) were built with the aim of removing the variations in impedance caused by changes of lift-off from the defect signal.

7.4 Slot Detection with Differential Probes

Three air-cored differential probes (Table 4.2, Section 4.3.2) were constructed to enable a comparison of their performances with those of the single coils 1S to 3S. The components of impedance of the corresponding differential and single coil probes were measured at frequencies between 100 and 500 kHz, both whilst increasing the lift-off distance from a defect-free part of the mild steel calibration

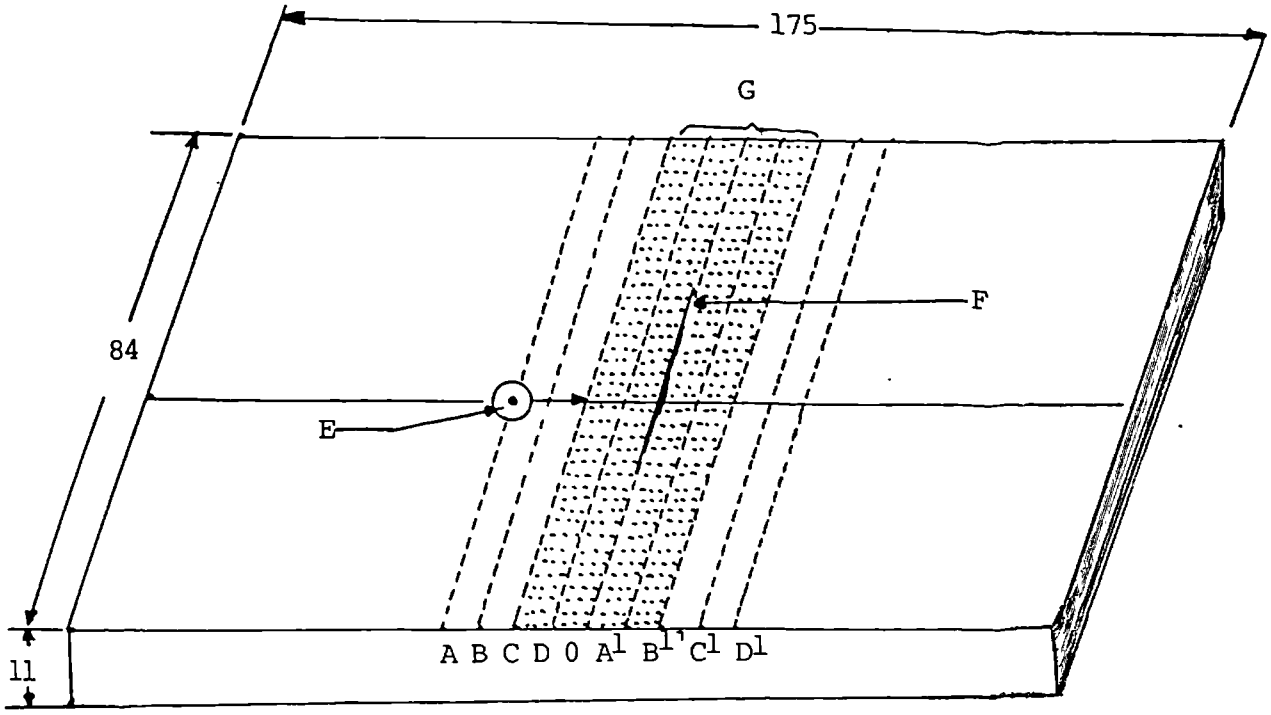

Figure 7.12: Reference points for scanning the 50D steel plate containing a fatigue crack in the heat affected zone (HAZ).

A to D, 0, A' to D' = Points of Measurement
E = Direction of Scanning
F = Crack, Revealed with Magnetic Particle Inspection
G = Weld and Heat Affected Zone

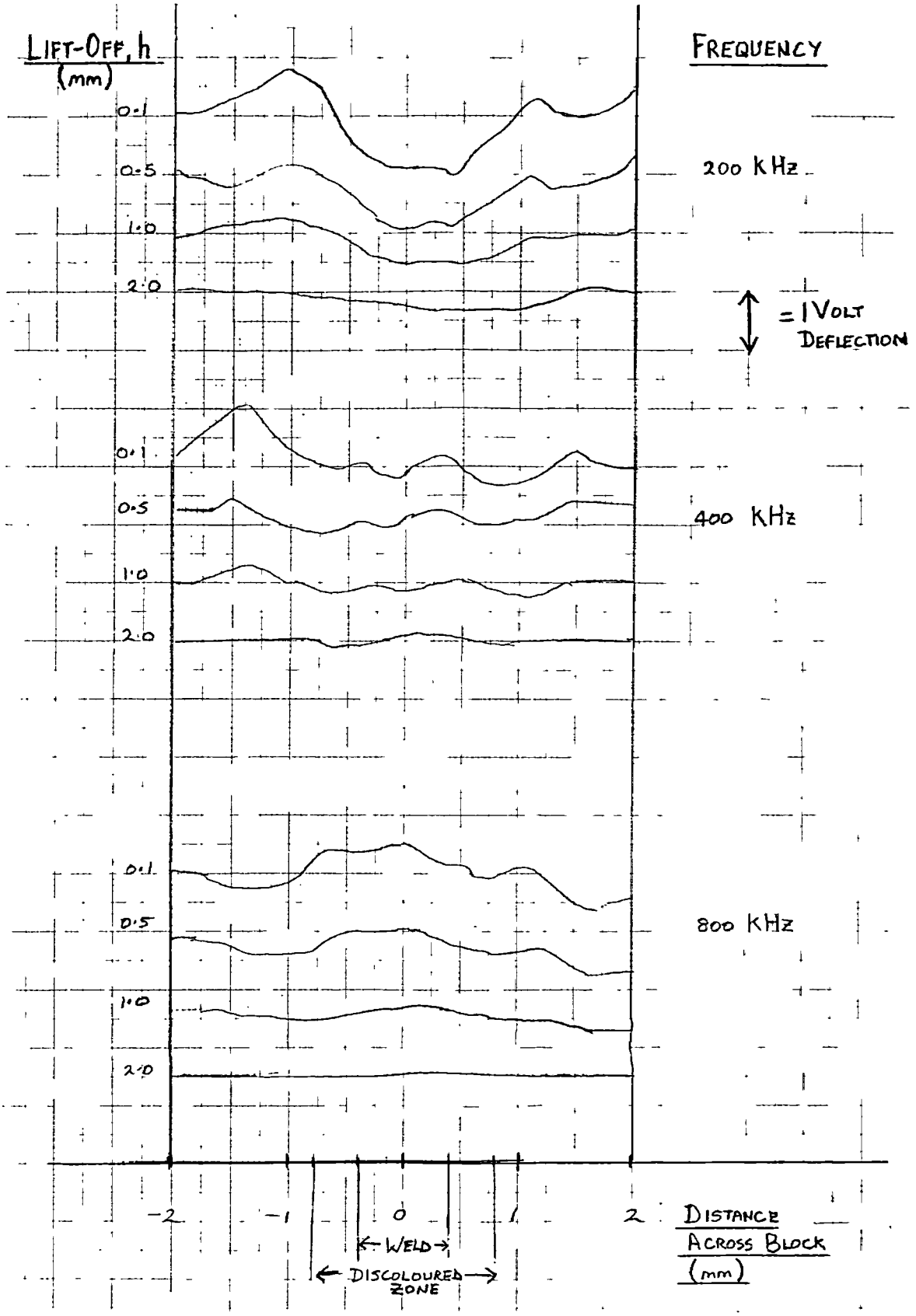

Figure 7.13: Variations of out-of-balance voltage amplitude with distance across the HAZ of a weld, for increasing values of lift-off, using probe AS2.

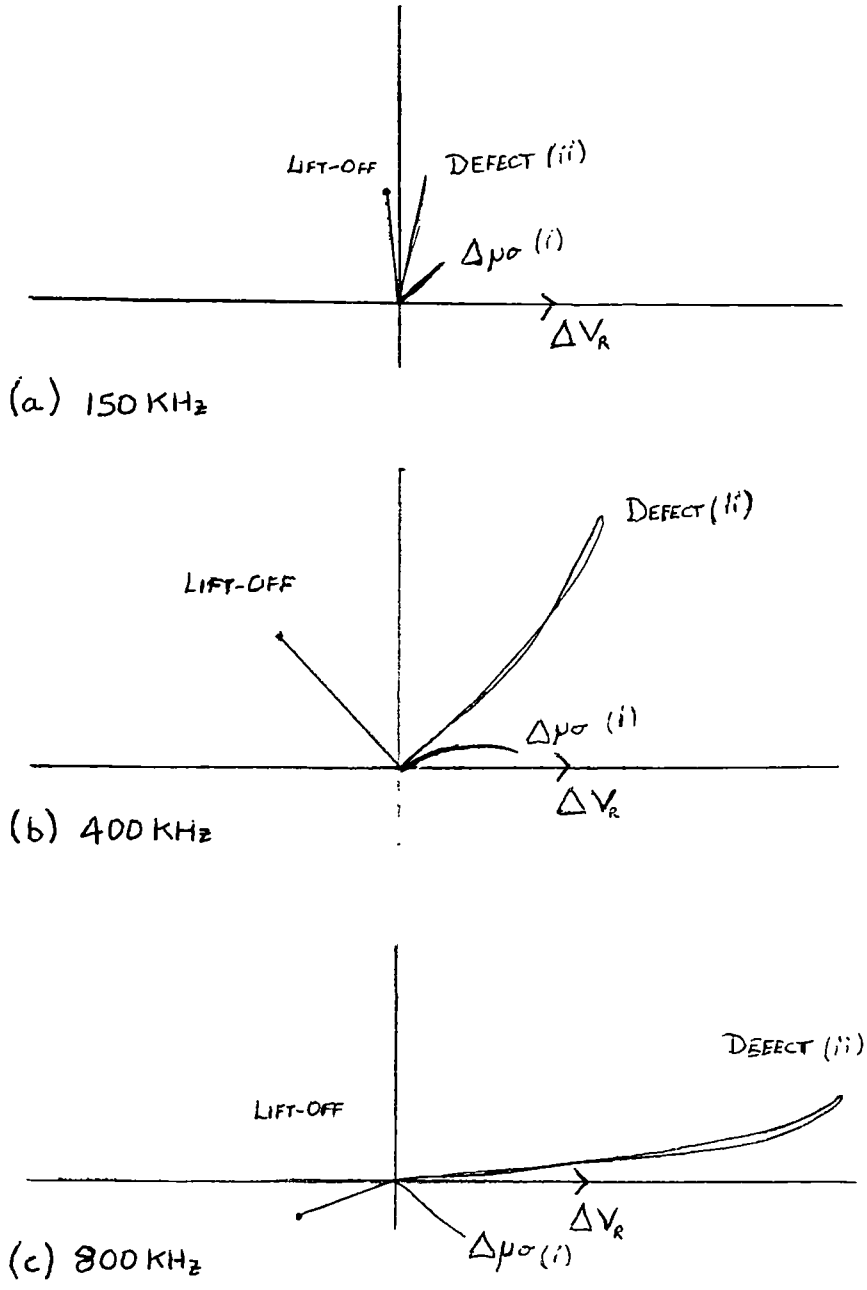

Figure 7.14: Typical responses of probe AS2 to changes in

i) σμ alone across a HAZ and ii) a slot in a plain plate.

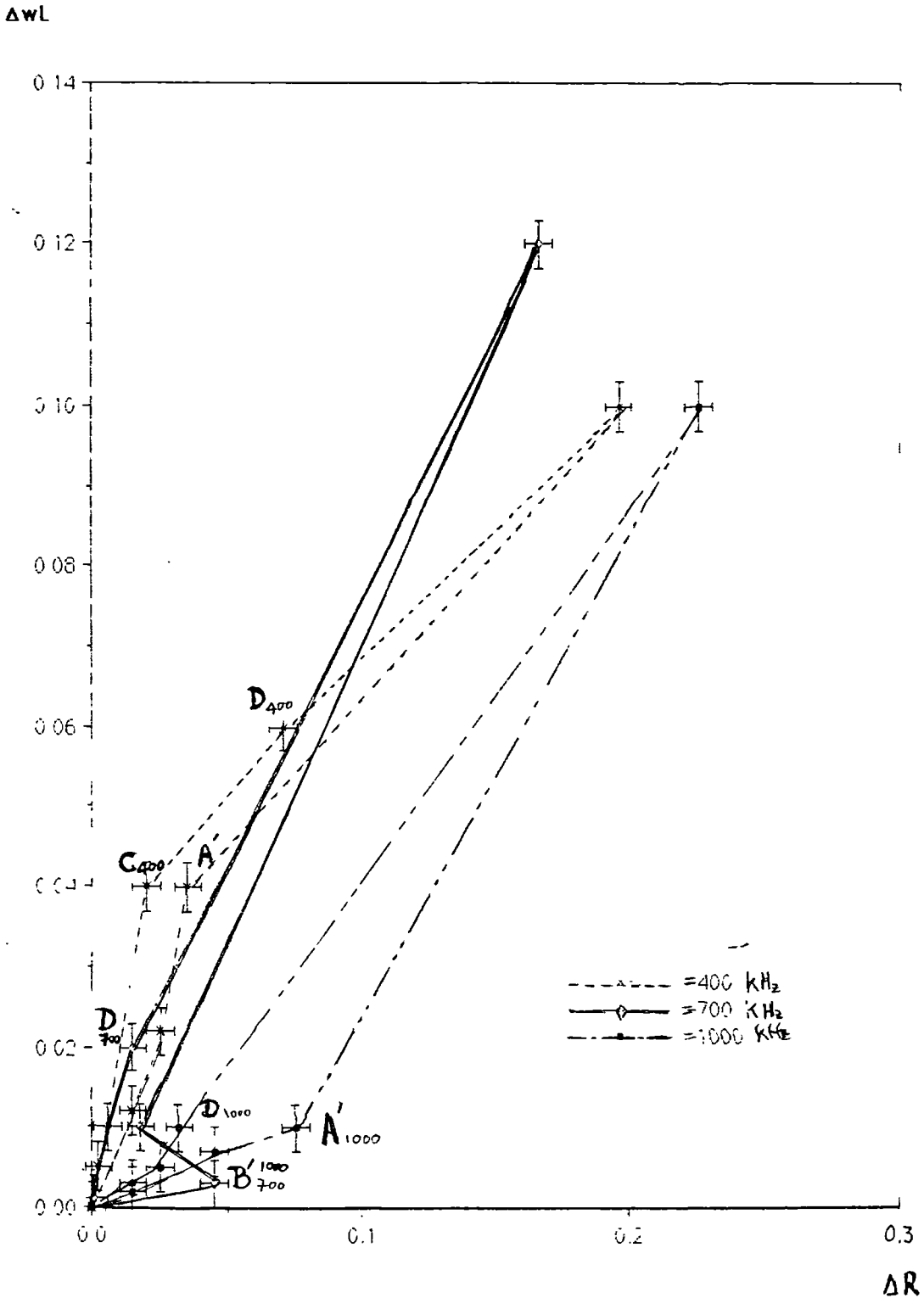

Figure 7.15: Changes in impedance ΔR and ΔωL across the weld and HAZ of the welded 50D plate containing a crack, using probe AS2 with a lift-off of 0.5mm. The points correspond those in Fig.7.12.

block 1 (Section 4.4), and when scanning the saw cuts from 0.5mm to 4mm deep at different values of lift-off and frequency.

Typical responses to variations of lift-off from the defect-free sample are shown in Figs. 7.16 and 7.17, for coils 3S and 3D. For the differential probe, unlike the single coil probe, there was no increase in the amplitude of the normalised impedance $|\Delta Z|/\omega L_0$ with increasing lift-off, for values of lift-off greater than 1.5 times the coil radius, below which any small differences in the dimensions and relative positions of the two coils within the probe became significant and the effects of lift-off were not completely eliminated.

When scanning the saw cuts, the differential probes appeared to be more sensitive to the defects than the single coils (Fig. 7.18), both because a differential probe receives two signals from a crack, one positive and the other negative, as compared with only one signal from a single coil probe, and also because a single coil is influenced to a greater extent by noise, such as from variations in either lift-off or the parameter $\sigma\mu$ of the metal, whereas the responses of the two coils of a differential probe balance each other to give a null output when surface properties are constant. Figs. 7.19 and 7.20 show the variations in the components of impedance of a single and differential probe respectively, from a balance point over a defect-free area, with lift-off and defect depth. For the single coil probe, the changes of impedance due to changes in lift-off can be seen to be much higher than those caused by defects. However, when using differential probes the effects of lift-off are diminished, leaving just the defect signal. Fig.7.21 compares the responses of probes 1D, 2D and 3D to defects of different depths.

For all probes the depths of shallow defects were detected with a greater sensitivity than the depths of deeper defects, because of the eddy current skin effect. Here sensitivity S is defined as the change of impedance per unit change of defect depth, i.e.,

$$S = \Delta Z/\Delta d \quad (m\Omega/mm) \qquad (7.2)$$

Figs. 7.22 and 7.23 show the sensitivity S of probes 2S and 2D with lift-off for different depths of defect. The maximum value of lift-off at which defects could be identified and depths estimated was up to 9mm with probe 3S, whereas probe 3D was capable of sizing defects at values of lift-off up to 12mm. Beyond these values defects could still be identified, but a depth could not be estimated with any certainty. It should be noted that for effective sizing of defects with a differential probe, the degree of lift-off has to be known, because the magnitude of any impedance change caused by a defect depends on lift-off. A method of monitoring the lift-off from uneven surfaces is to use either an extra single coil built into the differential probe, or one of the existing coils of the probe, at a lower frequency more sensitive to lift-off changes, whilst detecting the defects with the differential probe at a higher frequency.

Probes 2S and 2D were used to scan the heat affected zone (HAZ) of a 50D steel plate containing a crack (Fig. 7.12), at frequencies between 100 kHz and 1MHz and values of lift-off from 0.1 to 4.0 mm. The differential probe was capable of measuring the defect with negligible influence from the changing material properties of the HAZ.

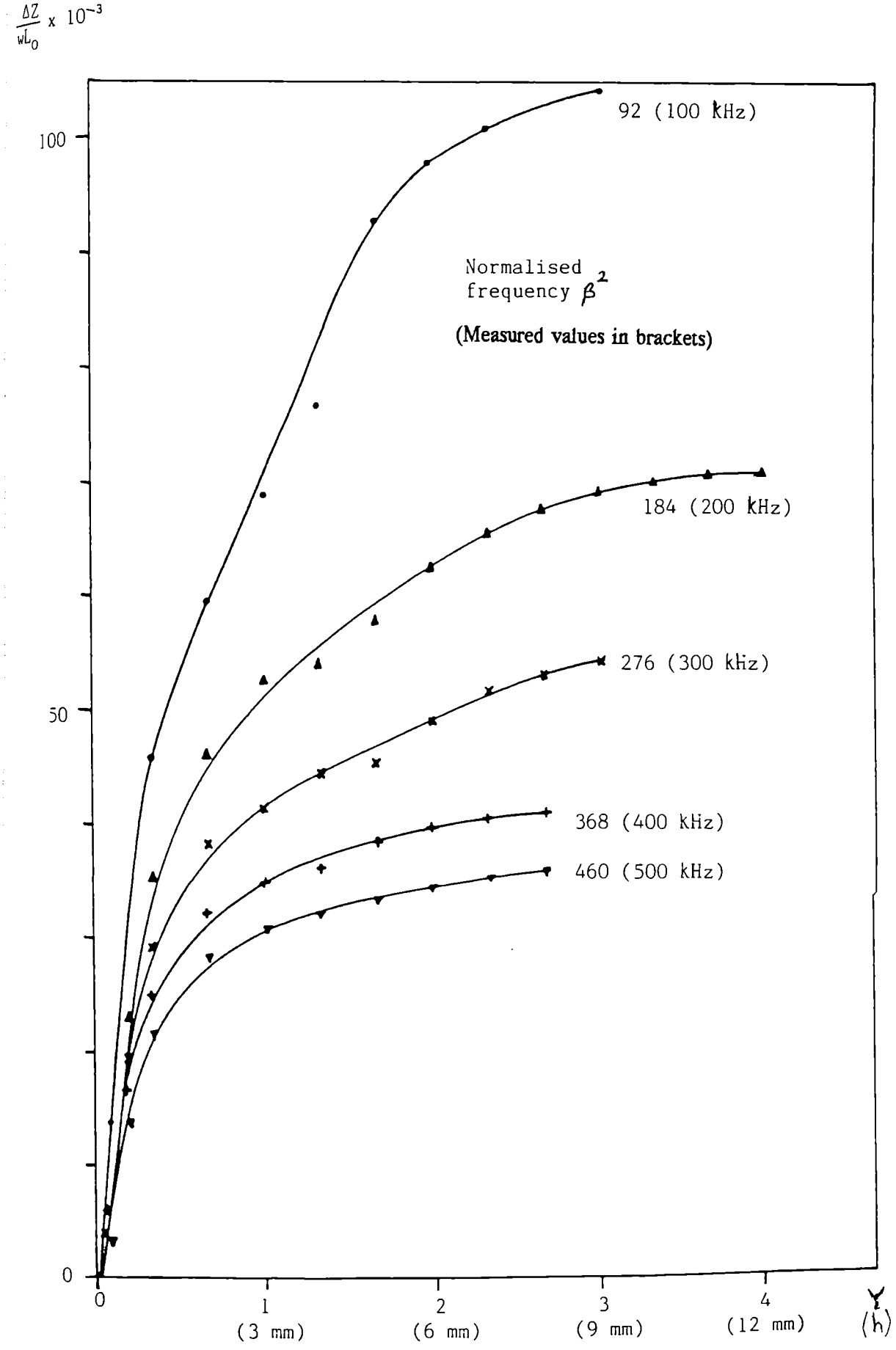

Figure 7.16: Magnitude of the normalised impedance of probe 3S with normalised lift-off Y, for different values of normalised frequency.

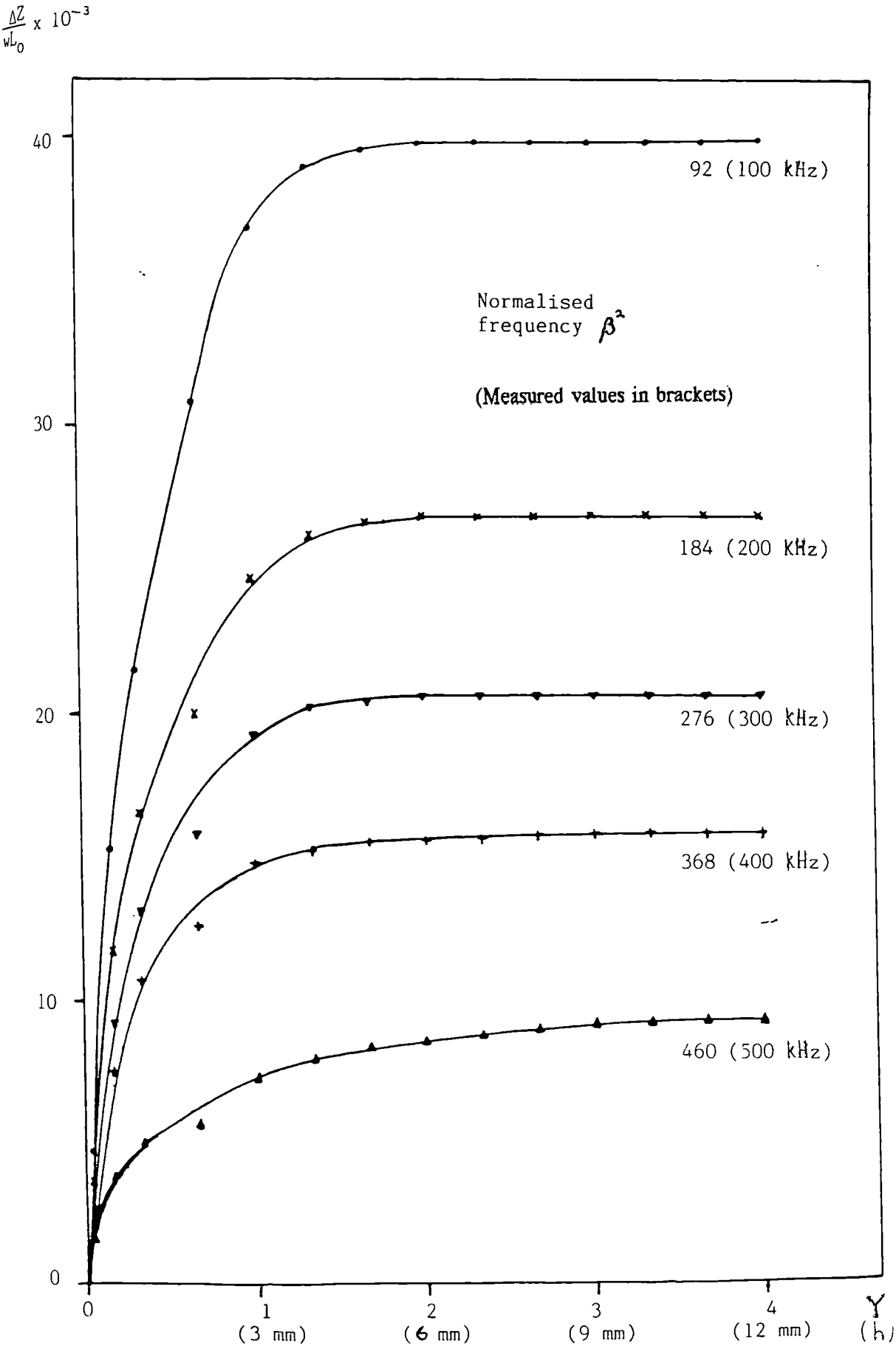

Figure 7.17: Variations of the normalised impedance of probe 3D with normalised lift-off Y, for different values of normalised frequency.

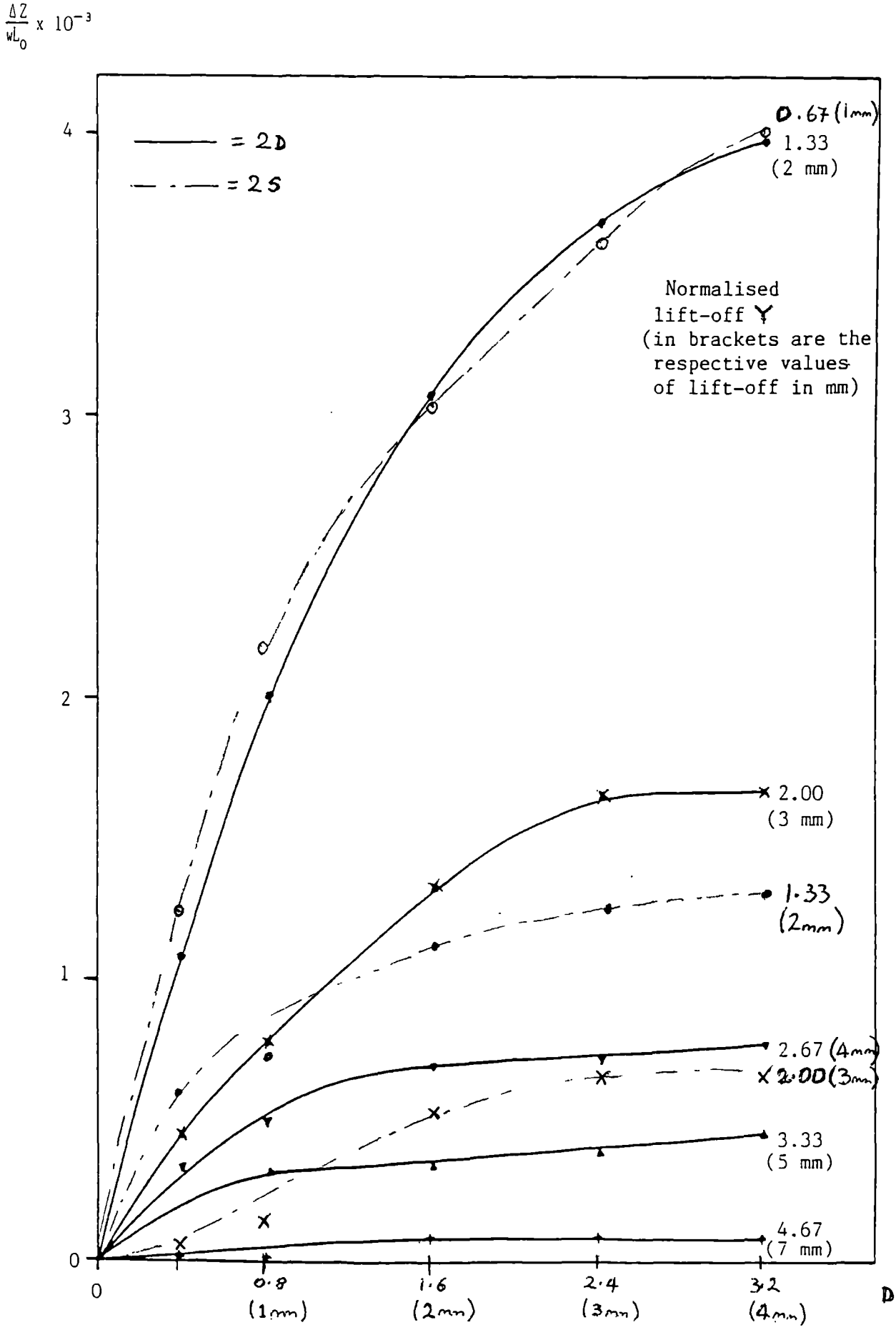

Figure 7.18: Variations of the normalised impedance of probes 2D and 2S with depth of defect D, and normalised lift-off Y. (f = 400 kHz).

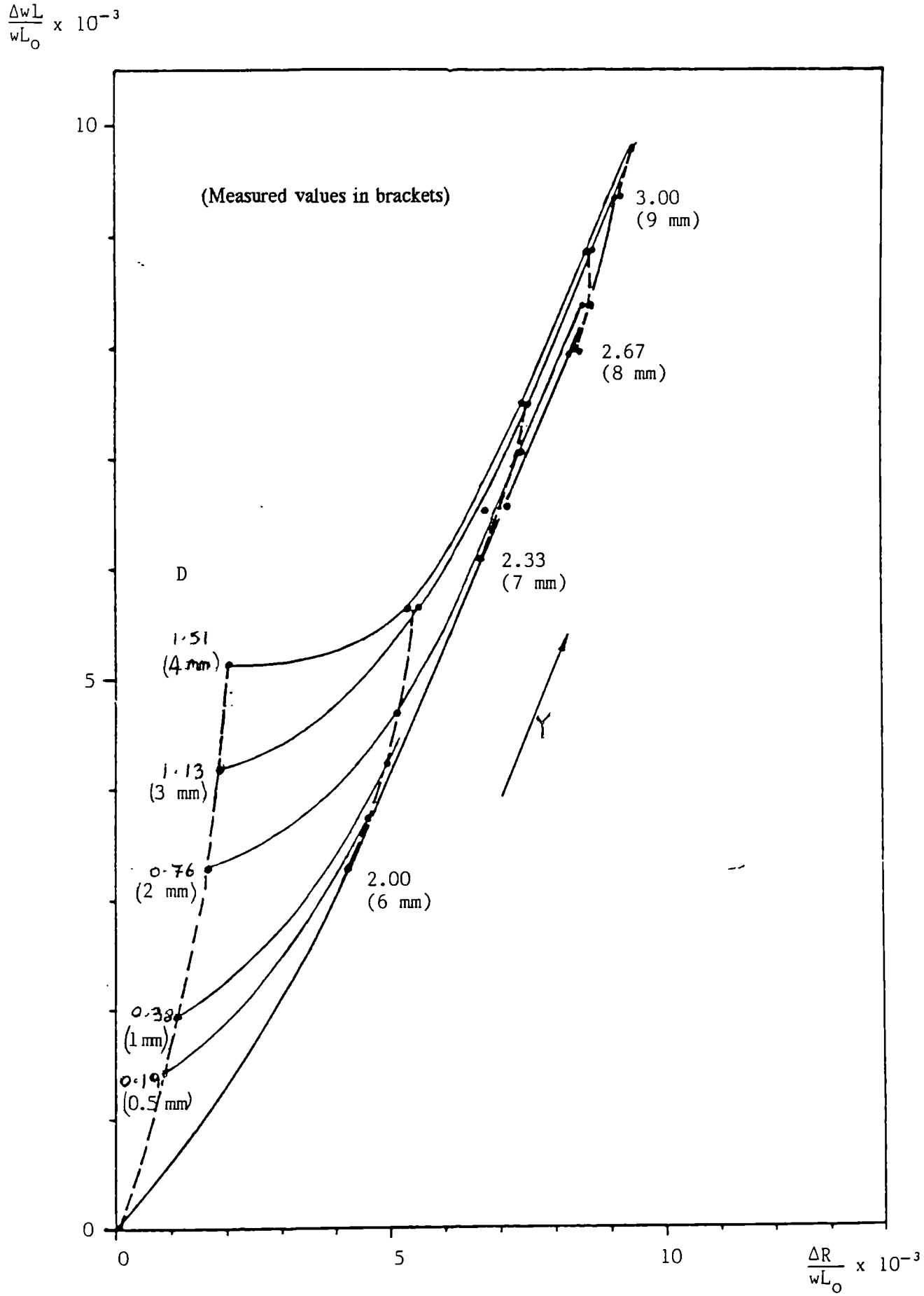

Figure 7.19: Normalised impedance components of probe 3S for different values of normalised lift-off Y, and defect depth D. (f = 200kHz).

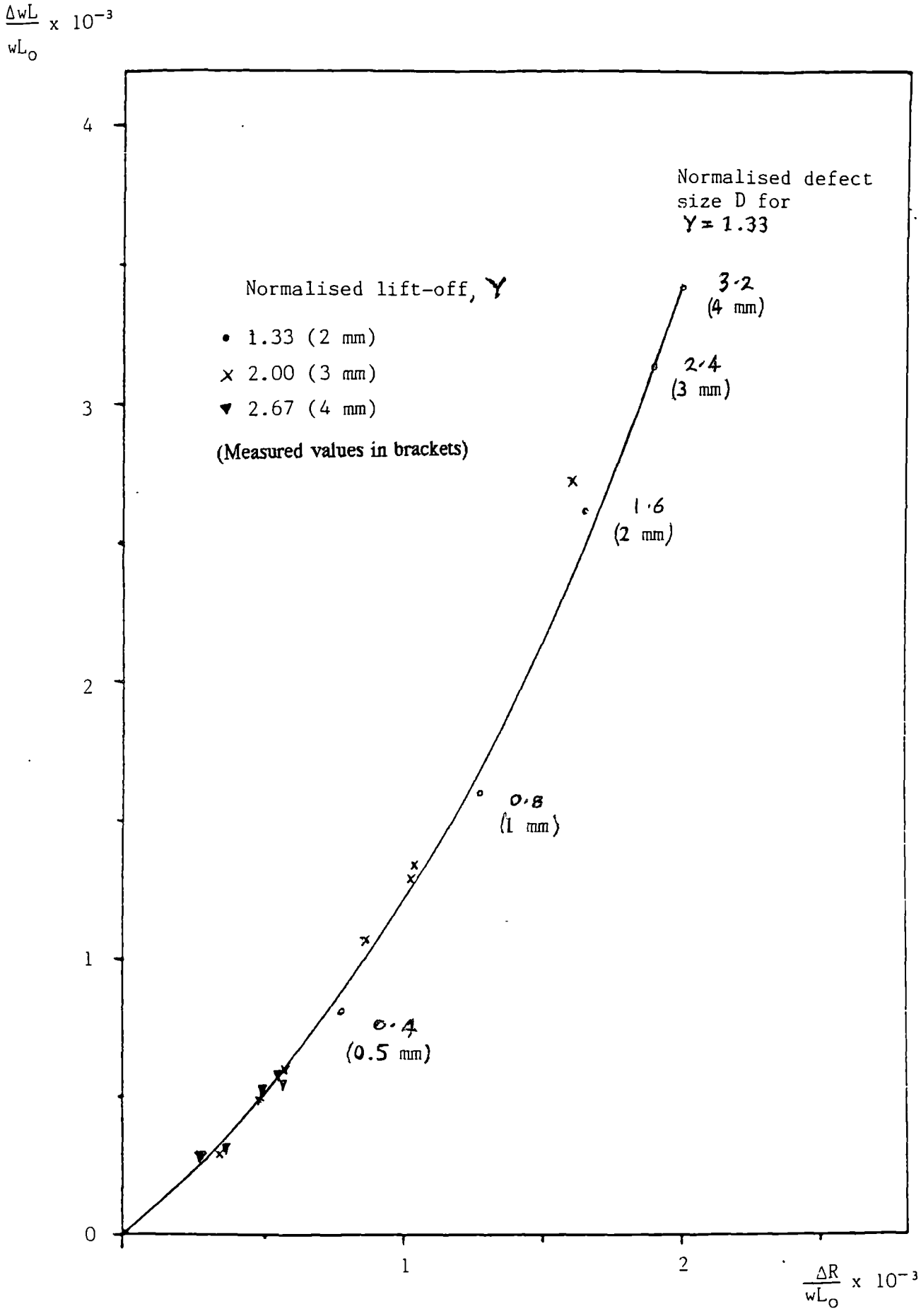

Figure 7.20: Normalised impedance components of probe 2D for different values of lift-off Y and defect depth D. (f = 400kHz).

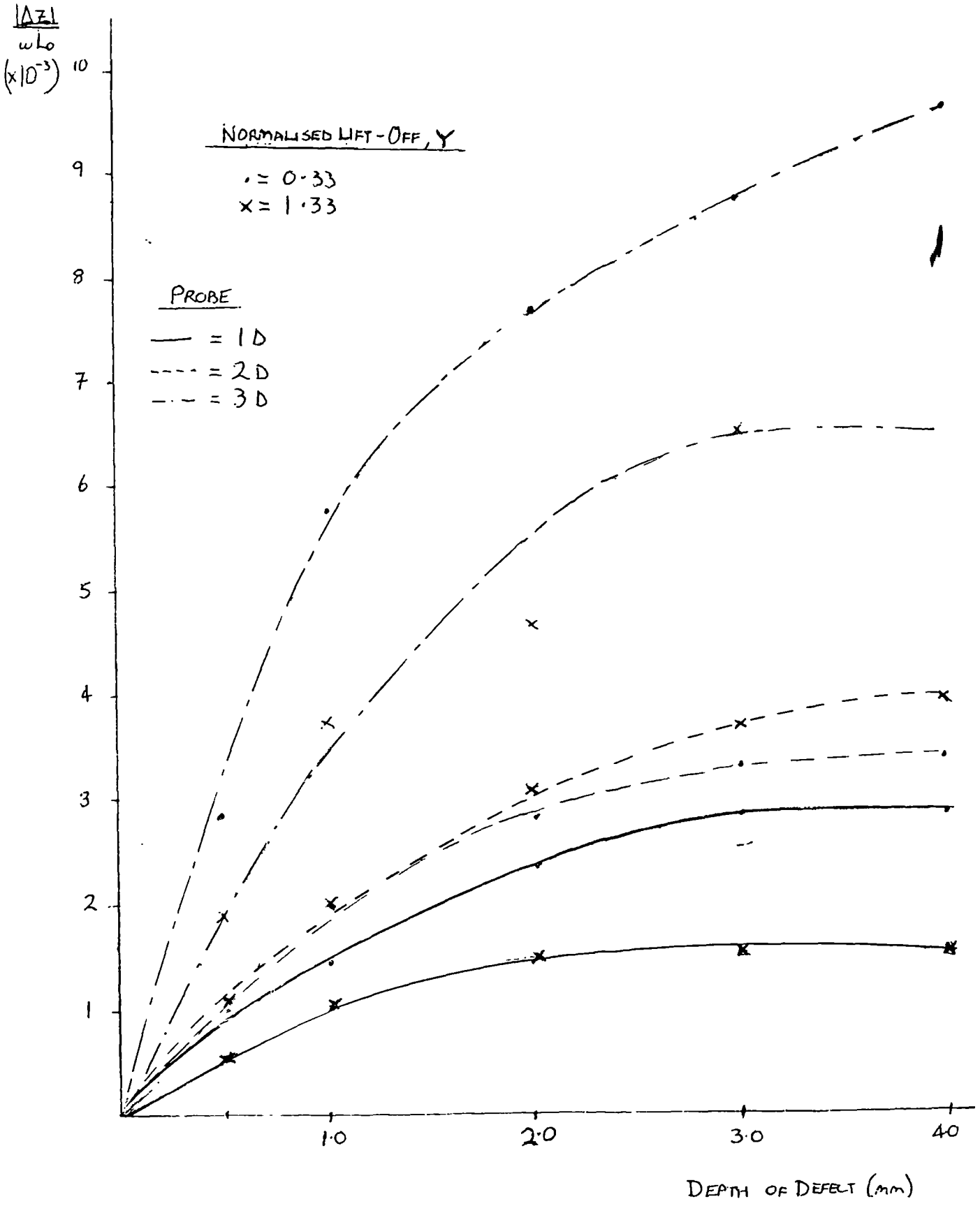

Figure 7.21: Comparison of the normalised impedance with depth of defect for probes 1D to 3D. f = 400 kHz, Y = 0.33 and 1.33

S (mΩ/mm)

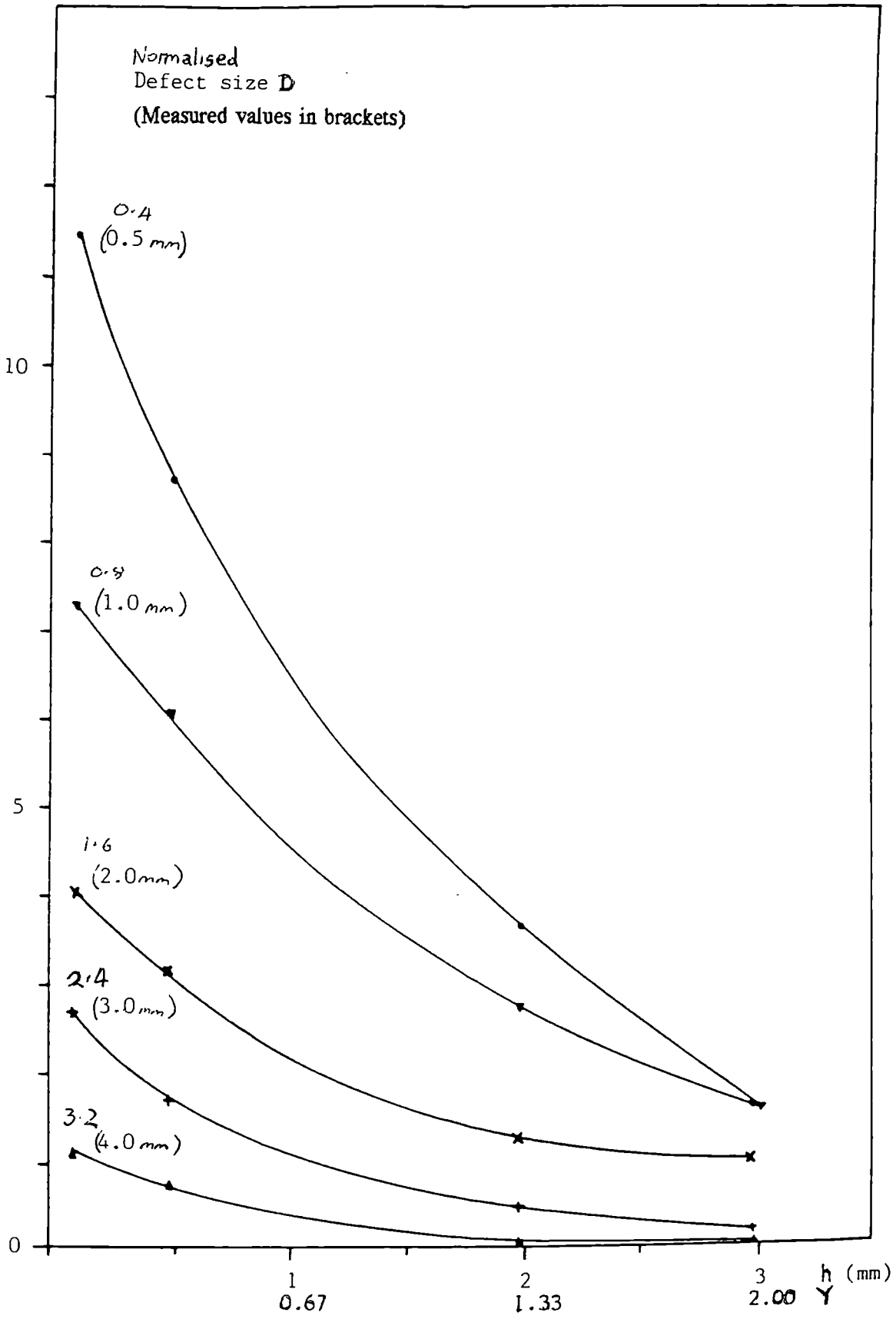

Figure 7.22: Variation of defect sizing sensitivity S with lift-off of probe 2S, for different depths of defect D. (f = 400 kHz).

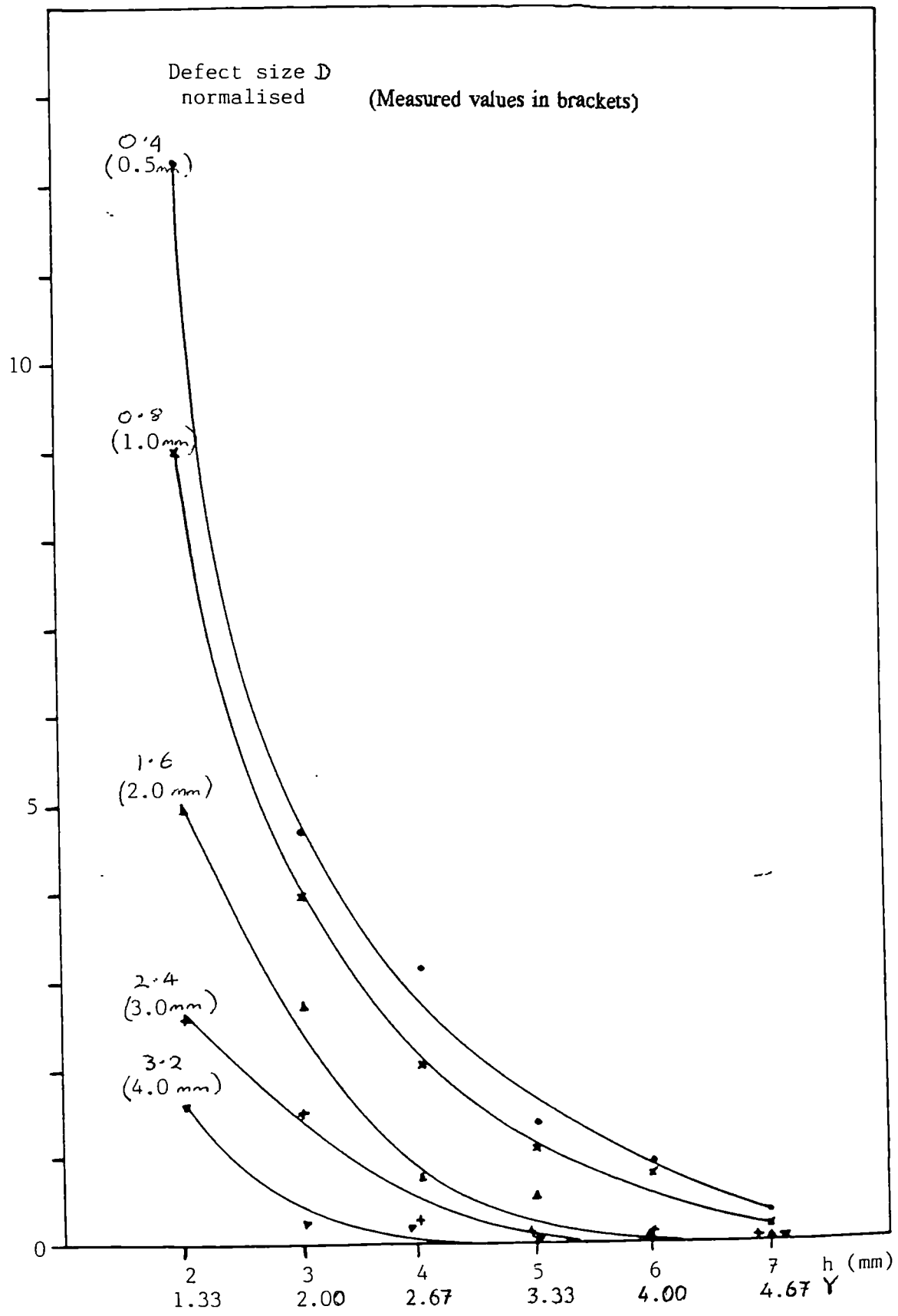

Figure 7.23: Variation of defect sizing sensitivity S with lift-off of probe 2S, for different depths of defect D. (f = 400 kHz).

7.5 Cracks Inclined to the Normal

The effect of crack inclination on the impedance of a coil was studied briefly, using single coils AS2 and FS1, and transformer coil 1T. A block of BS970 mild steel 240mm x 38mm x 25mm was machined with 5 slots each 1.5mm deep at angles between 30° and 90° to the sample surface. The depth of the slots was restricted by the ability to machine the fine saw cuts at the required angles. The probe was positioned perpendicular to the surface at a lift-off of 0.1mm, using the scanning rig (Section 4.2). Each defect was scanned slowly, while recording the output with an x-y plotter, at frequencies between 10kHz and 200kHz for probe 1T and 100kHz to 1MHz for probes AS2 and FS1. When testing a non-ferromagnetic material, the angle of a crack can be related to the area of the loop formed by the defect signal whilst scanning across the crack (Fig. 7.24) [39,40]. When testing the ferromagnetic sample, no measurable differences in the defect signal were found for the defect depth selected. Further work is needed to qualify the effect of crack inclination on the sizing of a defect in ferromagnetic metals with eddy currents, varying both the natural crack depth (Fig. 7.25(a)) and the depth below the surface of the crack tip (Fig. 7.25(b)).

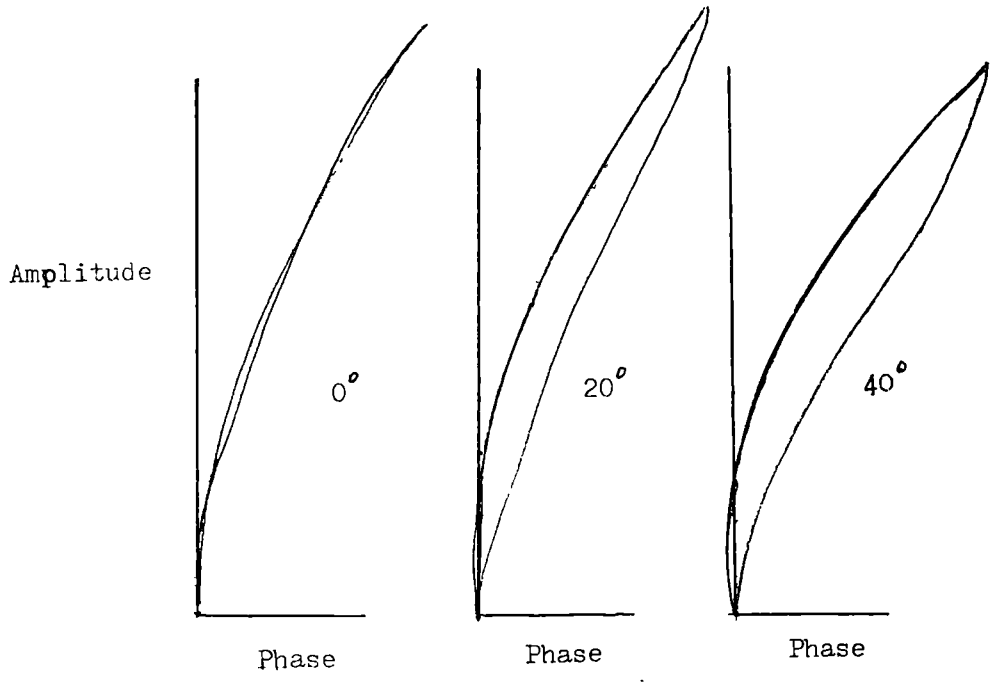

Figure 7.24: Amplitude-phase diagrams for a probe scanning the surface of aluminium, with defects orientated at 0, 20 and 40 degrees [40]

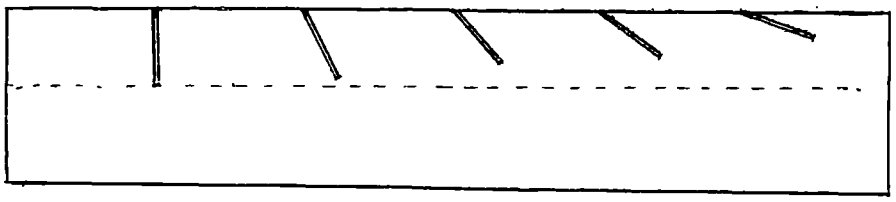

(a)

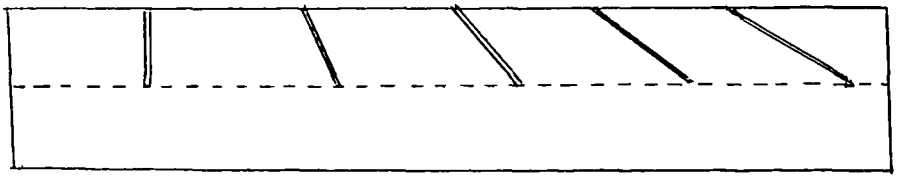

(b)

Figure 7.25: Samples containing oblique cracks of

(a) equal natural defect depth and

(b) equal depth of the crack tip below the surface.

CHAPTER 8

THE LIFT-OFF METHOD OF FLAW DETECTION ("TOUCH" METHOD)

8.1 Introduction

With conventional methods of eddy current testing, variations in coil impedance with lift-off may cause difficulties in the detection of flaws in metals having rough or uneven surfaces, such as weld caps, or areas covered with deposits, i.e, marine growth and chemically formed products. The use of differential probes may alleviate these difficulties, provided that the degree of lift-off is the same for each coil of the probe (Section 7.4). However, the sizing of flaws may still remain a problem because a knowledge of the degree of lift-off is needed for reliable predictions. In this chapter the lift-off method, or "touch" method [28] of eddy current testing is described. This method was developed by the author to overcome problems in detecting and measuring defects in ferromagnetic metal objects having uneven surfaces. Previously this method has been used only with flaw-free samples to sort metals and establish their relative material properties. Here it is shown that defects may be characterised by the change in phase of impedance resulting from variations in lift-off distance from a defective area relative to that from a defect-free area. Fig. 8.1 shows typical variations of the components of impedance of a probe coil with small changes in normalised values of frequency, lift-off and defect depth.

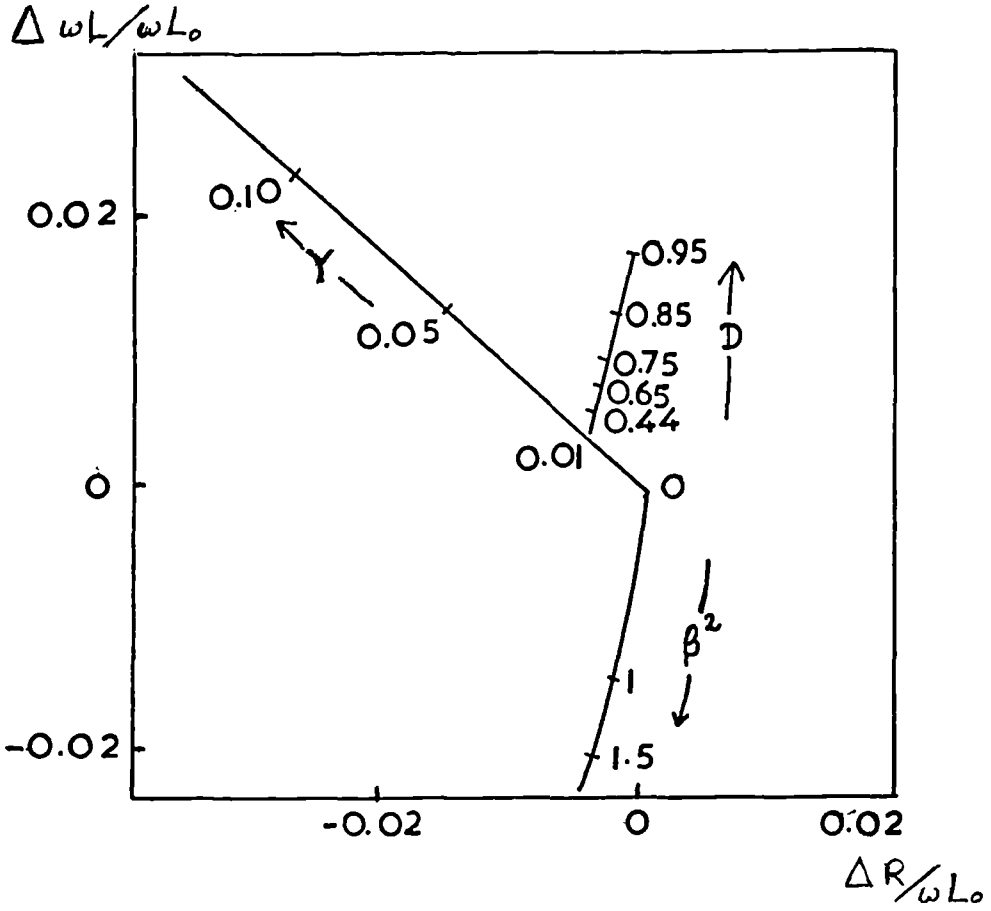

Figure 8.1: Typical variations of impedance of a probe coil with normalised values of frequency β^2, lift-Off Y and defect depth D.

8.2 The Lift-Off Method

With the lift-off, or "touch", method of testing a metal, the lift-off of an eddy current surface-scanning probe is varied repeatedly over a distance from the point at which the probe touches the surface of the sample towards "infinity". When the probe, excited at a frequency $f = \omega/2\pi$, is remote from any metal, the impedance Z_0 is purely reactive, i.e., $Z_0 = j\omega L_0$, where L_0 is the self inductance of the coil in air and $j = (-1)^{1/2}$. As the coil approaches the surface of a metal, the value of impedance changes and becomes a complex quantity, i.e., $Z = R + j\omega L$. The change of impedance ΔZ, where $\Delta Z = Z - Z_0$, is a function of the product $\sigma\mu$ for the sample, which gives rise to a useful method for sorting metals (Fig. 8.2). The presence of a defect also affects the value of the coil impedance presenting a change $\Delta Z + \Delta Z'$. When scanning a ferromagnetic metal with a fixed value of lift-off, the amplitude of the change $\Delta Z'$ of the complex impedance due to the presence of a defect such as a crack varies with the depth of the defect, but there is no significant change in phase. When using the lift-off method, the size of a crack is identified by a change in phase of the lift-off vector, relative to that from a defect-free area, suggesting a change in the product $\sigma\mu$. A maximum change in phase of the lift-off vector may be realised with the selection of a suitable frequency. Fig. 8.3 shows the relationship between the responses of the probe to a defect when using the conventional scanning method and the lift-off method. The method is quick and easy to perform for defect testing of ferromagnetic metals, especially those having uneven surfaces. A simple calibration chart can be produced so as to indicate the extent of a defect, even in the presence of small changes in the material properties within the sample.

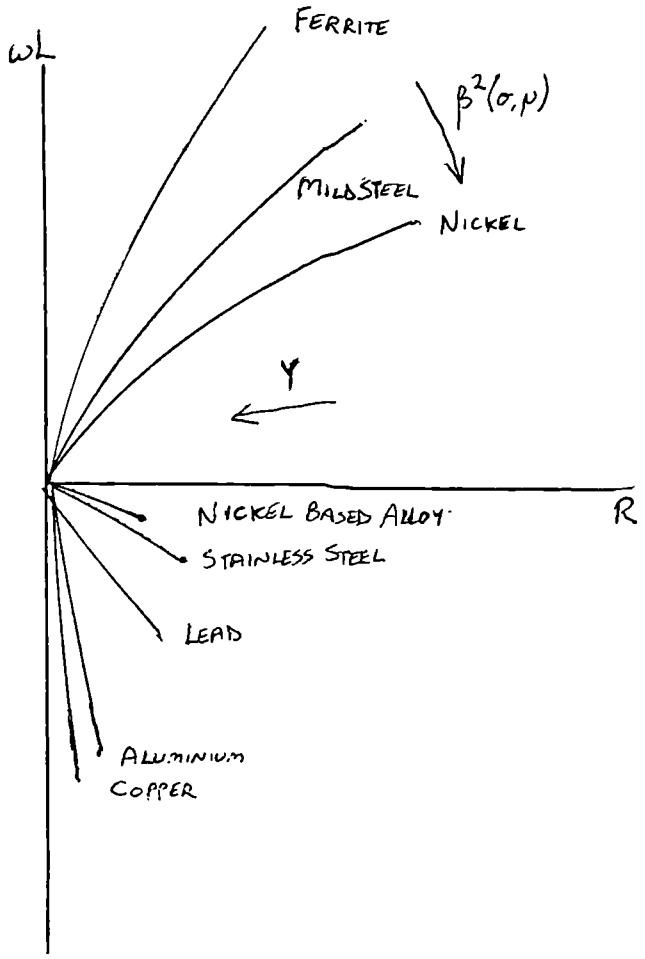

Figure 8.2: Typical changes of impedance with lift-Off from metals with different values of $\sigma\mu$.

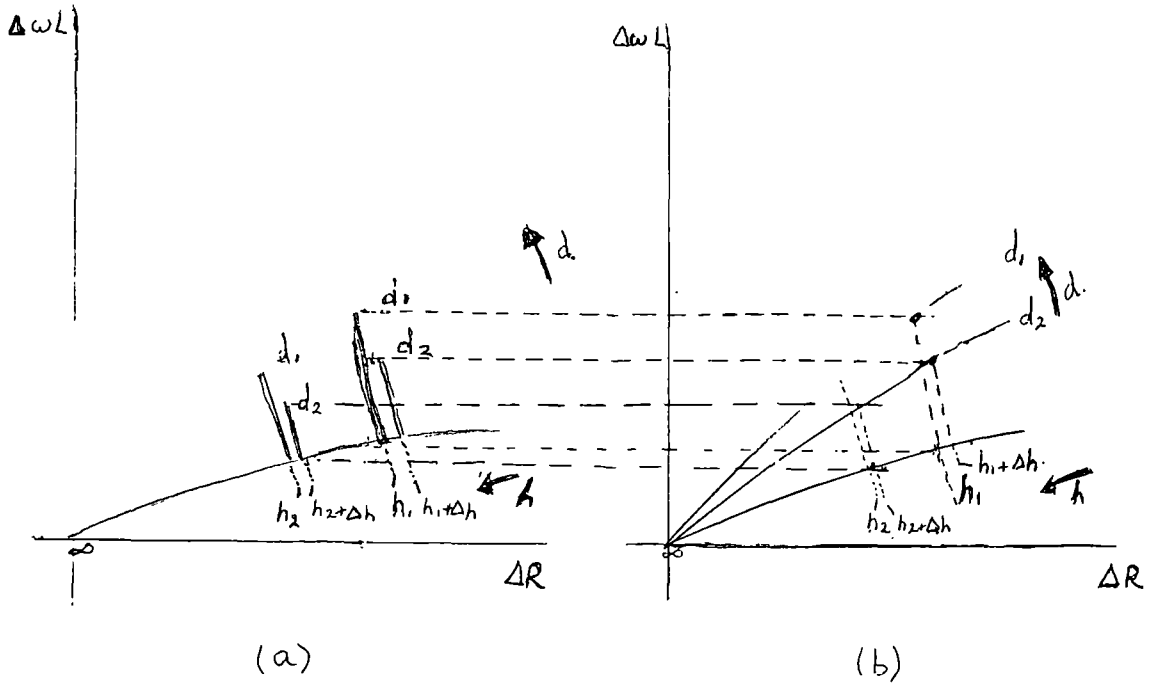

Figure 8.3: Typical voltage responses of a coil to different depths of cracks in steel

(a) using conventional scanning methods

(b) using the lift-off method

The lift-off method does not lend itself to testing non-ferromagnetic metals, since for these metals the defect signal can vary significantly in phase with defect depth, and the phase of the lift-off vector and defect signal are too similar.

8.3 Measurements of Simulated Cracks in Steels

8.3.1 Defects in Mild Steel

Two blocks of EN1A mild steel 240mm x 38mm x 25mm, block 1 and block 2 (Section 4.4), each with saw cuts spaced evenly to simulate a series of cracks, were tested with the Hocking Electronics Vector S900 flaw detector (Section 4.1.2) with air-cored probe AS2 (Table 4.1), at frequencies ranging from 100 kHz to 1MHz. 600kHz was found to be the optimum frequency, i.e, that at which the change in phase of the lift-off vector for any particular depth of saw cut was maximised with reference to that from a defect-free area. Initially the saw cuts were scanned at fixed values of lift-off from 0.1 to 3.0 mm. For each value of lift-off, the flaw detector bridge was balanced with the probe above a defect-free area and the defects were scanned while keeping the lift-off constant. It was noted that only the amplitude of the defect signal varied significantly with defect depth. The instrument was then balanced with the probe remote from any metal, to provide a reproducible reference independent of the condition of the sample surface. The changes in the real (ΔR) and imaginary ($\omega\Delta L$) components of coil impedance were then measured whilst varying the lift-off above both a defect-free area and each saw cut. The output of the instrument was related directly to the changes in impedance of the probe [37] and a family of lift-off curves was produced in the shape of a fan for the different depths of saw cut (Fig. 8.4). The degree of change in phase between the lift-off vectors decreased with increasing depth of saw cut, making large depths difficult to predict, but small depths of crack could be characterised readily.

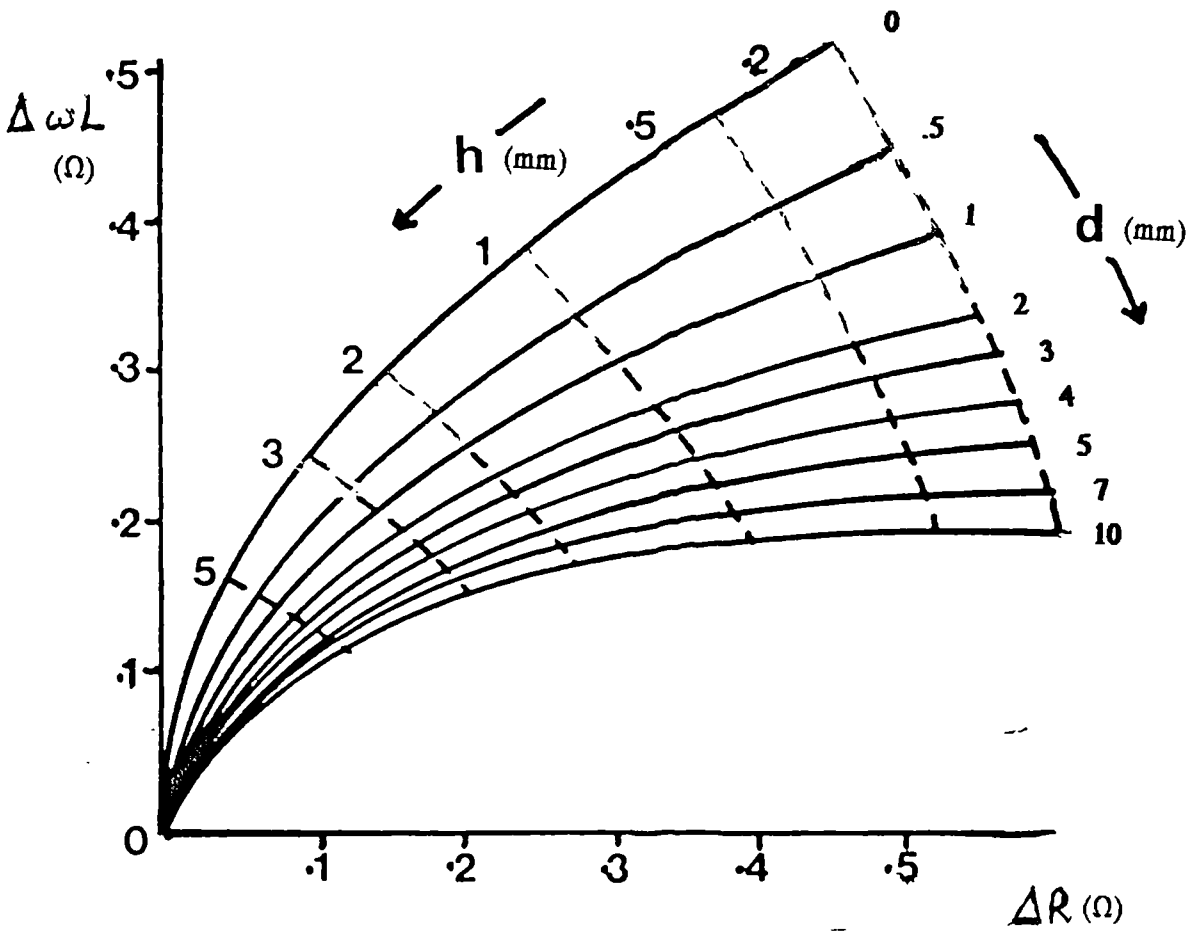

Figure 8.4: Lift-off impedance vectors obtained from a mild steel sample containing saw cuts 0.5mm to 10mm deep, measured with probe AS2 at 600 kHz. $L_0 = 17\mu H$.

The curves were recorded on acetate sheets, to enable direct comparisons to be made for different samples, when used as a graticule located in contact with the screen of the flaw detector. In this way the depths of cracks in real samples could be predicted (Section 8.4).

8.3.2 Effects of Variations in Electrical and Magnetic Properties

A calibration block of DPH24 pipe-steel, of the same dimensions as the mild steel calibration block 1, was prepared with slots cut to depths of between 0.5 and 4.0 mm. The lift-off impedance vectors produced from the defect-free and defective areas of the sample were compared with those from the mild steel sample for each defect depth, using probe AS2 at the optimum frequency of 600kHz. With the "touch" method it was found that the difference in material properties between the two types of steel had the effect of rotating the lift-off impedance vectors for both defect-free and defective areas of one block with respect to those of the other (Fig. 8.5). When scanning the saw cuts at a fixed value of lift-off, the magnitude of the impedance changes due to the presence of the defects did not appear to vary significantly with the difference in the material properties of the two metals. It was also observed that, for a given value of lift-off, the phase of a given defect impedance vector was similar for each metal with respect to the instrument reference axes, although it was different with respect to the lift-off impedance vectors for each metal (Fig. 8.6). On rotating the lift-off impedance vector for a defect-free area of one type of steel, it was found that it could be made to coincide with that from the other type of steel (curve OA, Fig. 8.7). This led to the conclusion that a simple correction could be used to relate a defect indication from one type of steel to that from a defect of the same size in another type of steel. Hence, the size of a defect in one metal could be predicted from a calibration performed using another metal, using the following method:

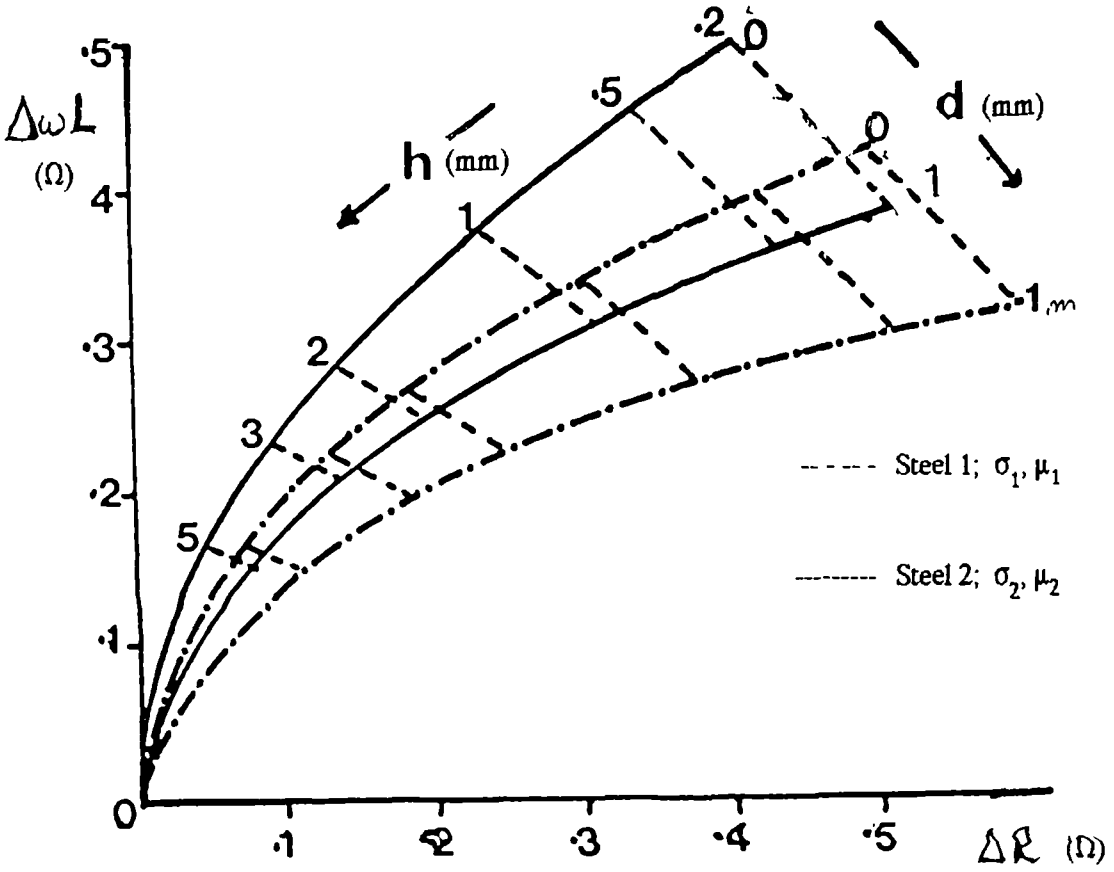

Figure 8.5: Lift-off curves obtained for a defect-free area and a saw cut 1mm deep for both mild steel and DPH24 pipe-steel samples, measured with probe AS2 at 600 kHz. $L_0 = 17\mu H$.

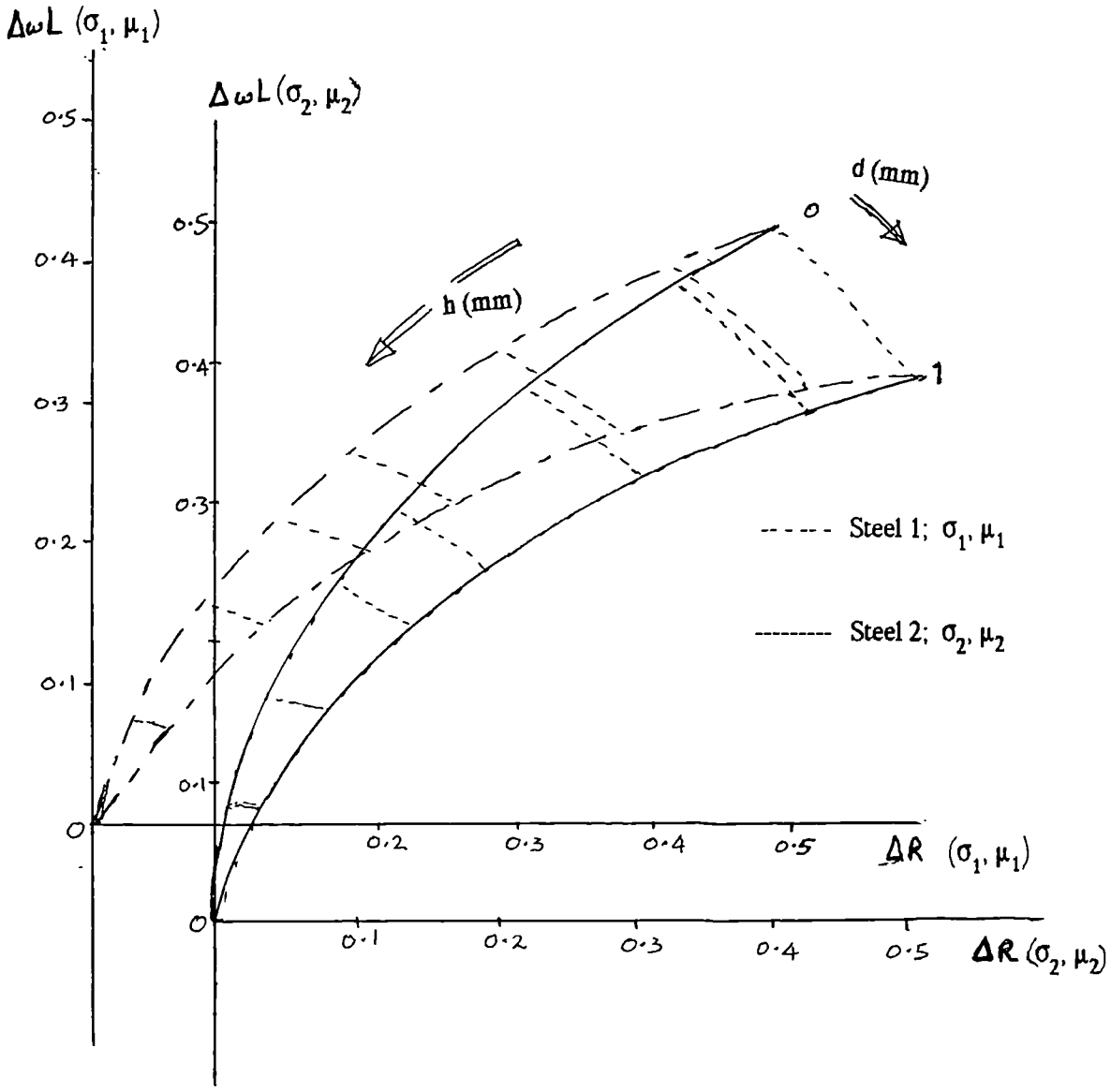

Figure 8.6: Impedance changes caused by a 1mm deep saw cut relative to the lift-off impedance vectors for defect-free areas of both mild steel and DPH24 pipe-steel samples (Fig. 8.5)

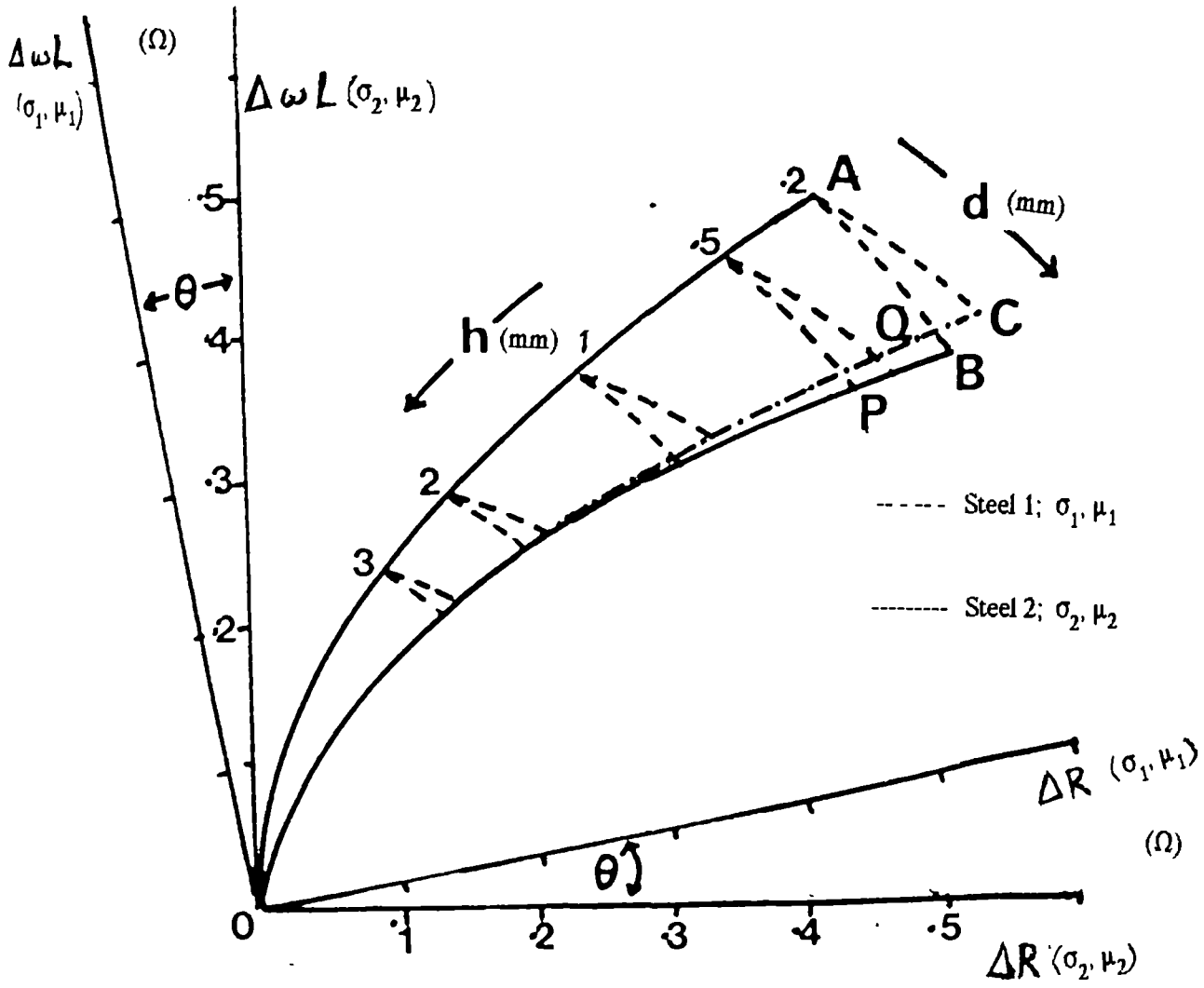

Figure 8.7: Rotation of the axes of the lift-off curves for DPH24 pipe-steel (Fig. 8.5) by an angle Ø, to align the lift-off impedance vectors for defect-free areas of both steels.

(a) Obtain calibration curves by producing the lift-off impedance vectors for a defect-free area and for different known depths of defect in the calibration sample (Fig. 8.4).

(b) Obtain a lift-off impedance curve for a defect-free area of the new material, for which there is no calibration sample available.

(c) Rotate the "defect-free" lift-off vector of the new material to coincide with that of the calibration sample, noting the angle of rotation, Ø.

(d) Use Ø to correct the calibration curves for different depths of defect in the new material (Fig. 8.7). For example, a defect of a given depth in material 2 would produce an impedance vector AC (Fig. 8.7), of the same magnitude but at an angle Ø to an impedance vector AB from the same depth of defect in material 1, if measured at the same value of lift-off.

Two blocks of pipe-steel types EN3B and EN6A, with dimensions 40mm x 20mm x 12mm, both containing slots 0.1mm wide and 1mm deep cut along the centre of the longest side, were tested using the lift-off method, and the results were compared with those from 1mm slots in mild steel and DPH24 pipe-steel to confirm the assumptions made above. Values of relative magnetic permeability were estimated for the four different types of steel (Table 8.1) from their characteristic B-H curves (Figs. 8.8 (a) to (d)), plotted using an automatic permeameter [32]. The values of electrical conductivity of the four samples did not vary by more than 10% and, for simplicity, the value was assumed to be constant. As expected, the phase of the "defect-free" lift-off vectors varied with respect to one another. However, after making the above-mentioned corrections, the phases of the lift-off impedance vectors for the 1mm defects did not vary significantly with respect to the "defect-free" vectors. It was not known at the time of the investigations as to what degree the above assumptions would hold for two metals whose material properties differed considerably from one another and further investigation is necessary.

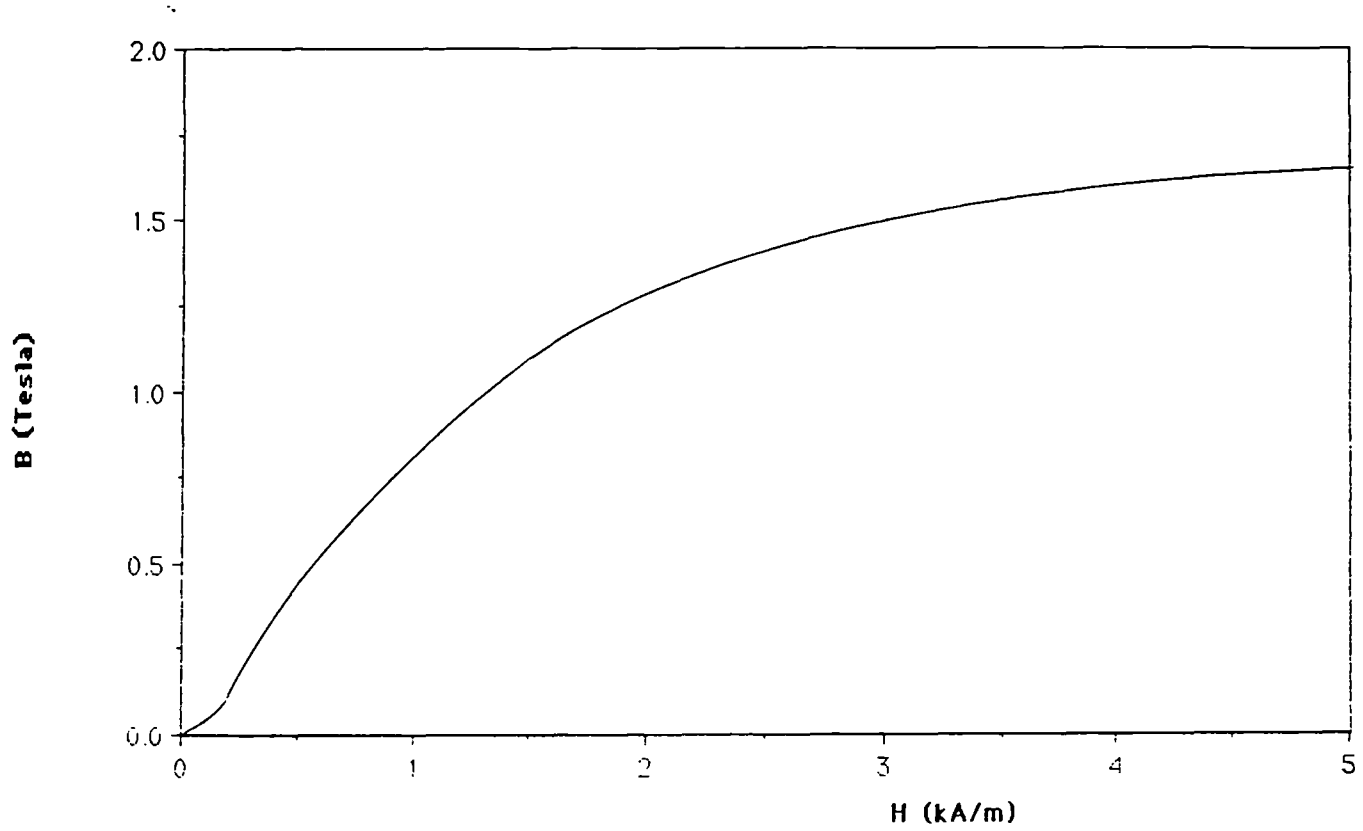

Figure 8.8(a): Characteristic B-H curve of mild steel EN1A

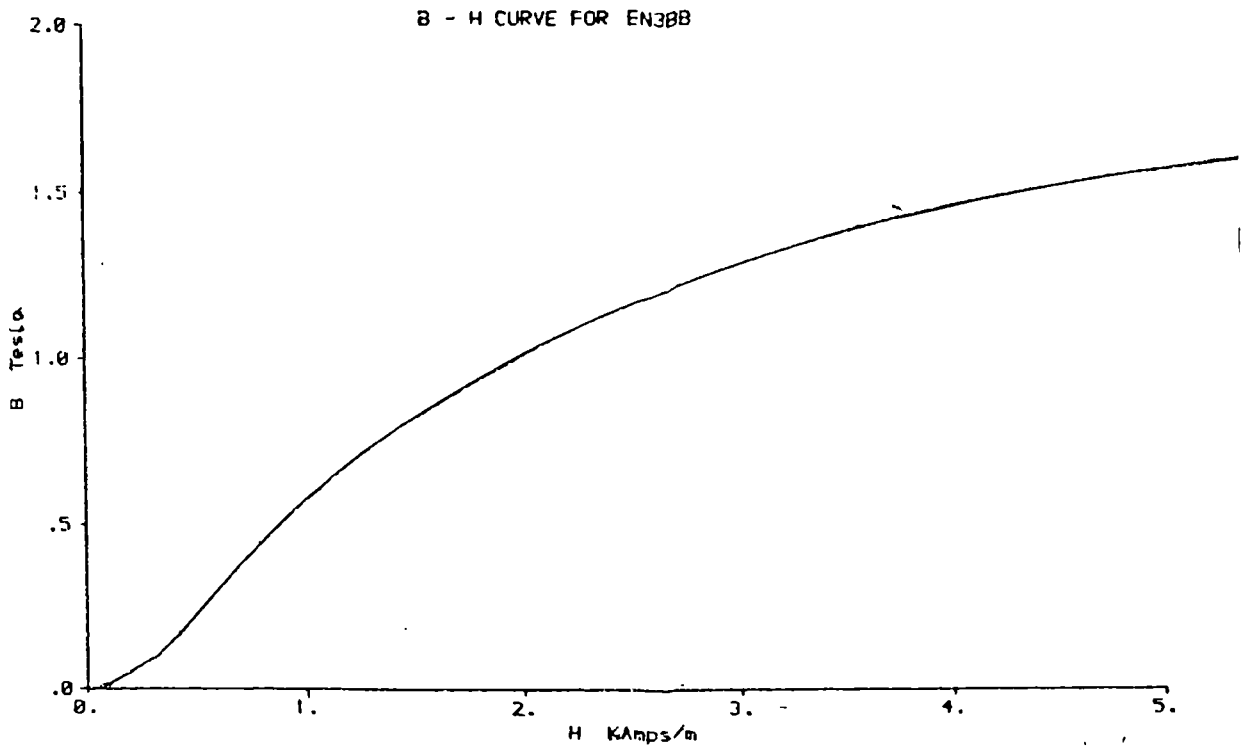

Figure 8.8(b): Characteristic B-H curve of pipe-steel EN3B

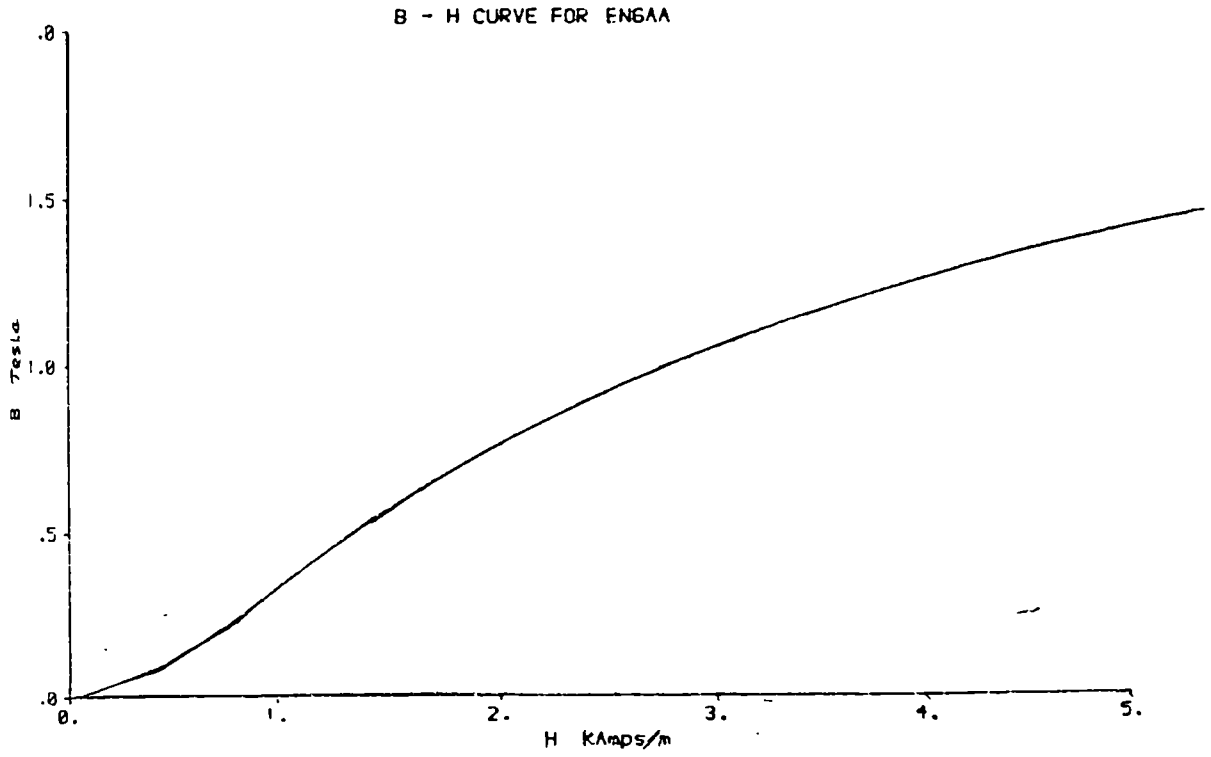

Figure 8.8(c): Characteristic B-H curve of pipe-steel EN6A

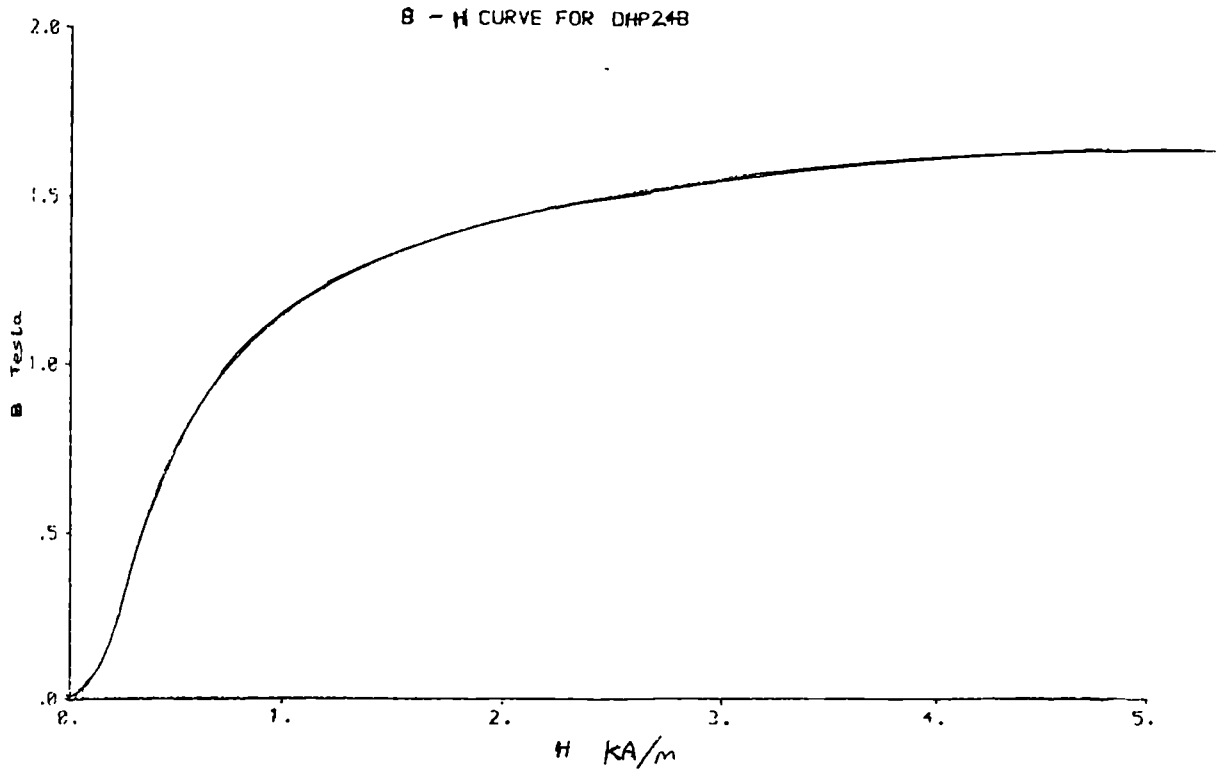

Figure 8.8(d): Characteristic B-H curve of pipe-steel DPH24

Table 8.1: Approximate Values of Relative Magnetic Permeability μ_r Estimated from the Characteristic B-H Curves of the Metals.

Steel Type	μ_r	
	initial	maximum
EN1A	80	540
EN3B	110	620
EN6A	90	410
DPH24	250	1790

8.4 Evaluation Of Real Defects Of Unknown Depth In Samples Of Differing Material Properties

A mild steel plate was prepared by University College London, having dimensions 175mm x 82mm x 11mm, containing a region of changing material properties typical of that found in the heat affected zone (HAZ) of a weld (Fig. 4.14, Secton 4.4). The HAZ was simulated by laying a bead of weld across the centre of the plate. A fatigue crack was grown in the root of the weld, and then the weld was ground off to leave a flat plate containing a fatigue crack about 40mm long. The HAZ was scanned with the 17μH coil AS2 at intervals of 5mm across the plate, using a frequency of 500kHz. A scanning rig (Section 4.2) was used to allow precise positioning of the coil, and the mild steel blocks 1 and 2 were used for calibration. The plate was scanned with constant values of lift-off between 0.1mm to 5.0mm, to obtain a profile of the crack (Fig. 8.9). The "touch" method was then applied over the same area. The crack depths estimated with both methods were found to be similar, with a maximum depth of 5.2mm. As expected, the HAZ produced a small rotation of the lift-off impedance vector. An alternative electromagnetic method of non-destructive testing of ACPD [41] was then applied to confirm the estimations of crack depth. Some uncertainties were introduced to the results obtained by the ACPD, because the method assumed that the field applied across the plate was constant, but the small length of the plate caused the applied feild to distort, especially at the edges of the plate. Table 8.2 compares the crack depths estimated by the eddy current and ACPD methods. The eddy current method gave a much better indication of the crack position, as confirmed using magnetic particle inspection. ACPD measurements obtained from near the centre of the plate agreed to between 3% and 15% of those obtained with the eddy current methods.

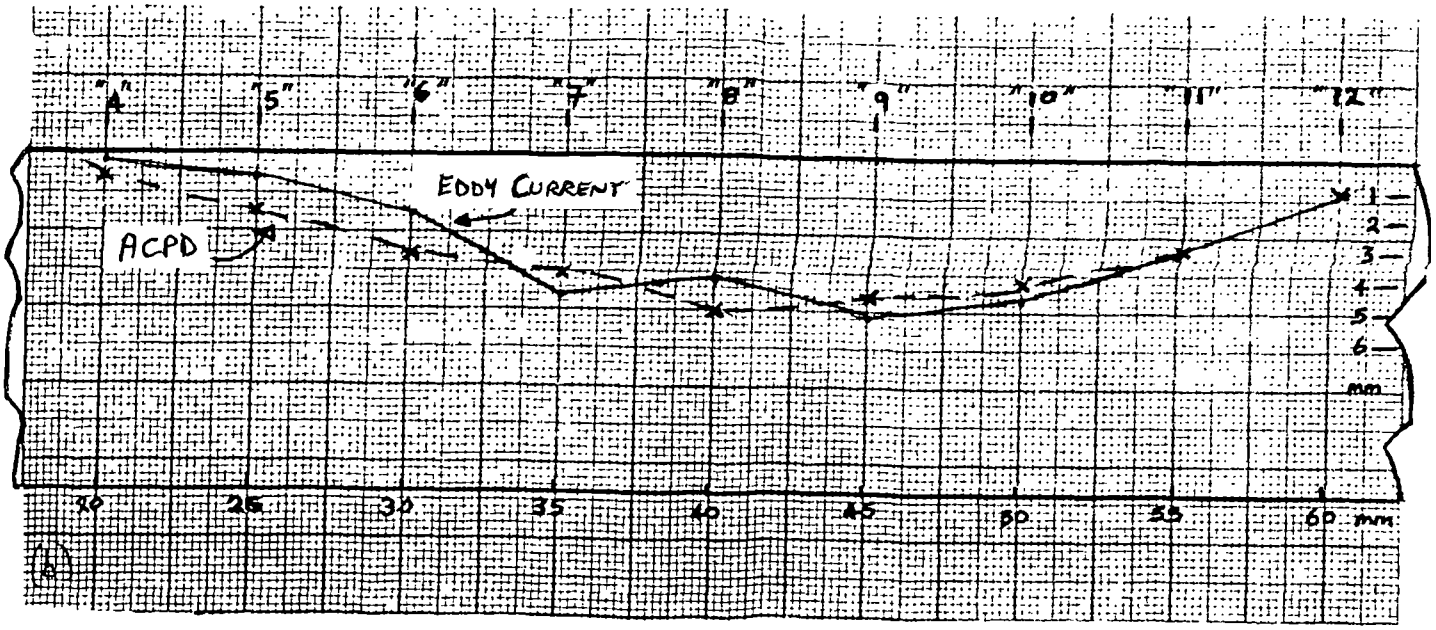

Figure 8.9: Depth profile of a fatigue crack in a 50D plate with HAZ, predicted using eddy current and ACPD methods.

Table 8.2: Estimates of Crack Depth in a 50D Steel Welded Block

h = value of lift-off of the probe from the sample surface

Position	Eddy Current Results			ACPD Results
from edge	depth	error		depth
		h = 1mm	h = 5mm	
(mm)	(mm)	(mm)	(mm)	(mm)
20	0.2	±0.0(5)	±0.0(5)	0.7 ± 0.3
25	0.7	±0.0(5)	±0.1	1.8 ± 0.3
30	1.8	±0.1	±0.3	3.2 ± 0.3
35	4.5	±0.5	±0.6	3.8 ± 0.3
40	4.0	±0.3	±0.5	5.0 ± 0.3
45	5.2	±0.5	±0.8	4.6 ± 0.3
50	4.5	±0.5	±0.6	4.0 ± 0.3
55	3.0	±0.2	±0.3	2.9 ± 0.3
60	1.0	±0.0(5)	±0.0(5)	1.0 ± 0.3

Two welded plates of mild steel containing lack of root fusion were prepared by D. Walsh at Brunel University, as part of a parallel investigation. Measurements were made at 600 kHz with the "touch" method, using the 17μH probe AS2, calibrated with mild steel calibration block 1. The samples were subsequently broken open to confirm the estimated defect depths (Table 8.3).

Table 8.3: Lack of Root Fusion in Mild Steel Welded Plates

Plate	Estimation of Defect Depth (mm)	
	Eddy Current	Visual
3	1.20 ± 0.1(5)	1.00 ± 0.10
4	1.65 ± 0.1(5)	1.40 ± 0.05

The lift-off method was used with probe 2S, to predict the depths of cracks of between 3mm and 6.5mm in 10 bars of pipe-steel of different types, having dimensions 15mm x 33mm x 220mm (Fig. 8.10). The degree of rotation of the lift-off impedance vector for a defect-free region, with respect to that from the mild steel calibration block, varied for samples of the same type of steel. The bars were found to be magnetised by different degrees, and the crack in each sample was evaluated with the "touch" method before and after demagnetisation of the bars. The degree of magnetisation was assessed from the deflection produced on a ballistic galvanometer, when the sample was passed through a coil consisting of 1100 turns of fine wire. Confirmation of the estimated crack depths was made by OLIC, British Gas Corporation, by breaking some samples along the crack and measuring the extent of the crack directly.

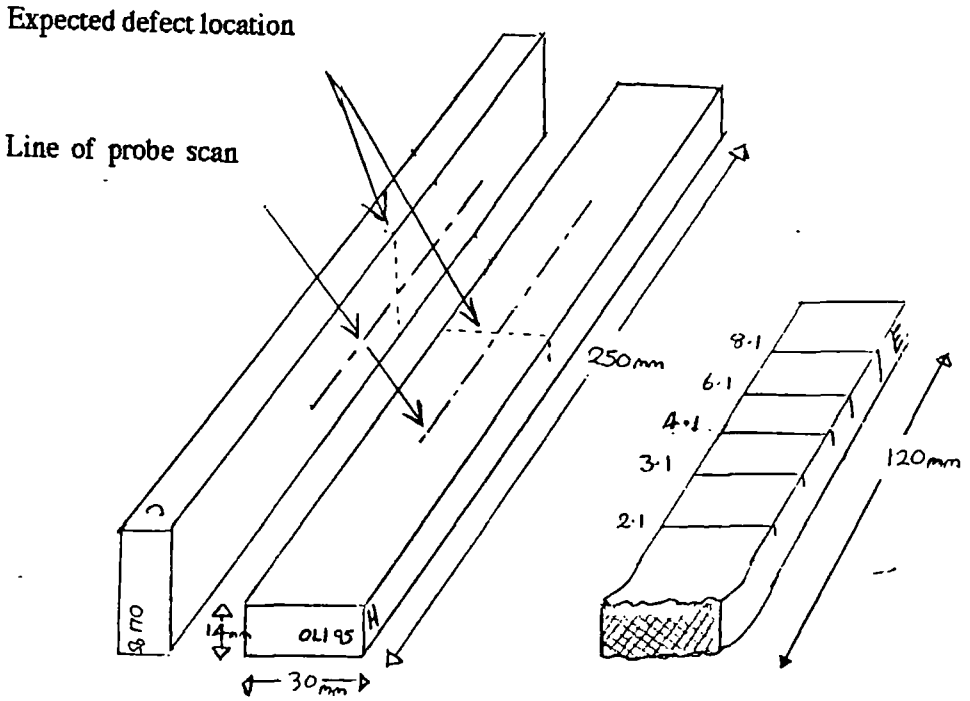

Figure 8.10: Bars of pipe-steel containing fatigue cracks of unknown depths.

The depths of the cracks in the 10 demagnetised bars were estimated both before and after making a correction to the calibration in the manner described in Section 8.3.2. Four of the samples were broken open for confirmation. Table 8.4 shows the eddy current estimates for these four bars before and after correction.

Table 8.4: Crack Depth Measurements in Pipe-Steel Bars.

Eddy current estimation of crack depth: 1 = uncorrected estimation

2 = corrected estimation

Sample	Eddy current estimate			Direct	Galvanometer
	crack depth (mm)		error	measurement	deflection
	1	2	(mm)	(mm)	≈ μ B (divs)
A	0.6	0.8	± 0.2	0.8 ± 0.1	10.5
C	2.2	3.1	± 0.5	3.3 ± 0.2	14.0
D	3.5	6.0	± 0.5	6.0 ± 1.0	12.0
E	2.3	3.7	± 0.5	3.8 ± 0.1	7.5

The ability of the eddy current methods to predict the size of defects away from ideal laboratory conditions were assessed at the on-site locations listed below. Samples containing defects were produced industrially by E.R.S., British Gas corporation, Killingworth, Newcastle-Upon-Tyne, the Welding Institute, Abingdon, Cambridgeshire, and the Marine Technology Directorate at City University, London. The depths of defects obtained were compared with estimates made with alternative NDT methods, for example MPI (magnetic particle inspection) and ACPD, or from direct measurement after breaking open the samples.

(a) British Gas Corporation, ERS, Killingworth

Eight different samples of welded 50D and pipe-steel, from either pipes or marine installations, were examined using conventional eddy current scanning methods with both single coil probes and differential probes. Both stress cracks in plain sections and fatigue cracks in welds were located successfully and their positions confirmed with MPI. The problems of excessive wear and interference from lift-off effects were overcome by using the "touch" method to confirm the positions of cracks and to estimate their depths when compared with slots in the mild steel calibration block 1. Air-cored single coil probes having low inductances and operated at frequencies between 500 and 800 kHz were found to be most effective for sizing defects with the "touch" method. The relatively large diameters of the probes available prohibited resolution of individual stress cracks when in a close-set group. One pipe-steel sample (LS2), a section of pipe approximately 3 feet in diameter containing stress cracking, was broken open by OLIC, British Gas Corporation, for confirmation of the depth measurements. The sample was assumed to contain a single crack, the profile of which was measured at intervals of 5mm along its length. The differences in electrical and magnetic properties between the pipe-steel sample and the mild steel calibration block were small and were assumed to have no effect on the estimations of depth (Fig. 8.11). On breaking the sample open it was found that the crack was inclined to the normal, in the manner shown in Fig. 8.12. With the exception of the ends of the crack, the depths predicted with eddy currents were similar to the directly measured values of the inclined crack depth, rather than the depth of the crack tip below the surface of the sample. With a non-ferromagnetic material, the angle of inclination of a crack may be determined from the area of the loop produced by the "defect" impedance vector while scanning the crack [39] (Section 7.5). Although a slight loop was noted when scanning LS2, no conclusive measurements of crack inclination were made.

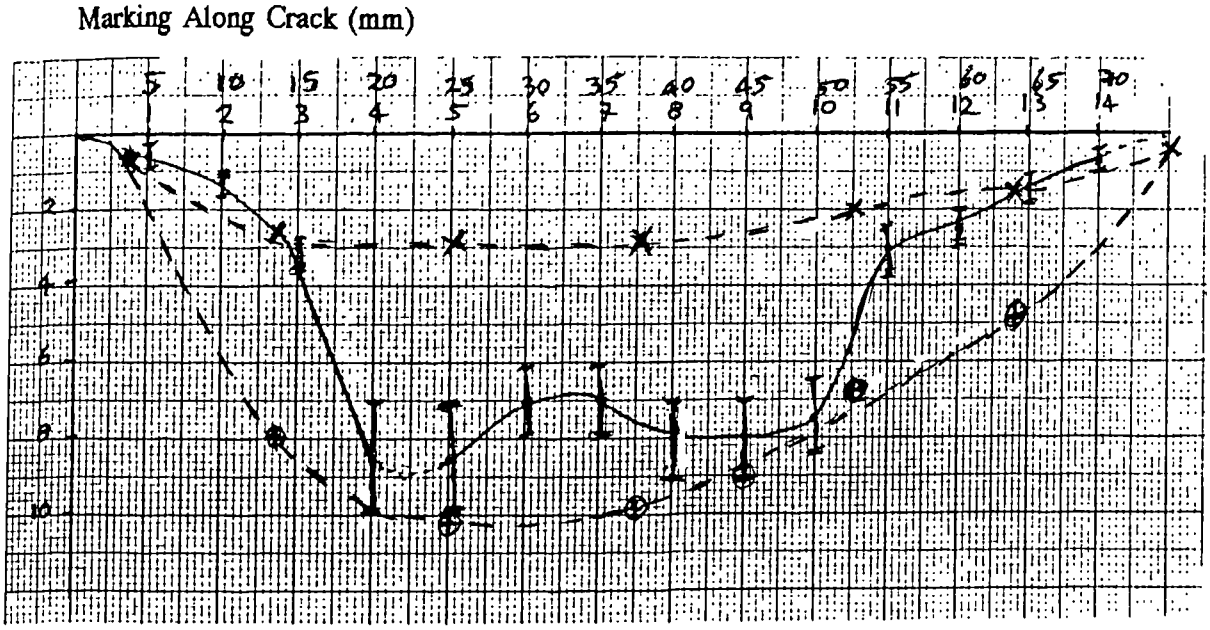

Figure 8.11: Estimated depth profile of the stress crack LS2, assuming the defect to be one simple crack normal to the sample surface.

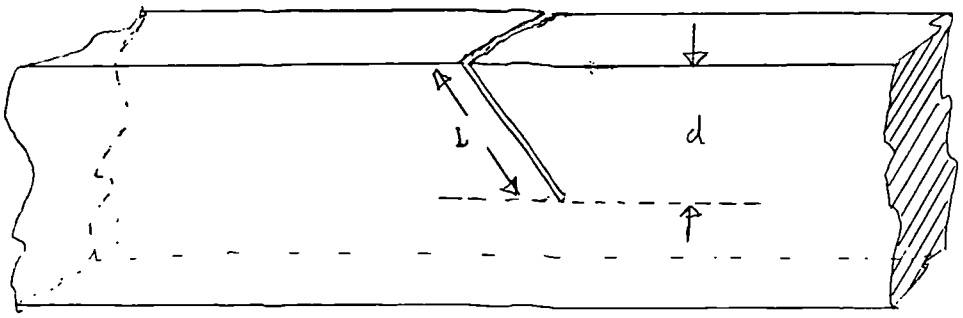

L = Crack Profile Length

d = Depth Of Crack Tip

Figure 8.12: Inclination of stress crack LS2, found on breaking open the sample.

(b) City University, London. - Samples Supplied by Marine Technology Directorate

The lift-off method was used to test the two welds, A-B and C-D (Fig. 8.13), of a double T-node of 50D steel, in which fatigue cracks had been grown mechanically, using the 17μH air-cored probe AS2 at a frequency of 600kHz. The probe was calibrated with the mild steel calibration blocks 1 and 2 and the differences in electrical and magnetic properties between the metals were found to be negligible. Cracking was found in the side regions of each weld (Fig. 8.13). The depths of the cracks were estimated at 10mm intervals and confirmed using ACPD [41] measurements made by University College, London (Fig. 8.14). There was good agreement for the depths of cracks estimated to be less than 8mm, especially for those less than 3mm (Table 8.5). For cracks deeper than 8mm, the eddy current estimates could not be made with any degree of certainty with the equipment available, because of eddy current skin effects.

(c) City University, London. - Samples from the Welding Institute

Seven fillet welds located in T-shaped plate samples (Fig. 8.15), were tested using the "touch" method at 5mm intervals around the welds, using different single coil probes. The welds were marked every 10mm (Fig. 8.16) and the samples were then cut open along the markers by ERS, British Gas Corporation, using a saw blade approximately 3mm thick. The depths of the defects revealed were measured optically. The maximum depths of the defects estimated with eddy currents, using the air-cored single coil 2S at 600kHz, are compared with those measured directly in Table 8.6. The depths of several defects were underestimated with eddy current methods, and these were subsequently found to be sub-surface cracks. The estimated depths of surface-breaking cracks agreed well with the direct measurements. Figs. 8.17 to 8.22 show the locations of the defects in the samples.

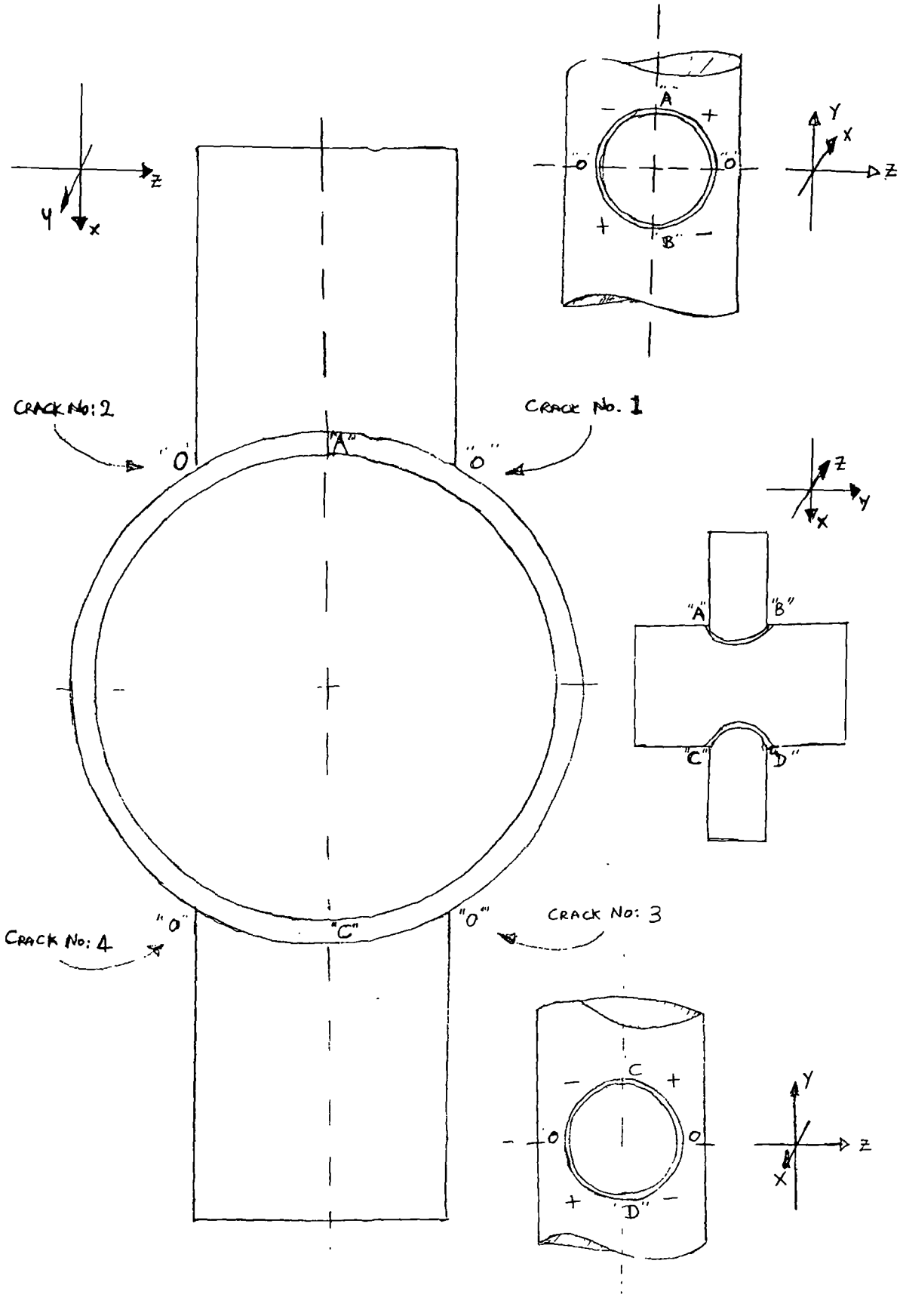

Figure 8.13: Double T-node of 50D steel, containing fatigue cracking in the weld areas A to B and C to D.

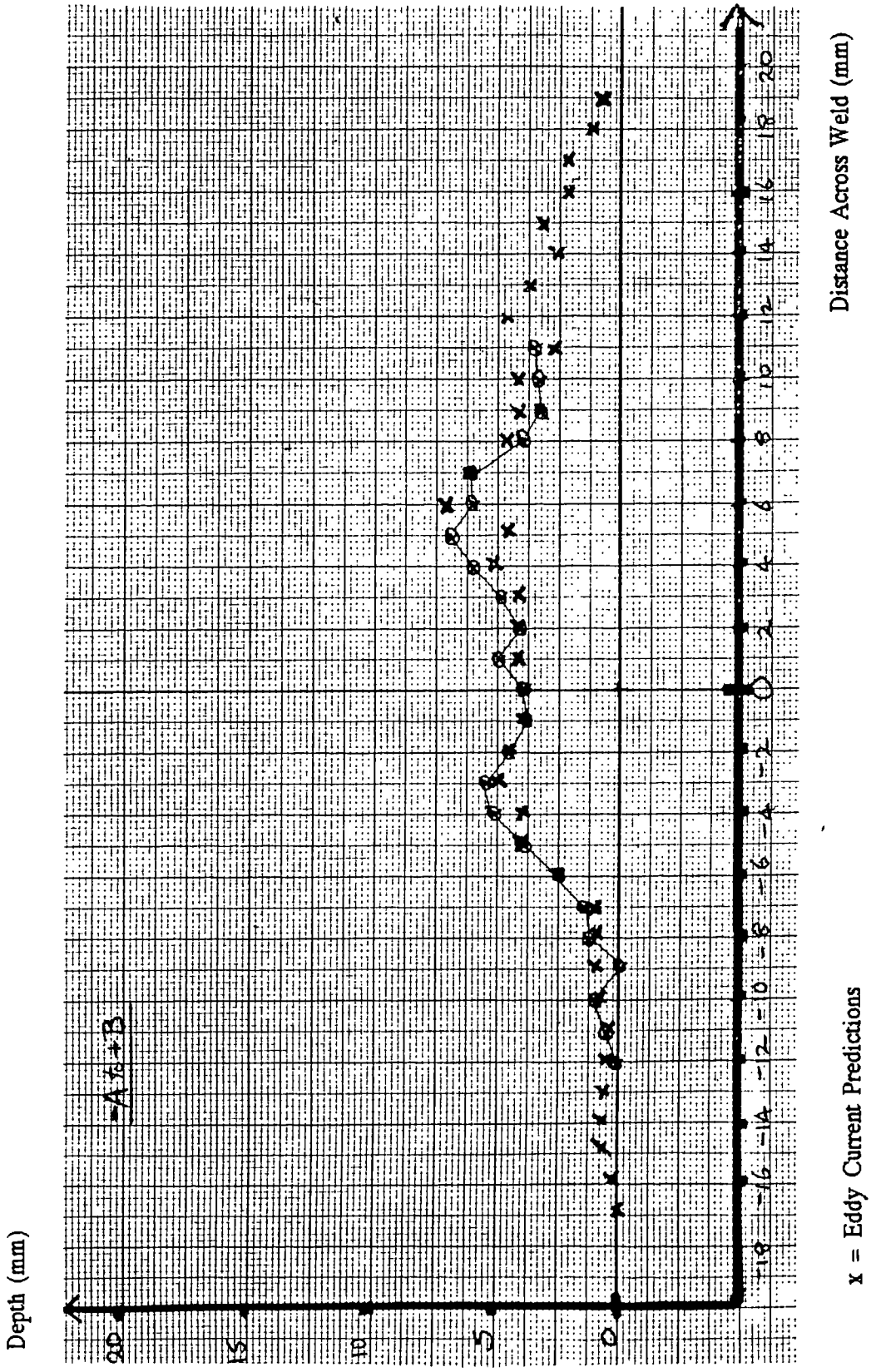

Figure 8.14(a): Comparison of crack depth profile estimated with eddy currents and ACPD, crack no: 1, +A to -B.

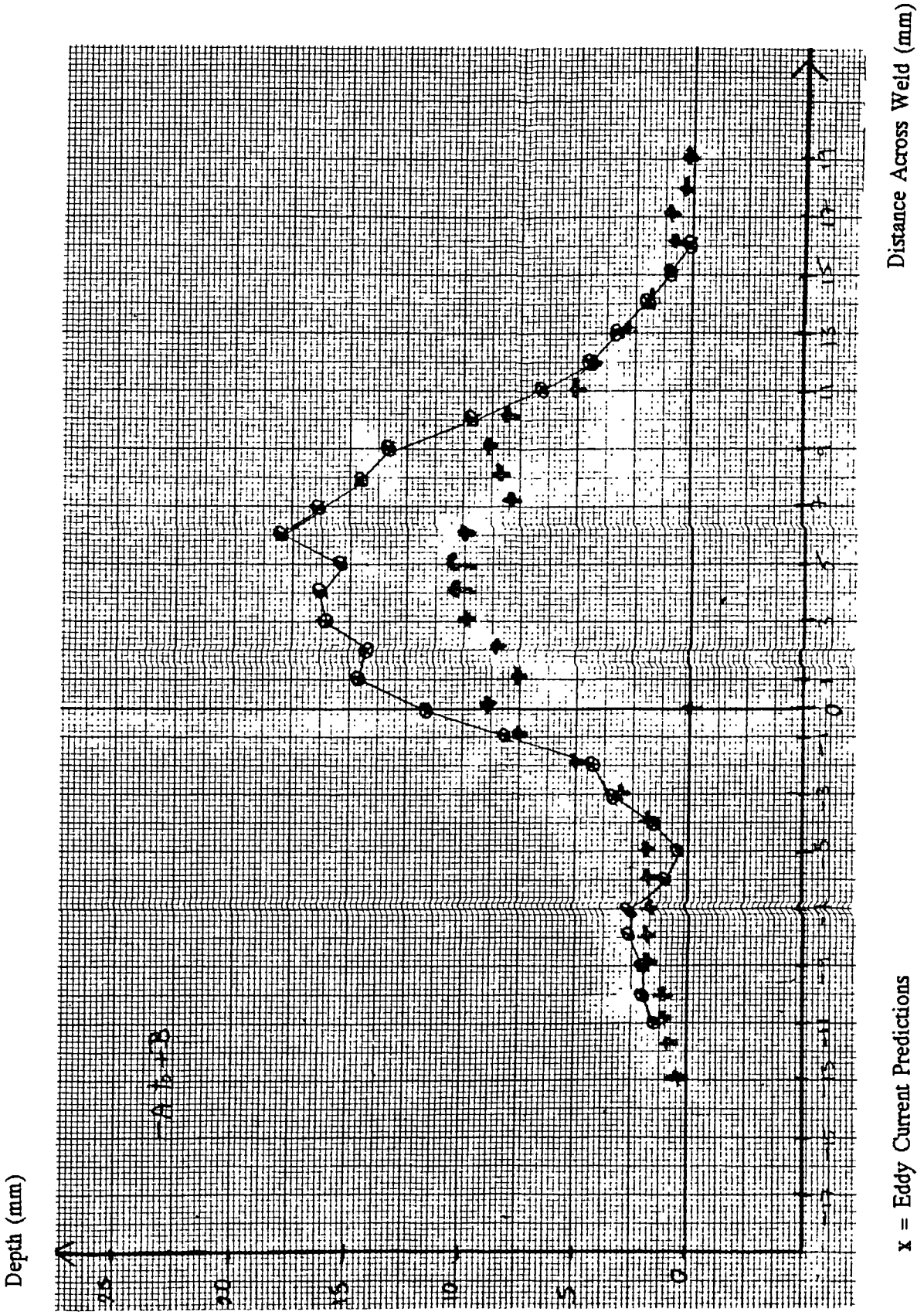

Figure 8.14(b): Comparison of crack depth profile estimated with eddy currents and ACPD, crack no: 2, +B to -A.

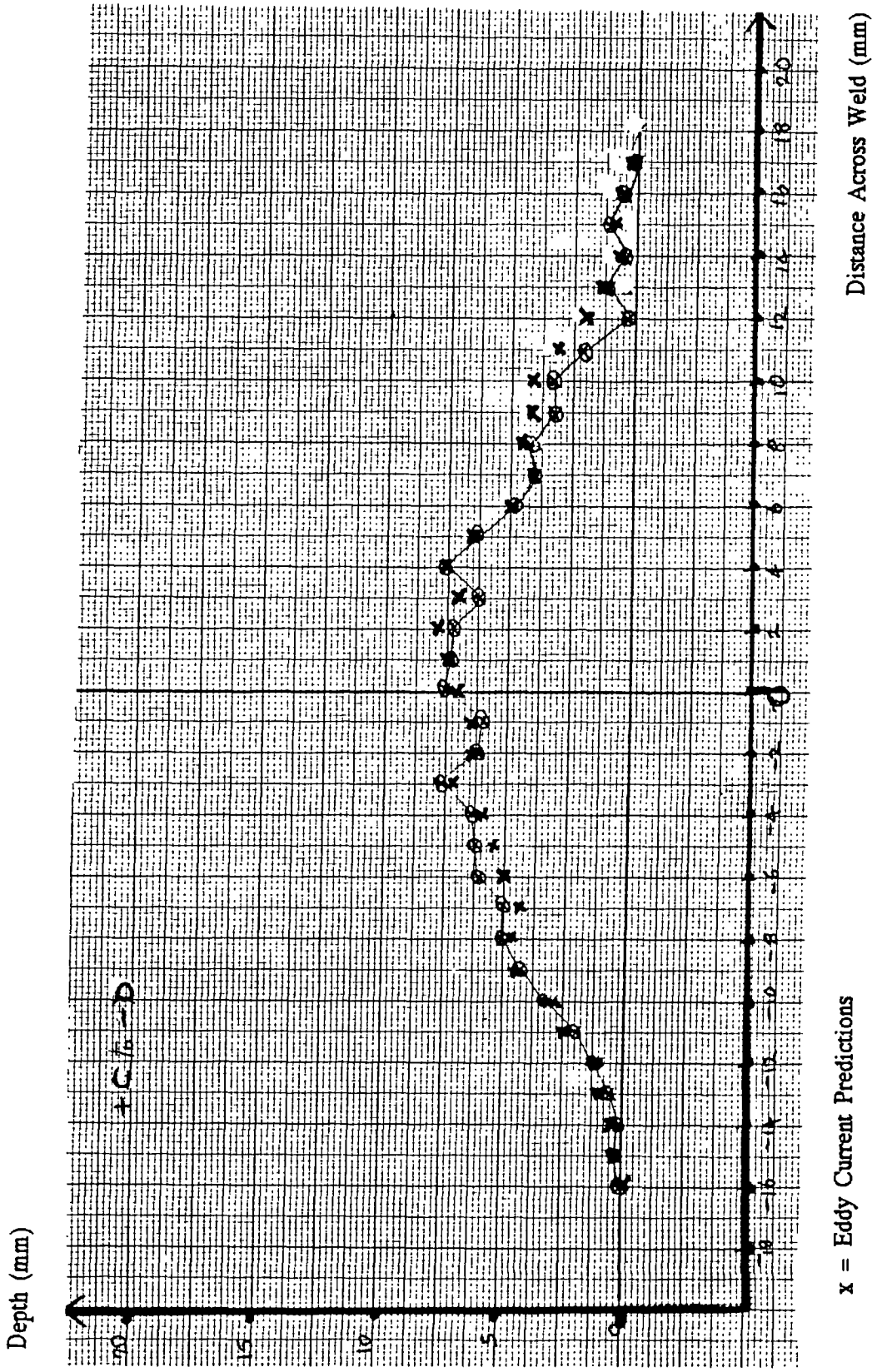

Figure 8.14(c): Comparison of crack depth profile estimated with eddy currents and ACPD, crack no: 3, +C to -D.

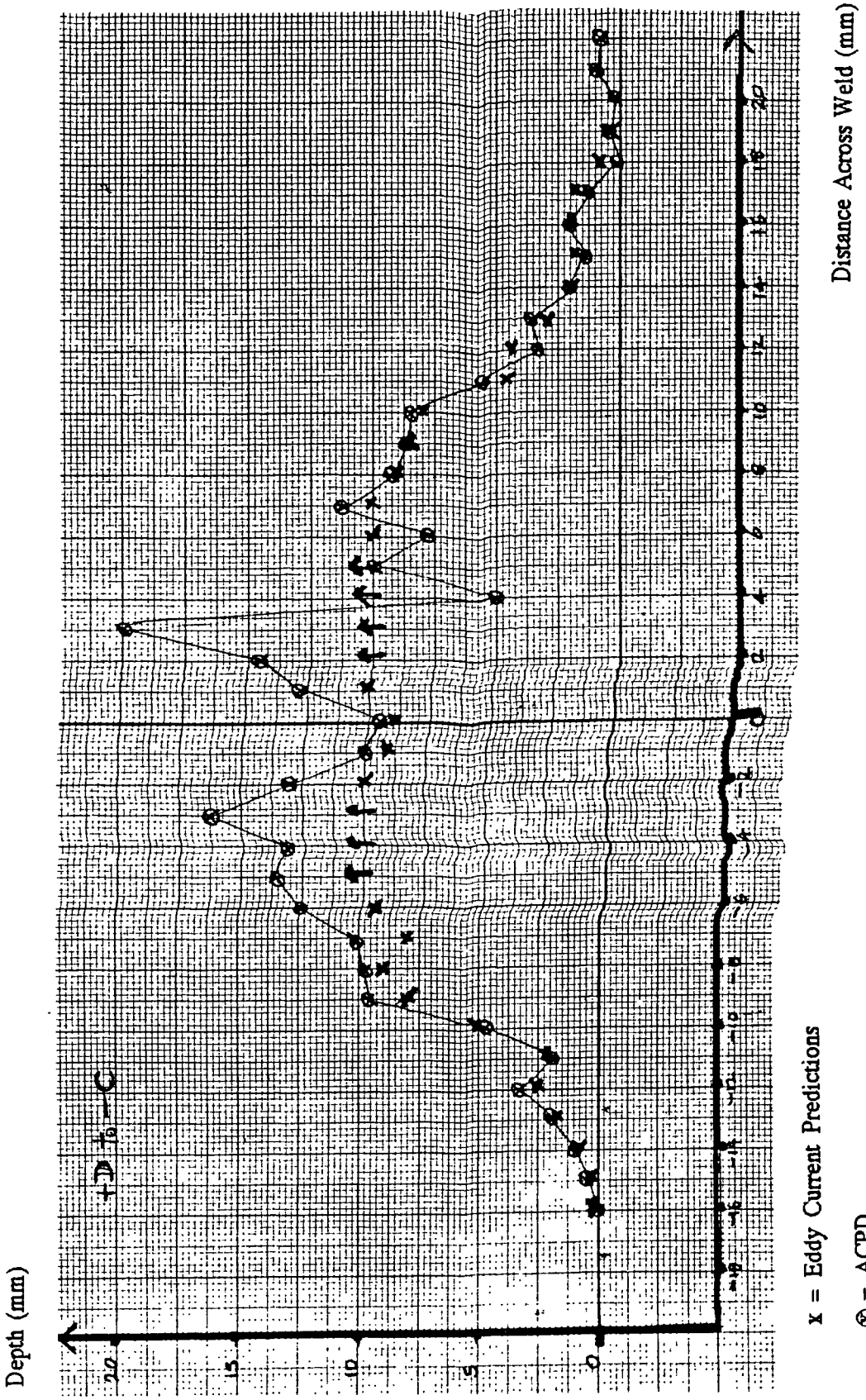

Figure 8.14(d): Comparison of crack depth profile estimated with eddy currents and ACPD, crack no: 4, +D to -C.

Table 8.5: Comparison of Crack Depths Estimated with the Eddy Current "Touch" Method and the ACPD Method in the Welds of a Double T-Node

"Touch" Method at 600kHz depth (mm)	ACPD depth (mm)
0.5 ± 0.0(5)	0.5 ± 0.03
1.0 ± 0.0(5)	1.0 ± 0.03
2.0 ± 0.1	2.0 ± 0.03
3.0 ± 0.1	3.0 ± 0.03
4.0 ± 0.1(5)	4.0 ± 0.03
5.0 ± 0.2	4.8 ± 0.03
7.0 ± 1.0	7.0 ± 0.03
8.0 ± 1.5	7.5 ± 0.03
>10.0	18.0 ± 0.03

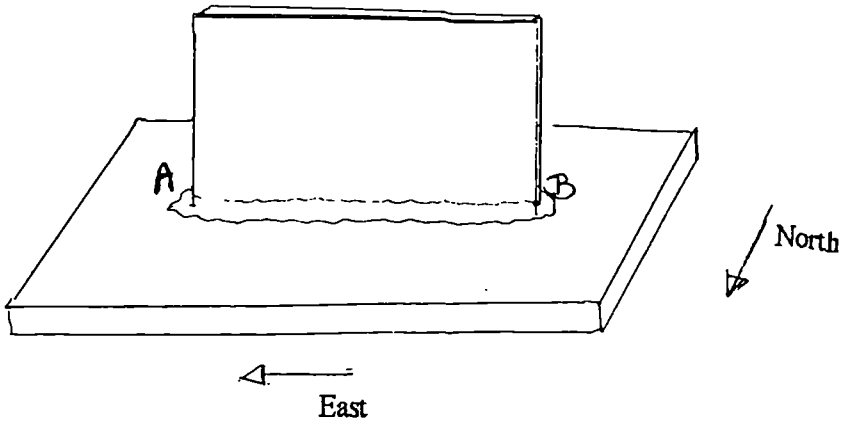

(a) General Lay-Out

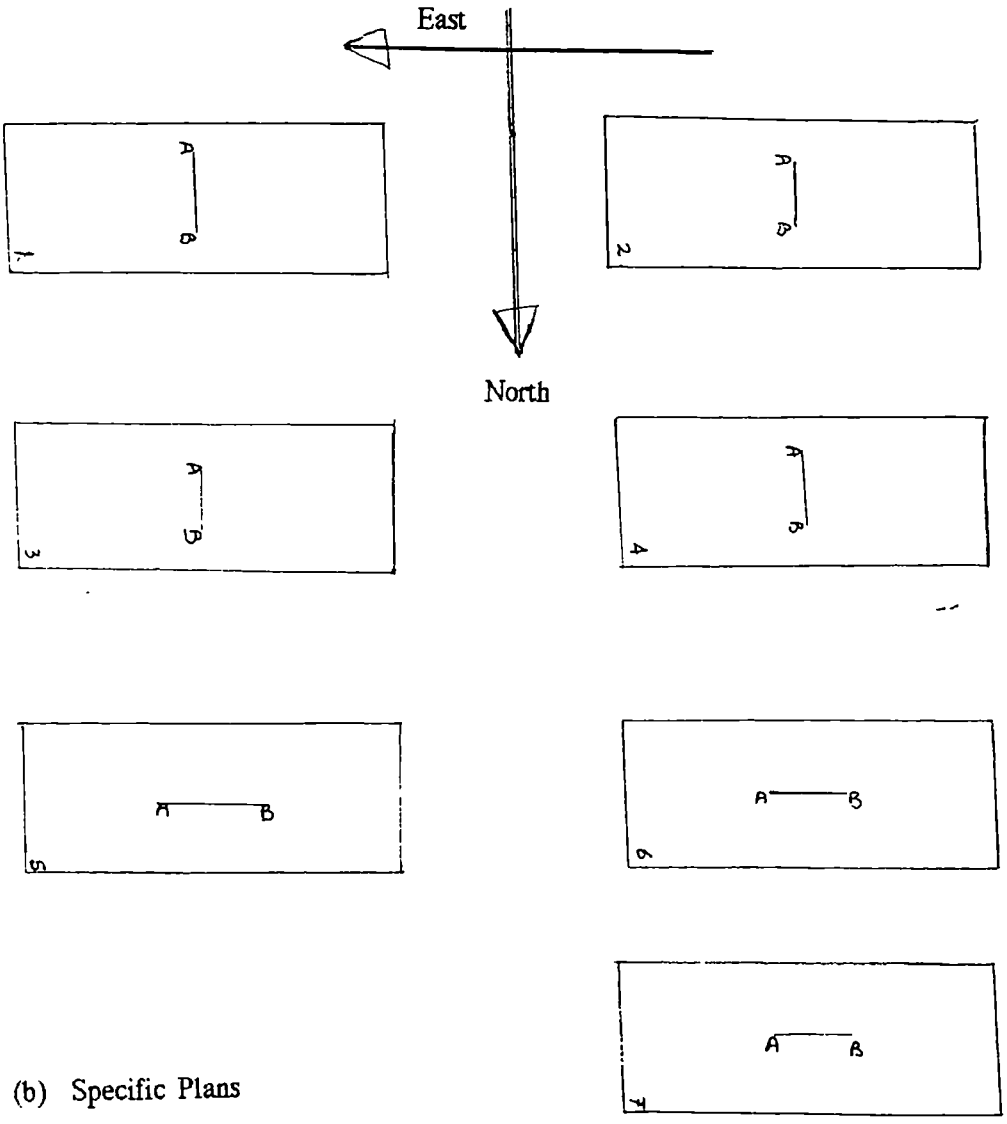

(b) Specific Plans

Figure 8.15: Schematic diagrams of the seven fillet welds tested.

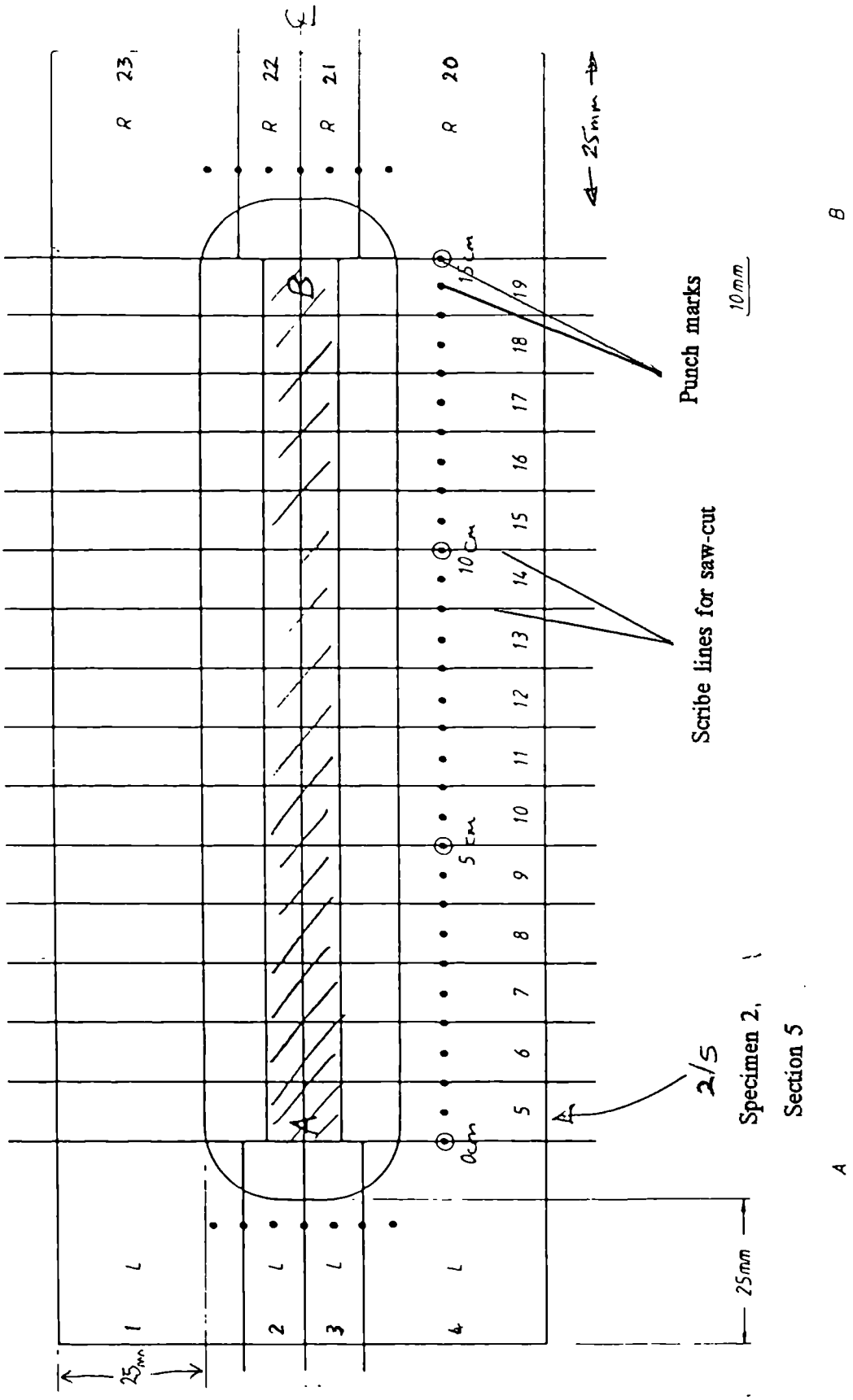

Figure 8.16: Sectioning plan of the seven fillet welds for optical inspection

Table 8.6: Maximum Depths of Cracks in Fillet Welds

Sample	Crack depths measured (mm)		Comments
	Eddy Current	Direct (±0.1)	
1	0 defects	0 defects	
2	0.8 ± 0.0(5)	1.3	Sub-surface defect
	2.4 ± 0.2	2.5	
	2.5 ± 0.2	2.7	
3	0.5 ± 0.0(5)	0.5	
	1.0 ± 0.1	4.2	Sub-surface defect
	4.0 ± 0.5	4.9	
4(E)	1.0 ± 0.1	1.1	
	2.0 ± 0.1(5)	2.3	
	6.0 ± 1.0	6.8	
4(W)	2.0 ± 0.15	1.9	
	1.0 ± 0.1	1.1	
	1.6 ± 0.2	1.8	
	2.2 ± 0.2	2.5	
5	1.0 ± 0.1	1.2	
6	1.0 ± 0.1	1.2	
7	1.0 ± 0.1	1.0	

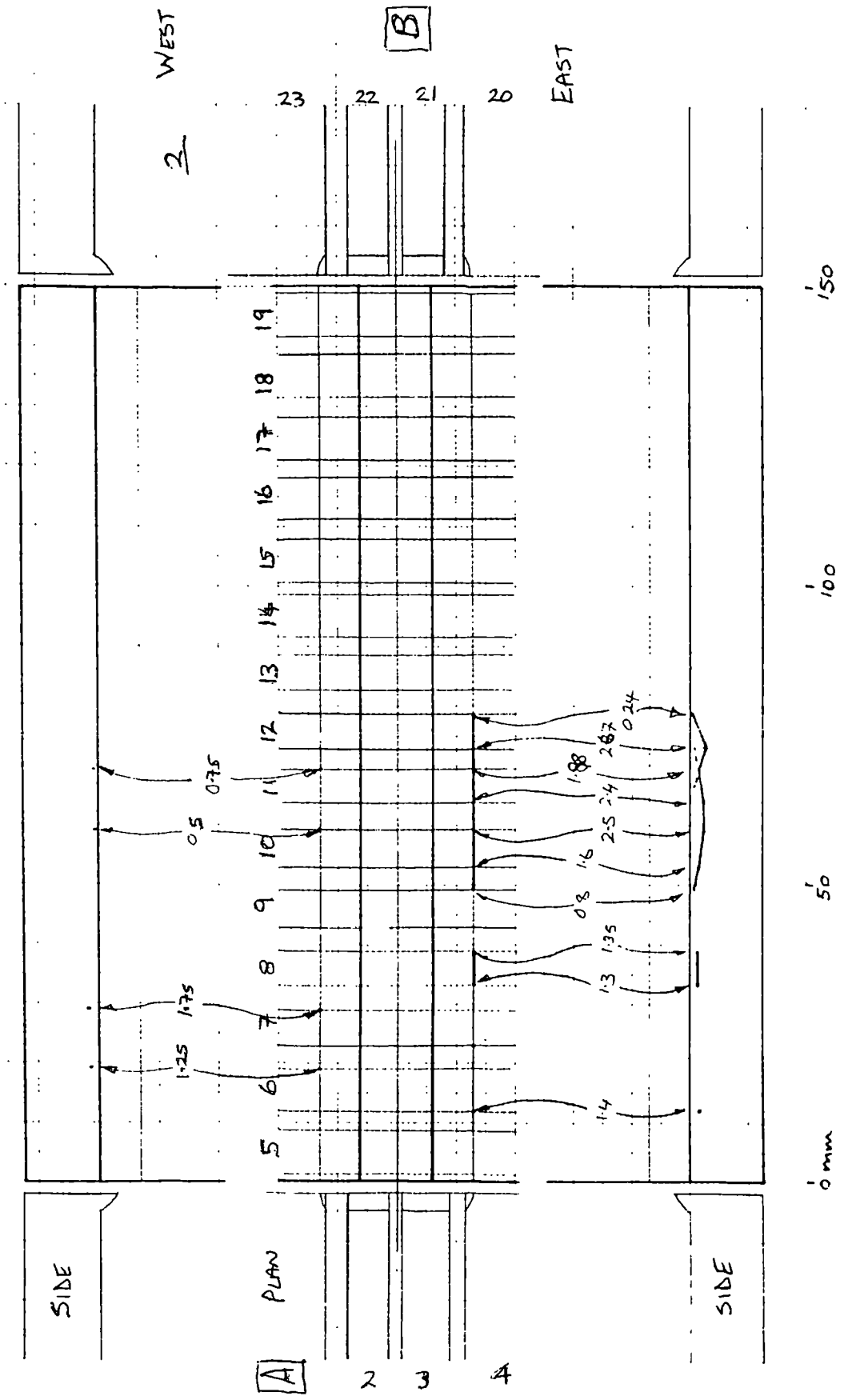

Figure 8.17: Analysis of defects in plate number 2. No: discontinuities = 7.

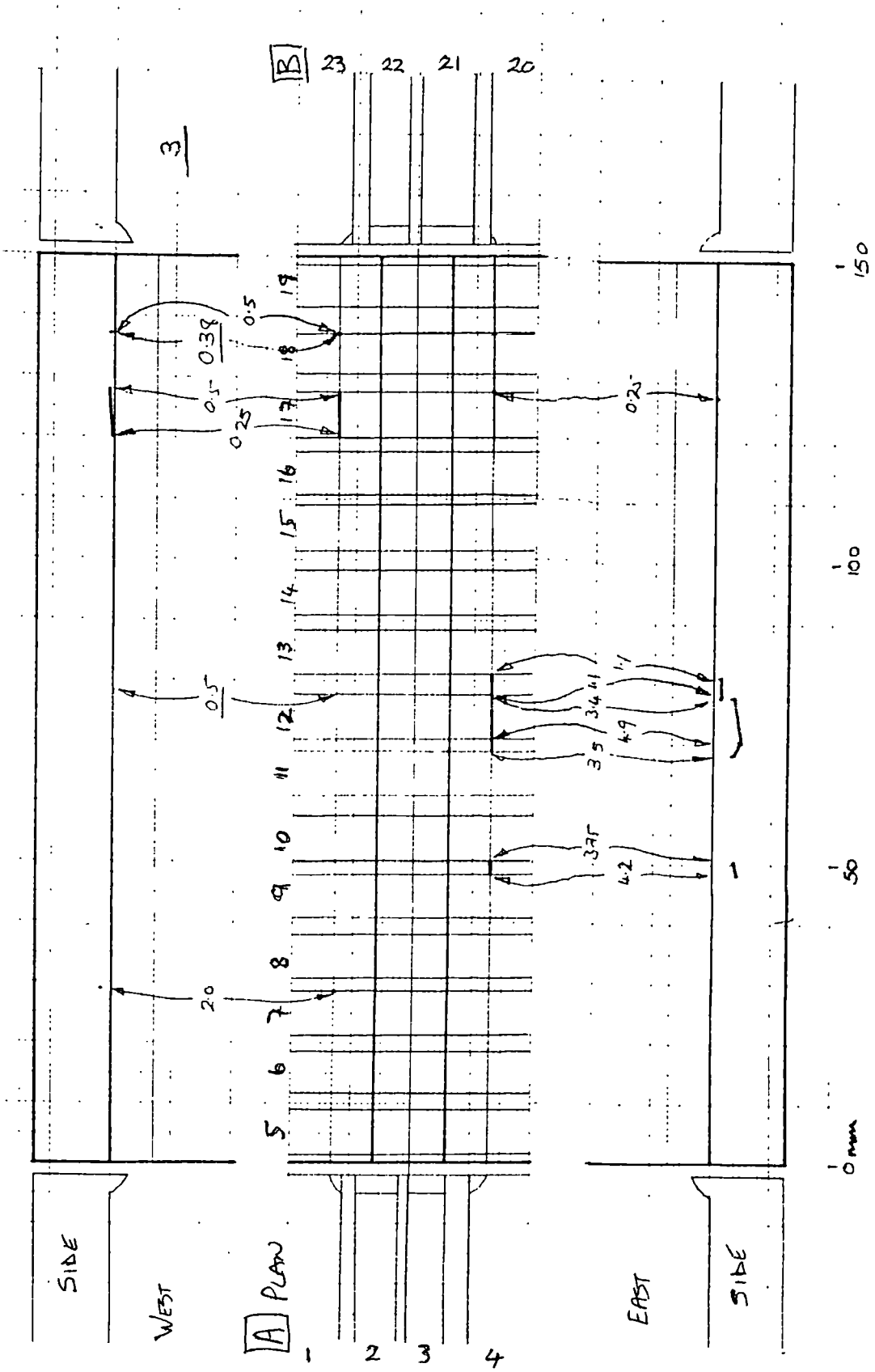

Figure 8.18: Analysis of defects in plate number 3. No: discontinuities = 5.

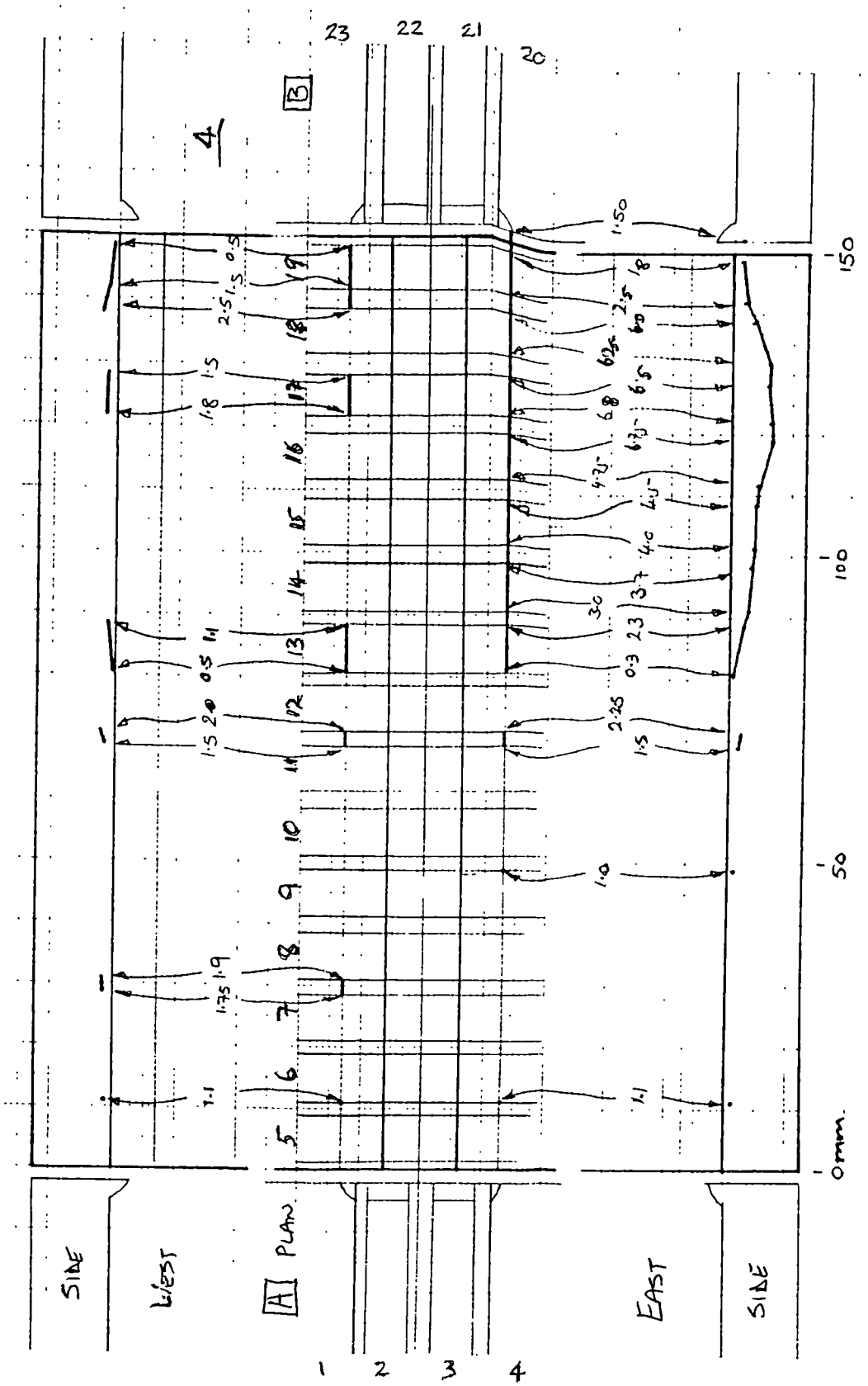

Figure 8.19: Analysis of defects in plate number 4. No: discontinuities = 10.

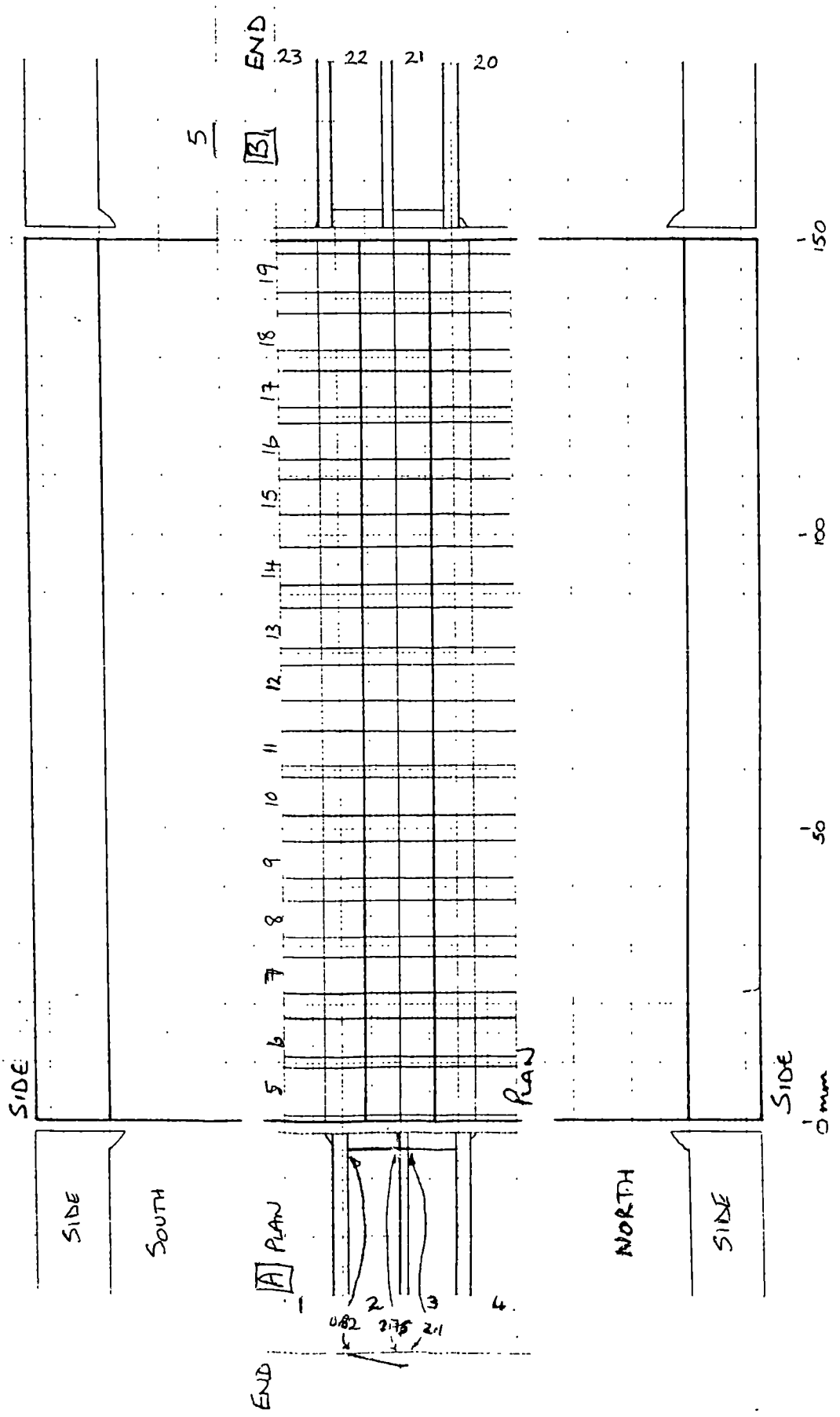

Figure 8.20: Analysis of defects in plate number 5. No: discontinuities = 1.

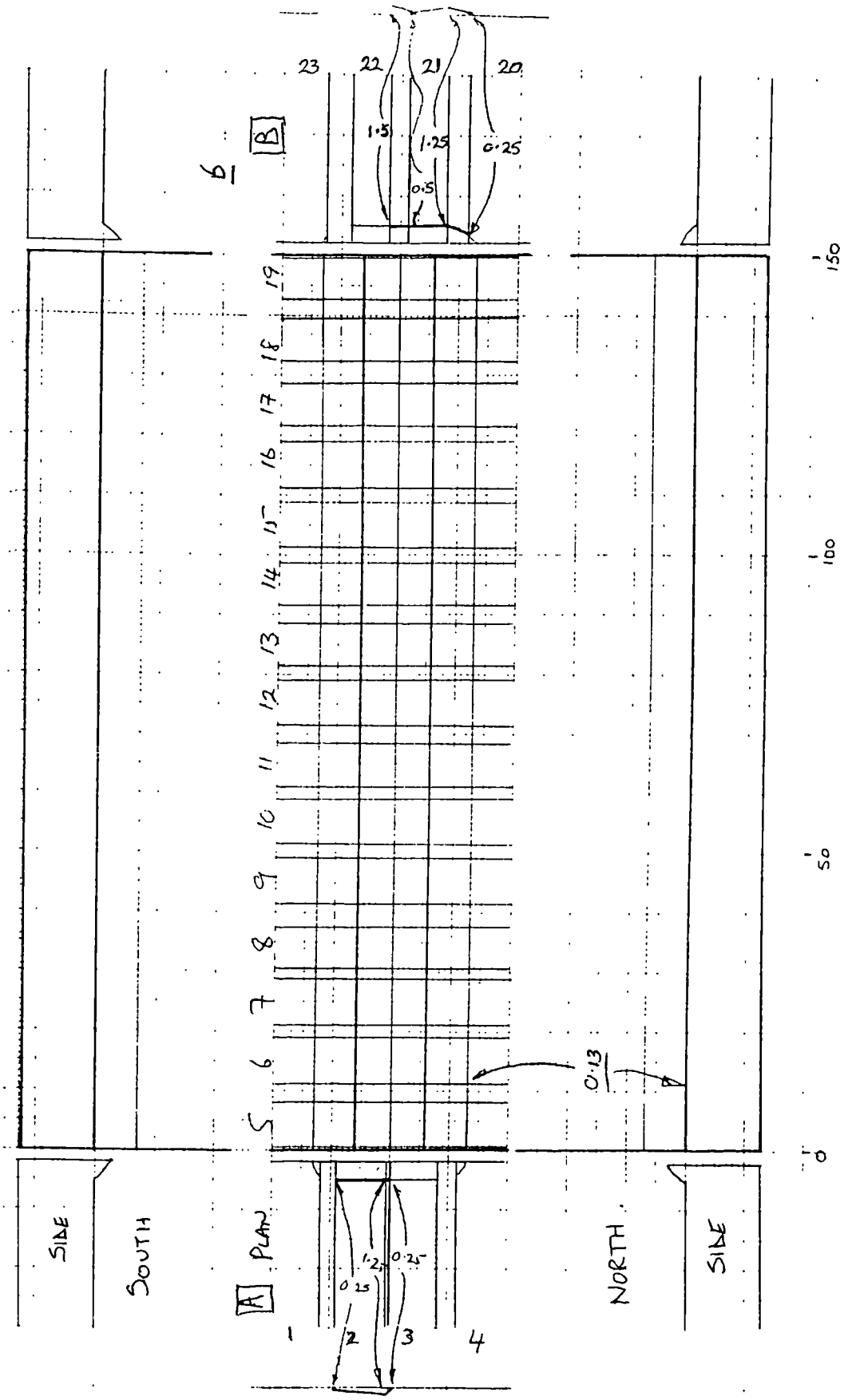

Figure 8.21: Analysis of defects in plate number 6. No: discontinuities = 2.

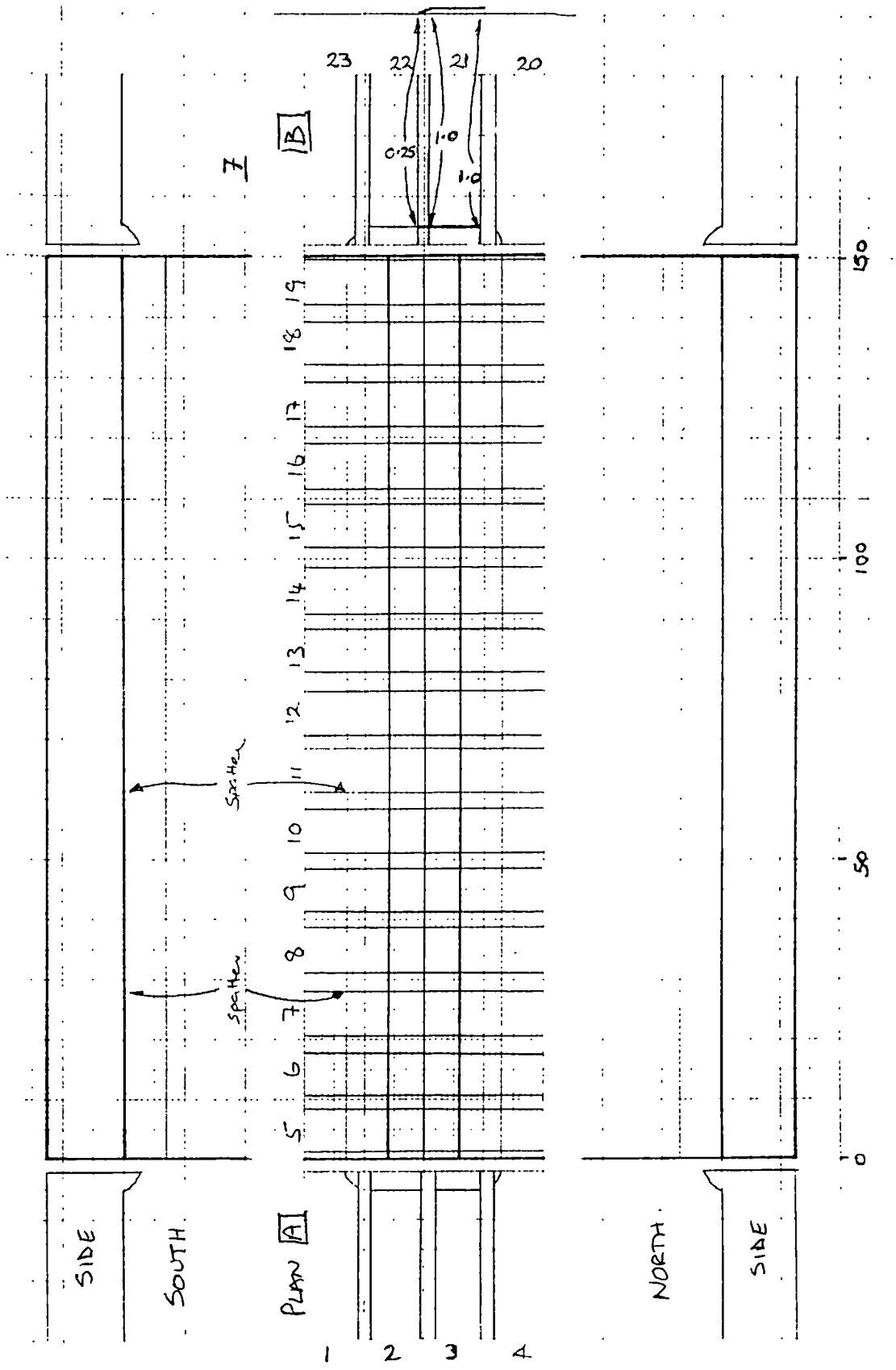

Figure 8.22: Analysis of defects in plate number 7. No: discontinuities = 1.

In general, there was good agreement between depths of defects estimated with eddy current methods and those found either directly from optical measurements after breaking open the samples, or using non-destructive methods, such as MPI and ACPD. The eddy current "touch" method appeared to be more sensitive to shallow cracks than the ACPD method, but not for deeper cracks. The depths of cracks deeper than 8mm could not be estimated with any certainty with the eddy current probes used here. Further work is necessary to qualify the effects of crack inclination and sub-surface cracks on the estimation of the size of cracks in ferromagnetic metals using eddy current methods.

CHAPTER 9

CONCLUSION

Success has been achieved in

(a) deriving relationships analytically between the real and imaginary components of the normalised impedance as functions of lift-off, frequency, electrical conductivity and magnetic permeability, for an air-cored coil scanning a defect-free ferromagnetic metal, for eddy current testing,

(b) verifying the values obtained from the application of the abovementioned relationships with those obtained experimentally,

(c) improving the design of eddy current scanning coils to achieve maximum sensitivity for the testing of ferromagnetic metals which (i) are defect-free and (ii) contain defects,

(d) devising a method of assessing defect sizes in ferromagnetic metals which is entirely independent of the degree of lift-off of the detecting coil.

A purely analytical approach was used to predict the components of normalised impedance of surface coils scanning ferromagnetic metals and, although the approach differed somewhat, the expressions obtained here agreed with those of Hajian for non-ferromagnetic metals, when values of $\mu_r = 1$ were inserted. By considering Förster's work with encircling coils one would expect a change in magnetic permeability to be indicated by two components of impedance, one orientated in the direction of normalised frequency $\beta^2 = \omega\sigma\mu r^2$, and the other in the direction of normalised lift-off. Here, $\omega = 2\pi f$ where f is frequency, r is the coil radius and σ is electrical conductivity and μ magnetic permeability of the metal. However, it was noted that for surface scanning probes, changes in magnetic permeability were indicated mainly by changes in the impedance vector in the same direction as

normalised frequency, with virtually no change in the direction of the normalised lift-off. This is not surprising because of the low degree of flux linkage of a surface scanning coil with the flat surface of the sample as compared with a coil encircling a metal rod. At a constant frequency and constant lift-off, a small increase in the value of μ produced a change in the value of impedance corresponding to decreasing β^2, i.e., in the opposite direction to the impedance change caused by a variation in σ. The impedance change for a 10% change in magnetic permeability was of the order of two times greater in magnitude than that for a similar degree of change in conductivity. The impedance changes brought about by a change in μ_r reduced with increasing frequency and was negligible at values of β^2 of 15,000, when μ_r was of the order of 100.

For testing ferromagnetic metals, the recoil magnetic permeability was used to evaluate the term μ_r contained in the expression for β^2, in view of the fact that it was necessary to excite the eddy current coils with only small currents, thus avoiding hysteresis effects.

Different criteria had to be applied to the design of coils used for defect testing of ferromagnetic metals than for non-ferromagnetic metals, and the radius of the coil was a more important parameter than the length. Air-cored probes were more suitable for testing ferromagnetic metals than ferrite-cored coils, because with the latter the cores were sensitive to changes in magnetic permeability and temperature of the metal. Low frequency transformer probes were not advantageous, because their sensitivity to small changes in magnetic permeability masked indications of defects. With single coils the use of high frequencies were found to be advantageous, in that they reduced the adverse effects of changes in magnetic permeability such as, for

example, in the heat affected zone of a weld. The optimum frequency range of air-cored coils of typical radius 1.25 mm and length 4 mm for flaw detection lay between 600 kHz and 1 MHz, corresponding to a value of normalised frequency in the region of 15,000.

With flaw detection, the lift-off effects and gradual changes in the product $\sigma\mu$ could be eliminated by using differential probes, but the prediction of the defect depth requires a separate measurement of the degree of lift-off of the probe. What would normally be the adverse effects of changing values of lift-off could be used to advantage with the lift-off or "touch" method of eddy current testing as developed in the investigations described in this thesis. This method was highly effective for defect detection in samples with irregular surfaces. The lift-off impedance vectors produced above simulated defects in the form of slots in mild steel were related to those from a different pipe-steel. Thus a single mild steel calibration block could be used to assess defects in other types of steel. The positions and depths of surface breaking cracks predicted in different industrially-produced samples using the lift-off method were afterwards confirmed either by breaking the samples open, or by using magnetic particle and AC potential difference NDT methods.

These investigations have been restricted to the study of simple surface-breaking cracks. Further work is required to predict the eddy current responses to angles of inclination of oblique cracks and sub-surface defects. It is also desirable to investigate the effects of varying the depth-to-width ratio of cracks on the impedance of eddy current coils.

REFERENCES

1. Förster, F. "Non-Destructive Testing Handbook, 2nd edition", Vol.4, (ed. McMaster, R.C., McIntire, P. and Mester, M.L.) American Society for Nondestructive Testing Inc., Cleveland, 1986

2. Libby, H.L. "Introduction to Electromagnetic Non-Destructive Test Methods", Wiley-Interscience, New York, 1971.

3. Förster, F. "Theoretishe und Experimentelle Grundlagen der Zerstörungsfreien Werkstoffprüfung mit Wirbelstromverfahren" Z. Metallk, Vol.45, no.4, 1954, translated in "Nondestructive Testing Handbook", Vol.II (ed. R.C. McMaster) Ronald, New York, 1959, Sections 39-42.

4. Freeman, E.M., El-Markabi, M.H.S. "2-Dimentional Field Analysis and Input Impedance of a Finite-Length Solenoidal Coil" Proc. IEE, Vol.126, no.1, pp. 135-139, 1979

5. Dodd, C.V., Deeds, W.E. "Analytical Solutions to Eddy Current Probe-coil Problems" J. Applied Physics, Vol.39, pp.2829-2838, 1968

6. Cheng, D.H.S "The Reflected Impedance of a Circular Coil in the Proximity of a Semi-Infinite Medium" IEEE Trans. Instrum. and Meas., vol. IM-14, no.3, pp.107-116, 1965

7. Burrows, M.L "A Theory of Eddy Current Flaw Detection" University Microfilms, Ann Arbor, Michigan, 1964

8. Dodd, C.V. "A Solution to Electromagnetic Induction Problems" PhD Thesis, University of Tennessee, 1967.

9. Dodd, C.V., Deeds, W.E., Spoeri, W.G. "Optimising Defect Detection in Eddy Current Testing" Materials Evaluation, Vol.29, pp.59-63, 1981.

10. Dodd, C.V., Luguire, J.W., Simpson, W.A., Spoeri, W.G. "Computer Programs for some Eddy Current Problems - 1970" Oak Ridge National Laboratory, Tennessee, ORNL / w-7405-eng-26, 1971.

11. Hajian, N.T., Blitz, J., Hall, R.B. "Impedance Changes for Air-Cored Probe Coils of Finite Lengths used for Eddy Current Testing" N.D.T. International, Feb.1983

12. Blitz, J., Hajian, N.T. "Standardisation for Eddy Current Testing Procedures" 11th World Conference N.D.T. Las Vegas, Vol. 3, pp.2006-2013, 1985

13. Blitz, J. "Prediction of Impedance Components of Eddy Current Coils using a Personal Computer" NDT International, Vol.22, no.1, pp.3-6, 1989.

14. Bozorth, R.M. "Ferromagnetism" D. Van Nostrand Co., New Jersey, 1951.

15. Vroman, J. "The Influence of Magnetic Properties on Eddy Current Testing of a Tube" British J. NDT, pp. 307-310, Nov.1981.

16. Deeds, W.E., Dodd, C.V. "A Two-Dimensional Relaxation Program for Systems with Inhomogeneous Permeability" Oak Ridge National Laboratory, Tennessee, ORNL / TM-5333, 1976

17. Blitz, J., Oaten, S.R., Hajian, N.T. "The Testing of Ferromagnetic Metals with Eddy Currents" J. Nondestructive Testing Communications vol.2, pp.189-200, 1986.

18. Zaman, A.J.M., Long, S.A., Gardner, C.G. "The Impedance of a Single-Turn Coil Near a Conducting Half-Space" J. Nondestructive Evaluation, Vol.1, no.3, pp.183-189, 1980

19. Zaman, A.J.M., Gardner, C.G., Long, S.A. "Change in Impedance of a Single-Turn Coil due to a Flaw in a Conducting Half Space" J. Nondestructive Evaluation, Vol.3, no.1, pp.37-43, 1982

20. Long, S.A., Toomsawasdi, S. "An Experimental Investigation of the Changes in Impedance of a Multi-Turn Eddy Current Coil Due to a Conducting Half Space" 14th Symposium NDE, San Antonio, pp.475-479, 1983

21. Khan, A.H. "Impedance of a Coil in the Vicinity of a Crack" J. Research of the National Bureau of Standards, Vol.89, no.1, pp.47-54, 1984.

22. Kahn, A.H., Spal, R,. Feldman, A. "Eddy Current Losses due to a Surface Crack in Conducting Material" J. Applied Physics, Vol. 48, no.11, p.4454-9, 1977

23. Auld, B.A., McFetridge, G., Riaziat, M., Jeffries, S. "Improved Probe-Flaw Interaction Modelling, Inversion Processing and Surface Roughness Clutter" Review of Progress in Quantitative Nondestructive Evaluation-3 (ed.Thompson, D.O., Chimenti, D.E,) Plenum, New York, 1985 pp 62 63

24. Hwang, J.H, Lord. W. "Finite Element Modeling of Magnetic Field / Defect Interactions" J. Testing and Evaluation, JTEVA, Vol.3, no.1, pp.21-25, 1975

25. Lord, W., Bridges, J.M., Yen, W., Palanisamy, R. "Residual and Active Leakage Fields Around Defects in Ferromagnetic Materials" Materials Evaluation., ~~Vol. 47~~, pp 4 July 1978.

26. Ida, N., Lord, W. "3-D Finite Element Predictions of Magnetostatic Leakage Fields" IEEE Transactions on Magnetics, Vol. MAG-19, no.5, pp 1983.

27. Cecco, V.S., Bax, C.R. "Eddy Current In-Situ Inspection of Ferromagnetic Monel Tubes", Materials Evaluation, pp.1-4, Jan. 1975

28. Oaten, S.R., Blitz, J. "The Touch Method of Eddy Current Testing" J. Nondestructive Testing Communications, Vol. 3, pp.139-151, 1987.

29. Kip, A.F. "Fundamentals of Electricity and Magnetism" McGraw-Hill, London, 1969

30. McLachlan, N.W. "Bessel Functions for Engineers" Clarendon, Oxford, 1955.

31. Bell, W.W. "Handbook of Special Functions for Scientists and Engineers" Van Nostrand, London, 1968.

32. British Standards Institution, B.S. 6404: Part 4 :1986 "Magnetic Materials - Methods of Measurement of the D.C. Magnetic Properties of Solids Steels" (Replaces BS 5884:1980) pp.36.

33. Neosid Ltd. "Magnetic Materials" Welwyn Garden City, 1979.

34. Blitz, J. Williams, D.J.A., Tilson, J.P. "Eddy Current Investigations of Cracks in Metals" Parts II, III MOD Procurement Executive no: 2066 / 024 XR / STR

35. Dodd, C.V., Cheung, C.C. "The Analysis of Reflection-Type Coils for Eddy Current Testing" ORNL-TM-4107 March 1973 (Oak Ridge National Laboratory)

36. Bains, J.A "Improved Lift-Off Compensation of Reflection-Type Eddy Current Probes for Ferromagnetic Materials" 14th Symposium NDE, San Antonio, ~~1983,~~ pp. 464-467, 1983.

37. Blitz, J. Williams, D.J.A., Tilson, J.P. "Calibration of Eddy Current Test Equipment" N.D.T. International, Vol.14, pp.119-123, 1981

38. Blitz, J., Willstatter, V.J., Oaten, S.R. and Hajian, N.T. "Eddy Current Surface Crack Sizing in Steel with High Lift-Off" N.D.T. International, Vol.20, no.2, pp.105-110, 1987.

39. Aldeen, A.N., Blitz, J. "Eddy Current Investigations of Oblique Longitudinal Cracks in Metal Tubes using a Mercury Model" N.D.T. International, Vol.12, pp.211-216, 1979

40. Alagoa, K.A. "Modelling of Oblique Cracks in Wood's Metal for Eddy Current Measurements" MPhil Thesis, Brunel University, Sept. 1984

41. Dover, W.D. "Use of A.C. Field Measurements in Crack Detection" J. Meas. and Insp. Technol. ~~March 1982,~~ vol.4, no.3, 32-35, 1982

APPENDICES

APPENDIX 1

Computer Program to Calculate the Components of Impedance of a Coil above a Ferromagnetic Plane

A simple computer program, written in BASIC to run on a small personal computer by Blitz [13], was modified by the author to calculate the components of impedance $R/\omega L_0$ and $\omega L/\omega L_0$ of an air-cored coil at different values of lift-off from the surface of a ferromagnetic material to four decimal places. The integrals I_3 and I_4 (Section 3.1) were integrated using Simpson's rule. The number of decimal places could be adjusted by varying the number of steps of integration, which affected the time taken for each computation. Calculations to 4 decimal places appeared to be the optimum, for which 500 steps were needed, taking about 40 seconds for each calculation of $R/\omega L_0$ and $\omega L/\omega L_0$. Fig. A1.1 shows the flow chart of the program.

The program (Fig. A1.2) offers three options: Options 1 and 2 calculate single values of the components of impedance from absolute and normalised values of input data respectively. Option 3 calculates the components of impedance over a range of normalised frequencies from 10 to 100,000 (line numbers 430 to 620) and normalised values of lift-off from 0 to 3.0 in steps of 0.2.

The integrands of I_3 and real and imaginary components of I_4 are calculated in a sub-routine (line numbers 1180 to 1320). The Bessel functions are calculated using the equation [30]

$$J_1(X) = \sum_{r=0}^{\infty} (-1)^r (X/2)^{2r+1} / r!(r+1)! \qquad \text{(A1.1)}$$

It is found that there is no change in value of the Bessel function beyond 15 terms, where each term is built up by multiplying the last term by the factor $-(x/2)^2/r(r+1)$.

Simpson's rule is used to calculate the integrals I_3, $I_{4(real)}$ and $I_{4(imag.)}$ in another subroutine (line numbers 910 to 1140), where the value of I_3 is calculated in line 1120 and $I_{4(real)}$ and $I_{4(imag.)}$ are calculated in lines 1110 and 1130 respectively. Finally the values of $\omega L/\omega L_0$ and $R/\omega L_0$ are calculated and printed out in a table form (lines 790 to 870).

Initially a short program (Fig. A1.3) was written to calculate the integrals for a range of X values, to confirm that terms beyond X = 10 could be ignored. Generally values beyond X = 6 were negligible.

In these investigations the components of impedance were calculated using values of μ_r between 1 and 5000 and Y_0 from 0.1 to 3 (Section 3.2). The components of impedance were also predicted for the single coil air-cored probes 2S, 3S and 4S (Section 6.2) and compared with experimental values (Appendix 3).

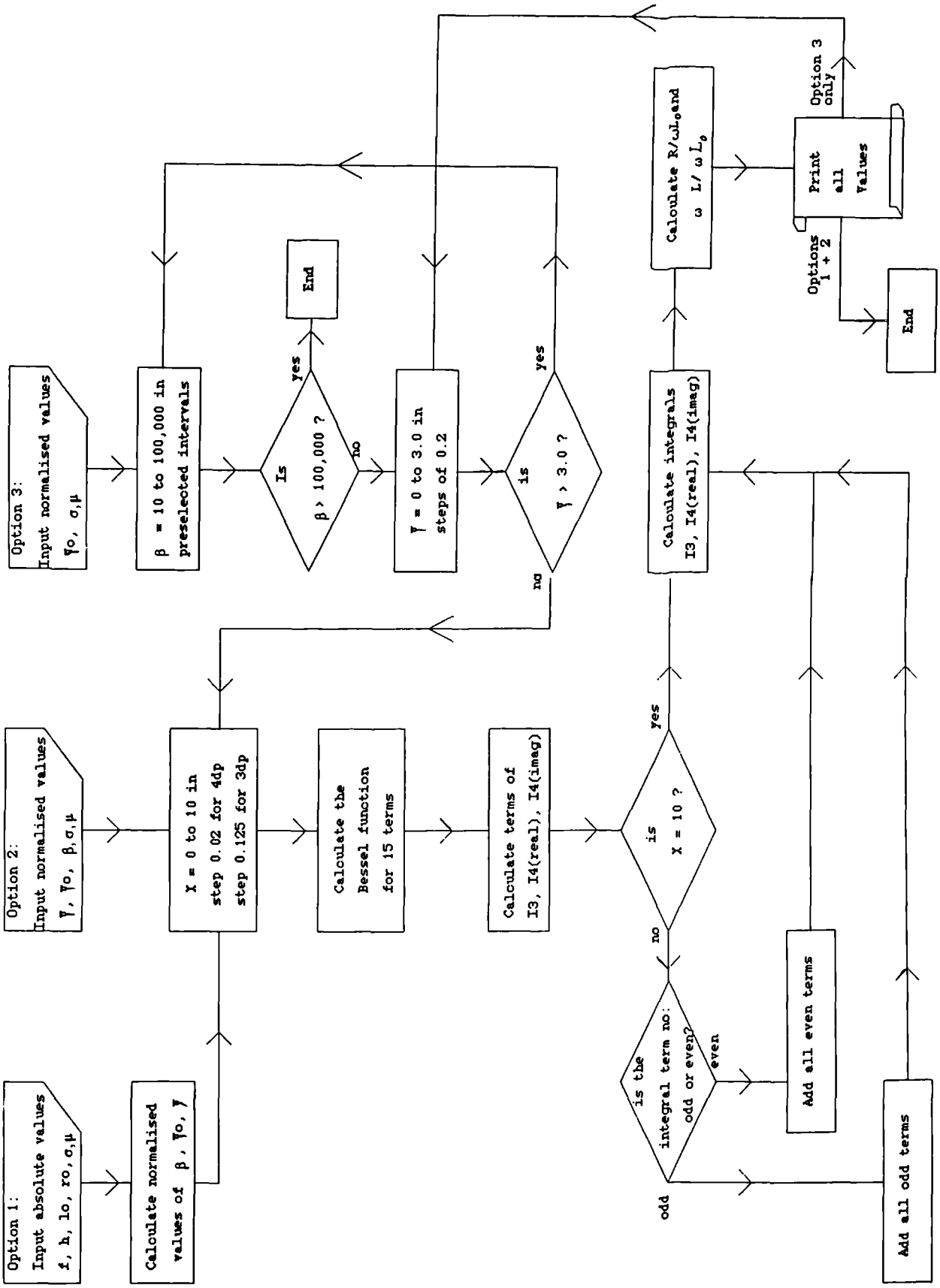

Figure A1.1: Flow chart of a program to calculate the components of impedance of an air-cored coil located above a metal.

```
10 PRINT "PREDICTION OF NORMALISED IMPEDANCES FOR AIR-CORED COILS"
20 PRINT "                    OVER FERROMAGNETIC METALS"
30 PRINT "_____"
40 PRINT
50 PRINT "Option 1= Input values are ABSOLUTE "
60 PRINT "Option 2= Input values are NORMALISED"
70 PRINT "option 3=  Calculate fixed range of f/fg and Lift-Off"
80 INPUT " TYPE OPTION NUMBER ;  ",p
90  pi = 3.1416
100 DIM q(2), h(2)
110 IF p=2 THEN 240
120 IF p=3 THEN 260

132 INPUT "Frequency (KHz) = ", f
140 INPUT "Electrical Conductivity (MS/m) = ", q(1)
150 INPUT "Relative Magnetic Permeability = ", q(2)
160 INPUT "lift-off (mm) = ", h(1)
170 INPUT "coil length (mm) = ",  h(2)
180 INPUT "coil radius (mm) = ",  r
190 b = 8*pi*pi*f*q(1)*q(2)*r*r/10^4
200 c = h(1)/r
210 d = h(2)/r
220 PRINT
230 GOTO 290

240 INPUT "normalised frequency f/fg = ", b
250 INPUT "normalised lift-off Y = ", c
260 INPUT "normalised coil length Yo = ", d
270 INPUT "Relative Magnetic Permeability = ", q(2)
280 INPUT "Electrical conductivity (MS/m) = ", q(1)

290 DIM s(3),u(3),i(2),m(3),w(3)
300 IF p = 3 THEN 330
310 LPRINT "Normalised frequency f/fg = ";USING "########.##";b
320 LPRINT "Normalised lift-off Y = ";USING "##.##";c
330 LPRINT "Normalised coil length Yo = ";USING "##.##";d
340 LPRINT "Relative Magnetic Permeability = ", q(2)
350 LPRINT "Electrical conductivity (MS/m) = ", q(1)
360 LPRINT:LPRINT
370 LPRINT "      f/fg      Y      wL/wLo      R/wLo      "
380 PRINT
```

Figure A1.2: List of the program Z-CALC.BAS (lines 10 to 380 of 1320)

```
390 '-------------------------------------------------
400 'Calculating Z/wLo over a range of l-o, c, for each frequency
410 '-------------------------------------------------
420 IF p<>3 THEN 650
430 IF p=3 THEN INPUT "start f/fg = ", b : c=0
440 GOSUB 630
450 IF b < 50 THEN 510
460 IF b < 100 THEN 530
470 IF b < 1000 THEN 550
480 IF b > 10000 THEN 570
490 b = b+2000:GOSUB 630
500 GOTO 450
510 b = b+10:GOSUB 630
520 GOTO 450
530 b = b+50:GOSUB 630
540 GOTO 450
550 b = b+200:GOSUB 630
560 GOTO 450
570 FOR ss=1 TO 5
580 PRINT "final b-loop no:= ";ss
590 b = b+20000
600 GOSUB 630
610 NEXT ss
620 END

630 LPRINT
640 FOR c=0 TO 3.2 STEP .2
650 PRINT "f/fg = ";USING "########.##";b
660 PRINT "V = ";USING "##.##";c
670 PRINT "normalised coil length Yo = "; USING "##.##";d
680 s(1)=0
690 s(2)=0
700 s(3)=0
710 u(1)=0
720 u(2)=0
730 u(3)=0
740 x=0
750 GOSUB 910
```

Figure A1.2(cont.): List of the program Z-CALC.BAS (lines 390 to 750 of 1320)

```
760 '-----------------------------------------------
770 ' Calculating the real and imaginary components of Z
780 '-----------------------------------------------
790 i(1) = 1 + w(1)/(d - 8/3/pi + 2*w(2))
800 i(2) = w(3)/(d - 8/3/pi + 2*w(2))
810 PRINT "wL/wLo = ";USING "###.####";i(1)
820 PRINT " R/wLo = ";USING "###.####";i(2)
830 PRINT
840 LPRINT USING "#######    ##.#    ###.####    ###.####  ";b,c,i(1),i(2)
850 IF p <> 3 THEN END
860 NEXT c
870 RETURN
880 '-----------------------------------------------
890 'Calculating odd terms, Simpson's rule
900 '-----------------------------------------------
910 FOR k=1 TO 499
920 x=x+0.2
930 GOSUB 1180
940 IF k/2 - INT(k/2) = 0 THEN 1020
950 s(1) = s(1) + l
960 s(2) = s(2) + v
970 s(3) = s(3) + e
980 GOTO 1050
990 '-------------------------------------------------
1000 ' Calculating even terms, and so whole of Simpson's rule
1010 '-------------------------------------------------
1020 u(1) = u(1) + l
1030 u(2) = u(2) + v
1040 u(3) = u(3) + e
1050 NEXT k

1060 x = 10
1070 GOSUB 1180
1080 m(1) = l
1090 m(2) = v
1100 m(3) = e
1110 w(1) = (m(1) + s(1)*4 + u(1)*2)/150
1120 w(2) = (m(2) + s(2)*4 + u(2)*2)/150
1130 w(3) = (m(3) + s(3)*4 + u(3)*2)/150
1140 RETURN
```

Figure A1.2(cont.): List of the program Z-CALC.BAS (lines 760 to 1140 of 1320)

```
1150 '-------------------------------------------------------------
1160 ' calculating integrals per x, incl. 15 terms of the Bessel function
1170 '-------------------------------------------------------------
1180 a = x/2
1190 t = x/2
1200 FOR j = 1 TO 15
1210 t = -(x/2)^2*t/j/(j + 1)
1220 a = a + t
1230 NEXT j
1240 y = (a/x)^2

1250 g = SQR(x^4 + b^2)
1260 n = (x* q(2)  )^2 + g + x* q(2)   *SQR(2*(g+x^2))
1270 z = y/EXP(2*c*x)*(1-1/EXP(d*x))^2
1290 l = z*((x* q(2)   )^2 - g)/n
1300 v = y/EXP(d*x)
1310 e = z*x* q(2)   *SQR(2*(g - x^2))/n
1320 RETURN
```

Figure A1.2(cont): List of the program Z-CALC.BAS (lines 1150 to 1320).

```
10  PRINT "Influence of I(3) and I(4 ) (real) and (imag.) with X
20  PRINT "   for a Ferromagnetic Metal"
30  PRINT "================================================="
40  PRINT:PRINT
50  LPRINT "Influence of I(3) and I(4 ) (real) and (imag.) with X"
60  LPRINT "   for a Ferromagnetic Metal"
70  LPRINT "================================================="
80  LPRINT: LPRINT
90  INPUT "REL. MAG. PERM. = ",Q(2)
100 INPUT "NORMALISED FREQ. = ",B
110 INPUT "NORM. L-0, Y  = ",C
120 INPUT "NORM. COIL LENGTH, Yo =",D
130  LPRINT "REL. MAG. PERM. = ",Q(2)
140 LPRINT "NORMALISED FREQ. = ",B
150 LPRINT "NORM. L-0, Y  = ",C
160 LPRINT "NORM. COIL LENGTH, Yo =",D
170 LPRINT:LPRINT
180 PRINT
190 PRINT "    x          i(3)        i(4)real        i(4)imag.   "
200 PRINT "_____________________________________________________"
210 LPRINT "    x       i(3)       i(4)real      i(4)imag.   "
220 LPRINT "_____________________________________________________"
230 X=0
240 FOR K=1 TO 80
250 X=X+.125
255 '-----------------------------------------
260 ' Calculating 15 terms of the Bessel function
265 '-----------------------------------------
270 A=X/2
280 T=X/2
290 FOR J=1 TO 15
300 T=-(X/2)^2*T/J/(J+1)
310 A=A+T
320 NEXT J
330 '-------------------------------------------------
335 'Calculating the integrals I(3) and I(4) for x=0 to 10
340 '-------------------------------------------------
350 Y=(A/X)^2
360 G=SQR(X^4+B^2)
370 N=(X* Q(2))^2+G-X* Q(2)*SQR(2*G+X^2)
380 Z=Y/EXP(2*C*X)*(1-1/EXP(D*X))^2
390 L=Z*((X* Q(2))^2-G)/N
400 V=Y/EXP(D*X)
410 e=z*x* Q(2) *SQR(2*(g-x^2))/n
420 LPRINT USING "  ##.###     #.######     #.######     #.######"; x, v, l, e
430 PRINT USING "  ##.###     #.######     #.######     #.######"; x, v, l, e
440 IF x=10 THEN END
450 NEXT k
```

Figure A1.3: **List of the program I3+I4.BAS**

APPENDIX 2

Experimental Values of the Components of Impedance of Coils 2S, 3S and 4S, when Located above a Metal

Table A2.1: Coil 2S above Aluminium Alloy

L_0 = 13 μH, r = 1.25 mm, Y_0 = 2.56.

Lift-Off (mm)	Freq. (kHz)	R (Ω)	ωL(Ω)	R/ωL₀	ωL/ωL₀
0	200	4.86 ± 0.005	41.28 ± 0.04	0.0035 ± 0.00006	0.967 ± 0.0025
0.5	"	4.77	41.89	0.0014	0.981
1.0	"	4.74	42.20	0.0007	0.989
1.5	"	4.73	42.37	0.0005	0.993
2.0	"	4.72	42.47	0.0002	0.995
2.5	"	4.72	42.55	0.0002	0.996
3.0	"	4.71	42.57	0.0000	0.997
3.5	"	4.71	42.60	0.0000	0.998
4.0	"	4.71	42.62	0.0000	0.999
"∞"	"	4.71	42.69	0.0000	1.000
0	400	5.40 ± 0.005	82.99 ± 0.08	0.0023 ± 0.00006	0.966 ± 0.0025
0.5	"	5.28	84.28	0.0093	0.981
1.0	"	5.24	84.94	0.0005	0.988
1.5	"	5.22	85.28	0.0002	0.992
2.0	"	5.22	85.48	0.0002	0.995
2.5	"	5.21	85.60	0.0001	0.996
3.0	"	5.21	85.69	0.0001	0.997
3.5	"	5.21	85.74	0.0001	0.998
4.0	"	5.20	85.79	0.0000	0.999
"∞"	"	5.20	85.94	0.0000	1.000
0	600	6.30 ± 0.006	125.7 ± 0.13	0.0015 ± 0.00005	0.964 ± 0.0025
0.5	"	6.20	127.8	0.0008	0.980
1.0	"	6.10	128.8	0.0000	0.988
1.5	"	6.10	129.3	0.0000	0.992
2.0	"	6.10	129.7	0.0000	0.995
2.5	"	6.10	129.9	0.0000	0.996
3.0	"	6.10	130.0	0.0000	0.997
3.5	"	6.10	130.1	0.0000	0.998
4.0	"	6.10	130.2	0.0000	0.999
"∞"	"	6.10	130.4	0.0000	1.000
0	800	7.60 ± 0.007	170.1 ± 0.18	0.0011 ± 0.00005	0.963 ± 0.0025
0.5	"	7.40	173.0	0.0000	0.979
1.0	"	7.40	174.5	0.0000	0.988
1.5	"	7.40	175.2	0.0000	0.992
2.0	"	7.40	175.7	0.0000	0.994
2.5	"	7.40	176.0	0.0000	0.996
3.0	"	7.40	176.1	0.0000	0.997
3.5	"	7.40	176.3	0.0000	0.998
4.0	"	7.40	176.4	0.0000	0.999
"∞"	"	7.40	176.7	0.0000	1.000

Table A2.2: Coil 3S above Aluminium Alloy

$L_0 = 17\,\mu H$, $r = 2.65\,mm$, $Y_0 = 0.6$.

Lift-Off (mm)	Freq. (kHz)	R (Ω)	ωL(Ω)	R/ωL₀	ωL/ωL₀
0	200	5.65 ± 0.005	9.63 ± 0.01	0.036 ± 0.0005	0.799 ± 0.001
0.5	"	5.45	10.53	0.020	0.873
1.0	"	5.35	11.09	0.012	0.920
1.5	"	5.29	11.41	0.007	0.946
2.0	"	5.26	11.60	0.004	0.962
2.5	"	5.24	11.73	0.002	0.973
3.0	"	5.23	11.82	0.002	0.980
3.5	"	5.22	11.88	0.000	0.985
4.0	"	5.22	11.92	0.000	0.988
"∞"	"	5.21	12.06	0.000	1.000
0	400	5.88 ± 0.005	19.05 ± 0.02	0.028 ± 0.0005	0.789 ± 0.001
0.5	"	5.57	21.02	0.015	0.871
1.0	"	5.42	22.14	0.009	0.918
1.5	"	5.34	22.79	0.005	0.944
2.0	"	5.29	23.20	0.003	0.961
2.5	"	5.26	23.46	0.002	0.972
3.0	"	5.25	23.63	0.002	0.979
3.5	"	5.24	23.76	0.001	0.985
4.0	"	5.23	23.84	0.001	0.988
"∞"	"	5.21	24.13	0.000	1.000
0	600	6.09 ± 0.005	28.29 ± 0.03	0.024 ± 0.0005	0.781 ± 0.001
0.5	"	5.68	31.40	0.013	0.867
1.0	"	5.49	33.12	0.008	0.914
1.5	"	5.39	34.14	0.005	0.943
2.0	"	5.33	34.78	0.003	0.960
2.5	"	5.29	35.18	0.002	0.971
3.0	"	5.28	35.46	0.002	0.979
3.5	"	5.26	35.64	0.001	0.984
4.0	"	5.25	35.78	0.001	0.988
"∞"	"	5.23	36.22	0.000	1.000
0	800	6.28 ± 0.005	37.55 ± 0.04	0.021 ± 0.0005	0.777 ± 0.001
0.5	"	5.81	41.72	0.011	0.863
1.0	"	5.57	44.13	0.006	0.913
1.5	"	5.45	45.52	0.004	0.942
2.0	"	5.38	46.38	0.002	0.959
2.5	"	5.35	46.94	0.002	0.971
3.0	"	5.32	47.31	0.001	0.979
3.5	"	5.31	47.56	0.001	0.984
4.0	"	5.30	47.74	0.001	0.988
"∞"	"	5.27	48.34	0.000	1.000

Table A2.3: Coil 4S above Aluminium Alloy

L_0 = 170 μH, r = 3.90 mm, Y_0 = 0.66.

Lift-Off (mm)	Freq. (kHz)	R (Ω)	ωL(Ω)	R/ωL0	ωL/ωL0
0	200	18.12 ± 0.01	44.15 ± 0.005	0.047 ± 0.0005	0.762 ± 0.001
0.5	"	17.09	48.40	0.029	0.835
1.0	"	16.52	51.11	0.019	0.882
1.5	"	16.15	52.99	0.013	0.914
2.0	"	15.92	54.23	0.009	0.936
2.5	"	15.77	55.13	0.006	0.951
3.0	"	15.67	55.77	0.004	0.962
3.5	"	15.59	56.24	0.003	0.970
4.0	"	15.55	56.58	0.002	0.976
"∞"	"	15.41	57.95	0.000	1.000
0	400	19.68 ± 0.01	86.58 ± 0.10	0.036 ± 0.0005	0.746 ± 0.001
0.5	"	18.07	95.86	0.022	0.826
1.0	"	17.18	101.72	0.014	0.876
1.5	"	16.62	105.67	0.009	0.910
2.0	"	16.30	108.32	0.006	0.933
2.5	"	16.07	110.20	0.004	0.949
3.0	"	15.92	111.54	0.003	0.961
3.5	"	15.82	112.54	0.002	0.970
4.0	"	15.74	113.26	0.002	0.976
"∞"	"	15.52	116.07	0.000	1.000
0	600	21.1 ± 0.02	128.3 ± 0.15	0.031 ± 0.0005	0.735 ± 0.001
0.5	"	19.1	142.3	0.019	0.815
1.0	"	17.9	151.8	0.013	0.869
1.5	"	17.2	158.1	0.009	0.905
2.0	"	16.8	162.4	0.006	0.930
2.5	"	16.5	165.4	0.005	0.947
3.0	"	16.3	167.5	0.003	0.959
3.5	"	16.1	169.1	0.002	0.968
4.0	"	16.0	170.2	0.001	0.975
"∞"	"	15.8	174.6	0.000	1.000
0	800	22.5 ± 0.02	170.5 ± 0.20	0.027 ± 0.0005	0.729 ± 0.001
0.5	"	20.0	190.1	0.017	0.813
1.0	"	18.6	203.1	0.011	0.868
1.5	"	17.8	211.7	0.007	0.905
2.0	"	17.3	217.4	0.005	0.292
2.5	"	16.9	221.5	0.003	0.947
3.0	"	16.7	224.4	0.002	0.959
3.5	"	16.6	226.4	0.002	0.968
4.0	"	16.4	228.0	0.001	0.975
"∞"	"	16.1	233.9	0.000	1.000

Table A2.4: Coil 2S above Mild Steel

L_0 = 13 μH, r = 1.25 mm, Y_0 = 2.56.

Lift-Off (mm)	Freq. (kHz)	R (Ω)	ωL(Ω)	R/ωL₀	ωL/ωL₀
0	200	4.572 ± 0.005	2.012 ± 0.002	0.007 ± 0.0005	1.026 ± 0.0025
0.5	"	4.566	1.986	0.004	1.013
1.0	"	4.563	1.975	0.003	1.007
1.5	"	4.562	1.969	0.002	1.004
2.0	"	4.560	1.966	0.001	1.003
2.5	"	4.560	1.965	0.001	1.002
3.0	"	4.559	1.963	0.001	1.001
3.5	"	4.559	1.963	0.001	1.001
4.0	"	4.559	1.962	0.001	1.001
"∞"	"	4.558	1.961	0.000	1.000
0	400	4.594 ± 0.005	4.005 ± 0.004	0.009 ± 0.0005	1.022 ± 0.0025
0.5	"	4.581	3.958	0.006	1.010
1.0	"	4.573	3.939	0.004	1.005
1.5	"	4.569	3.930	0.003	1.003
2.0	"	4.566	3.925	0.002	1.002
2.5	"	4.565	3.922	0.002	1.001
3.0	"	4.564	3.920	0.002	1.001
3.5	"	4.563	3.919	0.001	1.000
4.0	"	4.562	3.919	0.001	1.000
"∞"	"	4.558	3.918	0.000	1.000
0	600	4.619 ± 0.005	5.992 ± 0.006	0.010 ± 0.0005	1.020 ± 0.0025
0.5	"	4.595	5.927	0.006	1.009
1.0	"	4.583	5.900	0.004	1.004
1.5	"	4.575	5.888	0.003	1.002
2.0	"	4.571	5.882	0.002	1.001
2.5	"	4.568	5.879	0.002	1.001
3.0	"	4.566	5.877	0.001	1.000
3.5	"	4.564	5.876	0.001	1.000
4.0	"	4.563	5.875	0.001	1.000
"∞"	"	4.559	5.875	0.000	1.000
0	800	4.645 ± 0.005	7.972 ± 0.008	0.011 ± 0.0005	1.018 ± 0.0025
0.5	"	4.611	7.891	0.006	1.008
1.0	"	4.592	7.858	0.004	1.003
1.5	"	4.583	7.845	0.003	1.002
2.0	"	4.576	7.838	0.002	1.001
2.5	"	4.572	7.834	0.001	1.000
3.0	"	4.569	7.832	0.001	1.000
3.5	"	4.567	7.831	0.001	1.000
4.0	"	4.566	7.831	0.001	1.000
"∞"	"	4.561	7.831	0.000	1.000

Table A2.5: Coil 3S above Mild Steel

$L_0 = 17\,\mu H$, $r = 2.65$, $Y_0 = 0.6$.

Lift-Off (mm)	Freq. (kHz)	R (Ω)	ωL(Ω)	R/ωL₀	ωL/ωL₀
0	200	5.228 ± 0.005	0.671 ± 0.0005	0.032 ± 0.0005	1.200 ± 0.0005
0.5	"	5.222	0.626	0.021	1.120
1.0	"	5.218	0.600	0.014	1.073
1.5	"	5.216	0.585	0.011	1.047
2.0	"	5.214	0.577	0.007	1.032
2.5	"	5.213	0.571	0.005	1.021
3.0	"	5.212	0.568	0.004	1.016
3.5	"	5.212	0.565	0.003	1.011
4.0	"	5.211	0.564	0.002	1.009
"∞"	"	5.210	0.559	0.000	1.000
0	400	5.257 ± 0.005	1.319 ± 0.001	0.042 ± 0.0005	1.185 ± 0.0005
0.5	"	5.242	1.231	0.029	1.106
1.0	"	5.232	1.186	0.020	1.066
1.5	"	5.226	1.159	0.014	1.041
2.0	"	5.222	1.143	0.011	1.027
2.5	"	5.219	1.133	0.008	1.018
3.0	"	5.217	1.127	0.006	1.013
3.5	"	5.215	1.123	0.005	1.009
4.0	"	5.214	1.120	0.004	1.006
"∞"	"	5.210	1.113	0.000	1.000
0	600	5.289 ± 0.005	1.960 ± 0.002	0.047 ± 0.0005	1.176 ± 0.0005
0.5	"	5.263	1.836	0.032	1.101
1.0	"	5.245	1.769	0.021	1.061
1.5	"	5.235	1.730	0.015	1.038
2.0	"	5.228	1.708	0.011	1.025
2.5	"	5.223	1.694	0.008	1.016
3.0	"	5.220	1.686	0.006	1.011
3.5	"	5.218	1.680	0.005	1.008
4.0	"	5.216	1.676	0.004	1.005
"∞"	"	5.210	1.667	0.000	1.000
0	800	5.327 ± 0.005	2.589 ± 0.0025	0.053 ± 0.0005	1.166 ± 0.0005
0.5	"	5.287	2.429	0.035	1.094
1.0	"	5.262	2.344	0.023	1.056
1.5	"	5.246	2.297	0.016	1.035
2.0	"	5.236	2.270	0.012	1.023
2.5	"	5.229	2.253	0.009	1.015
3.0	"	5.224	2.242	0.006	1.010
3.5	"	5.221	2.236	0.005	1.007
4.0	"	5.218	2.231	0.004	1.005
"∞"	"	5.210	2.220	0.000	1.000

Table A2.6: Coil 4S above Mild Steel

L_0 = 170 μH, r = 3.90 mm, Y_0 = 0.66.

Lift-Off (mm)	Freq. (kHz)	R (Ω)	ωL(Ω)	R/ωL₀	ωL/ωL₀
0	200	15.49 ± 0.015	3.31 ± 0.0025	0.034 ± 0.0005	1.235 ± 0.001
0.5	"	15.47	3.10	0.026	1.157
1.0	"	15.45	2.96	0.019	1.104
1.5	"	15.44	2.88	0.015	1.075
2.0	"	15.43	2.82	0.011	1.052
2.5	"	15.42	2.78	0.008	1.037
3.0	"	15.42	2.76	0.007	1.030
3.5	"	15.41	2.74	0.004	1.022
4.0	"	15.41	2.72	0.004	1.015
"∞"	"	15.40	2.68	0.000	1.000
0	400	15.64 ± 0.015	6.52 ± 0.0055	0.045 ± 0.0005	1.221 ± 0.001
0.5	"	15.58	6.11	0.034	1.144
1.0	"	15.53	5.86	0.024	1.097
1.5	"	15.50	5.70	0.019	1.067
2.0	"	15.48	5.60	0.015	1.049
2.5	"	15.47	5.53	0.013	1.036
3.0	"	15.45	5.48	0.009	1.026
3.5	"	15.44	5.44	0.007	1.019
4.0	"	15.43	5.42	0.006	1.015
"∞"	"	15.40	5.34	0.000	1.000
0	600	15.82 ± 0.015	9.76 ± 0.0085	0.052 ± 0.0005	1.220 ± 0.001
0.5	"	15.71	9.12	0.039	1.140
1.0	"	15.63	8.76	0.029	1.095
1.5	"	15.58	8.53	0.022	1.066
2.0	"	15.54	8.37	0.018	1.046
2.5	"	15.51	8.27	0.014	1.034
3.0	"	15.49	8.20	0.011	1.025
3.5	"	15.47	8.15	0.009	1.019
4.0	"	15.45	8.11	0.006	1.014
"∞"	"	15.40	8.00	0.000	1.000
0	800	16.03 ± 0.015	12.90 ± 0.011	0.059 ± 0.0005	1.210 ± 0.001
0.5	"	15.86	12.09	0.043	1.134
1.0	"	15.74	11.62	0.032	1.090
1.5	"	15.65	11.32	0.023	1.062
2.0	"	15.59	11.12	0.018	1.043
2.5	"	15.55	10.99	0.014	1.031
3.0	"	15.52	10.90	0.011	1.023
3.5	"	15.49	10.84	0.008	1.017
4.0	"	15.48	10.79	0.007	1.012
"∞"	"	15.40	10.66	0.000	1.000

APPENDIX 3

Comparison of Predicted and Experimental Values of the Components of Impedance of Coils 2S, 3S and 4S

Table A3.1: Theoretical and Experimental Values for Coil 2S above Aluminium

L_0 = 13 μH, r = 1.25 mm, Y_0 = 2.56.

Lift-Off (mm)	Y (corrected)	Freq. (kHz)	Theoretical Impedance $R/\omega L_0$	$\omega L/\omega L_0$	Experimental Impedance $R/\omega L_0$	$\omega L/\omega L_0$
0	0.28	200	0.008	0.934	0.004	0.967
0.5	0.68	"	0.003	0.968	0.002	0.981
1.0	1.08	"	0.001	0.983	0.001	0.989
1.5	1.48	"	0.001	0.989	0.001	0.993
2.0	1.88	"	0.000	0.993	0.000	0.995
2.5	2.28	"	0.000	0.995	0.000	0.996
3.0	2.68	"	0.000	0.997	0.000	0.997
3.5	3.08	"	0.000	0.998	0.000	0.998
4.0	3.48	"	0.000	0.999	0.000	0.999
"∞"	"∞"	"	0.000	1.000	0.000	1.000
0	0.28	400	0.006	0.931	0.002	0.966
0.5	0.68	"	0.002	0.967	0.001	0.981
1.0	1.08	"	0.001	0.982	0.001	0.988
1.5	1.48	"	0.001	0.989	0.000	0.992
2.0	1.88	"	0.000	0.993	0.000	0.995
2.5	2.28	"	0.000	0.995	0.000	0.996
3.0	2.68	"	0.000	0.996	0.000	0.997
3.5	3.08	"	0.000	0.997	0.000	0.998
4.0	3.48	"	0.000	0.998	0.000	0.999
"∞"	"∞"	"	0.000	1.000	0.000	0.000
0	0.28	600	0.005	0.930	0.002	0.964
0.5	0.68	"	0.002	0.967	0.001	0.980
1.0	1.08	"	0.001	0.982	0.000	0.988
1.5	1.48	"	0.000	0.989	0.000	0.992
2.0	1.88	"	0.000	0.993	0.000	0.995
2.5	2.28	"	0.000	0.995	0.000	0.996
3.0	2.68	"	0.000	0.996	0.000	0.997
3.5	3.08	"	0.000	0.997	0.000	0.998
4.0	3.48	"	0.000	0.998	0.000	0.999
"∞"	"∞"	"	0.000	1.000	0.000	1.000
0	0.28	800	0.005	0.929	0.001	0.963
0.5	0.68	"	0.002	0.967	0.000	0.979
1.0	1.08	"	0.001	0.982	0.000	0.988
1.5	1.48	"	0.000	0.989	0.000	0.992
2.0	1.88	"	0.000	0.993	0.000	0.994
2.5	2.28	"	0.000	0.995	0.000	0.996
3.0	2.68	"	0.000	0.996	0.000	0.997
3.5	3.08	"	0.000	0.997	0.000	0.998
4.0	3.48	"	0.000	0.998	0.000	0.999
"∞"	"∞"	"	0.000	1.000	0.000	1.000

Table A3.2: Theoretical and Experimental Values for Coil 3S above Aluminium

L_0 = 17 μH, r = 2.65 mm, Y_0 = 0.6.

Lift-Off (mm)	Y (corrected)	Freq. (kHz)	Theoretical Impedance $R/\omega L_0$	$\omega L/\omega L_0$	Experimental Impedance $R/\omega L_0$	$\omega L/\omega L_0$
0	0.14	200	0.037	0.798	0.036	0.799
0.5	0.33	"	0.019	0.882	0.020	0.873
1.0	0.52	"	0.010	0.926	0.012	0.920
1.5	0.71	"	0.006	0.952	0.007	0.946
2.0	0.90	"	0.004	0.967	0.004	0.962
2.5	1.10	"	0.002	0.977	0.002	0.973
3.0	1.29	"	0.002	0.983	0.002	0.980
3.5	1.48	"	0.001	0.988	0.000	0.985
4.0	1.67	"	0.001	0.990	0.000	0.988
"∞"	"∞"	"	0.000	1.000	0.000	1.000
0	0.14	400	0.029	0.784	0.028	0.789
0.5	0.33	"	0.014	0.875	0.015	0.871
1.0	0.52	"	0.008	0.923	0.009	0.918
1.5	0.71	"	0.005	0.950	0.005	0.944
2.0	0.90	"	0.003	0.966	0.003	0.961
2.5	1.10	"	0.002	0.976	0.002	0.972
3.0	1.29	"	0.001	0.982	0.002	0.979
3.5	1.48	"	0.001	0.987	0.001	0.985
4.0	1.67	"	0.001	0.990	0.001	0.988
"∞"	"∞"	"	0.000	1.000	0.000	1.000
0	0.14	600	0.024	0.779	0.024	0.781
0.5	0.33	"	0.012	0.871	0.013	0.867
1.0	0.52	"	0.007	0.921	0.008	0.914
1.5	0.71	"	0.004	0.949	0.005	0.943
2.0	0.90	"	0.002	0.965	0.003	0.960
2.5	1.10	"	0.002	0.975	0.002	0.971
3.0	1.29	"	0.001	0.982	0.002	0.979
3.5	1.48	"	0.001	0.987	0.001	0.984
4.0	1.67	"	0.001	0.990	0.001	0.988
"∞"	"∞"	"	0.000	1.000	0.000	1.000
0	0.14	800	0.021	0.774	0.021	0.777
0.5	0.33	"	0.011	0.870	0.011	0.863
1.0	0.52	"	0.006	0.920	0.006	0.913
1.5	0.71	"	0.003	0.948	0.004	0.942
2.0	0.90	"	0.002	0.965	0.002	0.959
2.5	1.10	"	0.002	0.975	0.002	0.971
3.0	1.29	"	0.001	0.982	0.001	0.979
3.5	1.48	"	0.001	0.986	0.001	0.984
4.0	1.67	"	0.001	0.990	0.001	0.988
"∞"	"∞"	"	0.000	1.000	0.000	1.000

Table A3.3: Theoretical and Experimental Values for Coil 4S above Aluminium

L_0 = 170 μH, r = 3.90 mm, Y_0 = 0.66.

Lift-Off (mm)	Y (corrected)	Freq. (kHz)	Theoretical Impedance $R/\omega L_0$	$\omega L/\omega L_0$	Experimental Impedance $R/\omega L_0$	$\omega L/\omega L_0$
0	0.09	200	0.043	0.775	0.047	0.762
0.5	0.22	"	0.026	0.846	0.029	0.835
1.0	0.35	"	0.017	0.890	0.019	0.882
1.5	0.47	"	0.012	0.920	0.013	0.914
2.0	0.60	"	0.008	0.940	0.009	0.936
2.5	0.73	"	0.006	0.955	0.006	0.951
3.0	0.86	"	0.004	0.965	0.004	0.962
3.5	0.99	"	0.003	0.972	0.003	0.970
4.0	1.12	"	0.002	0.978	0.002	0.976
"∞"	"∞"	"	0.000	1.000	0.000	1.000
0	0.09	400	0.033	0.759	0.036	0.746
0.5	0.22	"	0.020	0.836	0.022	0.826
1.0	0.35	"	0.013	0.884	0.014	0.876
1.5	0.47	"	0.009	0.916	0.009	0.910
2.0	0.60	"	0.006	0.938	0.006	0.933
2.5	0.73	"	0.004	0.953	0.004	0.949
3.0	0.86	"	0.003	0.963	0.003	0.961
3.5	0.99	"	0.002	0.971	0.002	0.970
4.0	1.12	"	0.002	0.977	0.002	0.976
"∞"	"∞"	"	0.000	1.000	0.000	1.000
0	0.09	600	0.028	0.752	0.031	0.735
0.5	0.22	"	0.017	0.832	0.019	0.815
1.0	0.35	"	0.011	0.882	0.013	0.869
1.5	0.47	"	0.007	0.914	0.009	0.905
2.0	0.60	"	0.005	0.936	0.006	0.930
2.5	0.73	"	0.004	0.952	0.005	0.947
3.0	0.86	"	0.003	0.963	0.003	0.959
3.5	0.99	"	0.002	0.971	0.002	0.968
4.0	1.12	"	0.001	0.977	0.001	0.975
"∞"	"∞"	"	0.000	1.000	0.000	1.000
0	0.09	800	0.025	0.748	0.027	0.729
0.5	0.22	"	0.015	0.829	0.017	0.813
1.0	0.35	"	0.010	0.880	0.011	0.868
1.5	0.47	"	0.006	0.913	0.007	0.905
2.0	0.60	"	0.004	0.936	0.005	0.292
2.5	0.73	"	0.003	0.951	0.003	0.947
3.0	0.86	"	0.002	0.962	0.002	0.959
3.5	0.99	"	0.002	0.971	0.002	0.968
4.0	1.12	"	0.001	0.977	0.001	0.975
"∞"	"∞"	"	0.000	1.000	0.000	1.000

Table A3.4: Theoretical and Experimental Values for Coil 2S above Mild Steel

L_0 = 13 μH, r = 1.25 mm, Y_0 = 2.56.

Lift-Off (mm)	Y (corrected)	Freq. (kHz)	Theoretical Impedance $R/\omega L_0$	$\omega L/\omega L_0$	Experimental Impedance $R/\omega L_0$	$\omega L/\omega L_0$
0	0.28	200	0.014	1.057	0.007	1.026
0.5	0.68	"	0.008	1.024	0.004	1.013
1.0	1.08	"	0.005	1.012	0.003	1.007
1.5	1.48	"	0.003	1.007	0.002	1.004
2.0	1.88	"	0.002	1.004	0.001	1.003
2.5	2.28	"	0.002	1.002	0.001	1.002
3.0	2.68	"	0.001	1.002	0.001	1.001
3.5	3.08	"	0.001	1.001	0.001	1.001
4.0	3.48	"	0.001	1.001	0.001	1.001
"∞"	"∞"	"	0.000	1.000	0.000	1.000
0	0.28	400	0.017	1.050	0.009	1.022
0.5	0.68	"	0.009	1.020	0.006	1.010
1.0	1.08	"	0.006	1.010	0.004	1.005
1.5	1.48	"	0.004	1.005	0.003	1.003
2.0	1.88	"	0.003	1.003	0.002	1.002
2.5	2.28	"	0.002	1.002	0.002	1.001
3.0	2.68	"	0.001	1.001	0.002	1.001
3.5	3.08	"	0.001	1.001	0.001	1.000
4.0	3.48	"	0.001	1.000	0.001	1.000
"∞"	"∞"	"	0.000	1.000	0.000	1.000
0	0.28	600	0.020	1.046	0.010	1.020
0.5	0.68	"	0.010	1.018	0.006	1.009
1.0	1.08	"	0.006	1.008	0.004	1.004
1.5	1.48	"	0.004	1.004	0.003	1.002
2.0	1.88	"	0.003	1.002	0.002	1.001
2.5	2.28	"	0.002	1.001	0.002	1.001
3.0	2.68	"	0.001	1.001	0.001	1.000
3.5	3.08	"	0.001	1.000	0.001	1.000
4.0	3.48	"	0.001	1.000	0.001	1.000
"∞"	"∞"	"	0.000	1.000	0.000	1.000
0	0.28	800	0.021	1.042	0.011	1.018
0.5	0.68	"	0.011	1.016	0.006	1.008
1.0	1.08	"	0.006	1.007	0.004	1.003
1.5	1.48	"	0.004	1.003	0.003	1.002
2.0	1.88	"	0.003	1.002	0.002	1.001
2.5	2.28	"	0.002	1.001	0.001	1.000
3.0	2.68	"	0.001	1.000	0.001	1.000
3.5	3.08	"	0.001	1.000	0.001	1.000
4.0	3.48	"	0.001	1.000	0.001	1.000
"∞"	"∞"	"	0.000	1.000	0.000	1.000

Table A3.5: Theoretical and Experimental Values for Coil 3S above Mild Steel

L_0 = 17 μH, r = 2.65, Y_0 = 0.6.

Lift-Off (mm)	Y (corrected)	Freq. (kHz)	Theoretical Impedance $R/\omega L_0$	$\omega L/\omega L_0$	Experimental Impedance $R/\omega L_0$	$\omega L/\omega L_0$
0	0.14	200	0.033	1.209	0.032	1.200
0.5	0.33	"	0.021	1.115	0.021	1.120
1.0	0.52	"	0.014	1.069	0.014	1.073
1.5	0.71	"	0.010	1.043	0.011	1.047
2.0	0.90	"	0.007	1.028	0.007	1.032
2.5	1.10	"	0.005	1.019	0.005	1.021
3.0	1.29	"	0.004	1.014	0.004	1.016
3.5	1.48	"	0.003	1.010	0.003	1.011
4.0	1.67	"	0.002	1.008	0.002	1.009
"∞"	"∞"	"	0.000	1.000	0.000	1.000
0	0.14	400	0.043	1.194	0.042	1.185
0.5	0.33	"	0.027	1.105	0.029	1.106
1.0	0.52	"	0.019	1.065	0.020	1.066
1.5	0.71	"	0.013	1.039	0.014	1.041
2.0	0.90	"	0.010	1.024	0.011	1.027
2.5	1.10	"	0.007	1.016	0.008	1.018
3.0	1.29	"	0.005	1.012	0.006	1.013
3.5	1.48	"	0.004	1.008	0.005	1.009
4.0	1.67	"	0.004	1.006	0.004	1.006
"∞"	"∞"	"	0.000	1.000	0.000	1.000
0	0.14	600	0.049	1.182	0.047	1.176
0.5	0.33	"	0.031	1.097	0.032	1.101
1.0	0.52	"	0.020	1.056	0.021	1.061
1.5	0.71	"	0.014	1.034	0.015	1.038
2.0	0.90	"	0.010	1.021	0.011	1.025
2.5	1.10	"	0.007	1.014	0.008	1.016
3.0	1.29	"	0.006	1.009	0.006	1.011
3.5	1.48	"	0.005	1.007	0.005	1.008
4.0	1.67	"	0.004	1.005	0.004	1.005
"∞"	"∞"	"	0.000	1.000	0.000	1.000
0	0.14	800	0.055	1.173	0.053	1.166
0.5	0.33	"	0.034	1.091	0.035	1.094
1.0	0.52	"	0.022	1.052	0.023	1.056
1.5	0.71	"	0.015	1.031	0.016	1.035
2.0	0.90	"	0.011	1.019	0.012	1.023
2.5	0.10	"	0.008	1.012	0.009	1.015
3.0	0.29	"	0.006	1.008	0.006	1.010
3.5	0.48	"	0.005	1.006	0.005	1.007
4.0	0.67	"	0.004	1.005	0.004	1.005
"∞"	"∞"	"	0.000	1.000	0.000	1.000

Table A3.6: Theoretical and Experimental Values for Coil 4S above Mild Steel

L_0 = 170 μH, r = 3.90 mm, Y_0 = 0.66.

Lift-Off (mm)	Y (corrected)	Freq. (kHz)	Theoretical Impedance $R/\omega L_0$	$\omega L/\omega L_0$	Experimental Impedance $R/\omega L_0$	$\omega L/\omega L_0$
0	0.09	200	0.036	1.235	0.034	1.235
0.5	0.22	"	0.027	1.154	0.026	1.157
1.0	0.35	"	0.020	1.105	0.019	1.104
1.5	0.47	"	0.015	1.074	0.015	1.075
2.0	0.60	"	0.012	1.053	0.011	1.052
2.5	0.73	"	0.009	1.039	0.008	1.037
3.0	0.86	"	0.008	1.030	0.007	1.030
3.5	0.99	"	0.006	1.023	0.004	1.022
4.0	1.12	"	0.005	1.017	0.004	1.015
"∞"	"∞"	"	0.000	1.000	0.000	1.000
0	0.09	400	0.047	1.218	0.045	1.221
0.5	0.22	"	0.034	1.142	0.034	1.144
1.0	0.35	"	0.026	1.096	0.024	1.097
1.5	0.47	"	0.019	1.067	0.019	1.067
2.0	0.60	"	0.015	1.048	0.015	1.049
2.5	0.73	"	0.012	1.035	0.013	1.036
3.0	0.86	"	0.010	1.026	0.009	1.026
3.5	0.99	"	0.008	1.019	0.007	1.019
4.0	1.12	"	0.006	1.015	0.006	1.015
"∞"	"∞"	"	0.000	1.000	0.000	1.000
0	0.09	600	0.055	1.206	0.052	1.220
0.5	0.22	"	0.039	1.132	0.039	1.140
1.0	0.35	"	*0.029*	*1.089*	*0.029*	*1.095*
1.5	0.47	"	0.022	1.062	0.022	1.066
2.0	0.60	"	0.017	1.044	0.018	1.046
2.5	0.73	"	0.013	1.032	0.014	1.034
3.0	0.86	"	0.011	1.023	0.011	1.025
3.5	0.99	"	0.009	1.017	0.009	1.019
4.0	1.12	"	0.007	1.013	0.006	1.014
"∞"	"∞"	"	0.000	1.000	0.000	1.000
0	0.09	800	0.060	1.195	0.059	1.210
0.5	0.22	"	0.043	1.125	0.043	1.134
1.0	0.35	"	0.032	1.083	0.032	1.090
1.5	0.47	"	0.024	1.057	0.023	1.062
2.0	0.60	"	0.018	1.040	0.018	1.043
2.5	0.73	"	0.014	1.029	0.014	1.031
3.0	0.86	"	0.011	1.021	0.011	1.023
3.5	0.99	"	0.009	1.016	0.008	1.017
4.0	1.12	"	0.007	1.012	0.007	1.012
"∞"	"∞"	"	0.000	1.000	0.000	1.000